EXPERIMENTAL AND COMPUTATIONAL STUDIES ON SENSING OF DNA DAMAGE IN ALZHEIMER'S DISEASE

By

Bayu Tri Murti

(Reg. No: 21557640)

Submitted in fulfilment of the requirements of the degree of Master of Applied Science: Chemistry in the Faculty of Applied Sciences at the Durban University of Technology

June 2017

DECLARATION

I **Bayu Tri Murti** declare that the thesis submitted for the degree of Master of Applied Science (M.App.Sci.): Chemistry at the Durban University of Technology is a result of my own investigation and has not already been accepted in substance for any degree, and is not being concurrently submitted for any other degree. All the work was done by the author.

Student Name: Bayu Tri Murti

Student Signatur [redacted] **Date:** 24/8/2017

Supervisor Name: Professor K. Bisetty

Signature: [redacted] **Date:** 24/8/17

Co-Supervisor Name: Assc. Prof. Ashutosh Tiwari, Linköping University (Sweden)

S [redacted] **Date:** 24/8/2017

ACKNOWLEDGEMENTS

First, I thank the Almighty Allah, the most gracious, the most merciful, for granting me a chance to follow His destiny for visiting this wonderful country and as a master's student at Department of Chemistry, Durban University of Technology. I praise unlimitedly for showering me with the patience and guidance in life, therefore keeping me on the track towards the right directions.

I would like to greatly thank my supervisor Professor K. Bisetty, Head, Department of Chemistry, Durban University of Technology. My best regards and gratitude to him for allowing me to join his dynamic research group and provided any support and guidance while studying and completing this research project under his supervision. His computational expertise has directed me to the new world of science and the synergy with experimental research enabled me to conduct this research work. His door always open whenever I needed guidance, and face to face discussions related to my research and any other matters. Thank you for helping me to complete this thesis with patience, constructive suggestions, and all matters.

It is my privilege to express my gratitude and indebtedness to my co-supervisor Professor Ashutosh Tiwari, Associate Professor and Group Leader, Smart Materials and Biodevices at the world premier Biosensors and Bioelectronics Centre, IFM-Linköping University, Sweden, for his valuable assistance, critics, motivation, inspiration, and direction towards experimental section of my research. His keen sense of scientific thought and publications are source of inspiration to me.

Further, I thank the Centre of High Performance Computing (CHPC), Cape Town, South Africa for providing tremendous computational powers and facilities related to my work.

My special thanks goes to all member and former member of Computational Modeling and Bio-analytical Chemistry (Dr. Suvardhan Kanchi, Myalowenkosi I. Sabela, Dr. Mohammad Shahbaaz, Dr. Deepali Sharma, Athika Darumas Putri, Nosipho Cele, Kwanele Kunene, Keval Balgobind etc.) for the knowledgeable and supportive discussions.

I would like to express my gratitude to the Durban University of Technology for providing me financial assistance.

My heartfelt thanks to the embassy of Indonesia in South Africa (Mr. Suprapto Martosetomo as ambassador, Mr. Michael Pasaribu, Mr. Maulana, Mr. Choyrul Anam etc.), all Indonesian (Lalu Irham, Salman Al Farisi, Mrs. Maryam Danka, Mrs. Suki Muller, Mrs. Leli etc.), South African friends (Sulayman, Waseem Khan, Adilla, Hassan Aboud etc.) and colleagues (Mr. Yunus Vawda, Mrs. Salma Vaheed, Faiz Ansari, Poonam, Dr. Abhiseek, Dr. Anand, Sureesh, Muthu, Vasant, Arul, Nandha, Bibuthi, Dr. Raam, Venkat, Kunle Oparinde, Dennies Ochieng etc.) for unconditional support for the duration of my stay in Durban.

I dedicate this thesis to my lovely mother Satir Radiah and father Adi Rahtomo, as well as to my beloved brother Ifan Huzaini as of their prodigious supports through prayers, loves, and cares. I thank Allah for them, they are absolutely great blessings.

Bayu Tri Murti

ABSTRACT

DNA damage plays a pivotal role in the pathogenesis of Alzheimer's disease (AD) therefore, an innovative ss-DNA/dopamine/TiO_2/FTO electrode strategy was developed to detect the genotoxicity upon photocatalytic reactions. This study involves a computational and electrochemical investigation towards the direct measurement of DNA damage. Computational chemistry was useful to resolve the intricate chemistry problems behind electrode constructions. The computational protocols were simultaneously carried out comprising of density functional theory (DFT) calculations, Metropolis Monte Carlo (MC) adsorption studies, and molecular dynamics (MD) simulations. The DFT calculations elucidated the structural, electronics, and vibrational properties of the electrode components resulting in a good agreement with the experimental parameters. The MC simulations carried out using simulated annealing predicted the adsorption process within layer-by-layer electrode as well generating reliable inputs prior to MD simulations. A 100 ns MD simulations were performed using a canonical ensemble provided information on the thermodynamics parameters such as total energy, temperature, and potential energy profiles, including radius of gyrations and atomic density profiles. Binding energies calculated from the MD trajectories revealed increasing interaction energies for the layer-by-layer electrode, in agreement with the electrochemical characterization studies (i.e. gradual decrease of cyclic voltammogram (CV) as well as increasing diameter of electrochemical impedance spectroscopy (EIS) semicircle upon electrode modification). The higher binding energies may lead to smaller changes in the electrochemical polarizability which directly affect to the decreasing of redox peak current and charge transfer resistance enhancement. Instead, HOMO-LUMO DFT levels are also taken into account to explain electron transfer

phenomena within layer construction leading to the alteration of CV behaviours. Experimentally, the ss-DNA was electronically linked to TiO_2/FTO surface through dopamine as a molecular anchor. Electrochemical measurements using cyclic voltammetry and EIS were employed to characterize the electrode modifications. The square wave voltammetry was subsequently used to measure the DNA damage and the potency of antioxidant treatment using ascorbic acid (AA) due to its ability in protecting the DNA from the damages. The presence of AA significantly protected the DNA from the damage, therefore was able to be used as a potential treatment in AD. Theoretically, guanine residues predicted by DFT as the most reactive sites of the ss-DNA involved in the genotoxic reactions. Overall, the theoretical studies successfully validated the experimental study as well as providing the molecular basis of interaction phenomena towards electrode constructions. Our results highlight the potential application of this methodology to screen the genotoxicity in Alzheimer's, suggesting the important role of theoretical studies to predict the molecular interaction and validation of the DNA-based sensors and bioelectronics.

LIST OF CONFERENCE PRESENTATIONS AND PUBLICATIONS

Poster Presentations

10th Center for High Performance Computing (CHPC) National Meeting held at ICC, East London, South Africa. 5th to 9th December **2016**. "Computational Study of The Regioselective Dopamine Adsorption onto Multilayer Surface of FTO/TiO_2".

10th Center for High Performance Computing (CHPC) National Meeting held at ICC, East London, South Africa. 5th to 9th December **2016**. "A DFT Study of The Interaction of Functionalized Graphene Oxide with DNA/RNA Nucleobases".

Publications

Athika Darumas Putri, **Bayu Tri Murti**, Suvardhan Kanchi, Krishna Bisetty, and Myalowenkosi I. Sabela. **2017**. Nanopolymer Chitosan in Cancer and Alzheimer Biomedical Application. *In:* Shakeel Ahmed & Saiqa Ikram (eds.) *Chitosan: Derivatives, Composites and Applications.* USA: John Wiley & Sons - Scrivener Publishing LLC (ISBN: 1119363500, 9781119363507).

Bayu Tri Murti, Ashutosh Tiwari, and Krishna Bisetty. Experimental and Computational Studies on Sensing of DNA Damage in Alzheimer's Disease (in preparation).

Bayu Tri Murti, Athika Darumas Putri, Krishna Bisetty, and Ashutosh Tiwari. Recent Development in Alzheimer's Biosensor (in preparation).

Bayu Tri Murti, Athika Darumas Putri, Krishna Bisetty, and Ashutosh Tiwari. Density Functional and Molecular Docking Studies of Drug-Loaded PEGylated-Prospective Nanomaterials onto Active Site of BACE1 Protein: A Comparative Study for Alzheimer's Drug Nanocarrier (in preparation).

Athika Darumas Putri, **Bayu Tri Murti**, Krishna Bisetty, and Ashutosh Tiwari. Computational Studies of MK-8931-Carbon Nanotube Complex in Inhibiting β-Secretase Activity (in preparation).

TABLE OF CONTENTS

LIST OF FIGURES

LIST OF TABLES

LIST OF ACRONYMS AND SYMBOLS

AD	Alzheimer's Disease
ss-DNA	Single-stranded Deoxyribonucleic Acid
RNA	Ribonucleic Acid
ROS	Reactive Oxygen Species
QM	Quantum Mechanics
DFT	Density Functional Theory
MM	Molecular Mechanics
MC	Metropolis Monte Carlo
MD	Molecular Dynamics
GGA	Generalized Gradient Approximation
PBE	Perdew-Burke-Ernzerhof
B3LYP	Becke 3-parameter exchange-correlation functional; Lee, Yang, and Parr
GSH	Gluthatione
CSF	Cerebrospinal Fluids
MRI	Magnetic Resonance Imaging
NFT	Neurofibrillary Tangle
BACE	β-Amyloid precursor protein Cleaving Enzyme
POC	Point-of-Care
EIS	Electrochemical Impedance Spectroscopy
LOD	Limit of Detection
MWCNT	Multi-Walled Carbon Nanotube
SWV	Square Wave Voltammetry
LSPR	Localized-Surface Plasmon Resonance
ELISA	Enzyme-Linked Immunosorbent Assay
FTO	Fluorine-doped Tin Oxide
DA	Dopamine
SCF	Self-Consistent Field
PBC	Periodic Boundary Conditions
HF	Hartree-Fock
LDA	Local Density Approximation
DNP	Double Numerical plus Polarization
DFTB	Density Field-based Tight Binding
COMPASS	Condensed-phase Optimized Molecular Potentials for Atomistic Simulation Studies
UFF	Universal Force Field
NVT	The constant-Number of particles, Volume, and Temperature ensemble
MS	Material Studio software
DS	Discovery Studio software
IR	Infra-red
DSPP	DFT-Semi Core Pseudopotential
DOS	Density of State
p-DOS	Partial Density of State
t-DOS	Total Density of State
CBM	Conduction Band Minimum
VBM	Valence Band Maximum
3D	3-Dimensional
SEM	Scanning Electron Microscope
UV	Ultraviolet

XRD	X-ray Diffraction
AA	Ascorbic Acid
LAMMPS	Large-scale Atomic/Molecular Massively Parallel Simulator
AMBER	Assisted Model Building with Energy Refinement

CHAPTER 1

INTRODUCTION

This chapter provides details about Alzheimer's disease (AD), an incurable neurodegenerative disorder which can slowly cause brain problems resulting in a decrease of memory, thinking, and behaviour. The causes of AD and the current progress of the therapies and diagnosis are included in this section. This chapter also provides an overview of DNA damage by reactive oxygen species (ROS) in AD to better understand the underlying molecular process of DNA damage induced by free radicals. Previous reports of diagnostic approaches toward Alzheimer's dementia, present focus of the research community, and the *state-of-the-arts* have been discussed briefly. Furthermore, the synergies between computational chemistry tools in relation to DNA sensor systems developed for the early detection of AD are presented in this section. This is followed by the aims and objectives and a brief outline of the thesis.

1.1 Alzheimer's Disease

Alzheimer's disease corresponds to an extremely harmful and incurable neurodegenerative disorder which can slowly cause brain problems, resulting in a decrease of memory, thinking and behaviour (de la Torre, 2010). AD is not a normal part of ageing (Alzheimer's Association, 2015) and belongs to dementia. As the most probable evidence of dementia, AD has spread out extensively all over the world. According to Alzheimer's Disease International, the people who suffered from dementia worldwide in 2016 was reported at 47 million, predicted to gain 74.7 million in 2030, and 131.5 million in 2050 (Azheimer's

Disease International, 2016). Among these reports, 60 - 70% of the evidence contributes to Alzheimer's (Duthey, 2013).

During the last decade, studies on Alzheimer's neuropathology have suggested its intimate association with oxidative stress (Santos *et al*., 2012) since oxidative impairment of oligonucleotide (i.e. DNA) plays a vital role in ageing and neurodegenerative diseases. Studies for the essential role of oxidative stress have been specified from examining damages to various biomolecular components of the brain by oxygen-derived free radicals (Gabbita *et al*., 1998). The outbreak on DNA by ROS, predominantly -OH radicals yielding DNA damage, can lead to DNA and protein related damages, sister chromatid translocation and exchange, as well as in the production of more than 20 (twenty) oxidized-based adducts (Markesbery and Lovell, 2006). Gella and Durany have reported that corroboration of Alzheimer's oxidative stress are demonstrated through the abundance of oxidized proteins, advanced glycation and lipid peroxidation end products, establishment of several toxic species, and oxidative alterations in mitochondrial and nuclear DNA (Gella and Durany, 2009).

Tremendous scientific data have supported the oxidative stress associated with dementia, mainly *via* molecular, biochemical, and genetic studies (Coyle and Puttfarcken, 1993, Christen, 2000). Studies have shown the increment of specific biomarker levels of oxidative damage, mitochondrial disruption, gene mutation, modification of the specific antioxidant systems, and numerous linkages within amyloid plaques and oxidative stress (Gella and Durany, 2009, Pohanka, 2014a). Nevertheless, previous studies have not successfully demonstrated an explicit advantage of antioxidant intervention in dementia (Polidori and

Schulz, 2014), particularly for Alzheimer's (Galasko *et al*., 2012, Persson *et al*., 2014), regardless of its clinical approaches. Therefore, there is a need for further research towards discovering the role of antioxidant therapy in Alzheimer's and the detection of DNA damage (rather 'diagnosis') over its early pathogenesis in order to the effectively obviate the disease.

In the past 20 years, sensor technology has been widely driven in the field of diagnostic area of many diseases including AD. Several reports on Alzheimer's biosensor have been revealed which were enable to reach optimum level of detection performance comprising of different transducer's type i.e. electrochemical-, plasmonic-, immuno-, fluorescent-, optical sensors etc. Among many, electrochemical biosensor seems to be frequent technique due to the capability of achieving extreme detection limit down to picomolar (Lin *et al*., 2011, Pohanka *et al*., 2013, Rushworth *et al*., 2014, Liu *et al*., 2014, Liu *et al*., 2015, Kurzątkowska *et al*., 2016) and even femtomolar concentrations (Diba *et al*., 2017). Indeed, specific biomarkers have been incorporated towards *state-of-the-art* of Alzheimer's electrochemical biosensor including amyloid-β (Aβ), acetylcholinesterase enzyme, S100B protein, ApoE, brain glutamate, DNA, dopamine, brain metals, nicotine, tau protein, and Aβ precursor protein cleaving enzyme. Several of them have been remarkably used for routine analysis, therefore open a closer pave way to POC diagnostics of Alzheimer's. However, the recent findings still remain critical issues to be resolved, mainly about the capability of the device to detect biomarkers in very early stage of the Alzheimer's as the key of preventing and curing the disease. To do so, the DNA-based biosensor have been developed herein, towards the detection of DNA breakdown occurred in early stage of Alzheimer's followed by a better understanding of underlying molecular processes, characterization, and validation of the method using computational chemistry tools.

Complementarily, computational modeling is currently emerged to validate the experimental findings, especially in biosensor, through simulation of the systems ranging from small molecules to macromolecules, including metal-based nanoclusters and nucleotide-based structures. The use of high performance computing in conjunction with complex and well-organized numerical algorithms renders computational modeling to be an effective way to resolve intricate problems of chemical and biological natures (Ramachandran *et al*., 2008). In general, this technique can provide useful information such as structural, electronic, and vibrational properties of atoms, molecules, or nanoclusters thereby enabling the validation of experimental results (Young, 2001). As a part of quantum mechanical (QM) method, density functional theory (DFT) is the most commonly used technique in computational studies. DFT calculations can be used to study the influence of particle's size on the structure and properties of nanomaterials. DFT is also an attractive tool to predict electronic structure, such as conductivity, and other related properties of transition metal complexes (Harvey, 2006) including macromolecule-like DNA duplexes (Tsukamoto *et al*., 2009).

On the other hand, molecular mechanics (MM) is also a well-known technique to simulate the behaviour of large macromolecular systems. Theoretically, MM approach refers to the use of modest potential-energy functions to predict a molecular system (Adcock and McCammon, 2006). Among various techniques of MM, Metropolis Monte Carlo (MC) adsorption study and molecular dynamics (MD) simulations are two profitable techniques used to mimic the experimental circumstances and therefore, can accurately predict the interactions within molecules on the designed system. MC is a specific type of MM simulation on the basis of repetitive random sampling followed by statistical analysis in order to calculate the computed descriptors. This particular method can reproduce an accurate

result related to arbitrary experiment which is previously unknown (Raychaudhuri, 2008). Furthermore, MD is a key tool in biomolecular and material chemistry simulations which enables the prediction of the time evolution for a system of interacting particles i.e. atoms, solids, molecules etc. (Allen, 2004).

Herein, we have successfully constructed a novel sensing method based on layer-by-layer system for ultradetection of Alzheimer's DNA damage using the innovative electrode composing of fluorine-doped tin oxide (FTO), TiO_2, dopamine (DA), and single-stranded DNA (i.e. ss-DNA/DA/TiO_2/FTO). Dopamine is well-known as an anchor molecule in a triad system of macromolecules (i.e. oligonucleotide or protein) and TiO_2 nanoclusters. Moreover, FTO and TiO_2 have been widely employed in several applications such as gas sensor, solar energy, etc., due to their excellent photocatalytic features (Hartnagel *et al*., 1995, Fujishima *et al*., 2000, Pelaez *et al*., 2012). In this study, the constructed electrochemical electrodes were fashioned to detect the DNA breakdown under visible light penetration. In order to obtain better understanding of the sensing phenomena and molecular interactions within layer-by-layer component of the constructed electrode, a series of computational calculations have been performed. The DFT calculations followed by MC and MD simulations have been conducted to provide the sophisticated grasp of molecular interaction either in atomic or molecular level of the layer-by-layer mechanism. Overall, the computational studies have been successfully reproduced effective evaluation and validation to the constructed ultrasensitive detection method relied on a novel electrochemical sensors strategy in DNA damage experiments. The overall workflow of the current computational research is depicted in **Figure 1.1**, while the scheme of electrode modification and electrochemical measurements are represented in **Figure 1.2**.

1.2 Aims and Objectives

This study is aimed at developing a new ultrasensitive detection of ROS-mediated DNA oxidation damage applied to screen the genotoxicity of new bio-conjugations and to monitor the oxidative damages in AD using ascorbic acid as antioxidant.

The objectives of this thesis are to:

- Fabricate a biosensor for DNA damage detection in Alzheimer's.
- Perform characterization studies of the developed biosensor.
- Predict the adsorption process.
- Perform validation studies using DFT calculations.
- Perform MD studies to predict nanomaterials or molecules behaviour under certain circumstances i.e. temperature etc.

This study involved computational and experimental works towards the development of sensor approach in detecting the DNA damage in AD. Since this project formed part of a collaboration between Sweden and South Africa (SA), all computational studies were undertaken at Durban University of Technology, while the experimental work involving electrode construction, characterization, and electrochemical studies were done at Linköping University, Sweden (Imani *et al*., 2014).

1.3 Thesis Outline

This thesis is divided into seven chapters. Following the introduction, further chapters in this thesis are divided as follows:

Chapter 2-Literature Review

The chapter describes the literature survey of the study including an insightful understanding of AD and its evidence. Additionally, the *state-of-the-art* electrochemical biosensor applications in the detection of Alzheimer's biomarkers are presented including the use of recent nanomaterials in Alzheimer's biosensor.

Chapter 3-Theoretical Principles

This chapter deals with the theoretical principles underlying the computational study. More specifically, it focuses on the equations and rigorous foundation of theoretical studies in relation to sensing applications of AD.

Chapter 4-Materials and Methods

A description of the materials and methods used in the design of computational and experimental works is presented in this chapter. For the computational work, the three foremost studies were employed i.e. DFT, MC adsorption studies, and MD simulations. Whilst, the four-folds of observations were involved in the experimental study including fabrication of modified electrode, characterization studies, measurement of DNA damage, and examination of ascorbic acid on DNA protection ability.

Chapter 5-Results and Discussion

A discussion of the results obtained from the computational and experimental methods is presented here. Moreover, the synergies between computational and experimental studies is also discussed.

Chapter 6-Concluding Remarks and Future Perspectives

A summary of the overall conclusions is presented in this chapter. This also deals with future perspectives.

Chapter 7-References

Finally, the last chapter comprises of a list of references cited throughout this thesis.

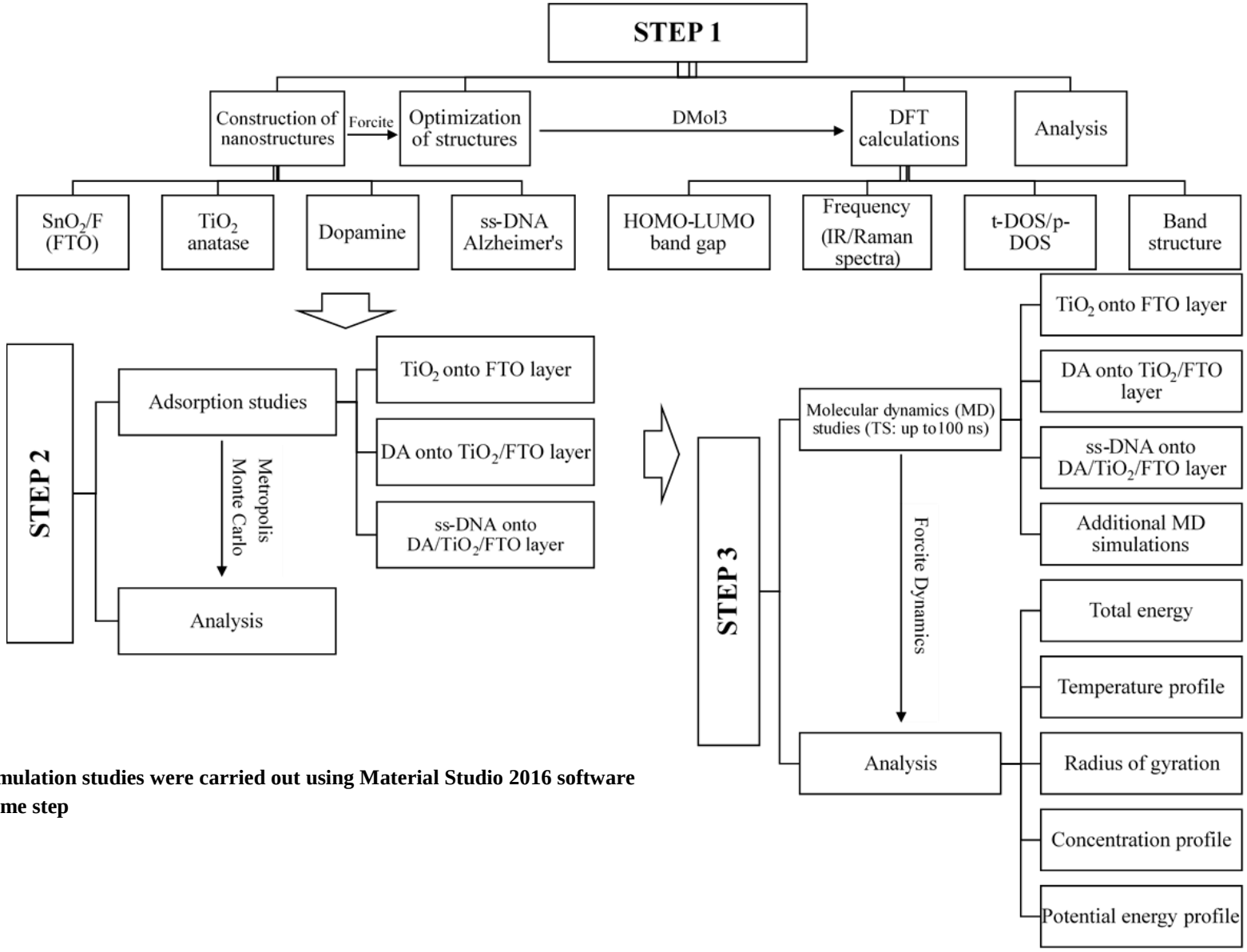

***All simulation studies were carried out using Material Studio 2016 software**
***TS: time step**

Figure 1.1 Computational workflow of the present study.

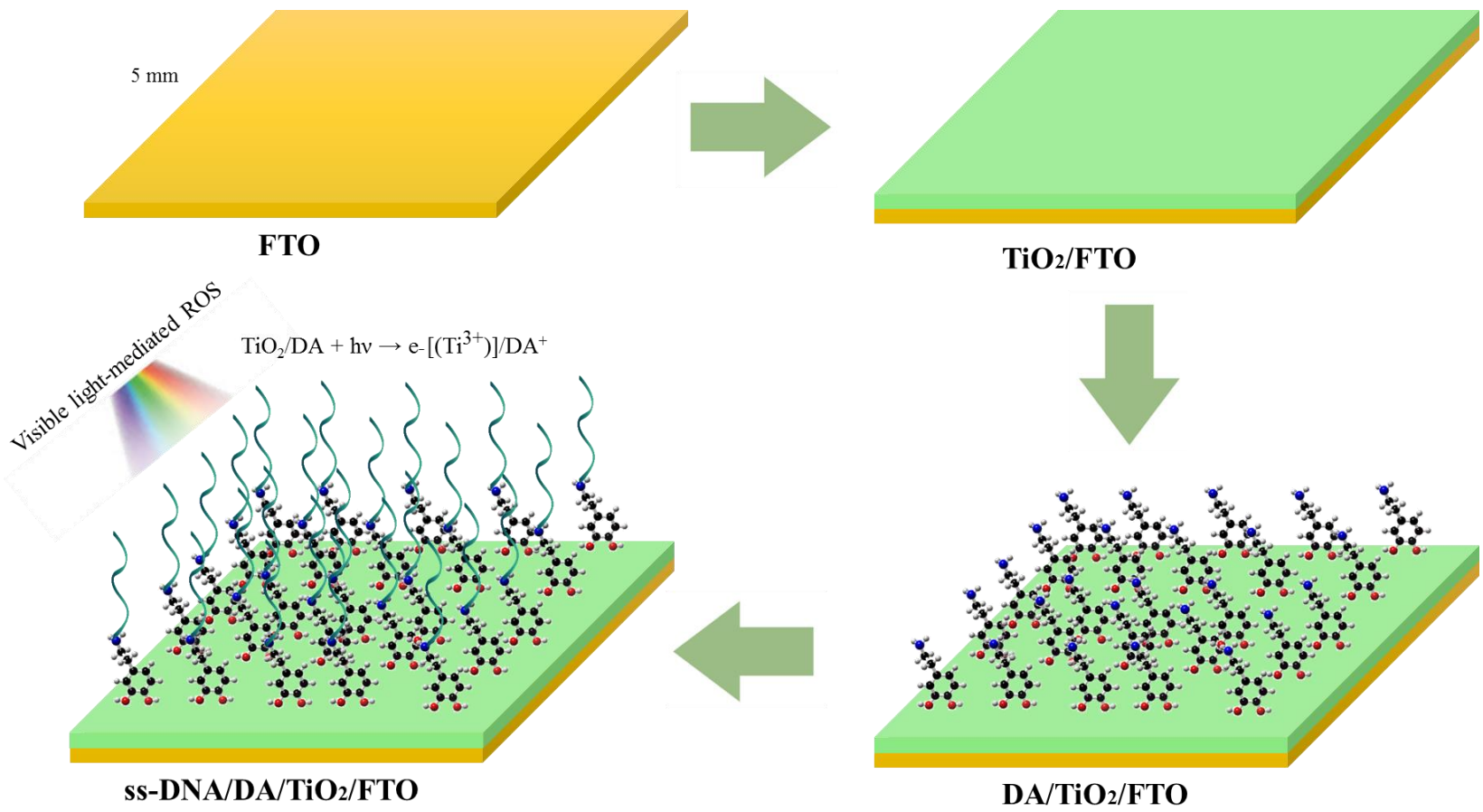

Figure 1.2 Scheme for electrode modification and electrochemical measurement.

CHAPTER 2

LITERATURE REVIEW

This chapter highlights an overview of Alzheimer's disease (AD) comprising of the historical aspects, general understanding, its correlation with dementia, the global evidence, pathogenesis, and current biomarkers. A review of recent diagnostic methods including electrochemical biosensor applications particularly aimed at the use of primary (amyloid-β (Aβ) acetylcholinesterase (AChE), and Aβ precursor protein cleaving enzyme (BACE1)) and secondary (S100B, apolipoprotein E (ApoE) gene, brain glutamate, DNA, dopamine, brain metals, nicotine, and tau proteins) biomarkers is also presented. Recent developments using nanomaterials in diagnostics of AD either through *in vitro* or *in vivo* applications are also highlighted in this section. Additionally, current trends in utilizing nanomaterials to construct biosensors for Alzheimer's including carbon nanostructures (e.g. carbon nanotube, graphene, graphene oxide etc.), inorganic nanomaterials (e.g. gold nanoparticles), and quantum dots are included. The focus of this review is aimed at novel applications of nanomaterials such as fluorine doped tin oxide (FTO) and TiO_2 in the applications of biosensor architecture in the early detection of AD.

2.1 Historical Aspects

Alzheimer's disease was firstly introduced by Dr. Aloysius Alzheimer, a German psychiatrist and neuropathologist in 1906 at a conference in Tübingen, Germany (Alzheimer *et al*., 1995, Korolev, 2014). In his remarkable lecture, Alzheimer presented a 51-year-old woman patient who suffered from a disruptive cognitive damage, hallucinations, and lack of psychosocial ability. He, in his laboratory observation, found arteriosclerotic alterations and

neurofibrillary tangles at patient's necropsy. In respect to his noteworthy observation, the eponym of 'Alzheimer' was used to term this impairment known as dementia today (Kraepelin, 1910, Maurer *et al.,* 1997).

2.2 Alzheimer's Disease

The distinctive clinical manifestation of Alzheimer's is deficit of cognitive and memory functions, eventually leading to the loss of the patient's independence and therefore, triggering a serious personal problem of Alzheimer's sufferer as well as their family/care giver. In the United States (USA), the costs of AD in 2010 amounted to over $172 billion and is estimated to reach a trillion dollars by 2050, unless developments on the diagnosis and treatment are augmented (Bateman *et al*., 2012).

In this particular disorder, neuronal impairment ultimately attacks the brain's part, which is responsible for basic physical functions such as swallowing and walking. The cronical stage of Alzheimer's can lead to the patients being bed-bound and therefore, require a full time care giver (Alzheimer's Association, 2015). Currently, early detection of Alzheimer's has been defined as the key step to preventing, reducing, and probably discontinuing this neurodegerative disorder. Therefore, tremendous efforts have been conducted in order to overcome early stage detection obstacles of Alzheimer's during the last decade (Albert *et al*., 2011, Sperling *et al*., 2011, Jack *et al*., 2011, McKhann *et al*., 2011).

2.3 Dementia and Its Correlation with Alzheimer's

Dementia is a collection of co-occurring symptoms and signs which includes progressive decline of cognitive functions. Several intellectual abilities can be damaged including

language ability, memory and perceptive function, visuospatial function, decision construction, orientation, and attention. In individuals with dementia, impairment on the cognitive functions are attended by emotional control, personality alteration, and social manners. Importantly, the intellectual and behavioral changes of dementia impacts on the social activity, workload, and the lack of abilities to accomplish daily activities such as cooking, eating, managing finance, housekeeping, shopping, driving etc. (Gilman and Manji, 2010).

There are several roots of dementia which are distinguished as reversible and irreversible causes (Gilman and Manji, 2010, Larson, 2015). The reversible dementias (also referred to as 'pseudo-dementias') are relatively rare but potentially treatable and secondary including depression, nutritional deficiencies (e.g. vitamin B12), metabolic and endocrine disorders (e.g. hypothyroidism), space occupying lesions (e.g. brain tumor), normal pressure hydrocephalus, or substance abuse. Certain classes of medications also potentially cause cognitive impairment in elderly patients such as anti-cholinergic, psychotropic, analgesics, sedative-hypnotics. On the other hand, irreversible (primary) dementia encompasses neurodegenerative and/or vascular processes in the brain. Alzheimer's is the leading cause of irreversible dementia, counting up to 70% of all cases in the USA (Plassman *et al*., 2007). Other types of primary dementia include vascular dementia (10-20%), Parkinson's disease related to dementia, frontotemporal dementia, and Lewy body dementia (Korolev, 2014).

2.4 Global Evidence of Alzheimer's Disease

The increase in Alzheimer's worlwide has noted the increasing number (rather 'population') of elderly people, ageing baby boomers, and lengthier life expectancies (Alzheimer's

Association, 2015). Further, ageing is deliberated as a major jeopardy leading to Alzheimer's. The underlying mechanisms of the ageing process in AD progression are not fully understood (Mao and Reddy, 2011). In fact, there are other factors influencing the evidence of AD i.e. economic issue (poverty), genetic (DNA), education, and gender type (Alzheimer's Australia, 2003, Alzheimer's Disease Education and Referral Center, 2015, Alzheimer's Association, 2015).

As the most probable number of dementia, AD has spread out across various countries world wide. The statistical figure of Alzheimer's prevalence was well-reported in which majority affected the developing; low- and middle-income countries (**Figure 2.1**) (Alzheimer's Disease International, 2015). In the USA, prevalence was estimated at over 5.4 million in 2015, and as many as 13.8 million (an increase of almost 3-fold) are projected to have Alzheimer's in 2050, excluding the development of curative breakthroughs either prevention or curing the disease (Alzheimer's Association, 2016).

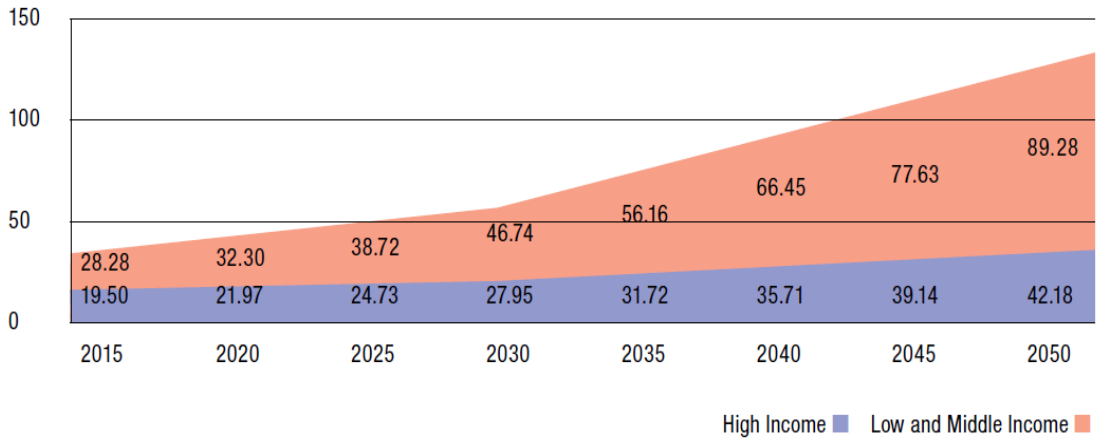

Figure 2.1 Progress of individuals with dementia (in million) comprising high-, low-, and middle-income countries (Alzheimer's Disease International, 2015).

Projected prevalence for people aged 60 years and above can be directly evaluated within 21 Global Burden of Disease regions, between 2009 and 2015 estimation (**Figure 2.2**). The uppermost areas with high incidences of dementia were found in North Africa or Middle East and Latin America with total prevalences of 8.7% and 8.4%, respectively, while the lowermost prevalence was in Central Europe with 4.7% total prevalence. Other regions showed a moderately similar in prevalence ranging from 5.6% to 7.6% (Alzheimer's Disease International, 2015). The prevalence for East Asian and sub-Saharan African regions increased from the range of 4.98% to 6.99% and 2.07% to 4.00%, to 4.76%, respectively. The recent data, as the availability of more updated information, showed a decrease in variation among world regions (World Health Organization, 2015). However, the prevalence was also augmented by the increment of age, growing from 3% for 65-74 years, to nearly 50% for those 85 or over (Evans, 1990, Small *et al*., 1998).

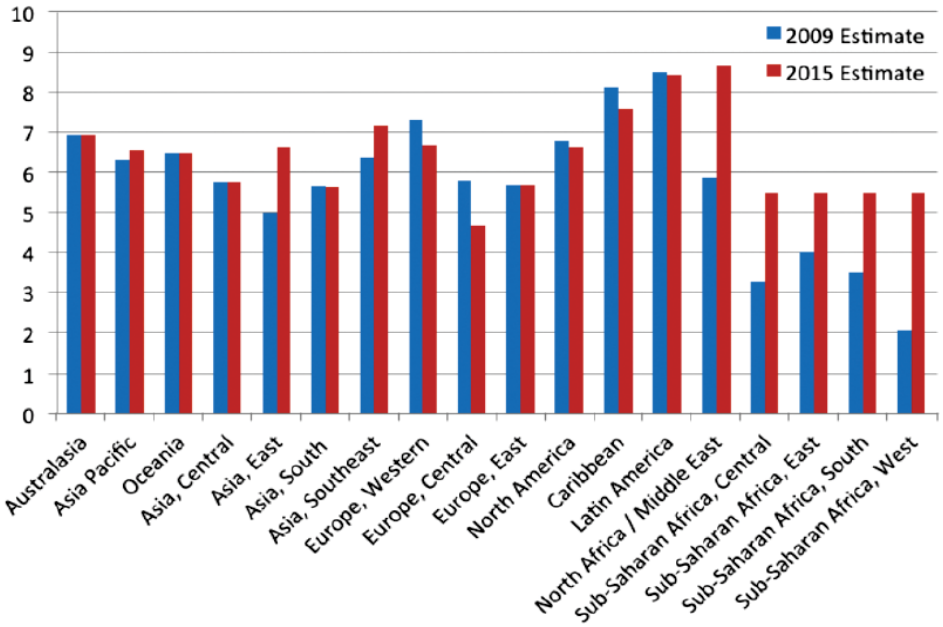

Figure 2.2 The demography of people suffering from dementia among those aged 60 and over. The data was provided by Global Burden of Disease region through standardization with Western Europe population (Alzheimer's Disease International, 2015).

2.5 Alzheimer's Pathogenesis *via* Oxidative Stress

To-date, the origin of Alzheimer's is clearly undefined (Williams, 2013). Therefore, the remedy to effectively block the initiation and progression is ongoing (de la Torre, 2010). Among several hypotheses, oxidative stress is one of the foremost basis due to its involvement in numerous psychiatric and somatic pathological states (Padurariu *et al*., 2013). Oxidative stress is described by a disproportion in reactive oxygen species (ROS) radical production and anti oxidative defence. Both incidences are considered to play vital roles in regulation of cognitive impairment and neurodegeration (Barnham *et al*., 2004, Sayre *et al*., 2008). The damage on memory functions associated with a reduction of antioxidant's defence ability in the plasma and brain (Perrig *et al*., 1997, Berr, 2000). Gluthatione (GSH) has a vital role herein, (Thornalley, 1998) due to electron donation to ROS and therefore, scavenge the free radicals. According to *in vivo* studies, the concentration of intracellular GSH reduces along with the age increment (Sandhu and Kaur, 2002, Wang *et al*., 2003, Donahue *et al*., 2006, Zhu *et al*., 2006). The reduction of GSH leads to overproduction of ROS over antioxidant ability, producing an oxidative stress. Another cause of this oxidative stress is in the discrepancy of the radical detoxifying enzymes in Alzheimer's (Gsell *et al*., 1995).

DNA damage, involving altered abasic sites, bases, and single- and double-stranded nucleotide disruptions, has been observed as neurotoxic factors in either ageing or pathogenesis of Alzheimer's (McKinnon, 2013, Madabhushi *et al*., 2014). DNA bases are susceptible to the oxidative damage including protein carbonylation, hydroxilation, and nitration (Collins *et al*., 1996, Gabbita *et al*., 1998, Lovell and Markesbery, 2007). ROS stimulates Ca-influx, *via* glutamate receptors and activates an excitotoxic response facilitating cell apoptosis (Mattson and Chan, 2003). ROS are produced upon the reactions

within oxygen and unregulated redox-active metals (White *et al*., 2006).

Oxidation of DNA and RNA is manifested by increment of 8-hydroxyguanosine and 8-hydroxy-2-deoxyguanosine levels (Nunomura *et al*., 1999, Lovell *et al*., 1999, Nunomura *et al*., 2001). Furthermore, these markers have been localized in both of neurofibrillary tangles (NFTs) and Aβ plaques (Mecocci *et al*., 1994). Interestingly, the increment on level of DNA strand breaks caused by oxidative damage has been discovered in Alzheimer's. This phenomenon is consistent with the increased levels of free carbonyls in the glia and neurons. Instead, the production of antioxidant enzyme, heme oxygenase-1, is also increased and is firmly associated with NFTs (Gella and Durany, 2009). In addition, DNA damage markers could be useful to distinguish people with Alzheimer's and other types of dementia as well as to discriminate Alzheimer's patient with healthy individuals (Malpass, 2012). DNA damage, apart from Alzheimer's biomarker, is a leading detection factor (rather 'sensing') of Alzheimer's in extremely early stages which can be interogated for further therapy. The description with regards to general biomarkers and the *state-of-the-art* of biomarker-based biosensor systems are highlighted in the subsequent sections.

2.6 Alzheimer's Biomarkers

Currently, observation on Alzheimer's biomarkers has been critical towards a successful diagnostic and therapeutic interventions, as well as exhibiting a pivotal role in preventive strategies. A clear understanding of the biomarker may provide a 'guarantee' to define Alzheimer's diagnosis and prognosis. Despite the recent clinical research failure to give a clear explanation for the exact biomarkers which are responsible for Alzheimer's (because of the variation of cohort while it was applied for clinical studies etc.) (O'Bryant *et al*., 2015),

it still plays a pivotal role in its early stage diagnosis. Since the last decade, the discovery on reliable biomarkers for the diagnosis and prognosis purposes has grown rapidly. Most of them are related to cerebrospinal fluid (CSF) and neuroimaging (Thal *et al*., 2006). In terms of Alzheimer's biomarker, there are two major classifications accepted by researchers and clinicians based on sample collection; blood-based biomarker (BbB) and neuroimaging (O'Bryant *et al*., 2015). In another report, the biomarker was divided into three groups viz., molecular neuroimaging, structural magnetic resonance imaging (MRI), and CSF (Dubois *et al*., 2007) which basically belongs to proteins, enzymes, metabolites, etc. In addition, BbB is also classified as biomarker due to several reported works (Ray *et al*., 2007, O'Bryant *et al*., 2015). According to the Alzheimer's theranostics, the two main biomarkers might be classified which are primary and secondary (downstream) biomarkers (Blennow *et al.*, 2014). Primary biomarkers can be used to define specific biochemical change upon the drug treatment e.g. Aβ, AChE, and BACE1, while the secondary type refers to biomarkers used to determine the downstream effect of the primary target of the drug e.g. S100B, ApoE gene, brain glutamate, DNA, dopamine, brain metals, nicotine, and tau proteins. The scheme of recent biochemical markers used in Alzheimer's detection is depicted in **Figure 2.3**, while the details including the advantages and limitations of each biomarker are presented in **Table 2.1** below.

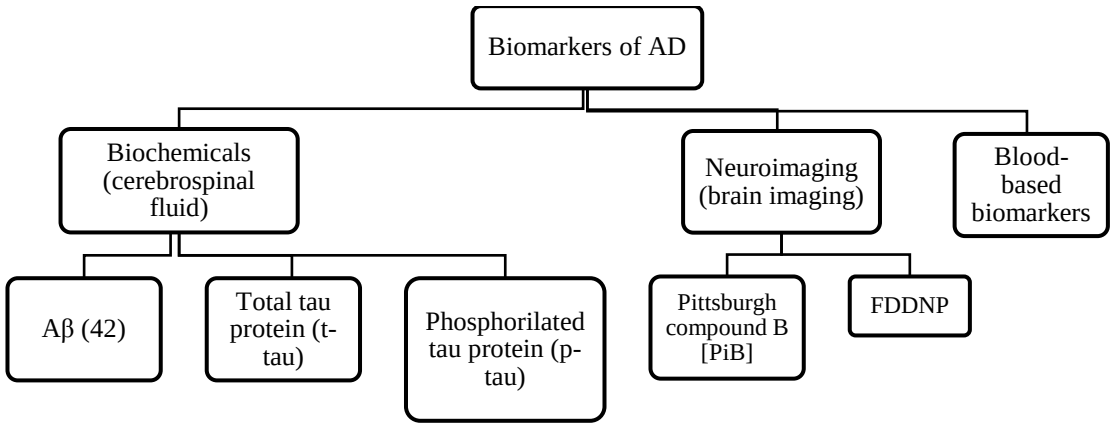

Figure 2.3 Biomarkers for the detection of Alzheimer's.

Recently, most of the research in biomarkers has relied on either fluid-based or brain imaging biomarkers. Brain imaging biomarkers give a reliable result for diagnosing AD, but it is very expensive and needs special handling for the laboratory analysis. The *antemortem* detections of Alzheimer's and mild cognitive impairment were mostly unsuccessful. Therefore, the need for more sensitive chemical or biochemical markers increases which are capable of diffusing amyloid plaque or tightly binding oligomers (Anoop *et al.*, 2010). In blood-based research, samples are collected very easily (compare with brain imaging and CSF). O'Bryant and co-workers stated that BbB potentially became the first step in a multistep process of AD diagnostic (O'Bryant *et al.*, 2015). It might be followed by CSF and brain imaging as the further steps. However, findings on biomarkers still has limitations for the clear correlation with Alzheimer's.

Cerebrospinal fluid (CSF) has been observed to be a first-choice biomarkers source due to numerous causes. CSF is closely associated with the brain, and thus, the biochemical alterations in the brain influences directly the markers composition in CSF. Instead, many brain-related proteins are accumulated in CSF, and any alteration in these proteins indicates

the disease progression. The sensitivity of CSF markers caused by brain composition changes is also important to define the preclinical stages of Alzheimer's. Sampling methods *via*., lumbar puncture is the foremost issue due to its invasiveness leading to patient's inacceptability. Another concern is in the data inconsistency during sample analysis (**Table 2.1**) (Anoop *et al*., 2010). However, CSF still remains as the most reliable fluid-based sample, specifically for diagnosis in symptomatic and preclinical stages of AD (Anoop *et al*., 2010).

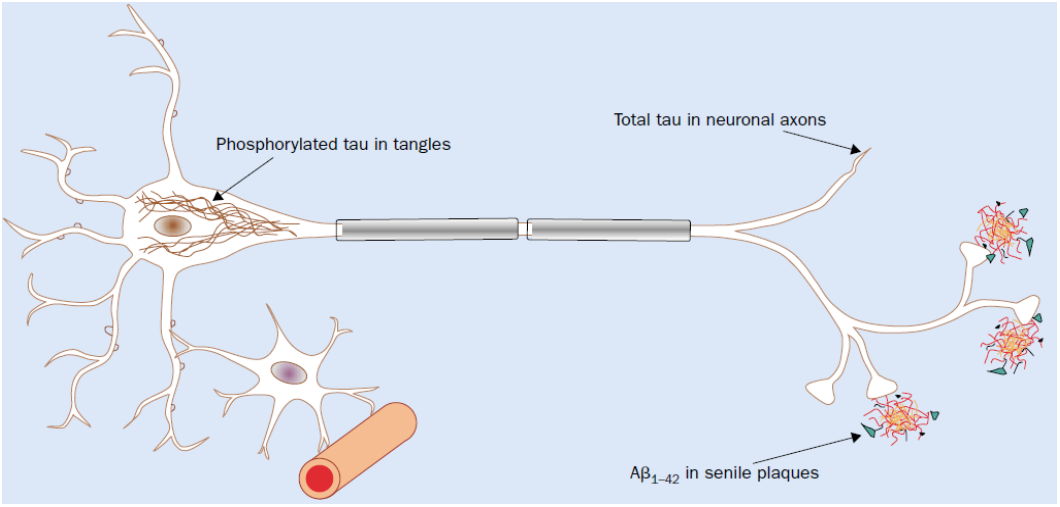

Figure 2.4 The illustrative depiction of Alzheimer's biomarkers accumulated in neuron (capillary and astrocyte). The t-tau is a biomarker for axonal and neuronal collapse, Aβ (42) level is an indication of plaque disposition, and p-tau is a biomarker for the formation of NFT and tau proteins hyperphosphorilation (Blennow and Hampel, 2003).

As a part of CSF substances, Aβ (42) implements better indications in 5-10 years prior to Alzheimer's, while total tau protein (t-tau) and hyperphosphorilated tau (p-tau) show better predictability in 0-5 years before disease conversion (Buchhave *et al*., 2012). CSF t-tau indicates the level of neuroaxonal collapse (Blennow *et al*., 2010) and are not specific to Alzheimer's. High levels of t-tau will be discovered in all types of neurodegeneration-based central nervous system syndrome, mainly in Creutzfeld-Jakob disease (Otto *et al*., 1997) and

acute stroke (Hesse *et al*., 2000). Whilst, p-tau is associated with NFT pathology (Blennow *et al*., 2010). Taken together, the depiction of Aβ, t-tau, and p-tau along with each function was shown in **Figure 2.4**. However, Aβ (42) is considered as the ideal marker for the further research towards successfully diagnose of the early stage of Alzheimer's and due to its major contribution to the pathogenesis (described in further details).

Table 2.1 Resume of biomarkers in the early stage diagnosis of Alzheimer's[a].

Type	Biomarkers	Advantage	Limitations	Reference
CSF	Aβ, t-tau, p-tau	Correlate with AD directly High sensitivity, specificity, and accuracy Available to detect AD progression	Invasive, sample has to be collected from lumbar puncture Irreproducible diagnosis due to sample storage and transportation	(Maddalena *et al*., 2003, Blennow and Hampel, 2003, Dubois *et al*., 2007, Blennow *et al*., 2010)
Brain imaging	CT, PET, PIB-PET, MRI, PET with FDG, FDDNP	Non-invasive Provides structural and functional details of brain immediately High accuracy Available to reveal AD progression	Expensive The specificity and sensitivity to AD is not satisfactory	(Killiany *et al*., 2000, Silverman *et al*., 2002, Shoghi-Jadid *et al*., 2002, Mathis *et al*., 2003, Moulin *et al*., 2007)
Blood (plasma and serum)	*α*-2 macroglobulin, complement factor H, Aβ	Non-invasive Samples are easily accessible Can serve as the first step in a multistep diagnostic process	Less correlation to AD Less sensitive and specific for AD diagnosis (due to epitope masking) Unsuccessfully towards describing the responsible biomarker	(Kuo *et al*., 2000, Fukumoto *et al*., 2003, Hye *et al*., 2006, Schneider *et al*., 2009)

[a] Adapted from Anoop *et al.* (2010) with minor modifications including some update reports.

[b] *Abbreviations*: CT; computerized tomography, PET; positron emission tomography, PIB-PET; (N-methyl-[^{11}C] 2-(4L′-methylaminophenyl)-6-hydroxybenzothiazole)-positron emission tomography; MRI; magnetic resonance imaging, FDG; fluorodeoxyglucose, FDDNP; (2-(1-[6-[(2-[^{18}F] fluoroethyl](methyl)amino]-2-naphthyl]ethylidene)malononitrile).

2.6.1 Amyloid-β

Alzheimer's is mainly characterized by accumulations of extracellular amyloid plaque and thus, it is well-known as the major disease-modifying target in the diagnosis and treatment (Hardy and Selkoe, 2002). Aβ is cleaved from the large amyloid-precursor protein by β-secretase, *aka* β-amyloid precursor protein cleaving enzyme (BACE) and a process through amyloidogenic pathways generates 42-amino acid peptide/Aβ(42) which is able to be aggregated under certain circumstances. The pathophysiology of Aβ plaques formation is mostly induced by an excess of β-secretase enzyme released within brain cells extracellular (Humpel, 2011). Further, mutations occurred in specific genes (APP, PSEN1, and PSEN2) have been pinpointed as the responsible factor for Aβ alterations leading to Alzheimer's (Lopera *et al*., 1997). Indeed, the knowledge on the basis of DNA sequences which are responsible for the Aβ peptide formation is valuable to determine the early stage of initiation and therefore, can be utilized as DNA biomarkers in the detection system.

2.6.2 ss-DNA encoding Aβ peptide

Investigations on amino acid sequences responsible for cerebrovascular amyloid protein formation are well-documented by Glenner and Wong (1984) and Robakis and co-workers (1987) (Glenner and Wong, 1984, Robakis *et al*., 1987). Glenner and Wong have isolated a purified protein derived from the twisted β-pleated sheet fibrils in cerebrovascular amyloidosis using column chromatography and a high-performance liquid chromatography. The resulting sequence of amino acid is represented as follows:

NH_2---Asp-Ala-Glu-Phe-Arg-His-Asp-Ser-Gly-Tyr-Gln-Val-His-His-Gln-Lys-Leu-Val-Phe-Phe-Ala-Glu-Asp-Val---**COOH**

Further, Robakis and co-workers employed the oligonucleotide encoding abovementioned amino acid sequence to synthesize oligonucleotide probes specific for the gene encoding amyloid peptide. The corresponding sequences had 72-mers of nucleobases and is shown as in details below,

5'- GAT GCT GAG TTC C(A)GC(G) CAT GAC A(T)G(C)T GGC TAT CAG GTG CAC CAT CAG AAG CTG GTG TTC TTC GCT GAG GAT GTG - **3'**

This finding is useful to determine the initial stage of Aβ development as well as to be utilized as molecular analyte of biosensor system targeting Alzheimer's. Therefore, in this present study, the nucleobase sequences are tailored as an important component in electrode materials, a pivotal part of this study of the DNA damage associated with Alzheimer's. The computational study was also employed to this particular sequences to better understand the electronic nature of the ss-DNA as well as its interaction with other nanomaterials assembled in the fabricated electrode.

2.7 Biosensor Applications in Alzheimer's

A biosensor is well-defined as a bioanalytical sensing device which is utilized for detecting or quantifying biological analyte/target recognized by (bio)molecular recognition entity integrated within a physicochemical transducer (**Figure 2.5**). Today, biosensor has been tailored as a high throughput disease diagnostic device in order to meet the point-of-care (POC) diagnostic criteria. Biosensors can be classified as POC diagnostic tool for analyzing

clinical samples in the patient's home (bedside monitoring) or at the doctor's surgery as well as in providing portable devices (i.e. integrated with mobile phone applications etc.) with excellent sensor performances. Further, POC technologies provide platforms for complex testing by non-specialists with an advantage of improved reliability and robustness (Soper *et al*., 2006).

In order to develop sophisticated biosensor devices, specific markers/biomarkers require to be identified as the sensing target to ensure their sensitivity and specificity. Biosensors offer advanced platforms for the analysis of biomarkers with the benefits of being easy to use, low-cost, rapid, and robust as well as providing multi-analyte testing ability (Tothill, 2009).

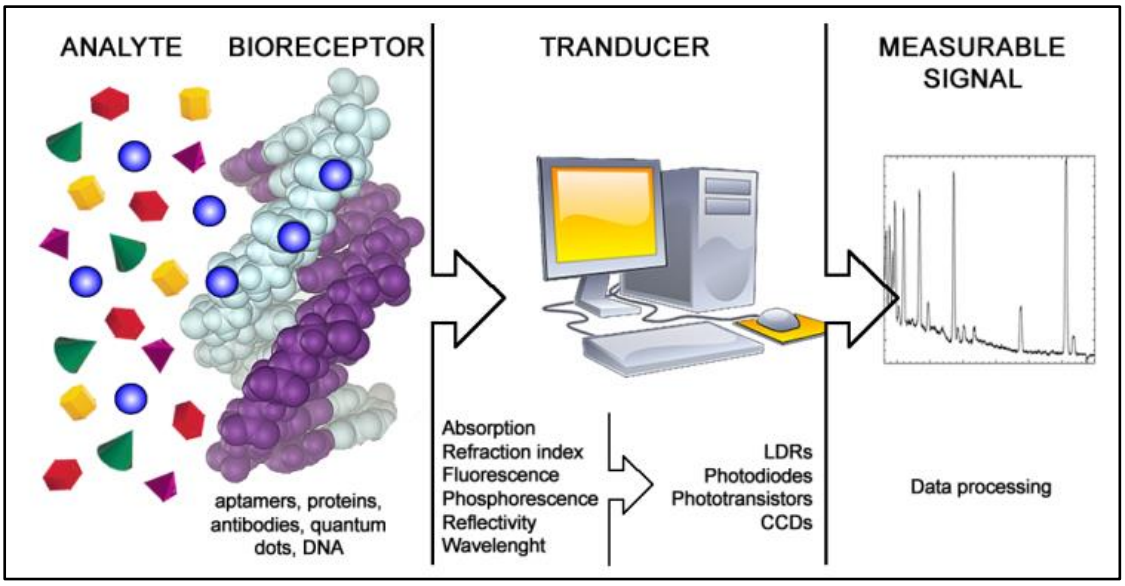

Figure 2.5 Construction of a biosensor (Shruthi *et al*., 2014).

Generally, biosensor consists of three main parts (**Figure 2.6**): first element is biorecognition materials (a biomimic or biological materials involves enzyme, tissue, microorganism, nucleic acids, cell receptor, and biological sensitive elements created with genetic

engineering) which used to recognize specific analyte or biomarker; the second is physicochemical transducer (e.g. optical, piezoelectric, electrochemical) used to transform the signal which produced by interaction between analyte and biorecognition material into measurable signal that can be translated by signal processor, etc.; and the third is signal processing which able to translate the signal into the visual graphic, diagram, or other user-friendly signal display (Cavalcanti *et al*., 2008). Several biosensors, e.g. the use of protein and enzyme as biorecognition molecules, require a process of immobilization to attach the bioreceptor to the transducer system by employing physical or chemical interaction within both i.e. adsorption (physical or chemical), sol-gel entrapment, crosslinking, covalent bonding etc. The details of immobilization techniques used in recent biosensor were well-reviewed in previous reports (Dave *et al*., 1994, Scouten *et al*., 1995).

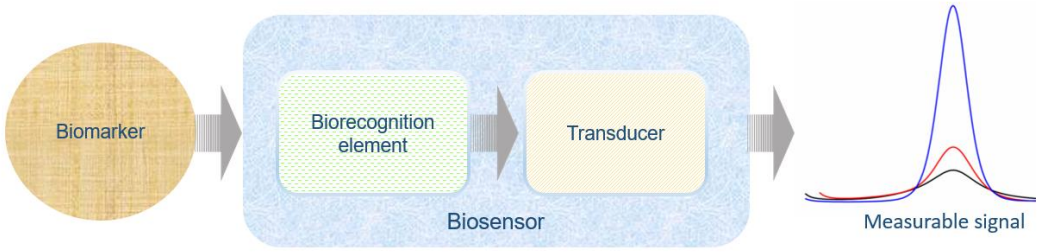

Figure 2.6 A schematic representation of a biosensors system.

Biosensors can be classified based on their applications, (i.e. in environmental monitoring, food safety, medical diagnosis, and clinical analysis) or on the basis of their chemical and biological-recognition element used for sensing (i.e. antibody/antigen, specific enzymes, nucleic acids, aptamer, whole cells etc.). DNA fragments, organelles or intact cells, and membrane components have recently complemented the set of components available for biorecognition (Teles and Fonseca, 2008). Recently, DNA-based sensor has widely been

developed due to the high sensitivity of the output (recognizable down to DNA level). Herein, the DNA-based biosensor is proposed in order to detect the DNA damage level in Alzheimer's by using an electrochemical transducer. Other classification types based on the principle of tranducer have also been established involving electrochemical (Yogeswaran and Chen, 2008), optical (Wolfbeis, 2008), and piezoelectric (Muramatsu *et al*., 2002) sensors.

2.7.1 *State-of-the-art* of electrochemical biosensors for Alzheimer's biomarkers detection

Electrochemical biosensor is merely the most common detection technique used in Alzheimer's biomarker detection. Indeed, electrochemical biosensor enables to provide semi-quantitative and quantitative analytical data by employing biorecognition element which is derived from direct spatial contact with electrochemical transducer. Several types of transducing mode have been widely used in construction of electrochemical biosensor including amperometry, voltammetry, impedimetry, conductometry, voltammetry, and ion charge or field effect (Thévenot *et al*., 2001). In the following section, the *state-of-the-art* of electrochemical biosensor is discussed in order to represent the current development of electrochemical biosensors relied on primary and secondary biomarker in Alzheimer's.

2.7.1.1 Primary biomarkers

(i) Amyloid-β

According to the amyloid hypothesis, Alzheimer's is primarily marked by coexistence of Aβ plaque depositions as it has been widely accepted as the most hypothetical marker during initiation and progression stage (Hardy and Selkoe, 2002). Entirely, CSF contains many types

of Aβ plaques in which the major compounds correspond to Aβ (40) and Aβ (42), whereas other forms of peptides are also generated from amyloid precursor protein i.e. Aβ (37) and Aβ (38) in minor percentage (Blennow and Hampel, 2003, Hampel *et al*., 2004).

Recently, a carbon nanotube-based biosensor (CNT) using films to detect Aβ in human serum was developed by Oh and co-workers (Oh *et al*., 2013). Authors compared the use of CNTs in its combination with metal semiconductor field effect transistor (CNT-MESFET) and CNT with field effect transistor structure (CNT-FET) as the transducer. According to their results, the sensitivity of CNT-MESFET was found to be higher than CNT-FET by using antibodies as biorecognition elements (Oh *et al*., 2013). Instead of CNT, noble metals i.e. gold nanoparticles (AuNPs) have been widely used in a nanocomposite construction of electrochemical biosensors. An electrochemical impedance spectroscopy (EIS) biosensor using deposited AuNPs was designed for the specific detection of Aβ (42). The limit of detection (LOD) of Aβ (42) was found to be 0.01 pg ml^{-1} which was over four orders lower than the lowest values reported by conventional measurement using ELISA (~100 pg ml^{-1}). Interestingly, this study also demonstrated that Aβ (42) could be aggregated under a very small concentration (1 µg mL^{-1}) (Wu *et al*., 2014).

Likewise, a carbon disposable electrochemical printed chip remained a breakthrough in the detection of Aβ (40) by using EIS. Lien and colleagues fabricated three types of Aβ (40) immune-based electrochemical sensors in a step-wise manner towards understanding the effect each surface modifications in the form of sensitivity. Regarding this study, authors revealed that immobilization of AuNPs could increase the stability of recognition elements, amplified the surface area for immobilization and thus, lowered the LOD within three studied

electrodes (from 2.04 μM to 2.65 nM). Indeed, they extended the modification using protein G and it successfully reduced the LOD down to 0.57 nM. Excellent selectivity has been achieved with protein interferences (bovine serum albumin) (Lien *et al*., 2015). Another ultrasensitive detection of Aβ (42) using Au electrochemical electrode was presented by Liu and co-workers (Liu *et al*., 2014a). The voltammetric measurement exhibited LOD down to 5 pM, better than those reported using the EIS methods (Lien *et al*., 2015). In this biosensor system, p-aminophenol redox cycling on antibody-modified Au electrode was used to detect Aβ (42) and the total Aβ in artificial CSF samples (Liu *et al*., 2014a).

By using microfluidic electrochemical biosensors, Islam and co-workers have successfully evaluated exceedingly small-scale concentrations of Aβ (42). Their biosensor was made from grafted-AuNPs by modification *via* thiol groups of self-assembled 1,6-hexandithiol cross-linker (Islam *et al*., 2011). This method has opened up the possibility to bring natural conditions into biosensor systems (protein immobilization) due to the use of minimum amounts of reagent and the high sensitivity of the analyte's detection.

Instead of peptide forms, Aβ in oligomeric structure (AβO) found in blood serum was proposed to be ideal biomarker for Alzheimer's because it initially resembles Aβ (42) fibrils (Kasai *et al*., 2013) and showing non-invasive features. Several biosensors were successfully conducted to detect AβO (Rushworth *et al*., 2014, Liu *et al*., 2015b, Shin *et al*., 2015b). Rushworth and co-workers constructed a label-free impedimetric biosensor to specifically detect AβO. Their study employed cellular prion protein fragment (residues 95-110) as biorecognition element and yielded a low detection limit of ~0.5 pM (Rushworth *et al*., 2014) which is lower than other similar studies (Liu *et al*., 2015b, Shin *et al*., 2015b). Besides,

biosensor targeting Aβ in the monomeric form was observed by Shin and colleagues and could reach 1 pg/ml of LOD (Shin *et al*., 2015a). These aforementioned findings showed that Aβ, in the form of oligomer and monomer, is a potential biomarker for Alzheimer's and therefore, open up the avenues to be utilized as new biosensor analyte or marker.

Magnifying the invasiveness of the method, saccharides which are commonly manifested on the cell surfaces, offered a breakthrough in terms of non-invasive way of Aβ revealing. Recently, it has been discovered that the cell surface saccharides have correlation with AD *via* sialic acid-Aβ interaction (Miura *et al*., 2007). Saccharides-based electrochemical sensor taken advantage on interactions of saccharide-protein *via* twosome of sialic sub-products and Aβ was constructed by Chikae and co-workers. Sialic acid was introduced compactly over the partial self-assembled monolayer on the screen printed carbon electrode *via* electrodeposition with AuNPs (Chikae *et al*., 2008). Another non-invasive method was recently reported by Li and colleagues *via* the employment of magnetic nitrogen-doped graphene. This method has successfully achieved a very low concentration of analyte up to 5 pg/ml. The illustrative way to prepare Aβ antibody-magnetic nitrogen-doped graphene is presented by **Figure 2.7**. In this study, Aβ (28) antibody was utilized to recognize the Aβ (42) peptide (Li *et al*., 2016).

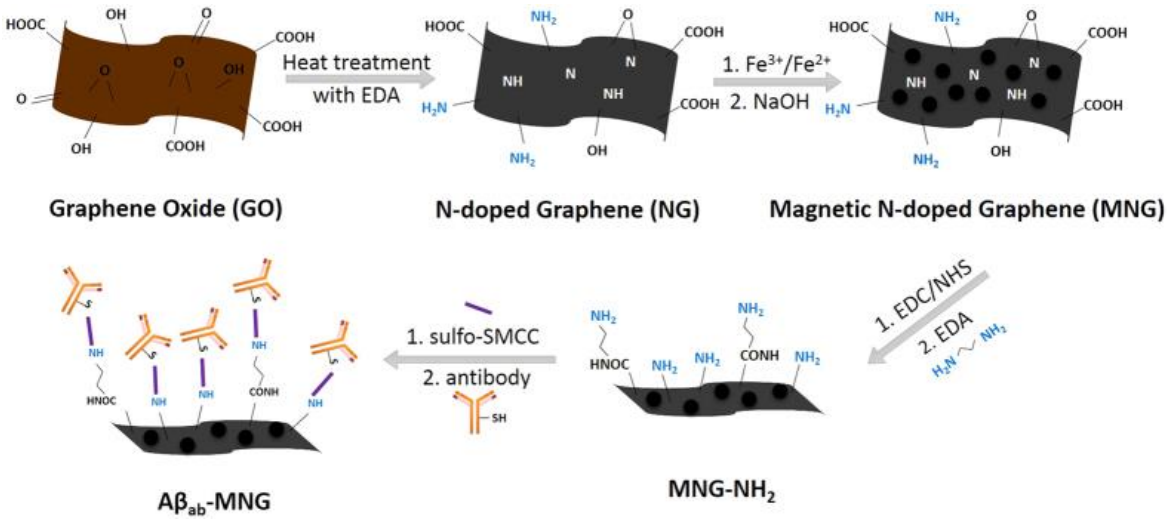

Figure 2.7 Scheme for Aβ (42)-MNG preparation (Li *et al*., 2016).

Recently, Suprun and co-workers made several extended studies by using square wave voltammetry and screen printed carbon electrode in order to investigate conformational alterations of Aβ (16) peptides (Suprun *et al*., 2016b), including metal induced changes (Suprun *et al*., 2015, Suprun *et al*., 2016a). Overall, authors revealed that electrochemical approach could emerge as an auspicious tool for studying metal ion-amyloid protein interactions to afford deeper understanding into molecular mechanisms of Alzheimer's.

(ii) Cholinesterases enzyme

Alzheimer's is not only characterized by Aβ plaques but also insufficiencies of other metabolites i.e. cholinergic system (Anand and Singh, 2013). The cholinergic imbalance has been found in elderly patient suffering from AD. The deficits of cholinergic system are remarked by the reduced level of the acetylcholine (ACh) receptor (Nordberg, 2001), producing the impairment of signal transmission of the cholinergic system which could be responsible for Alzheimer's symptoms appearance (Kihara and Shimohama, 2004). AChE is

primarily responsible for cholinergic deficits. Instead of AChE, butyrylcholinesterase (BuChE), known as pseudocholinesterase (Darvesh *et al*., 2003), is an enzyme whose role is in the catalyzation of the hydrolytic processes of ACh producing choline, acetic acid, and water molecules. Studies have clearly shown that both enzymes were important targets for the diagnosis and treatment of AD (De Ferrari *et al*., 2001). However, BuChE is less abundant compared to AChE in the brain region (Anand and Singh, 2013).

In the past several years, cholinesterases enzyme has been able to be utilized as a recognition component of biosensors. Pohanka's research group is remarkably noted for their extensive contribution in the development of cholinesterase-based biosensors (Pohanka *et al*., 2013). The basic strategy of biosensors construction is depicted in **Figure 2.8**. From this depiction, cholinesterase enzyme used as biorecognition molecule to sense/detect analyte at the circumstance and its physicochemical alteration is subsequently analyzed using transducers followed by translating the signal by the detector device. The biosensor is suitable to assay choline level or cholinesterase inhibitors such as neurotoxic compounds representing a serious risk of human health or life (Pohanka *et al*., 2013). In case of inhibitor detection, cholinesterase acted as a suicidal biorecognition element. The enzymatic process confirming the existence of the analyte was revealed by an irreversible process and the reduction of produced signal. On the other hand, some inhibitors exhibited reversible process and facilitated easy split and the recovery of enzyme activity. Commercially available and reliability of this technique have been emphasized the use of cholinesterase-based sensor as one of the strategies towards development of diagnosis device as well as screening of Alzheimer's novel therapy (Pohanka, 2014b).

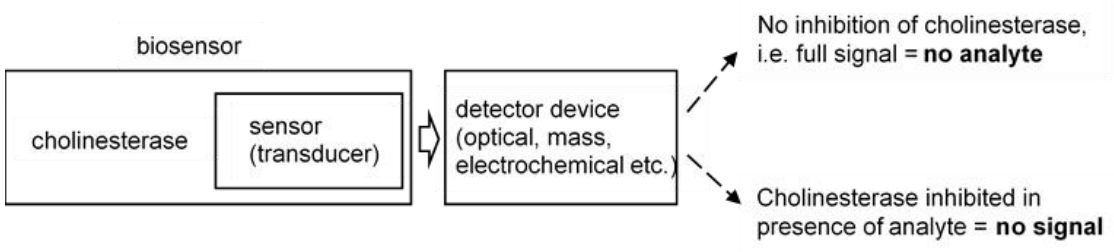

Figure 2.8 Simplified scheme of the biosensor with cholinesterase applicable for assay of neurotoxic compounds (Pohanka, 2014b).

In term of Alzheimer's diagnosis and treatment, some types of electrochemical biosensors have been used to detect various analytes such as ACh and choline (Pundir *et al*., 2012, Chauhan and Pundir, 2014), nerve agents (Pohanka *et al*., 2013), and potential inhibitor of AChE/BuChE from selected phytochemical compounds (Dzyadevych *et al*., 2004, Benilova *et al*., 2006). Hydrolysis reactions of either ACh or butyrylthiocholine caused by cholinesterase enzyme and the subsequent oxidation of thiocholine by an applied voltages, are relatively common methods developed in cholinesterase-based biosensors (Pohanka, 2014b). Indeed, **Figure 2.9** shows the principle reaction of biosensor applied in an electrochemical measurement.

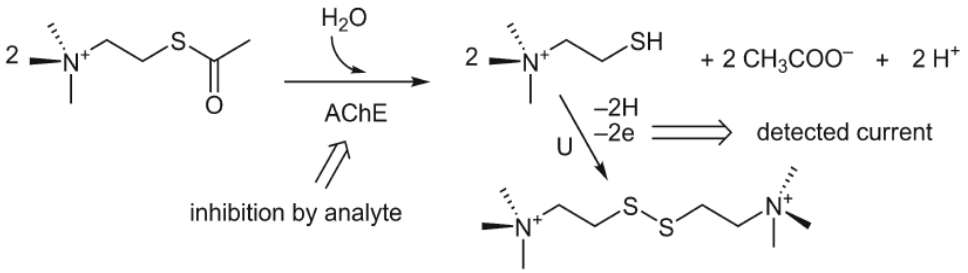

Figure 2.9 The basic principle of electrochemical measurement through AChE inhibition (Pohanka, 2014b).

Most of the researchers on cholinesterases biosensor focused on drug screening. Pohanka and co-workers have conducted extensive research on the cholinesterase-based detection (Pohanka *et al*., 2013, Pohanka, 2014b). The reports proposed were mostly to detect nerve agent or neurotoxic compound which potentially destructed brain associated Alzheimer's. Instead, several reports were available on the basis of AChE/BuChE for the detection of choline or ACh (Wang *et al*., 2006, Hsieh *et al*., 2007, Pundir *et al*., 2012, Khan and Ab Ghani, 2012, Chauhan and Pundir, 2014). Hsieh and co-workers assembled choline biosensor by using amperometric flow injection techniques. This biosensor was constructed by the utilization of a chitinous membrane to support the immobilization of biocatalyst (Choline oxidase) *via* covalent binding and subsequently attached to the platinum electrode. The 10.0 µM of LOD was achieved through this constructed sensor (Hsieh *et al*., 2007).

Likewise, a flow injection coupled to amperometric biosensors composed of choline oxidase (ChO) and a bi-enzyme system of ChO and horseradish peroxidase was employed by Wang and co-workers to detect choline. The enzymes were immobilized onto multi-walled carbon nanotubes (MWCNT) grafted on a glassy carbon electrode. The biosensor yielded LODs of 0.1 µM with a few seconds response time (Wang *et al*., 2006). In addition, choline detection was also achieved by Pundir and co-workers by using bienzyme system (AChE and ChO) co-immobilized onto nanocomposite of carboxylated MWCNT (c-MWCNT) and zirconium oxide NPs (ZrO_2) deposited on the glassy carbon electrode surface (**Figure 2.10(a)**). It observed quite low LOD of 0.01 µM and was directly applied to human serum. This biosensor successfully discriminated samples between Alzheimer's and healthy person (Pundir *et al*., 2012). Further, Chauhan and Pundir developed an amperometric ACh biosensor by covalently co-immobilizing AChE and ChO onto chitosan/Au coated ferric oxide NPs

deposited onto Au electrode surface. It has been applied to blood plasma sample and showed an excellent specificity. Compared to their previous reports, this biosensor yielded much lower LOD of 0.005 µM with a rapid response time of 3 s (Chauhan and Pundir, 2014).

Another electrochemical biosensor was constructed based on polymer (poly(o-phenylenediamine) coupled to bienzyme system (AChE and ChO) (Khan and Ab Ghani, 2012). These biorecognition molecules were fabricated onto carbon fiber substrate and the electrode assembly was completed by deposition of functionalized CNT and nafion. The detection limit was shown as 0.045 µM with relatively rapid response time of less than 5 s (Khan and Ab Ghani, 2012).

(iii) BACE1

Amyloid-β precursor protein cleaving enzyme is known as a pivotal proteolytic enzyme in the initial production of Aβ (Cai *et al*., 2001, Vassar *et al*., 2009). An electrochemical biosensor was designed to probe BACE1 activity and its inhibitors. Typically, this biosensor method employed peptide-heme complex formed on the electrode surface which subsequently detached by BACE1. In addition, this study also reported the inhibitor screening of BACE1 leading to finding new agents for Alzheimer's treatment (Xia *et al*., 2015).

2.7.1.2 Secondary biomarkers

(i) S100B protein

Besides amyloid and cholinergic as major biomarkers, Alzheimer's is also potentially marked by raised levels of several S100 family proteins, comprising S100B protein (Tahany Ramzy,

2011). S100B is known as a calcium-binding protein which belongs to EF-hand (helix-loop-helix assembly) cluster produced by astrocytes. The increasing amount of this protein has been observed in the blood serum and CSF samples of AD (Bianchi *et al*., 2011). Greater amounts of S100B role in the pathogenesis task of Alzheimer's (Tahany Ramzy, 2011). Detection of S100B level is apparently useful to discriminate the severity of Alzheimer's or to discover the progression of dementia (Lopez-de-Ipina *et al*., 2013).

A biosensor on the measurement of S100B was first introduced by Mikula and co-workers. Authors constructed an electrochemical biosensor using modified Au electrode and utilized His-tagged VC1 receptors domains for advanced glycation end products as biorecognition fragments which subsequently attached *via* covalent binding on a modified monolayer of thiol derivative of pentetic acid complex with Cu (II) deposited on the electrode. The simplified scheme of biosensor construction is depicted in **Figure 2.10(b)**. Osteryoung square-wave voltammetry (OSWV) was employed as the transducer and it successfully achieved 0.52 pM of LOD with a good selectivity through diluted human plasma sample (Mikula *et al*., 2014). Likewise, a similar technique was also used for the detection of S100B. This extended study employed different diluent type and resulting LOD of 0.9 and 2.7 pM for two dissimilar diluents (*N*-acetylocysteamine and 4-mercaptobutanol). According to this study, they concluded that *N*-acetylocysteamine diluent exhibited more sensitive result compared to 4-mercaptobutanol (Kurzątkowska *et al*., 2016).

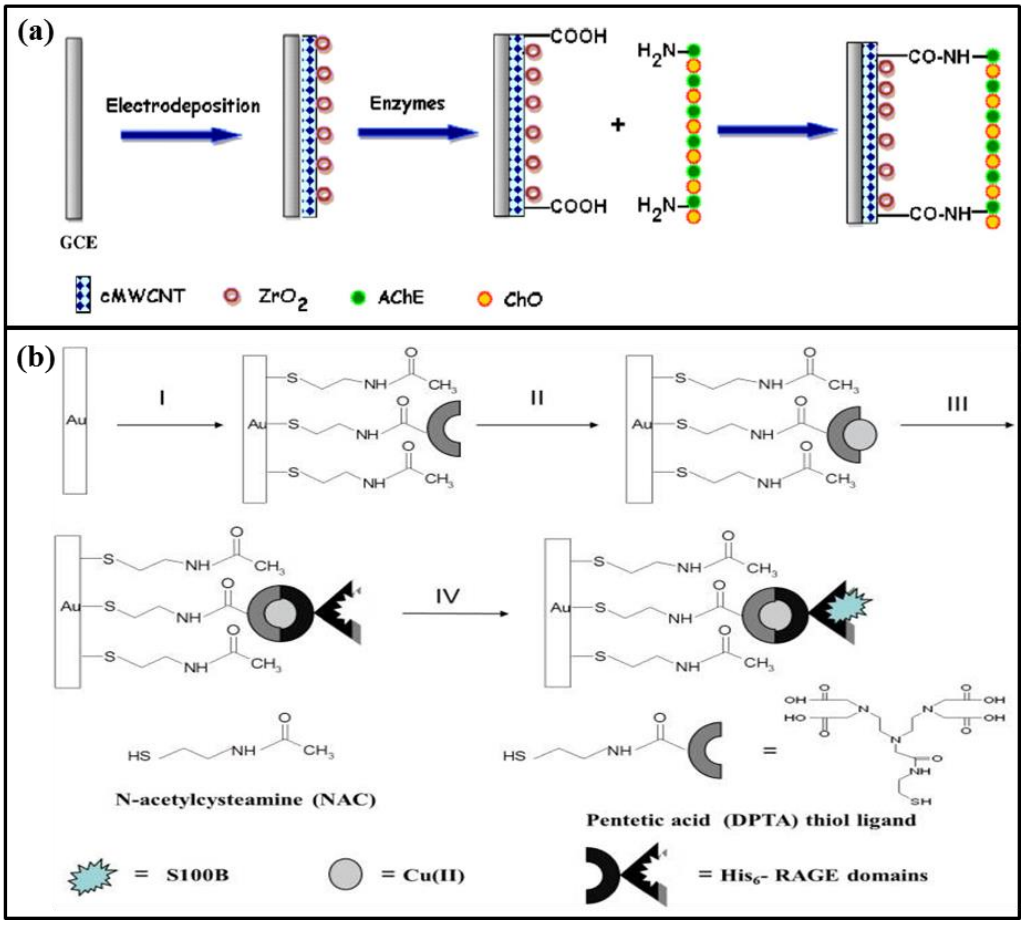

Figure 2.10 The illustration of (a) preparation of modified electrode containing MWCNT, ZrO_2, and bi-enzyme system (Pundir *et al*., 2012) and (b) S100B biosensor relied on NAC/thiol sub-product of pentetic acid (NAC/DPTA)-Cu (II) SAM (Mikula *et al*., 2014).

(ii) ApoE gene

The demand of an improved diagnostic performance has raised in terms of integrating the sample processing into the sensing device. This is well-understood since the future diagnosis would be possibly heading toward the miniaturization of the advanced testing device that can deliver a cost-effective POC, personalized healthcare treatment, quick and easy sample's handling, and effectively monitoring the disease progress of patient. Therefore, a decentralized device, so called *lab-on-chip* (LOC), is a concern in some areas focusing on

how to develop an efficient and effective POC diagnostic from maintaining the sample preparation (e.g. separation, diluting, and labeling) till obtaining the test result (Lafleur *et al*., 2016, van Reenen *et al*., 2014). Incorporating the microfluidic architecture in LOC along with the electrochemical technique has proposed this type of biosensor to be beneficial in executing entire analysis in a micro system, which is suitable for *in vitro* diagnostic for ageing persons at home. There are still few literatures of Alzheimer's biosensors reported in this regards. One of the fundamental studies was proposed using LOC integrated QDs nanomaterials for ApoE biomarker detection (Medina-Sánchez *et al*., 2014). The LOC platform was based on immunocomplex construction which was fabricated onto polydimethylsiloxane-polycarbonate polymeric bases assembled to SPE, followed by cadmium-selenide/zinc-sulfide QDs as the labeling probe of the immunocomplex (Medina-Sánchez *et al*., 2014). This device revealed the use of LOC in detecting secondary markers of Alzheimer's.

Instead, DNA hybridization of a particular site mutation at ApoE gene could be detected through dual detection platforms using EIS and localized surface plasmon resonance (LSPR). ApoE was previously known as a gene which responsible to Alzheimer's progression. EIS and LSPR were accomplished on the glass surfaces which was coated with AuNPs-modified indium tin oxide. The illustration of this detection platform is shown in **Figure 2.11(a)**. The biosensor yielded the LOD of 512 nM and 286 nM *via* LSPR and EIS techniques, respectively (Cheng *et al*., 2014b). More recently, chronoamperometry technique was applied to detect ApoE together with Aβ. This nanobiosensor shown the LOD down to 80 and 19 pg mL^{-1} for ApoE and Aβ (de la Escosura-Muñiz *et al*., 2015).

(iii) Brain glutamate

Glutamate alterations might lead to excitotoxicity and triggering multiple neurodegenerative diseases involved Alzheimer's (Walton and Dodd, 2007). *In vivo* glutamate detection by electrochemical biosensor platform using various electrode sizes were summarized in a comprehensive review reported by Hamdan and Mohd Zain. Briefly, this report showed that modification of the electrode could elevate the sensitivity in the glutamate detection and due to the smaller size of the electrode, the higher level of sensitivity might be reached. However, the sensor device was depended on the type of electrode modification in which it directly affected the signal response of biosensor outcome (Hamdan and Mohd Zain, 2014). Recent development of glutamate biosensor found quite low LOD down to 0.5-4 µM (Soldatkin *et al*., 2015) and 5 nM (Şimşek *et al*., 2016).

(iv) DNA

The construction of a biosensor based on nucleotide (i.e. DNA) is a highly promising device in order to diagnose Alzheimer's due to its simplicity, ease to develop, selectivity, sensitivity, and low-cost fabrication. DNA is known as the smallest structural unit of a living organism. Therefore, most of DNA-based sensors were driven to develop advanced theranostics methods.

Current efforts on the development of DNA sensor based on electrochemical transductions was extensively reviewed by Lubin and Plaxco (Lubin and Plaxco, 2010). Nanomaterials gain an outstanding role in the development of DNA-based Alzheimer's biosensor. Graphene corresponds to a material of choice and sophisticated entity which is extensively used by biomaterial scientists (Parlak *et al*., 2014, Tiwari and Syväjärvi, 2015, Chen *et al*., 2015b,

Patra *et al*., 2016, Osikoya and Tiwari, 2016). Recently, an electrochemical DNA biosensor designed by using DNA-graphene platform was developed to reach a simple construction, biocompatible, ultrasensitive and robust Alzheimer's detection device. The ss-DNA was directly attached to the graphene surface *via* π-π stacking interaction. The schematic diagram of the DPV-based electrochemical biosensor is clearly shown in **Figure 2.11(b)**. This biosensor exhibited an excellent performance of biosensor with LOD value down to 72 pM and was capable of distinguishing the corresponding sequence as of the single-base mismatch sequence (Lin *et al*., 2011).

(v) Dopamine

Dopamine, a neurotransmitter is related to several neurodegenerative diseases such as Alzheimer's and Parkinson's disease (Maguire-Zeiss *et al*., 2005). Dopamine was firstly utilized as a bioanalyte for a system of electrochemical Alzheimer's biosensor by using an antimicrobial peptide of dermaseptin 01 from the *Phyllomedusa hypochondrialis*, frog's skin secretion. Subsequently, the antimicrobial peptide was immobilized onto nanolayered films through layer-by-layer technique, in combination with nickel tetrasulfonated phthalocyanines. The result yielded sensitive detection limit of 10^{-6} M (Zampa *et al*., 2012). Further, oligonucleotide was successfully applied in order to enhance the sensitivity of dopamine biosensor. The use of aptamers (Zhou *et al*., 2014) and ds-DNA (Rezaei *et al*., 2015) as biorecognition molecules showed better sensitivity rather than previous methods (1 nM on the basis of aptamer and 6 nM *via* ds-DNA).

(vi) Brain metals

Brain metals emerge as a putative role in the initiation and progression processes of neurodegenerative diseases. Particularly, copper (Cu) is one of the crucial components of human metabolism, even though it is highly toxic materials. The inequality of Cu levels could induce reactive oxygen species, initiated the oxidative impairment, which was associated with neurodegenerative diseases including Alzheimer's, Menkes and Wilson's diseases, and familial amyotrophic lateral sclerosis. Instead, the capacity of Cu to form a steady Cu^{2+} and unsteady Cu^{+} ions were utilized by cuproenzymes, for example, Zn, Cu superoxide dismutase, and cytochrome oxidase to inhibit the enzymatic reactions (Smith *et al*., 2007, Lim *et al*., 2010, Giacovazzi *et al*., 2014).

Recently, a ratiometric study on Cu^{2+} and L-cysteine in living brain with Alzheimer's was conducted by Luo and co-workers. In this study, *N,N*-di-(2-picoly) ethylenediamine was used for the specific recognition of Cu^{2+} by forming a complex resulting in 320 nM of detection limits (Luo *et al*., 2015). Likewise, Zhang and co-workers have reported a ratiometric method to determine Cu^{2+} level in rat brain by utilizing a nanostructure surface. The LOD value was found to be 80.3 nM, lower than previous report (320 nM). **Figure 2.11(c)** illustrates a description of developed ratiometric sensor for monitoring Cu^{2+} (Zhang *et al*., 2015).

(vii) Nicotine

Nicotine is widely-known as a toxic molecule but it is also associated with Alzheimer's (Ly *et al*., 2012). An electrochemical biosensor was constructed to detect nicotine levels in urine samples *ex vivo* using a voltammetric method based on graphite pencil and modified CNT's electrode. The biosensor performed detection limits of 0.6 µg/L for graphite pencil electrodes

and 0.07 µg/L for modified CNT electrodes. Thereby, the modified CNT's electrode showed a better sensitivity rather than graphite pencil. In addition, this method was applied to either non-treated urine or *ex vivo* biological diagnostics sample (Ly *et al*., 2012).

(viii) Tau proteins

In terms of tau-based biosensors, only a few reports are available in literature, which specifically used the tau protein as the prior target as sensing devices. Previously, the detection of tau proteins revealed using other transducing techniques, such as Surface Plasmon Resonance (SPR), ELISA, and cytometry (Skrabana *et al*., 2006, Vestergaard *et al*., 2008, Holmes *et al*., 2014). Recently, an electrochemical biosensor for protein tau detection was developed by Esteves-Villanueva and co-workers. This biosensor harnessed protein's misfolding mechanisms as the basis of measurement and EIS was used to monitor tau-tau interactions *via* regulation of charge transfer resistance (**Figure 2.11(d)**). A linear relationship among charge transfer resistance and concentration of solution tau was discovered from 0.2 to 1.0 µM. Interestingly, this report provided qualitative as well as quantitative data in the domain of tau-tau binding event comprising the initial stage of tau protein self-assembly mechanisms (Esteves-Villanueva *et al*., 2014). Further, an electrochemical study was reported to be capable to (or rather 'firstly') introduce the detection phosphorylation, antibodies binding to substrate, and phosphorylation inhibition. This approach was also allowed to effectively identify the phosphorylation inhibitor *via* targeting tau protein substrate rather than protein kinase (Esteves-Villanueva and Martic-Milne, 2016).

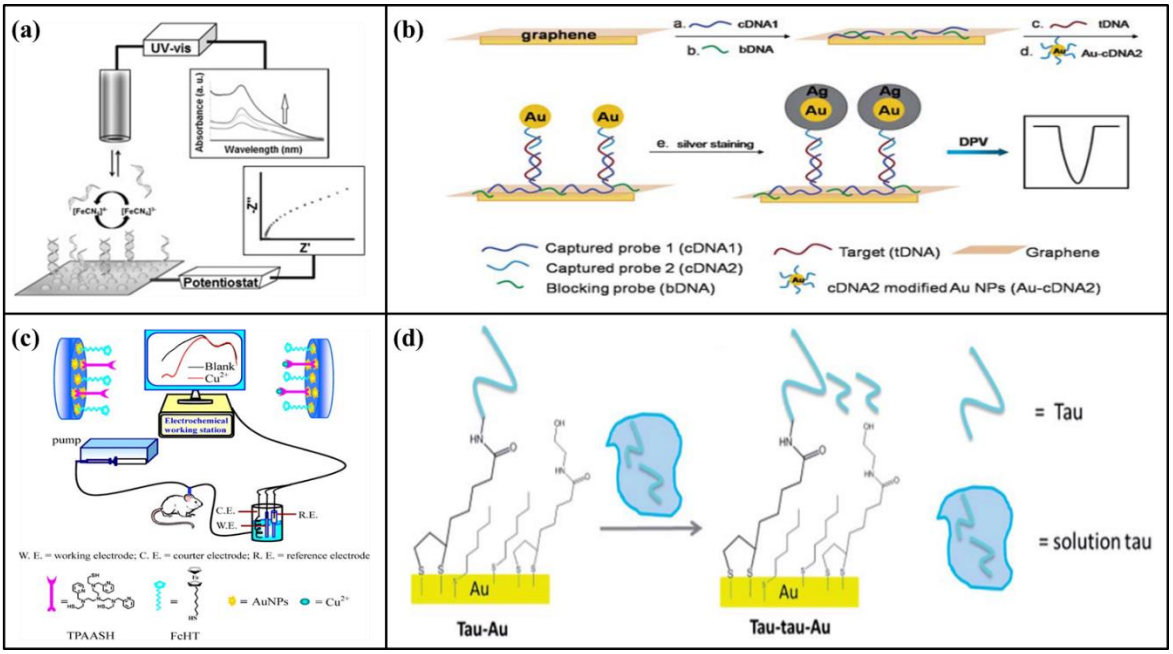

Figure 2.11 The depiction of (a) dual detection system for detecting DNA hybridization using EIS and LSPR measurements (Cheng *et al*., 2014b), (b) design of DNA-graphene platform fabrication and measurement (Lin *et al*., 2011), (c) schematic biosensor system for detecting Cu^{2+} in brain microdialysates (Zhang *et al*., 2015), and (d) tau-based biosensor mechanism (Esteves-Villanueva *et al*., 2014).

2.8 Nanomaterials in Alzheimer's Biosensor Applications

Recently, nanomaterials have offered an outstanding performance in diagnostics and therapeutics of Alzheimer's diseases either *in vitro* or *in vivo* applications (Nazem and Mansoori, 2011). Their unique properties enable to be integrated with various molecular recognitions in purpose of multiple disease detections (Bruls *et al*., 2009, Frasco and Chaniotakis, 2010), especially in its early pathogenesis phase (Misra *et al*., 2010, Kim *et al*., 2011, Cheng *et al*., 2011) in order to prevent the unhandled chronic stage. Tailoring those elements in a biosensor compartment, a real-time, simplicity in sample treatment, and cost-effective measurement is able to achieved for the detection of bioanalytes or sensing target (Vashist *et al*., 2012).

Furthermore, nanomaterials contribute in long-term benefits as their utilization in a modified electrode or as the key role in another portion of biosensor construction. With regards to Alzheimer's biosensors, nanomaterials grafted Alzheimer's biorecognition molecules are usually figured in various designs of diagnostics tools and treatments, in turn, improving the specificity of the detection i.e. *via* brain capillary endothelial cells access (Brambilla *et al*., 2011) as well as treatment efficacy. Tremendous nanomaterials have been used to construct biosensor of Alzheimer's including carbon nanostructures (e.g. carbon nanotube, graphene, graphene oxide etc.), inorganic nanomaterials (e.g. gold nanoparticles), and quantum dots (**Figure 2.12**). In this study, inorganic nanomaterials (i.e. SnO_2/F and TiO_2) were employed to the DNA damage detection due to several merits described in subsequent section.

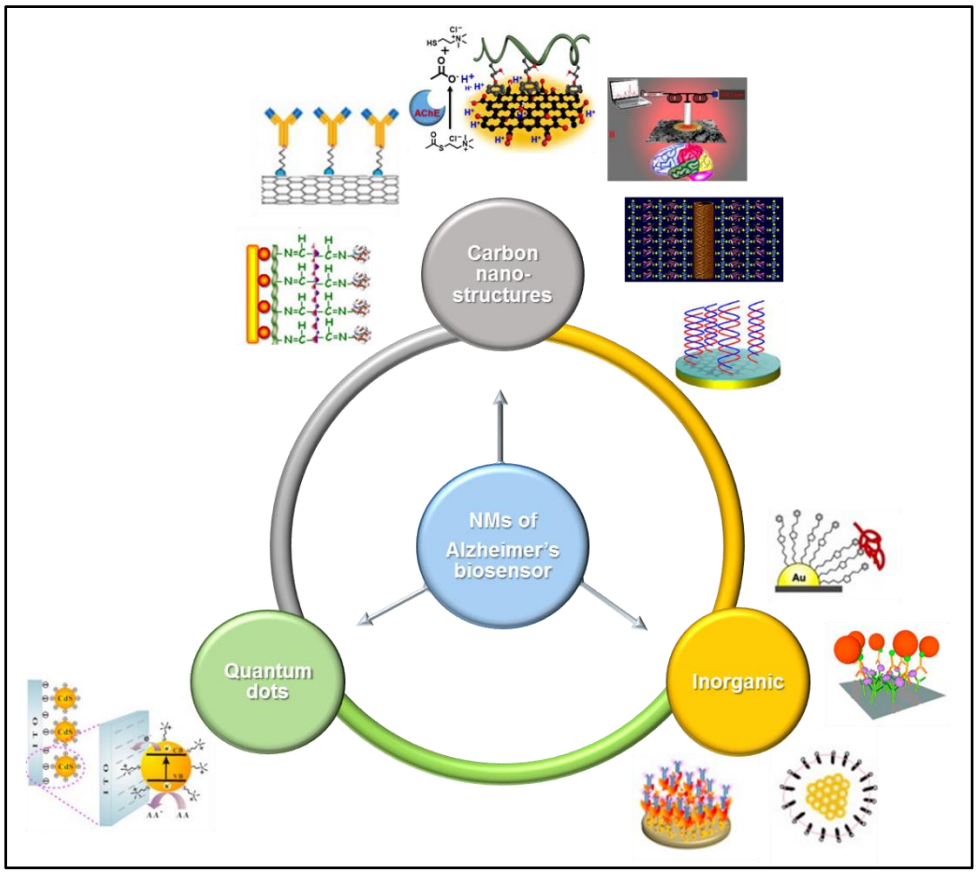

Figure 2.12 Summary of nanomaterials (NMs) used in Alzheimer's biosensor.

2.8.1 Fluorine-doped tin oxide

Un-doped tin oxide (SnO_2) is well-known as semiconductor materials and has been extensively used in gas sensor fabrication, catalysis, dye-based solar cell, transistor, supercapacitor, transparent conducting electrode, photodegradation of organic compound etc. (Liu *et al*., 2014b, Bhattacharjee *et al*., 2015). The origin of this structure remains possessing wide band gap (>3.0 eV) which exhibits high optical transparency (T ≥85%) semiconductor, an n-type character due to oxygen vacancies, and is a part of Binary Transparent Conducting Oxides (Nakajima and Groult, 2005).

One of the unique attributes of semiconductors is in their electronic properties which can be controlled in a variety of ways i.e. by the addition of foreign impurities (dopant), by adjusting the size and dimensionality of semiconductor and the physical structure into which it is placed, and the exposure of the light and external electric fields (Gersten and Smith, 2001). For the SnO_2, the most preferential dopants are antimony that substitutes the cation (Sn) or fluorine (F) by replacing the anion (oxygen; O) (Schaefer *et al*., 1997, Nakajima and Groult, 2005). Fluorine doped tin oxide (FTO; SnO_2/F) remains excellent visible transparency due to its wide band gap while retaining a low electrical resistivity owing to the high transporter concentration triggered by the O vacancies and the substitutional F dopant (Subba Ramaiah and Sundara Raja, 2006). FTO is chemically, mechanically, and electrochemically stable (Tesfamichael *et al*., 2003), and has been used in several applications i.e. thin film solar cells (Kim and Riu, 2011), gas sensors applications (Sankara Subramanian *et al*., 2006), dielectric layer in low emissivity coatings for windows (Gerhardinger and McCurdy, 1996), liquid crystal displays (Yadav *et al*., 2009), and as electrochemical electrode material (Tang *et al*., 2010).

2.8.2 Titanium dioxide

Titanium dioxide (TiO_2) is one of the most versatile semiconductors, applied mostly in solar energy conversion, photocatalyst, separation, gas sensor, electrical circuit varistor, optical coating, structural ceramic, spacer material for magnetic spin valve systems, and biocompatible material for bone implants (Hagfeldt and Grätzel, 2000, Varghese *et al*., 2003, Livraghi *et al*., 2005, Reyes-Coronado *et al*., 2008). TiO_2 has three different phases comprising of anatase, brookite, and rutile (**Figure 2.13**).

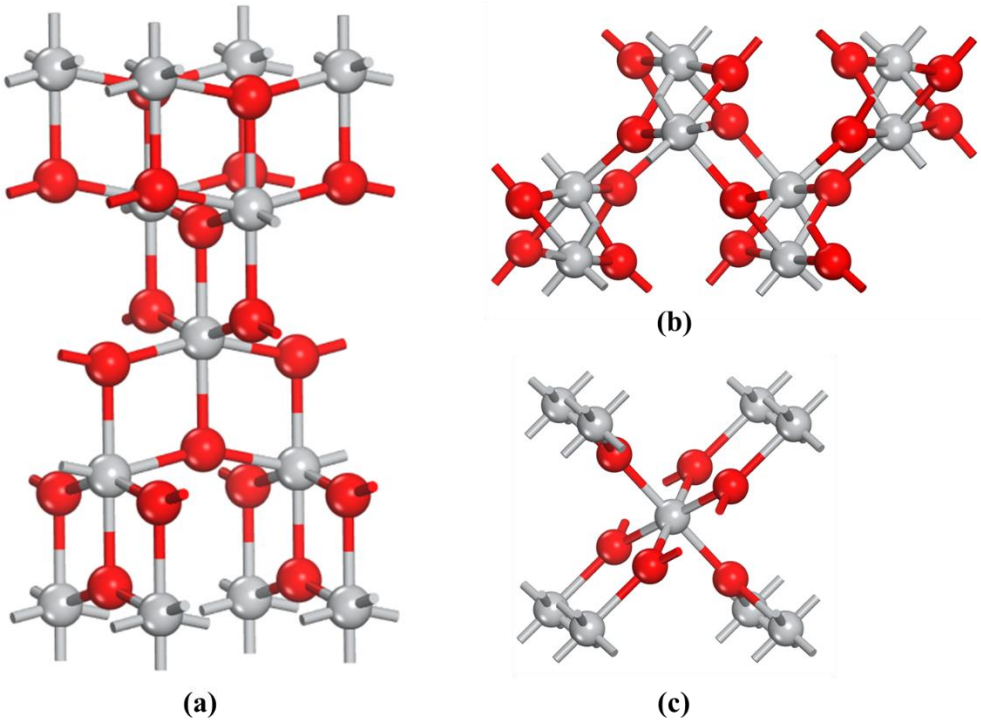

Figure 2.13 Three main polymorphs of TiO_2: (a) anatase, (b) brookite, and (c) rutile.

As a bulk material, rutile corresponds to stable phase, while anatase structure is generally favorable from the solution-phase methods (Zhang *et al*., 1998, Zaban *et al*., 2000, Oskam *et al*., 2003). These observations are attributed from the effect of surface energy and precursor

chemistry. From the surface energy point of view, TiO_2 anatase has a lower energy than those of rutile and brookite phases (Zhang and F. Banfield, 1998, Naicker *et al*., 2005). It indicates that anatase is more stable as compared to other forms and therefore, more favorable in synthesis and application. Instead of surface chemistry, the crystal structure has been described on the basis of molecular features, where the nucleation and growth of different TiO_2 polymorphs are discovered by precursor chemistry depending on the reactants itself (Cheng *et al*., 1995, Yin *et al*., 2001, Li *et al*., 2007).

CHAPTER 3

THEORETICAL PRINCIPLES

This chapter focuses on the theoretical principles underlying the computational study. The role of computational chemistry in Alzheimer's biosensor is highlighted. Furthermore, the equations and rigorous foundation of three foremost quantum chemical methods i.e. density functional theory (DFT), Metropolis Monte Carlo (MC), and molecular dynamics (MD) simulations, in relation to biosensor construction are presented. DFT comprises of rigorous foundations, Self-Consistent Field (SCF), DFT-based DMol3, exchange-correlations functionals, numerical basis sets, and density field-based tight binding (DFTB+) code. Whilst, the fundamental equations and underlying simulation steps are elaborated at the MC subsection. Lastly, the essential basis of MD simulations is provided including basic principles, Forcite code, force field, summation methods, periodic boundary condition (PBC), thermodynamics ensemble, and thermostat implementation.

3.1 Role of Computational Chemistry in Alzheimer's Biosensor

Computational chemistry is a fast emerging field which deals with the computer simulation and modeling of molecule systems i.e. small molecule, macromolecules, ligand, drugs, biomolecules, biopolymers, inorganic and organic molecules, and metal-based nanoclusters. By using powerful performance computing in conjunction with complex and well-organized numerical algorithms, computational chemistry remains to be an effective way to resolve intricate problems of chemical and biological obstacles (Ramachandran *et al*., 2008). Technically, computational chemistry utilizes computers (or rather 'high-performance computers') to generate information such as properties of molecules or reproducing

experimental results (Young, 2001) through operator-based system in the form of code or software.

Recently, computational chemistry has led a better understanding of biological systems, nanomaterials behavior at atomic or molecular level, nanomaterials properties, as well as interaction between nanomaterials and biomolecules/receptors. The molecular modeling approach has been used to make useful predictions and calculations of some molecular mechanism such as MD, investigation of electronic properties, highest occupied molecular orbital (HOMO) - lowest unoccupied molecular orbital (LUMO) energy gap, and providing predictive vibrational properties. In term of Alzheimer's sensors, computational simulations predominantly helps to simulate the optimized structures of materials recognition, to understand the interaction between the substrate materials and target analyte, to compute the interaction or adsorption energy, and to observe the structural, electronic, and vibrational properties of the employed materials and molecules.

3.2 Density Functional Theory

DFT is known as the most popular method used in computational chemistry which can be used to observe the impact of particle size on the structure and molecular features of nanomaterials (Fadeel, 2014). DFT has been widely employed to study and predict electronic structure i.e. conductivity and other related properties of transition metal complexes (Harvey, 2006) as well as macromolecules such as DNA duplexes (Tsukamoto *et al*., 2009). It is also useful in the modeling and prediction of interaction energies.

DFT, a scheme of classical first-principles, is commonly employed to calculate the atomic or molecular properties at the ground-state level. DFT is also known as *minimum-information* theory. Instead of dealing with the many-body wave function $\Psi\ (r_1 \ldots\ldots, r_N)$, DFT leads to the direct calculation of the simplest electronic properties of atom or molecule, i.e. the electronic density. Since 1980, DFT has been established as one of the main tools for calculating the properties of solid state physics and molecules (Fiolhais *et al*., 2003).

DFT was established by Hohenberg, Kohn, and Sham through their classic papers for justifying the replacement of the many-body wave function by one-electron orbitals. (Hohenberg and Kohn, 1964, Kohn and Sham, 1965, Lundqvist and March, 2013). Hohenberg and Kohn demonstrated a couple of theorems (Hohenberg and Kohn, 1964) in which the first theorem specified the electron density that has significant influence on the external potential (to within an additional constant), while the second was for several positive definite trial density (rt) i.e. $\int \rho t\ (\mathbf{r}) d\mathbf{r} = \mathrm{N}$ then $\mathrm{E}\ [\rho t] \geq E_{\mathrm{o}}$. They successfully provided a direct proof of aforementioned theorem in which the first theorem was expanded to involved schemes with degenerate states in proof contributed by Levy (1979) (Levy, 1979, Levy, 1982, Dreizler and da Providencia, 2013).

From the first Hohenberg and Kohn theorem, it can be defined that the trial density establishes a sole trial of Hamiltonian and therefore, the wave function remains to be (Ψ); $\mathrm{E}[\rho t] = \langle \psi t | H | \psi t \rangle \geq \mathrm{E_o}$ derived from the Schrödinger equation on variational theorem (**Equation 3.1**). This formula limits the DFT to discover on the ground state level particularly. A minor addition permits the variation with regards to excited state which can

be assured orthogonal to the ground state. The wave function is necessary in order to accomplish this knowledge of the ground state level. These couple of theorems set the basic equation of DFT (Harrison, 2003);

$$\delta[E[\rho] - \mu(\int \rho(\mathbf{r})d\mathbf{r} - N)] = 0 \quad (3.1)$$

The density and ground state energy refer to the minimum of several functional, $E[\rho]$, dependent on the restriction that the density covers the correct electrons number. Herein, the Lagrange multiplier corresponds to the electronic chemical potential (μ).

The abovementioned statement establishes the notable fact that there is a universal functional, $E[\rho]$, which is independent from external potential. If the functional form is already identified, it could be involved into **Equation 3.1** and subsequently optimized to obtain the obvious density at ground state level of energy (Harrison, 2003). The original DFT theorem is applied for observing the electronic energy on ground-state level of a molecule. Subsequently, a feasible theory of DFT was further established by Kohn and Sham who formulated an approach analogous to the Hartree-Fock (HF) method in terms of structure (Young, 2001).

3.2.1 The existence theorem of Hohenberg-Kohn: rigorous foundation

The former theorem of Hohenberg and Kohn is an existence theorem. It assumes that two different external potentials are able to be coherent with similar non-degenerate ground state density (ρ_0). It will call v_a and v_b potentials together with separate Hamiltonian operators which are H_a and H_b. Each operator will be related with Ψ_0 as a wave function in ground state level and its related eigenvalue, E_0. The theorem of variational of molecular orbital

theory orders which the expected value of Hamiltonian, *a*, over the wave function, *b*, will be greater compared to the ground state energy of *a* (Cramer, 2004), for example:

$$E_{0,a} < \langle \Psi_{0,b} | H_a | \Psi_{0,b} \rangle \tag{3.2}$$

Then the expression can be re-written as follows,

$$\begin{aligned} E_{0,a} &< \langle \Psi_{0,b} | H_a - H_b + H_b | \Psi_{0,b} \rangle \\ &< \langle \Psi_{0,b} | H_a - H_b | \Psi_{0,b} \rangle + \langle \Psi_{0,b} | H_b | \Psi_{0,b} \rangle \\ &< \langle \Psi_{0,b} | \upsilon_a - \nu_b | \Psi_{0,b} \rangle + E_{0,b} \end{aligned} \tag{3.3}$$

Since the potentials are single electron operators, the integral of the last line of **Equation 3.3** can be described as the ground-state density function,

$$E_{0,a} < \int [\nu_a(\mathbf{r}) - \nu_b(\mathbf{r})] \rho_0(\mathbf{r}) d\mathbf{r} + E_{0,b} \tag{3.4}$$

As there is no distinction between *a* and *b*, the equation can be considered as

$$E_{0,b} < \int [\nu_b(\mathbf{r}) - \nu_a(\mathbf{r})] \rho_0(\mathbf{r}) d\mathbf{r} + E_{0,a} \tag{3.5}$$

If the inequalities of **Equations 3.4** and **3.5** are added, it can be found

$$\begin{aligned} E_{0,a} + E_{0,b} &< \int [\nu_b(\mathbf{r}) - \nu_a(\mathbf{r})] \rho_0(\mathbf{r}) d\mathbf{r} + \int [\nu_a(\mathbf{r}) - \nu_b(\mathbf{r})] \rho_0(\mathbf{r}) d\mathbf{r} + E_{0,a} + E_{0,b} \\ &< \int [\nu_b(\mathbf{r}) - \nu_a(\mathbf{r}) + \nu_a(\mathbf{r}) + \nu_b(\mathbf{r})] \rho_0(\mathbf{r}) d\mathbf{r} + E_{0,a} + E_{0,b} \\ &< E_{0,a} + E_{0,b} \end{aligned} \tag{3.6}$$

Where the presumption which the ground-state densities corresponded with the wave functions *a* and *b*, it is allowed to remove the integrals as they will sum to zero. However,

the sum of two energies is less than itself, then it must be indicated which the earlier presumption was not correct. Therefore, the non-degenerate ground state density must discover the external potential, and thus can be applied to determine the Hamiltonian, and subsequently the wave function. Notably, the Hamiltonian defines the ground state as well as the excited state wave functions. Therefore, there is massive information encoded by the density (Cramer, 2004).

3.2.2 The variational theorem of Hohenberg-Kohn: rigorous foundation

As the existence of Hohenberg and Kohn's theorem is provocative with potential but is not helpful to provide any indication of how to predict the system density. Then, Hohenberg-Kohn showed the further theorem in which density obeys a variational principle (Cramer, 2004).

To proceed, it is assumed that some suitable candidate density which integrates to appropriate electrons number, *N* is well defined. In this case, the first theorem demonstrates that the density establishes a candidate of Hamiltonian and wave function. The value of energy expectation is evaluated as follows:

$$\langle \Psi_{cand} | H_{cand} | \Psi_{cand} \rangle = E_{cand} \geq E_0 \tag{3.7}$$

which, by the variational principle of molecular orbital theory, must be equal or higher to the exact ground-state energy.

In principle, various densities can be selected, and those which is able to provide lower energies (**Equation 3.7**), are closer to an accurate result. Up to this point, which there are

certain mappings from density onto the wave function and Hamiltonian, and hence the energy, but it is not suggested that some mechanical means in which the density can be used as an argument in several general characteristics of variational equation (Cramer, 2004).

3.2.3 Self-Consistent Field methodology of Kohn-Sham

Kohn and Sham (1965) proposed approximations which could be significantly simpler if the Hamiltonian operator was only applied to calculate non-interacting electron system (Kohn and Sham, 1965). The approximation expresses the boundary of functional of energy into explicit components to facilitate subsequent analysis, in particular,

$$E[\rho(\boldsymbol{r})] = T_{ni}[\rho(\boldsymbol{r})] + V_{ne}[\rho(\boldsymbol{r})] + V_{ee}[\rho(\boldsymbol{r})] + \Delta T[\rho(\boldsymbol{r})] + \Delta V_{ee}[\rho(\boldsymbol{r})] \qquad (3.8)$$

where terms of r.h.s. corresponds to electron-nuclear interaction, kinetic energy of non-interacting electrons, the kinetic energy correction generating from the electrons interacting nature, classical electron-electron repulsion, and overall corrections to non-classical repulsion energy of electron-electron interaction (Cramer, 2004).

For non-interacting electron system, the kinetic energy is calculated as the total amount of electronic kinetic energies of individual electron. Within the orbital expression for the density, **Equation 3.8** may be rewritten as

$$E[\rho(\mathbf{r})] = \sum_i^N \Big(\langle \chi_i \left| -\tfrac{1}{2}\nabla_i^2 \right| \chi_i \rangle - \langle \chi_i \left| \sum_k^{nuclei} \frac{Z_k}{|\mathbf{r}_i - \mathbf{r}_k|} \right| \chi_i \rangle \Big) +$$

$$\sum_i^N \langle \chi_i \left| \tfrac{1}{2} \int \frac{\rho(\mathbf{r}')}{|\mathbf{r}_i - \mathbf{r}'|} d\mathbf{r}' \right| \chi_i \rangle + E_{xc}[\rho(\mathbf{r})] \qquad (3.9)$$

Where *N* refers to the electrons number and it is used as the density for Slater-determinal wave function as simplified as

$$\rho = \sum_{i=l}^{N} \langle \chi_i | \chi_i \rangle \tag{3.10}$$

ΔT and ΔV_{ee} have been combined together towards E_{xc}, specifically correspond to the exchange-correlation energy.

If it is undertaken in the usual fashion to discover the orbitals χ that minimize E in **Equation 3.9**, it can be found that they satisfy the pseudoeigenvalue equations

$$h_i^{\mathrm{KS}} \chi_i = \varepsilon_i \chi_i \tag{3.11}$$

Where the single electron operator of Kohn-Sham is described as follows

$$h_i^{\mathrm{KS}} = -\frac{1}{2}\nabla_i^2 - \sum_k^{nuclei} \frac{Z_k}{|r_i - r_k|} + \int \frac{\rho(\mathbf{r}')}{|\mathbf{r}_i - \mathbf{r}'|} d\mathbf{r}' + V_{xc} \tag{3.12}$$

and

$$V_{xc} = \frac{\delta E_{xc}}{\delta \rho} \tag{3.13}$$

V_{xc} is possibly defined as the single electron in which the anticipation quantity for the determinant of KS Slater is described as E_{xc}. E of **Equation 3.8** is already exactly minimized, therefore the orbitals χ has to afford the exact density. Further, the orbitals which form the Slater-determinantal eigenfunction for the divisible non-interacting Hamiltonian, is defined as the sum of the Kohn-Sham operators (**Equation 3.12**) and subsequently defined as the following equation,

$$\sum_{i=l}^{N} h_i^{KS} \, |\chi_1 \chi_2 \dots \chi_2\rangle = \sum_{i=l}^{N} \varepsilon_i \, |\chi_1 \chi_2 \dots \chi_2\rangle \tag{3.14}$$

Further, **Equation 3.14** is expressed within a basis set of function $\{\phi\}$, and the coefficients of individual orbital are determined by solution of a secular equation completely similar to which applied for Hartree-Fock theory, except that the elements $K_{\mu v}$ described by

$$K_{\mu v} = \langle \phi_\mu \left| \frac{1}{2}\nabla^2 - \sum_k^{nuclei} \frac{Z_k}{|\mathbf{r}_i - \mathbf{r}_k|} + \int \frac{\rho(\mathbf{r}')}{|\mathbf{r}_i - \mathbf{r}'|} d\mathbf{r}' + V_{xc} \right| \phi_v \rangle \quad (3.15)$$

Since the density is essential for calculation of secular matrix elements, but the density is established using the orbitals derived from **Equation 3.10**, the Kohn-Sham procedure must be carried out as iterative SCF process (Kohn and Sham, 1965).

3.2.4 DFT-based DMol3 code

DMol3 corresponds to a standard, commercial, and academic software package which customs DFT method based on a numerical basis set (Delley, 1990). DMol3 computes the several features of clusters, molecules, crystalline solid materials, and nanomaterial surfaces (Delley, 2000) involved electronic, structural, optical, vibrational properties from the first principles calculations. Currently, DMol3 act as a bundle of Material Studio software developed by BIOVIA. DMol3 can be used in either vacuum (gas phase conditions; non-periodic) or three-dimensional periodic boundary conditions (PBC) for solid-based materials or modeling of lower-dimensional periodicity. DMol3 has several functions such as single point energy calculation, dynamics, restricted and unrestricted DFT calculation, geometry optimization, transition state search, frequency calculation, etc. DFT and dynamics are probably two favorable functions of DMol3. Basically, DMol3 allows geometry optimization as well as calculation of various derived features of the electronic configuration. This function is applicable for saddle point search with and without geometrical constraints.

Recently, DMol3 has been widely used to calculate structural, electronic, optical, and vibrational properties of metal oxide clusters (Rodriguez *et al*., 2000, Janousch *et al*., 2007, Kaneti *et al*., 2016), polymer (Delley, 2006, Low *et al*., 2009), as well as biomolecules (Basiuk and Bassiouk, 2008, Hayashi *et al*., 2013).

3.2.5 Exchange-correlations functionals

The foremost issue of DFT calculations is the unknown of exact exchange and correlation functional unless for the free electron in the gas phase. It may never be observed in the possible mathematical form. Nevertheless, approximations have been successfully used allowing the accurate computation of certain physical quantities (Burke and Wagner, 2013).

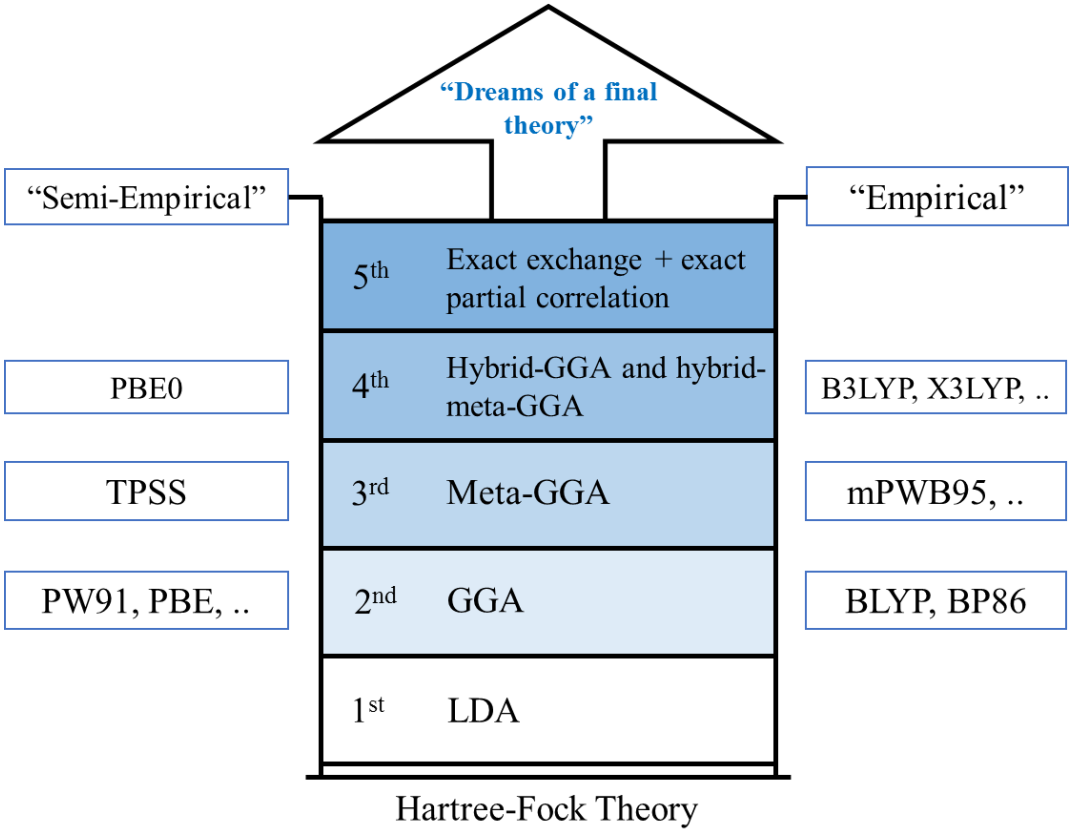

Figure 3.1 Representation of "Jacob's ladder" diagram of exchange-correlation functionals. This scheme was proposed by J. P. Perdew (Perdew and Schmidt, 2001).

Recently, the simple way to categorize exchange functionals have been introduced by J. P. Perdew which was well-defined as "Jacob's ladder" (**Figure 3.1)** (Perdew and Schmidt, 2001). Herein, exchange-correlation functionals are clustered based on their complexity on steps of a ladder which the "earth" corresponds to the Hartree approximation, while the "heaven" indicates the exact exchange-correlation functionals. In addition, the functionals can be classified into non-empirical derivation which is expressed by satisfying several physical rules and empirical derivation which is formulated through fitting to the defined results of either atomic or molecular features. Among many, Generalized Gradient Approximations (GGA) and Becke 3-parameter exchange-correlation functional; Lee, Yang, and Parr (B3LYP) exchange-correlations were used for DFT calculations in this thesis, due to the satisfying calculation of nanomaterials and small biomolecule properties.

3.2.5.1 Generalized Gradient Approximations

Generalized Gradient Approximations is so-called by "semi-local exchange functionals" owing to their dependence on density's gradient [$\nabla n(r)$]. GGAs generate improved results as compared to the local density approximations (LDAs) by means of several properties i.e. ground state energies and geometries of solids and molecules. In regards to weak bonding systems (i.e. covalent), numerous GGAs functionals produce a much better result than LDA.

There are several types of GGA exchange functionals available in DMol3 involving Perdew and Wang; PW91 (Perdew and Wang, 1992), Becke, Perdew and Wang; BP (Becke, 1988, Perdew and Wang, 1992), Perdew-Burke-Ernzerhof; PBE (Perdew *et al*., 1996), Becke, Lee-Yang-Par ; BLYP (Becke, 1988, Lee *et al*., 1988), one-parameter progressive Colle-Salvetti; BOP (Tsuneda *et al*., 1999), Vosko-Wilk-Nusair, Becke, Perdew and Wang; VWN-BP

(Vosko *et al*., 1980, Becke, 1988, Perdew and Wang, 1992), Revised-PBE; RPBE (Hammer *et al*., 1999), Hamprecht-Cohen-Tozer-Handy; HCTH (Boese *et al*., 2003), and PBESol (Perdew *et al*., 2008). Among others, PBE is very popular functional method which is applied in material science. GGA-PBE is well-known for its powerful applicability and ability to provides rather accurate results for a wide-ranging system.

3.2.5.2 B3LYP

B3LYP, Becke 3-parameter exchange-correlation functional; Lee, Yang, and Parr, is one of the hybrid density functional which combine conventional GGA functionals with Hartree-Fock exchange percentage. Herein, a particular empiricism degree is employed in order to optimize the weight factor for each element and the functionals which are combined. However, the exact amount of Hartree-Fock exchange unable to be assigned from the first principles and thus, is semiempirically fitted. Hence, fitting these coefficients to experimental total atomic energies, atomization energies, proton affinities, ionization potentials, and other data, for representative small molecules is the principal way to assign the Hartree-Fock exact amount (Becke, 1993, Sousa *et al*., 2007). The B3LYP is calculated based on mathematical model presented in **Equation 3.16**.

$$E_{xc} = (1 - a_0)E_x(LDA) + a_0E_x(HF) + a_xE_x(B88_x) + a_cE_c(LYP88_c)$$

$$+(1 - a_c)E_cVWN80_c \tag{3.16}$$

Where $a_0 = 0.2, a_c = 0.72, a_x = 0.81$

The main objective of B3LYP functional is to propose the hybrid nature of solids or molecules in a simple mathematical model. Notably, the various approximations involved in the **Equation 3.16** (LDA, Hartree-Fock, Becke-1988 (B88), Lee-Yang-Parr 1988 (LYP88), and Vosko, Wilks, Nusair 1980 (VWN80) entirely belong to B3LYP hybrid functional. The lower case of *x* corresponds to electron exchange calculation whereas the lower case of *c* denotes the observation of the electron correlation.

Hybrid functional allows a significant enhancement over GGA exchange functional and has been widely used for many molecular properties determination. However, the use of B3LYP in the scope of solid state physics or materials containing metals is poorly accurate owing to problems in calculating the exact-exchange portion within a plane-wave basis set (Sousa *et al*., 2007). It was thoroughly assessed by Paier and co-workers comprising the failure of B3LYP in calculating structure containing metals. The failure to accomplish the semiempirical construction as well as exact homogeneous electron gas limit are identified to be a major drawback of the B3LYP for the metals system calculation. It was proven that B3LYP are extremely poor in accuracy as compared to non-empirical density functional e.g. PBE03 and HSE03 (Paier *et al*., 2007). Therefore, in this present study, B3LYP was only used for calculating small molecule or biomolecule (i.e. dopamine) in order to reach a satisfied and accurate result, not for metal oxide structures.

3.2.6 Numerical basis sets

As the basis function, DMol3 employs numerical orbitals in which each function corresponds to an atomic orbital. Atomic basis sets are restricted to a set of defined cut-off value which is applicable for a specific level of calculations quality. This is a vital aspect of the numerical

basis set leading to much faster calculations, predominantly for solid state systems. Geometry optimization is efficient, even with small cut off values (BIOVIA, 2016b). **Table 3.1** below summarize the available basis sets incorporated with DMol3 code along with their description.

Table 3.1 Numerical basis sets of DMol3 code.

Basis Name	Description	Examples
MIN	○ Minimal basis set. ○ One atomic orbital for each occupied atomic orbital. ○ Produces less accuracy but fast computation (non-time consuming).	H: 1s C: 1s 2s 2p Si: 1s 2s 2p 3s 3p
DN	○ Double Numerical basis set. ○ MIN + a second set of valence atomic orbitals. ○ Enhanced accuracy over MIN.	H: 1s 1s' C: 1s 2s 2p 2s' 2p' Si: 1s 2s 2p 3s 3p 3s' 3p'
DND	○ Double Numerical plus d-functions basis set. ○ Similar to DN with a polarization d-function on overall non-H atoms. ○ The default basis set, providing reasonable accuracy for modest computational cost.	H: 1s 1s' C: 1s 2s 2p 2s' 2p' 3d Si: 1s 2s 2p 3s 3p 3s' 3p' 3d
DNP	○ Double Numerical plus polarization basis set. ○ Similar to DND including a polarization p-function on all H atoms. ○ Best accuracy, highest cost. ○ Important for hydrogen bonding.	H: 1s 1s' 2p C: 1s 2s 2p 2s' 2p' 3d Si: 1s 2s 2p 3s 3p 3s' 3p' 3d
TNP	○ Triple Numerical plus polarization basis set. ○ Similar to DNP involving added polarization functions on all atoms. ○ Available only for H to Cl except He and Ne. ○ Best accuracy but highest cost.	H: 1s 1s' 2p 1s'' 2p' 3d O: 1s 2s 2p 2s' 2p' 3d 2s'' 2p'' 3p 4d S: 1s 2s 2p 2s' 2p' 3s 3p 3s' 3p' 3d 3s'' 3p'' 3d' 4d
DNP+	○ Double Numerical plus polarization basis set, with addition of diffuse functions. ○ Good accuracy for cases requiring diffuse functions, very high cost coming mostly from very large atomic cut offs required for this set. ○ Important for anions, excited state calculations and for cases where long-range effects are non-negligible. ○ The bold components are the additional diffuse functions.	H: 1s 1s' 2p 1s'' 2p' C: 1s 2s 2p 2s' 2p' 3d 1s' 2p'' 3d' Si: 1s 2s 2p 3s 3p 3s' 3p' 3d 1s' 2p' 3d'

3.2.7 DFTB+

DFTB+ is an improved implementation of density field-based tight binding for studying the electronic properties of materials containing hundred atoms. DFTB itself is established on a

second-order extension of the Kohn-Sham (Kohn and Sham, 1965) total energy in density functional regarding fluctuations of charge density (Elstner *et al*., 1998). DFTB+ offers the flexibility to observe the optimization and dynamic properties with quantum mechanics (QM) accuracy but less in time-consuming. DFTB+ incorporated with BIOVIA Material Studio software uses libraries of parameters so-called Slater-Koster files to encapsulate the elemental interaction in the material. Recently, the use of DFTB+ (rather 'self-consistent charge-DFTB') has been reported in many literatures and is capable of calculating the electronic properties of the large biological systems such as oligonucleotides and protein (Elstner *et al*., 2003, Elstner, 2006, Nishimoto *et al*., 2014).

3.3 Monte Carlo Simulation

One of the most popular computational techniques for fluids modeling in atomic level is Monte Carlo statistical mechanic (Allen and Tildesley, 1987). MC simulation is a specific type of molecular mechanics (MM) simulation on the basis of repetitive random sampling and statistical analysis in order to predict the computed results. This particular method is able to reproduce an accurate result related to arbitrary experiment which is previously unknown (Raychaudhuri, 2008). It employs a setup involves molecules representation as the cluster of atom-centered interaction sites, application of classical force fields for calculating the potential energy, and the use of PBC. It has specific sampling methods of configuration spaces which are obtainable in the system. Initially, a new configuration is produced by choosing molecule in random, then translate and make a rotation of it. The last step is the accomplishment of several internal structures. Affirmation to those configurations is specified by Metropolis sampling algorithm in which application over sufficient configurations outcomes appropriate Boltzman-weighted means for the properties of

thermodynamics and structures. The force field controls the total energy (Jorgensen and Tirado-Rives, 1996).

The MC application in Materials Studio tends to tackle the huge number of probabilities into small portions so that the scope of MC can be classified. Materials Studio provides some genuine modules related, which are available in computational simulation paper work and advanced with a number of length and time scale possibilities. Mainly, this module is based on the QM, calculating the electronic properties. Shortly, the module methods are simply defined into three separated parts: (a) general configuration, (b) traditional Metropolis and biased sampling, and (c) optimization devices. The fundamental of MC as sampling method is to correlate the changes of transition probabilities occurred in an ensemble and its density $\rho(\Gamma)$:

$$\rho(\Gamma, \mathrm{n}+1) - \rho(\Gamma, \mathrm{n}) = \sum_{\Gamma'}(\mathrm{T}(\Gamma', \Gamma)\,\rho(\Gamma', \mathrm{n}) - \mathrm{T}(\Gamma, \Gamma')\rho(\Gamma, \mathrm{n})) \tag{3.17}$$

Because $\rho(\Gamma, \mathrm{n}) = \rho(\Gamma)$ when reached the density equilibrium status,

$$0 = \sum_{\Gamma'}(\mathrm{T}(\Gamma', \Gamma)\,\rho(\Gamma') - \mathrm{T}(\Gamma, \Gamma')\rho(\Gamma)) \tag{3.18}$$

This condition is satisfied if the transfer probabilities $\mathrm{T}(\Gamma, \Gamma')$ obey detailed balance,

$$\frac{\mathrm{T}(\Gamma,\Gamma')}{\mathrm{T}(\Gamma',\Gamma)} = \frac{\rho(\Gamma')}{\rho(\Gamma)} \tag{3.19}$$

As first put forward by Metropolis (Metropolis *et al*., 1953), choosing

$$\mathrm{T}(\Gamma, \Gamma') = \min\left(1, \frac{\rho(\Gamma')}{\rho(\Gamma)}\right) \tag{3.20}$$

satisfies detailed balance. Consequently, steps that increase the density (i.e. those that are more important to ensemble $\rho(\Gamma') > \rho(\Gamma)$ are always accepted, while steps that decrease the density (steps to a less important state) are accepted with lower probability. In molecular simulation, the most interesting density functional is due to:

$$\rho(\Gamma) = \left(\frac{\exp(-\beta E(\Gamma))}{\int d\Gamma' exp(-\beta E(\Gamma'))}\right) \tag{3.21}$$

$E(\Gamma)$ acts as the potential energy of system in field Γ and $\beta = 1/(k_B T)$ (k_B defines the Boltzman constant with T of the temperature). Kinetic energy is not involved in this equation as it needs only the momentum space integrated with the analysis, without any sampling. The acceptance probability follows from **Equation 3.20**:

$$\mathrm{T}(\Gamma, \Gamma') = \begin{cases} exp\big(-\beta(\mathrm{E}' - E)\big), & \mathrm{E}' > E, \\ 1, & \mathrm{E}' \leq E, \end{cases} \tag{3.22}$$

where $\mathrm{E}' = E(\Gamma')$.

The state is changed and being annotated as two type processes. First, providing initial step, which may be accepted or not. Then, the $\omega(\Gamma, \Gamma')$ will be a trial probability and $\alpha(\Gamma, \Gamma')$ will be the aceptance probability, then:

$$\mathrm{T}(\Gamma, \Gamma') = \omega(\Gamma, \Gamma')\alpha(\Gamma, \Gamma') \tag{3.23}$$

In the conventional MC, trials are made with equal probability in either direction, $\omega(\Gamma, \Gamma') = \omega(\Gamma', \Gamma)$ (Akkermans *et al*., 2013).

Several types of calculations are referred to MC calculations. Entire of MC calculations are designed throughout several random sampling sorts, which is modeled with a random number of generating algorithm. In this particular simulation, location, orientation, and perhaps

geometry of a group of molecule are selected according to statistical distribution. For example, choosing random conformation angles examine many possibilities of molecule conformation. When sufficient iterations are done, then results are weighted by Boltzman distribution. It gives valid result statistically. The workflow of common steps of MC calculation is represented in **Figure 3.2** (Young, 2001).

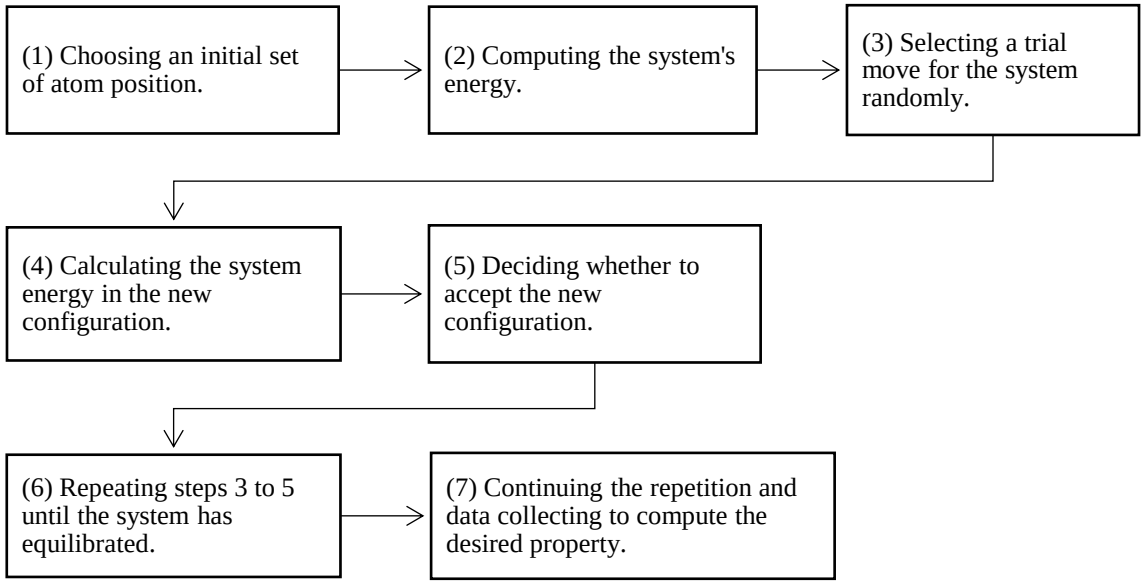

Figure 3.2 Step-by-step diagram of MC simulations.

There are several variations on the abovementioned procedure termed as importance and biased sampling which are used to reduce the number of repetition, then achieves more accurate result. These variations entirely change the steps three and five of the diagram (**Figure 3.2**). In step three, the size of the trial moves alters the efficiency of the simulation. Herein, the inefficient calculation occurrs while the simulation requires more repetitions to achieve the determined accuracy. When the size is very small, it is going to employ numerous repetition of atom locations to alter. If the size is exceedingly large, less number of moves

can be admitted. The efficiency associates with the acceptance ratio. It refers to a number of times in which the move was accepted, divided by total repetition number. Generally, the most effective MC calculation is that which has acceptance ratio between 0.5 and 0.7 (Young, 2001).

3.4 Molecular Dynamics

Today, computer-based simulation have been employed to overcome many-body issues in several fields i.e. physical chemistry, physics, biophysics (Attig *et al*., 2004), biology, bioinformatics, and chemistry. In several cases, it is not possible to discover how atomic level interaction establish continuum properties unless by employing computer simulation. The MM-based simulation which has been widely used, instead of MC, is MD (Allen and Tildesley, 1989, Grotendorst *et al*., 2002). This method is essentially used in statistical mechanics simulation (Attig *et al*., 2004).

MD is a part of MM approaches which corresponds to the employment of simple potential-energy functions to simulate molecular systems (Adcock and McCammon, 2006). MD has been broadly applied in obtaining the time evolution of biomolecules conformations such as protein and their kinetics as well as thermodynamic properties (Cheatham and Kollman, 2000, Norberg and Nilsson, 2002, Karplus and McCammon, 2002, Adcock and McCammon, 2006). MD has also been applied widely and routinely to discover the behavior of nanomaterials at the atomic level (Miao *et al*., 2005, Hu *et al*., 2009, Makarucha *et al*., 2011) as well as their biophysics (Adcock and McCammon, 2006). Employment of MD in materials simulation is rapidly growing along with the increment of the demand.

Theoretically, MD simulation describes the velocities, positions, and orientations of interacting particles in the function of time. Particles, herein, may correspond to atoms, a group of atoms, and larger bodies such as molecules or biomolecules. A set of mathematical models which enable to define atomic-scale interaction is fundamental basis of MD. The dynamics are governed by Hamiltonian system and equations of motion as shown in **Equation 3.24**.

$$\mathrm{H} = \mathrm{T} + \mathrm{U}, \dot{\mathrm{p}}_i = -\frac{\partial H}{\partial q_i}, \dot{\mathrm{q}}_i = -\frac{\partial H}{\partial P_i} \tag{3.24}$$

where H corresponds to the Hamiltonian, T is the kinetic energy; a momenta function, $\mathrm{T} = \frac{\mathrm{p}^2}{2\mathrm{m}}$, and U remains the potential energy; a position function in the atomic ensemble, $\mathrm{U} = \mathrm{U}(\mathrm{q})$.

For instance, the overall process of MD simulation can be described as follows:

I. Selecting the function of potential energy which is used to define the interatomic interactions.
II. Setting up the velocity and starting position of each atom as well as the simulation space dimensions.
III. Calculating the overall forces on total N atoms.
IV. Finding the accelerations of each atom.
V. Obtaining the velocity of each atom and position upon a selected timestep through numerical integration by a certain algorithm.
VI. Updating all position of atoms in the system.
VII. Repeating steps III - VI.

VIII. Finalization process, or analysis of produced atomic trajectory data and thermodynamics.

3.4.1 Forcite code

Forcite, a code available in BIOVIA Materials Studio software, is an advanced conventional MM tool, which permits rapid calculation of energy and reliable geometry optimization of non-periodic as well as periodic molecular system (i.e. PBC). For the periodic condition, the cell parameters optimization with molecular coordinates is allowed. Additionally, an external pressure of hydrostatics may be used. During the optimization of crystal structure's geometry, Forcite conserves the symmetry described by the space group, and the structure is minimized in regards to overall structural degrees of freedom or implementing the constraints system for the crystal structure (BIOVIA, 2016b).

Forcite code is able to perform a wide range of task by using classical method, such as geometry optimization, dynamics etc. The geometry optimization procedure of Forcite was performed using an iterative task where the coordinates of atoms were modified up to the total energy of structures was diminished. Geometry optimization relies on the decreasing the magnitude of the computed forces until they turn out to be smaller than certain value of convergence tolerance (Amoli *et al*., 2015). The geometry optimization task of Forcite allows to refine the structure geometry until it reaches certain specified criteria (i.e. convergence level, SCF etc.). In general, the optimized structure refers to a potential energy minima of a surface (Zhao *et al*., 2014b). As a part of MM simulations, Forcite-Geometry optimization calculation is drawn upon the force field type and parameter set up prior to running calculation. Therefore, determining the suitable force field is one of the important part of this

calculation. Apart of geometry optimization, the dynamics task was also employed in the present study in order to investigate the molecular interaction within layer components.

3.4.2 Force field

In terms of molecular modeling, a force field corresponds to the functional forms derived from mathematical models and parameter settings applied to determine the potential energy of an atomic system or coarse-grained particles in MM (Vanommeslaeghe *et al*., 2014) and MD (Nosé, 1984a) simulations. The energy function parameters may be generated from experiments in chemistry or physics, QM calculation, or both. The force field defines the estimated potential energy hypersurface wherein the atomic nuclei travels. Force fields selection typically depends on the specific groups of the systems and thus, there is no absolute force field for certain system unless it is rigorously adjusted by the type of structures (i.e. hydrocarbon, metal system, metal organics etc.) which is being discovered (BIOVIA, 2016b).

3.4.2.1 COMPASS

Condensed-phase optimized molecular potentials for atomistic simulation studies (COMPASS) is *state-of-the-art* force field technology which defined as the foremost *ab initio*-based approximations which allows simultaneous and accurate prediction of electronic, conformational, structural, and thermophysical features of inorganic and organic small molecules and polymers (Sun, 1998, Yang *et al*., 2000). It corresponds to a first sophisticated force field which strengthens parameters for organic and inorganic compounds previously observed in various force fields. The COMPASS emphasizes on the high-level accuracy of prediction comprising experimentally analogous accuracy in calculating molecular properties in condensed phases as well as in isolation. The COMPASS belongs to *ab initio* force field

due to most parameters were generated from the data of *ab initio* method. Indeed, *van der Waals* interaction was calculated by performing dynamics simulations of molecular liquids and matching the equilibrium densities and predicted cohesive energies to experimental informations (Sun, 1998, Sun *et al*., 1998). COMPASS has been accurately used to simulate transition metals oxides (Wagemaker *et al*., 2003, Alvarez-Ramirez and Ruiz-Morales, 2007, Yue *et al*., 2013, Sang *et al*., 2016), biomolecules as well as macromolecule system such as nucleotide (Ngaojampa *et al*., 2010, Chai *et al*., 2014).

3.4.2.2 Universal force field

Universal force field (UFF) is designed based on trouble shooting of traditional force field which unable to calculate new sets of elements, atoms or molecules. Particularly, the traditional force field can only cover certain combinations of atoms i.e. proteins, molecular organics or nucleic acids. UFF, in general, provide a set of rules and procedures for generating proper parameters across the entire periodic table. The UFF is fundamentally based on the atomic elements, its hybridization, as well as connectivity (Rappe *et al*., 1992).

In term of functional form, UFF is essentially harmonic and diagonal force field. Stretching of the bond is designated by angle bending by a three-term Fourier cosine torsions and expansion, a harmonic term, and inversions by expansion term of cosine-Fourier. The electrostatic interactions are defined by a partitioned (distance-dependent) Coulombic term and atomic monopoles, while *van der Waals* are characterized by the Lennard-Jones potential (BIOVIA, 2016b). UFF was successfully applied to organic and inorganic especially to the transition metal complexes (Rappe *et al*., 1992, Casewit *et al*., 1992, Rappe *et al*., 1993).

3.4.2.3 Dreiding

For the dreiding force field, geometry parameters and general force constants are described for considering simple hybridization rather than geometric parameters and individual force constants which rely on the specific combination of atoms including the terms of structural bond, torsion, or angle (Mayo *et al*., 1990). Dreiding does not generate parameters automatically like UFF does. Instead, explicit parameters of this force field were obtained by a rule-based approach (BIOVIA, 2016b). Dreiding is advantageous to predict structural geometry and dynamics comprising biological, organic, and main-group inorganic molecules particularly (Mayo *et al*., 1990).

3.4.3 Summation methods

Summation method is used for calculating non-bond energies of electrostatic and *van der Waals* interaction of a structure or molecule. For electrostatic interaction, the available summation methods are atom-based, group-based, Ewald, and Particle-Particle Particle-Mesh (PPPM), while for *van der Waals* interaction, atom-based, group-based, and Ewald can be used.

3.4.3.1 Atom-based cut-offs

Atom-based cut-offs is a direct summation method applied to determine long-range of non-bond interactions in which the non-bond parameters are merely computed based on a certain distance of cut-off and interactions beyond the cut-off are discounted. Nevertheless, this direct method is able to lead the breaks in term of energy and its derivatives. As the distance of a pair of atom travels in and out in the range of certain cut-off within calculation steps, the

energy will jump, since the non-bond energy is taken into account in one iteration step and omitted from its next step (BIOVIA, 2016b).

3.4.3.2 Group-based cut-offs

The term "charge group" is defined as a small atoms group close to each other and it has a net charge of absolutely or nearly zero. In practice, charge groups are similar to common group of chemical functional, for example, a methyl, carbonyl group, or carboxylate group which will be almost neutral in the charge groups. The potential energy which is exerted by specific group of atoms at a particular distance, R, from the group center can be achieved by formulating an extension with regards to the inverse powers of R:

$$\Phi + \frac{1}{4\pi\varepsilon}\left\{\frac{Q}{R} + \frac{\mu cos\theta}{R^2} + \frac{\Theta(3\cos 2\theta - 1)}{R^3} + \cdots\right\} \tag{3.25}$$

where Q corresponds to the total group charge, μ is the dipole moment of the group, and Θ is the quadrupole moment. Thus, when the group has neutral charge, the leading term will be comparative to $\frac{\mu}{R^2}$. Similarly, if a certain distance, R, is applied to the centre of another charge group, form the first, an identical expansion in regards to R can be expressed, and if the both charge group have neutral charge, it is possible to be described which the foremost interaction will be proportional to $\frac{\mu\mu'}{R^3}$ (Maitland, 1981), where μ' corresponds to dipole moment of the second charge group. This observation is the basis of the charge group method. For a specified cut-off value, charge groups can be anticipated to provide a better estimation of the Coulombic interaction rather than atom-based cut-off. Another benefit of the charge group is the capability to tend to be faster as compared to similar atom-based cut-off in the same

selected value. The interaction between two groups is calculated by the distance within their centres (BIOVIA, 2016b).

3.4.3.3 Ewald cut-offs

The Ewald technique (Ewald, 1921, Tosi *et al*., 1964) is a computation method of non-bond energies in PBC. The most suitable candidate for this method is crystalline solids due to the possibility of errors which are related to the use of certain cut-off value, is greater in periodic lattice. Nevertheless, the Ewald technique can also be used to solutions and amorphous solids. For example, the performance of an Ewald calculation with 10^{-4} accuracy can be analogous to an atom-based cut-off with quite large value (19 Å) over the range. Furthermore, the Ewald significantly increases the accuracy of the calculation (BIOVIA, 2016b). This method was accurately tested for calculating *van der Waals* interaction and long range electrostatic (Toukmaji and Board, 1996) of a large system (Osnis *et al*., 2012).

3.4.3.4 Particle-Particle Particle-Mesh Ewald cut-offs

The Particle-Particle Particle-Mesh method (PPPM) (Hockney and Eastwood, 1988) uses a Discrete Fourier Transform to evaluate the reciprocal space portion of the Ewald summation method. The performance can be significantly improved (rather 'faster') than the ordinary Ewald method mainly for large systems. In practice, the PPPM was tested to faster the calculation of larger systems due to the reducing time on fewer number of cores (BIOVIA, 2016b).

3.4.4 Periodic Boundary Condition

PBC is a set of boundary condition which is regularly applied for estimating an infinite number of system through a particular part called by a unit cell (Schlick, 2010). PBC are used in molecular mechanics (i.e. MD) simulation in order to make the system representing the infinite condition at the cost of possible periodicity effects. Inside the PBC, there are several types of simulation circumstance i.e. gas phase condition, solvated system, protonated environment etc. depends on the *state-of-the-art* of the calculation itself. The illustration of PBC is presented by **Figure 3.3** in which whole atoms in the box center are duplicated to all over the spaces forming an infinite lattice (PBC).

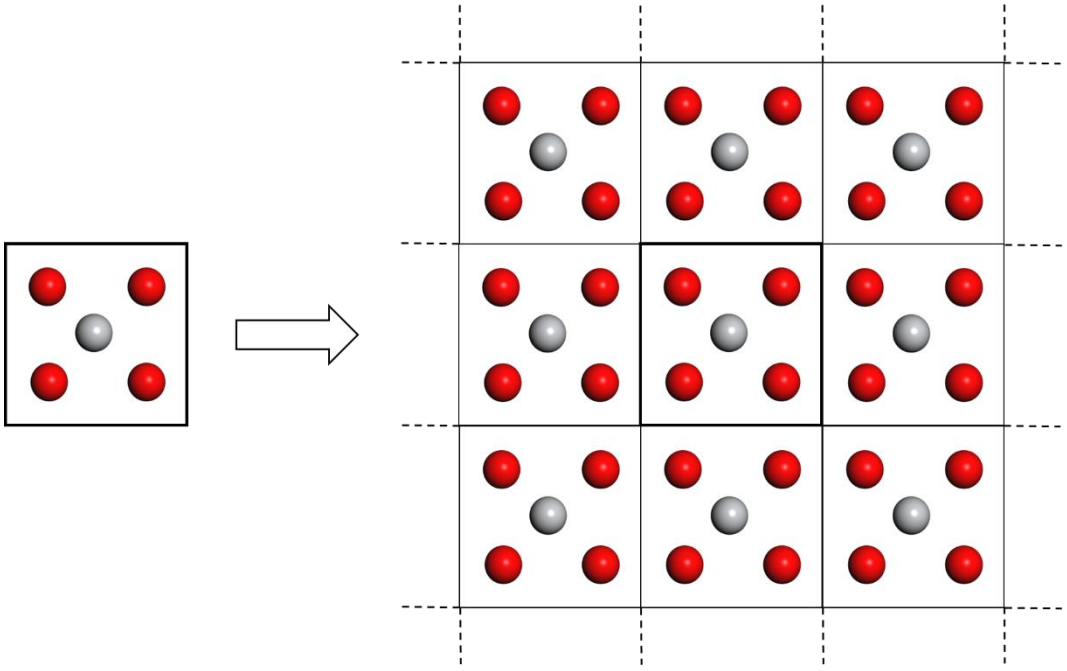

Figure 3.3 Representation of a PBC system. The left side shows the small unit cell which constructs the infinite structure (right side).

The consideration of maximum interatomic distance (r_{cut}) is thereby capable of the half of simulation box edge:

$$r_{cut} = \frac{L}{2} \tag{3.26}$$

If the atoms in the cell have positions (r_i), the PBC also generates mirror images at the positions described as

$$\vec{r}_i^{\,image} = \vec{r_i} + \overrightarrow{la} + \overrightarrow{mb} + \overrightarrow{nc} \tag{3.27}$$

where *l*, *m*, and *n* are any integers from -∞ to +∞ while *a*, *b*, and *c* are vectors which refer to the box edges of PBC.

3.4.5 Thermodynamics ensemble

Incorporating the motion equations of Newton's permits to discover the constant-energy surface of a particular system. Nevertheless, most of the natural phenomena happen under circumstances in which the external pressure and/or exchanges temperature exposes the system with the environment. Under these particular conditions, the total energy is not conserved and therefore, require an extended dynamics forms (BIOVIA, 2016b).

Depending on the constant variables including the number of particles (*N*), pressure (*P*), temperature (*T*), volume (V), and energy (*E*), various thermodynamics ensembles are available to be used in the MM simulations. Numerous structural, energetic, and dynamic features can be discovered from the fluctuations or the average value of these amounts over the selected ensemble. Both isothermal ensemble, which the heat is replaced by a temperature bath to maintain a fixed thermodynamic temperature, and adiabatic ensemble inwhich there is no heat replacement occurs, are shown in **Table 3.2** (BIOVIA, 2016b).

Table 3.2 Ensembles of MD simulations.

Thermodynamics ensemble	**Parameters to be kept in constant (instead of number of particles; *N*)**
NPT	Pressure and temperature
NVE	Volume and energy
NPH	Pressure and enthalpy
NVT	Volume and temperature
NST	Stress and temperature

NVT ensemble, also known as the canonical ensemble, is generated by governing the temperature *via* scaling the direct temperature throughout the initialization stage and by the coupling of temperature-bath throughout the data collection stage. The volume is kept fixed during simulation. NVT is a proper choice when the vacuum condition is employed (without PBC). In the system without PBC, density, pressure, and volume is not able to be defined. In another words, the constant-pressure cannot be performed. However, NVT ensemble dynamics with PBC is applicable as long as the pressure does not give substantial error, therefore the constant-volume and temperature ensemble allows the benefits of minor trajectory perturbation caused by lack of coupling to a pressure bath (BIOVIA, 2016b). The applicability of NVT ensemble in particular for clusters containing metal or metal oxide-based structure has been widely explored in the recent years (Lee and Rasaiah, 1996, Prathab *et al*., 2007, Cheng and Selloni, 2010, Yue *et al*., 2013).

3.4.6 Thermostat

Thermostat corresponds to a method to control the temperature during dynamics simulation. The choice of thermostat plays important role in order to facilitate the equilibration phase of

the system. Several thermostat techniques are commonly used in molecular dynamic simulations such as direct velocity scaling, Berendsen (Berendsen *et al*., 1984), Nosé (Nosé, 1984a, Nosé, 1984b, Hoover, 1985, Shuichi, 1991), Nosé-Hoover-Langevin (Samoletov *et al*., 2007), and Andersen (Andersen, 1980, Weinan and Dong, 2008). Herein, Andersen dynamics was employed in molecular dynamics trajectories involving equilibration and production phases.

The first type of Andersen technique of heat control includes randomizing the all atoms velocities at a certain collision period, while the other version comprises selecting collision times of atom from a Poisson distribution at each time step and altering their velocities according to the Boltzmann distribution. For the first version, the predefined collision period is proportional to $N^{2/3}$, where N corresponds to the atoms number of the simulation system.

CHAPTER 4

MATERIALS AND METHODS

This chapter focuses on two major methodologies involved in this research comprising of computational and experimental studies. The first subsection describes the computational investigation of the electrode consisting of FTO, TiO_2, dopamine (DA), and ss-DNA. Initially, construction of nanostructures is presented followed by structural examination using molecular mechanics (MM)-based geometry optimization. Afterwards, the density functional theory (DFT) calculations using numerical basis set is provided to observe the structural, electronic, and vibrational properties of the studied nanoclusters and molecules. This is followed by the interaction studies using Metropolis Monte Carlo (MC) method towards predicting the adsorption process by means of simulated annealing technique. Lastly, the molecular dynamics (MD) simulation which was accomplished to mimic the experimental circumstances of the electrodes construction as well as to generate an in-depth understanding of interactions phenomena, is thoroughly explained. The second subsection elucidates the experimental procedures including materials and instrumentation, preparation of the electrodes and photo-oxidative damage of the ss-DNA, fabrication of the modified electrode along with the characterization studies, and electrochemical detection of DNA damage and ascorbic acid (AA) activity measurements.

4.1 Computational

4.1.1 Construction of nanostructures and Forcite-Geometry-based structural analysis

4.1.1.1 Fluorine-doped tin oxide

Fluorine-doped tin oxide (FTO) was constructed through the doping of fluorine (F) atom into SnO_2 nanocluster. Rutile SnO_2 with (200) plane was chosen in overall study as one of the preferential orientation used in theoretical studies (Feng *et al*., 2009, Cao *et al*., 2013) which also has been experimentally observed in F-doped SnO_2 investigations (Thangaraju, 2002, Agashe and Mahamuni, 2010, Banyamin *et al*., 2014, Wang *et al*., 2014, Afzaal *et al*., 2016). Indeed, this specific plane was selected due to less surface energy of interaction (Agashe *et al*., 1988). In order to build the FTO structure, firstly, SnO_2 (200) was constructed using the simplest crystal structure of SnO_2 (further called by primitive or intrinsic structure) provided by Material Studio (MS) software's library. Nanocluster's surface was subsequently built along (200) plane orientation with the 0 Å top fractional and 18.49 Å thickness fractional. The 4 x 6 unit cell was chosen to obtain 288 of total atoms with the 96 Sn and 192 O atoms. Then, 20 Å of vacuum slab was selected to build periodic boundary condition (PBC) of FTO. For observing the feasibility of intrinsic SnO_2 structure, the geometry of SnO_2 primitive structure is optimized by Forcite module with ultrafine-COMPASS force field (Sun, 1998, Sun *et al*., 1998). The convergence criteria for the maximum values of energy alteration, force, stress, and displacement were set at 2×10^{-5} kcal/mol, 0.001 kcal/mol/Å, 0.001 GPa, and 10^{-5} Å.

Herewith, F atom substitutes the anion (oxygen; O) of SnO_2 cluster (Schaefer *et al*., 1997, Nakajima and Groult, 2005). FTO remains excellent visible transparency due to its wide

electronic band gap, whereas preserving a low electrical resistivity owing to the high transporter concentration triggered by the vacancies of O atoms and the substitutional F dopant (Subba Ramaiah and Sundara Raja, 2006). The 5.3% of dopant concentration was chosen in the FTO nanostructure as an optimum doping percentage of F onto SnO_2 (Banyamin *et al*., 2014). Introduction of F increases the coexistence of electrical conductivity and optical transparency of metal oxide by narrowing the band-gap (Edwards *et al*., 2004). This may be due to the similar electronegative nature of F and O atoms. In terms of dopant position, the F atoms was randomly deposited into SnO_2 surface which was initially created *via* random removal of oxygen atoms (Rhodes *et al*., 2008a, Rhodes *et al*., 2008b) positions of un-doped SnO_2 structure. The lattice parameter of un-doped and F-doped SnO_2 used in this study were calculated to be a = 18.949 Å, b = 19.118 Å, and c = 28.560 Å.

4.1.1.2 Titanium dioxide

Titanium dioxide (TiO_2) was constructed along with (101) plane direction as preferential orientation of computational (Sorescu *et al*., 2011, Di Valentin and Costa, 2012, Syres *et al*., 2012, Stashans *et al*., 2015) and experimental studies (Gong *et al*., 2006, Yang *et al*., 2008, He *et al*., 2009, Syres *et al*., 2010, Li *et al*., 2011). Moreover, most existing TiO_2 anatase crystals corresponds to the thermodynamically stable of (101) typical facets (over 94% based on the Wulff construction) (Lazzeri *et al*., 2001, Barnard and Curtiss, 2005, Yang *et al*., 2008). The surface was built from the crystal structure of TiO_2 anatase generated from MS structures library comprising 0 Å top fractional and 14.003 Å thickness fractional. The unit cell of 3 x 3 was built along with 20 Å vacuum slab (Kusama *et al*., 2008).

Anatase crystal structure of TiO_2 was chosen encompassing titanium (Ti) atom which is surrounded by six O atoms, but has only four Ti atoms nearest neighbours. TiO_2 is well-known as highly ionic semiconductor. The Ti (IV) atoms prefers a large number of O neighbours and strongly repels its Ti next nearest neighbours (Gaba *et al*., 2013). By optimizing the primitive structure using COMPASS commercial force field (Sun, 1998, Sun *et al*., 1998) with 'ultrafine' convergence quality as implemented in Forcite module, the structural parameters have been observed and compared to other previous theoretical and experimental results. The convergence criteria for accomplishment of geometry optimization were set as follows: 2×10^{-5} kcal/mol of maximum energy change, 0.001 kcal/mol/Å of maximum force, 0.001 GPa of maximum stress, and 10^{-5} Å of maximum displacement.

4.1.1.3 Dopamine

The molecular structure of dopamine was drawn using MS software. Fundamentally, the single dopamine molecule contains two hydroxyl groups (-OH), benzenoid ring, and an amide group. Forcite code was a preferable method to observe the low energy configuration (rather 'most stable conformation') of dopamine molecule, along with 'ultrafine' quality of COMPASS force field (Sun, 1998, Sun *et al*., 1998). The convergence criteria i.e. maximum value of energy change, force, stress, and displacement were set at 2×10^{-5} kcal/mol, 0.001 kcal/mol/Å, 0.001 GPa, and 10^{-5} Å, respectively.

4.1.1.4 ss-DNA of Alzheimer's

The oligonucleotide (ss-DNA) encoding cerebrovascular amyloid protein formation was used in the computational study (Glenner and Wong, 1984, Robakis *et al*., 1987)). It was a representative model of the experiment in order to molecularly observe the nature of ss-DNA

and its functionality to further undergo the interaction studies (MC adsorption studies and MD simulations). The sequence had 72-mers of nucleobases as shown at previous section. According to the experiment, the 5' of nucleotide was functionalized with carboxyl group (-COOH) in order to covalently linked to amine group of dopamine (composed as third layer in the system) (Rajh *et al*., 2004). Nevertheless, dopamine was successfully observed as an anchor molecule within oligonucleotide and TiO_2 nanocrystalline (Paunesku *et al*., 2003, Vega-Arroyo *et al*., 2007) due to their unique skeleton having two -OH and an amine groups. The amine group of dopamine was linked to -COOH of oligonucleotide, while the -OH groups was oriented to the surface of TiO_2 anatase cluster (Paunesku *et al*., 2003).

In this present simulation, the -COOH group was attached at the 5'end-phosphate of oligonucleotide terminus as its preferability from the synthetic point of view (i.e. visible synthesize region). The macromolecule ss-DNA structure was initially constructed through Discovery Studio (DS) software (BIOVIA, 2016a) followed by folding treatment using secondary structure observation. In order to predict the secondary structure with more details information, Mathews Lab RNA structure software (online: http://rna.urmc.rochester.edu/RNAstructure.html) was employed. This software allows to predict either ss-DNA or RNA structures into any possible folding. For predicting a 3D aptamer structure, firstly, MFold software was utilized to fold the initial sequence of each aptamer into its secondary structure. The folding temperature was set to 25°C with solvent condition in default setting. The model which had the lowest Gibbs energy was picked and its output, the dot-bracket (Vienna) format, was fetched for tertiary (3D) prediction. For this purpose, RNA Composer software was applied to generate the 3D structure automatically and available freely. The 3D construction concept is a kind of search-engine, based on the

translation of RNA Fragment Base Search Engine (FRABASE) database which associated to RNA 3D structure database. The Vienna format imported to the RNA Composer was generated into PDB format of 3D structure outcome. Notably, the RNA Composer only generates the Vienna format input into the PDB file of RNA. If compared to ss-DNA structure, a -OH group appears in 2'-carbon atom of ribose and uracil is placed at the thymine position. The DS Visualizer can adjust the RNA to be ss-DNA. To do this, each aptamer PDB file was activated individually and Macromolecule command was allowed to modify the ribose backbone into deoxyribose (all oxygen in 2'-carbon ribose atoms are changed into hydrogen atoms) and converted all the uracil bases into thymine (hydrogen assembled to the 5-carbon pyrimidine uracil atom was replaced by carbon atoms forming methyl group). The final structures were presented in ss-DNA assembly. Latter, each structure was optimized geometrically using steepest descent minimization of 32000 steps in DS (Hu *et al*., 2015, Heiat *et al*., 2016, Ahirwar *et al*., 2016). These steps were completed to generate the secondary structure (rather 'folded') of studied oligonucleotide, therefore can be reliable in further calculation.

Upon the minimization using DS, the oligonucleotide structure was subsequently shifted to MS environment. Due to their different circumstances, the geometry of oligonucleotide was optimized using Forcite code along with 'coarse' quality of Universal and Dreiding force fields incorporated with the current charge equilibration method. As described in previous chapter, the Universal force field (UFF) technique can be appropriately used to calculate the structure and energetics of elements across the periodic table (Rappe *et al*., 1992) involved molecules of organic i.e. DNA (Ogawa *et al*., 2003), while the Dreiding force field which uses hybridization rules (Mayo *et al*., 1990), is applicable for simulating proteins and DNA.

Both force fields are able to be functioned in simulation of large biomolecules (Ptasińska *et al*., 2010), since *ab initio* calculations are only adequate for smaller systems owing to restrictions of the computational facilities (rather 'resources'). Herein, the convergence criteria involved maximum energy change, force, stress, and displacement were set at 2×10^{-5} kcal/mol, 0.001 kcal/mol/Å, 0.001 GPa, and 10^{-5} Å.

4.1.2 DFT calculations

4.1.2.1 Fluorine-doped tin oxide

(i) Structure and energetics

DFT calculations of FTO was carried out using DMol3 code (Delley, 1990, Delley, 2000) as apart of MS software (BIOVIA, 2016b). It was used for the assessment of electronic properties such as conductivity (frontier orbitals, density of state (DOS), band structure etc.) as well as vibrational properties by means of predicted Raman and infra-red (IR) spectra. The Generalized Gradient Approximations - Perdew-Burke-Ernzerhof (GGA-PBE) correlation energy functional (Perdew *et al*., 1996) and Double Numerical plus Polarization (DNP) ver. 3.5 basis set were employed to determine the spin-unrestricted DFT calculation of all periodic structures. The spin-unrestricted polarization method calculates different methods for different spins and has been used for calculating DFT of metal oxide clusters (Zhang *et al*., 2014, Yan *et al*., 2015). Instead, DNP is known as the basis set which is equivalent to 6-31G** basis set (Gaussian) in size and even remains to be much more accurate at the same size (Benedek *et al*., 2005). The employment of numerical basis sets also diminishes the basis set superposition error (Matsuzawa *et al*., 1997). The cores are treated with DFT-semi core pseudopotential (DSPP) (Delley, 2002) treatment due to the metallic nature of the studied

structure (Zhang *et al*., 2011). The use of DSPP replace the effects of core electrons with a single effective potential. These core potentials comprise some degree of relativistic effects and therefore, very beneficial approximations for heavier elements. The DSPP-based calculation is less computationally expensive since the core electrons are dropped (Kakkar *et al*., 2006). In order to improve the calculations performance, 4.5 Å of global orbital cut off was used. The tolerances of energy, gradient, and displacement were selected to be 1×10^{-4} Ha, 2×10^{-2} Ha $Å^{-1}$, and 5×10^{-2} Å, respectively.

Prior to calculation of larger FTO structure, geometry optimization of SnO_2 intrinsic structure was required to validate the used parameters in DFT. A 'gamma' type k-point of 1 x 1 x 1 was set for overall geometry optimization and structural properties calculations comprising of the integration points number which is employed to incorporate the wave function in reciprocal space. Initially, the calculated DFT properties for FTO structure is considered in comparison with the native SnO_2 (200) cluster. The purpose of this calculation is to observe the impact of F-dopant to the structural properties of SnO_2 (200) cluster.

(ii) Electronic properties

The SnO_2 (200) structure previously built was optimized. Further, the 8 x 1 x 1 of Monkhorst-pack k-point mesh was specified for calculating the DOS, particularly. For the geometry optimization, 0.05 Ha of smearing value was applied in order to reach the satisfied convergence criteria of the larger cluster system. Electronic properties play pivotal role in understanding the nature of materials and biomolecules. In this present study, the electronic properties of FTO corresponds to frontier orbital analysis, DOS, and band structure. Frontier molecular orbitals is an application of molecular orbitals theory describing highest occupied

molecular orbitals and lowest unoccupied molecular orbitals (LUMO) in a certain energy level i.e. ground state. According to the Fukui's nobel lecture, discovering HOMO and LUMO is particularly a good approximation to understand the reactivity of molecule (Fukui, 1982a, Fukui, 1982b). The difference within HOMO and LUMO is so-called by band gap (ΔE), in which it is an important parameter to determine the classification of materials. The simple depiction of band gap influence corresponding to the different materials are shown at **Figure 4.1** below. In general, pure metal clusters has no band gap (0 eV) due to the overlapping phenomenon of conduction band minimum (CBM) and valence band maximum (VBM), while semiconductors has a band gap ≤ 3.2 eV and when it is larger than 3.2 eV, the materials/molecules correspond to insulator. Herewith, VBM is also known as HOMO, while CBM comprising of the LUMO plot. Indeed, the ground state level of orbitals calculation was used throughout the optimization process along with carrying out of 0.15 Å grid in order to increase the quality of HOMO-LUMO isosurfaces.

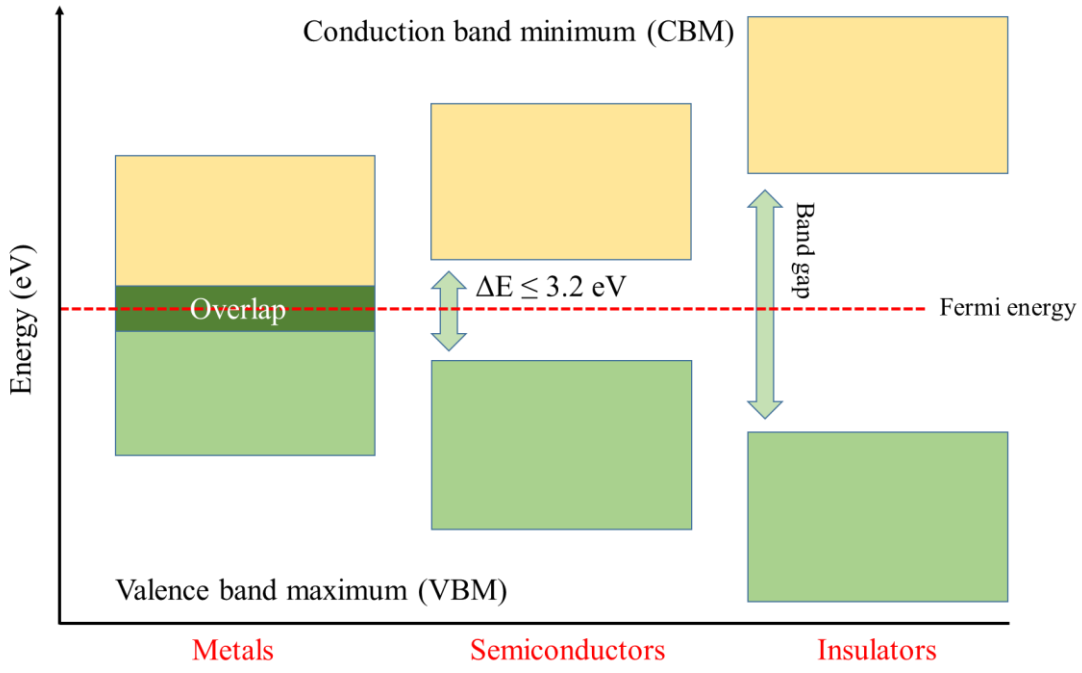

Figure 4.1 Classification based on electronic band gaps.

4.1.2.2 Titanium dioxide

(i) Structure and energetics

DFT calculations of TiO_2 was carried out using DMol3 code (Delley, 1990, Delley, 2000) along with GGA-PBE correlation energy functionals (Perdew *et al*., 1996) and DNP ver. 3.5 numerical basis. Similar to FTO cluster, the spin-unrestricted orbital calculation was applied to all the periodic structures. The cores are treated with DSPP (Delley, 2002) along with 4.5 Å global orbital cut-off. Similar to FTO, a DSPP (Delley, 2002) was used for core electron treatment due to the metallic nature of TiO_2 cluster (Zhang *et al*., 2011, Yang *et al*., 2013). The use of DSPP replace the effects of core electrons with a single effective potential. These core potentials comprise some degree of relativistic effects and therefore, very beneficial approximations for heavier elements. The DSPP-based calculation is less computationally expensive since the core electrons are dropped (Kakkar *et al*., 2006). The maximum acceptances of energy, gradient, and displacement were set as follows: 2×10^{-5} Ha, 4×10^{-3} Ha $Å^{-1}$, and 5×10^{-3} Å, respectively. Prior to calculation of large TiO_2 cluster, geometry optimization of TiO_2 intrinsic structure was required to validate the used parameter in DFT calculation. Herein, a 'gamma' type k-point set of 1 x 1 x 1 was used for geometry optimization and structural properties calculations.

(ii) Electronic properties

Electronic properties investigation was applied to TiO_2 (101) cluster which built in previous section. The 'gamma' type k-point (1 x 1 x 1) was chosen for overall geometry optimization and 8 x 1 x 1 of Monkhorst-pack k-point mesh was specified particularly for calculating the electronic properties. Herein, frontier orbitals, DOS, and band structure were considered to demonstrate the electronic nature of TiO_2 cluster. For the HOMO-LUMO investigation,

ground state orbitals level was used throughout the optimization along with 0.15 Å grid to increase the quality of orbital isosurfaces. For the DFT calculations of TiO_2 cluster, 0.05 Ha of smearing value was applied in order to reach the satisfied convergence criteria of the larger system.

(iii) Vibrational properties

The Raman and infra-red (IR) spectra were generated from DFT result by means of frequency calculation *via* computing a Hessian matrix during geometry optimization. According to the DMol3 system, the Hessian elements are calculated by dislocating every atom in the PBC model and calculating a gradient vector. This generates a comprehensive second derivative matrix (BIOVIA, 2016b). Upon the optimization, the Raman spectra can be generated from the lowest cluster's configuration, while IR spectra is generated from vibrational analysis tools along with 1.0 Å maximum amplitude and 'ultrafine' graphical quality. These results were further compared with spectroscopic data generated from the existing experimental studies or references.

4.1.2.3 Dopamine

(i) Structure and energetics

Dopamine is a small biomolecule which basically structured from benzenoid ring, hydroxyl, and amine groups. In this present study, dispersion corrected-DFT (DFT-D) was typically used to assess the molecular properties of dopamine. DFT-D was carried out using DMol3 code along with B3LYP hybrid functional (Becke, 1993, Stephens *et al*., 1994) and Grimme's empirical dispersion correction (Grimme, 2004, Grimme, 2006). The DFT-D method of Grimme is extensively appropriate for adjusting the performance of standard DFT (Grimme,

2004, Grimme, 2006, Shao *et al*., 2006) especially for defining the non-covalent forces such as hydrogen bonding and *van der Waals*. The original DNP ver. 3.5 basis set was used in order to increase the accuracy of theoretical results. Herein, the spin restricted polarization method was used describing the usage of similar orbitals for α and β spin. The cores are treated without any special treatment. On the other words, all electron core treatment was used in this calculation. In regards to improve the performance of calculations, a 'fine' quality of global orbital cut-off was employed. The maximum of energy, gradient, and displacement tolerances were selected to be 1×10^{-5} Ha, 2×10^{-3} Ha $Å^{-1}$, and 5×10^{-3} Å, respectively.

(ii) Electronic properties

For the electronic properties of dopamine, frontier orbital calculation was considered. The 0.15 Å grid was employed to increase the quality of orbital isosurfaces. The HOMO-LUMO calculation was carried out at the Fermi level (ground state orbitals). Herein, the 0.005 Ha of smearing value was employed in orbital occupation to accelerate the geometrical convergence.

(iii) Vibrational properties

Raman and vibrational (IR) spectra were generated from DFT frequency calculations. Upon the optimization, the Raman spectra can be obtained from the lowest cluster's configuration, while IR spectra is generated from vibrational analysis tools along with 1.0 Å maximum amplitude and 'ultrafine' graph quality. These results were subsequently compared with the spectroscopic data generated from the experimental studies or reference.

4.1.2.4 ss-DNA of Alzheimer's

(i) Structure and energetics

Single stranded-DNA is a macromolecule containing 2368 atoms and therefore, is not able to be optimized through common computational QM methods i.e. DMol3. Herein, DFTB+ code was considered to optimize the studied ss-DNA due to the capability of this method to calculate the DFT properties of macromolecule such as large nanocluster or biomolecules. The DFTB technique itself is relied on the expansion of second order of the Kohn-Sham total energy in density functional respecting the fluctuations of the charge density. Further, the zeroth order method is comparable towards a standard non-SCF calculation, while for the second order, a parameter-free, transparent, and computable parameters intended for universal matrix elements of Hamiltonian are able to be generated (BIOVIA, 2016b). Herein, non-SCC DFTB was used to reach the convergence during optimization. The 'mio' type of Slater-Koster library was employed along with 0.005 Å orbital occupancy. The energy tolerance was set to be 1×10^{-1} kcal/mol throughout optimization.

(ii) Electronic properties

For the electronic properties of ss-DNA macromolecule, frontier orbital calculations at ground state levels were considered. The 0.15 Å grid was applied to increase the quality of orbital isosurfaces.

4.1.3 Metropolis Monte Carlo adsorption studies

Metropolis Monte Carlo adsorption studies were applied to search the lowest energy configurations of adsorbate on the surface of selected substrates as the temperature is gradually decreased. The substrate and adsorbate systems were produced by mimicking the

experimental electrode. **Table 4.1** displays the substrate and adsorbate system used in this present study. In general, before performing the MC adsorption studies, the adsorbate molecules are optimized using Forcite-Geometry optimization in order to reach the stable conformation of adsorbate molecule. Herein, the adsorbate molecules are optimized using selected force field due to its capability to converge various adsorbate types i.e. TiO_2 as metal oxide (i.e. UFF), dopamine as small biomolecule (i.e. COMPASS), as well as ss-DNA as a large biomolecule (i.e. UFF-Dreiding). Upon the geometry optimization of adsorbate, the MC adsorption studies are performed using specified parameter set up.

Table 4.1 Substrate-adsorbate systems used in MC simulations.

System	Substrate	Adsorbate
Layer I	FTO	TiO_2
Layer II	TiO_2/FTO	dopamine
Layer III	DA/TiO_2/FTO	ss-DNA

The MC simulations procedure was used to observe the lowest energy level for the system. Initially, the adsorbate clusters are optimized till it reaches the selected convergence criteria. In this models, the configurations have certain ensemble by producing a configuration of chain i.e. *m, n…* in which the transformation step within *m* and *n* is a two-separate process (BIOVIA, 2016b).

4.1.3.1 Construction of substrate layers

The layers of studied nanostructure were constructed using 'build layer' selection of MS software. For the layer I, the constructed substrate containing FTO used in DFT calculation

was used. For the layer II, the TiO_2 (101) cluster was appended on the surface of FTO layer. This layer was denoted as TiO_2/FTO. Whilst, the dopamine was perpendicularly affixed on the TiO_2/FTO surface in order to build the layer III (i.e. DA/TiO_2/FTO). Dopamine acted as the third layer herein. For the layer III, larger adsorbate surfaces were employed according to the size of ss-DNA as the adsorbate. The lattice constant for layer III was recorded as a = 166.8 Å, b = 114.0 Å, and c = 178.9 Å. The selected vacuum slab thickness were applied to the overall surfaces which defined as follows: 20 Å for layer I and II, and 150 Å for layer III.

4.1.3.2 Adsorption studies of TiO_2 onto FTO layer

In this study, the automated temperature control was adopted and five temperature cycles were employed in the simulated annealing run. The substrate (layer I; FTO layer) and adsorbate (TiO_2) systems were reproduced representing the experimental electrode construction. By using the 'adsorption locator' module, single molecule of adsorbate was simultaneously adsorbed onto the FTO surface. Herein, various number of adsorbates i.e. 5, 10, and 50 molecules of TiO_2 were also considered to mimic the increasing adsorbate concentration. The calculation was carried out using the UFF (Rappe *et al*., 1992, Rappe *et al*., 1993) along with 'ultrafine' convergence tolerance. The charges were assigned by the current method. Prior to MC adsorption studies, the adsorbate molecules were initially optimized using Forcite-Geometry code with UFF in order to reach their most stable conformations. UFF is reliable force field for metals/ metal oxides system. For the energy parameters, the *Ewald & group-based* and *atom-based* summation methods were applied to compute the non-bonding electrostatic and *van der Waals* interactions throughout MC simulations.

4.1.3.3 Adsorption studies of dopamine onto FTO and TiO_2/FTO layers

Similarly, the automated temperature control was adopted and five temperature cycles were employed in the simulated annealing run. The substrate (layer II; TiO_2/FTO layer) and adsorbate (dopamine) systems were used to reproduce experimental electrode construction. By using the 'adsorption locator' module, single molecule of adsorbate was simultaneously adsorbed onto the TiO_2/FTO surface. Herein, five molecules of dopamine were also applied to mimic the increasing concentration of adsorbates. The employment of another single concentration is due to slab size limitation. The adsorption studies were carried out using the UFF (Rappe *et al*., 1992, Rappe *et al*., 1993) along with 'ultrafine' convergence tolerance. The charges were assigned by the current method. Prior to MC adsorption studies, the adsorbate molecules were initially optimized using Forcite-Geometry code with COMPASS (Sun, 1998, Sun *et al*., 1998) force field in order to reach their most stable conformations. COMPASS is well-known as a reliable force field for the small biomolecules such as dopamine. For the energy parameters, the *Ewald & group-based* and *atom-based* summation methods were applied to compute the non-bonding electrostatic and *van der Waals* interactions throughout MC simulations. As a comparison, the layer containing FTO (layer I) only was considered to discover its adsorption energy difference with the layer II system.

4.1.3.4 Adsorption studies of ss-DNA onto FTO, TiO_2/FTO, and DA/TiO_2/FTO layers

The automated temperature control was adopted and five temperature cycles were employed in the simulated annealing run. The substrate (layer III; DA/TiO_2/FTO layer) and adsorbate (ss-DNA) system reproduced the last step of experimental electrode modification. Single molecule of adsorbate was simultaneously adsorbed onto the DA/TiO_2/FTO surface using

'adsorption locator' module. The adsorption study was carried out using the UFF (Rappe *et al*., 1992, Rappe *et al*., 1993) along with the 'ultrafine' convergence tolerance. The charges were assigned by the current method. Prior to MC adsorption studies, the adsorbate molecules were initially optimized using Forcite-Geometry code with UFF and Dreiding (Mayo *et al*., 1990) force fields in conjunction with the current charge equilibration scheme in order to reach its most stable conformations. Both level of theories are applicable to very large biomolecules (Ptasińska *et al*., 2010) i.e. oligonucleotide. For the energy parameters, the *group-based* summation methods were applied to compute the non-bonding electrostatic and *van der Waals* interactions throughout MC simulations. As a comparison, the other layers composing FTO (layer I) and TiO_2/FTO (layer II) were considered to observe the adsorption energy difference with the layer III system containing DA/TiO_2/FTO.

4.1.4 Molecular dynamics simulations

MD simulations were carried out using a standard scheme as depicted at **Figure 4.2**. For the MD using Forcite, the last trajectories of MC adsorption studies are applicable as starting configuration containing stable substrate-adsorbate systems. It is due to the lowest energy conformation of the trajectories as common outcome of MC-based simulations. Afterwards, the system need to be optimized with respect to a certain force field in order to observe the lowest energy conformation of the adsorbate. The purpose of this optimization is also to remove the unphysical interaction within molecular system. Prior to optimization, the substrate bonds were removed due to the inapplicability of covalent bonding in metal oxides system. Afterwards, rigid-body constraint was applied to the substrate. Upon the minimization, the initial velocities of MD simulations were determined along with other important parameters involved type of ensemble, temperature, force field, convergence

criteria, time step, total time simulations, thermostat etc. When the dynamics started, the heating process will be carried out till reaching the equilibrium stage of the system (when plotting of energy and temperature *vs* time shows fluctuations within constant averages). In most of the cases, the equilibrium stage can be achieved by the employment of thermostat. Upon the equilibrium stage has been achieved, the production stage of MD simulations is run with a desired time simulations (from several ps to ns or even more) followed by data analysis based on the MD trajectories.

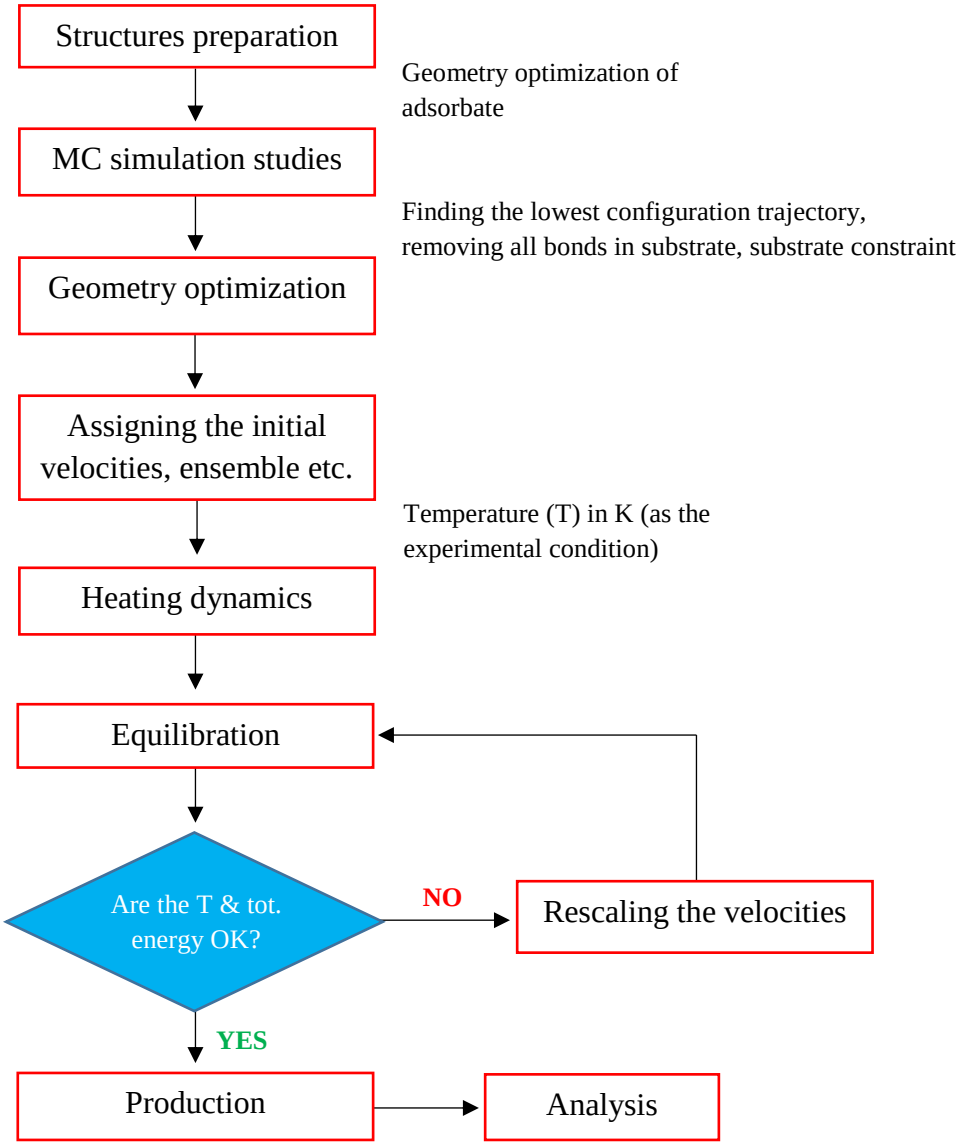

Figure 4.2 General scheme for set up and steps of MD simulations.

4.1.4.1 Molecular mechanics-based geometry optimization

MM-based geometry optimization was employed to optimize the structural geometry of the initial bulk prior to MD simulations. The bulks were taken from the output of MC adsorption studies containing substrate and adsorbate in their lowest energy configuration (rather 'most stable conformation'). The geometry optimization was carried out using Forcite code. The force fields and summation methods which were applied for this optimization are similar with the adsorbate pre-treatment of MC adsorption studies, particularly for TiO_2 and ss-DNA adsorbates. While for the dopamine as adsorbate and metal oxide systems as substrate, the UFF along with 'ultrafine' quality was used to reach the satisfied convergence criteria. Herein, the SCF iteration was set at 10000 for all optimizations. The purpose of this selection was to help in reaching the satisfied convergence levels for each adsorbate. Prior to geometry optimization, the bonds of metal oxide substrates (FTO and TiO_2) were removed due to the primarily ionic nature of the clusters. This means that the concept of a covalent bond is not applicable to metal oxide structures and therefore, the bond must be eliminated for the calculation to proceed (BIOVIA, 2016b). The minimization method was selected as 'smart', which refers to a bundle of the adjusted basis set Newton-Raphson (ABNR), steepest descent, and quasi-Newton methods. For the quasi-Newton method, Broyden-Fletcher-Goldfarb-Shanno (BFGS) and the Davidon, Fletcher, and Powell (DFP) algorithms were used respectively (BIOVIA, 2016b).

4.1.4.2 MD simulations of TiO_2 onto FTO layer

Upon geometry optimization of the TiO_2 adsorbate by MM (i.e. Forcite) method, MD simulations were performed on each of the aforementioned systems to arrive at the final energy-optimized systems. For the simulations with TiO_2 molecule and FTO layer, an NVT

canonical ensemble at room temperature (298 K; based on experiment) was used with 1.0 fs of time step and 100 ns of total dynamics time. The UFF was applied herein, to calculate the potential energy of metallic system throughout the simulations. An Anderson-thermostat was used with a collision ratio of 1.0 to control the temperature as well as to reach the equilibrium stage. The number of simulation steps were set at 10^8. The velocity initialization was set at random values temperature-dependent Gaussian distribution. The adsorbates number involved in this calculation are 1, 5, 10, and 50 molecules in order to mimic the increasing concentration of the TiO_2 molecules. The substrate cluster was being kept at constrained mode throughout the simulations.

4.1.4.3 MD simulations of dopamine onto FTO and TiO_2/FTO layers

Upon the geometry optimization of dopamine by MM (i.e. Forcite) method, MD simulations were performed on each of the systems to arrive at the final energy-optimized systems. For the simulations with dopamine as adsorbate, an NVT ensemble was set at room temperature (298 K; based on experiment) along with time step and total simulation time of 1.0 fs and 100 ns, respectively. The UFF was used throughout MD simulations. An Anderson-thermostat was used with a collision ratio of 1.0 and the number of simulation steps were set at 10^8. A random values temperature-dependent Gaussian distribution was used as initial velocities. The adsorbate number involved in this calculation are 1 and 5 molecules due to the limitation of the slab. This was also to mimic the increasing concentration of dopamine molecules overlaying the substrate surfaces. The substrate atoms were constrained during the simulations. As a comparison, the two types of substrate systems were considered corresponds to layer I (FTO) and layer II (TiO_2/FTO) with the similar adsorbate.

4.1.4.4 MD simulations of ss-DNA onto FTO, TiO_2/FTO, and DA/TiO_2/FTO layers

Upon geometry optimization of ss-DNA using Forcite-Geometry code, MD simulations were performed on each of the systems to arrive at the final energy-optimized systems of substrate and adsorbate. For the simulations with ss-DNA as adsorbate, an NVT ensemble at 277 K was used with 1.0 fs of time step and 10 ns of total dynamics time. The use of 277 K as heating system was based on the temperature of the electrodes construction in the experiment. The UFF was applied throughout the MD simulations along with an Anderson-thermostat with a collision ratio of 1.0 and the number of simulation steps were set at 10^8. Constantly, the random values were used as initial velocities. The single molecule of adsorbate was involved in the simulation to decrease the computational cost. The substrate atoms were constrained during simulations. As a comparison, the three types of substrate systems were applied corresponds to layer I (FTO), layer II (TiO_2/FTO), and layer III (DA/TiO_2/FTO).

4.1.4.5 Binding energy calculations

To calculate the binding energy (E_b) of layer-by-layer system i.e. within the substrate-adsorbate complex, the total energy (E_{tot}) is well-considered. E_{tot} is the sum of the energy of each separate system plus the interaction energy between the substrates (E_s) and adsorbates (E_a). Thus, E_b is calculated according to the **Equation 4.1** below.

$$E_b = E_{tot} - E_s - E_a \quad (4.1)$$

The E_s was calculated as follows: after the optimum configuration of the substrate-adsorbate complex was determined using MD, the adsorbate was removed from the system and carried out the single point energy calculation. The rigid-body constraint was removed prior to the calculation. Thereafter, single point energy calculations were also applied for the adsorbate

molecule only in which the substrate was removed and then, on the substrate-adsorbate complex.

4.2 Experimental

4.2.1 Materials and instrumentation

Nanocrystalline TiO_2 powders, absolute ethanol (97%), anhydrous terpineol, two types of ethyl celluloses (5-15 mPas at 5% in toluene: ethanol/80:20 at 25ºC; 30-50 mPas at 5% in toluene: ethanol/80:20 at 25ºC), dopamine hydrochloride (DA, N99%), ascorbic acid (AA, N99%), hexaammineruthenium chloride (N98%), potassium ferrocyanide (≥98.5%), and potassium ferricyanide (≥98.5%) were of analytical grade and purchased from Sigma-Aldrich. ss-DNA with 5′-terminal carboxyl group (HPLC grade, 5'- GGGCCT GGTCTACCAAGCAAACTCCAGTACAGCCAGGGAACATGAGAGGG - 3' were procured from Eurofins MWG Operon and stored in a 1.0 μM stock solution of phosphate buffer at pH 7.4. Alumina mortar was used as grinder in the preparation of TiO_2 microbead paste. In order to make the slurry, TiO_2 dispersion was stirred with a long stirrer magnet (4 cm). The Ti-horn-equipped sonicator was used to perform the ultrasonic homogenization. Hitachi S4700 field-emission scanning electron microscope (SEM, Hitachi, Japan) was used to observe the morphology of the particles. The features of TiO_2 microbeads crystal structure were generated from hard X-ray low-angle one reflectivity measurements (Philips PW1710 powder diffractometer, Philips, Netherlands). The electrochemical responses were measured in the system of a conventional three-electrode using the bare or fabricated FTO coated glass (TEC15, Hartford Glass), Ag/AgCl (3 M KCl), and a platinum wire as the working, reference, and counter electrodes, respectively. Whereas, Iviumstat (Ivium, Netherlands) was used to

record the electrochemical responds in a solution of phosphate buffer at physiological pH (7.4).

4.2.2 Preparation of the electrodes and photo-oxidative damage of the ss-DNA

4.2.2.1 Preparation of mesoporous TiO_2 microbeads paste

Mesoporous TiO_2 microbeads paste was prepared according to a previously reported procedure (Ito *et al*., 2007). For each following step, the mixture was adjusted *drop-by-drop* into alumina mortar. The condition was set at room temperature. The preparation steps of mesoporous TiO_2 microbeads were defined as follows: TiO_2 powder (6 g) and acetic acid (1 ml) were mixed and ground in a mortar for 5 min (i). The deionized water (1 ml) was subsequently added and ground in the mortar for 1 min. This particular step was replicated 5 times, so that the total amount of added deionized water was 5 ml (ii). Afterwards, 1 ml of ethanol was added and ground in a mortar for 1 min. This step was repeated 15 times and thus, the total amount of added ethanol was 15 ml. The 2.5 ml of ethanol was added again and ground in a mortar for 1 min. This step was repeated 6 times (iv). TiO_2 paste was transferred from mortar to a beaker using 100 ml ethanol (v). The solution was subsequently stirred with a magnet tip (1 min) and sonicated with ultrasonic horn. This step was repeated 30 times and stirred with a magnet tip for 1 min. The stirring was run at 300 rpm (vi). Then, 20 g of anhydrous terpineol was added to the beaker followed by stirring with a magnet tip for 1 min and sonication. This step was repeated 30 times then stirred with a magnet tip for 1 min. Ethyl cellulose (3 g: 30 g of 10% solution in ethanol) was added to the beaker (viii). The beaker was stirred with a magnet tip for 1 min and sonication. This step was repeated 30 times then stirred with a magnet tip for 1 min (ix). The ethanol was evaporated with a rotary

evaporator at 35°C with 120 mbar initially, until the pressure drops to 10 mbar (x). The solution was lastly ground with a three-roller mill in order to produce final paste of mesoporous TiO_2 microbeads (Ito *et al*., 2007). The morphology of mesoporous TiO_2 microbeads surface was determined using SEM, while the crystal structure properties was examined using Hard X-ray low-angle one reflectivity.

4.2.3 Fabrication of the electrodes and characterization studies

Initially, the mesoporous TiO_2 microbeads paste was coated using doctor blade method onto the FTO electrode. The active site was set of 5 × 5 mm (Mathew *et al*., 2013). The electrode was drought in the air and sintered at 500°C for half an hour. Diktak profilometer (VEECO/ SLOAN DEKTAK 3, New York, US) was used to determine the thickness of the fabricated mesoporous TiO_2 microbeads film. The resulting electrode was represented as TiO_2/FTO. Next, the TiO_2/FTO was carefully rinsed with deionized water then dipped in a fresh aqueous solution of dopamine (10 mM). To eliminate the excess of dopamine, the TiO_2/FTO was carefully rinsed few times with deionized water. At this stage, the electrodes were denoted as DA/TiO_2/FTO. The DA/TiO_2/FTO was dipped in a solution of ss-DNA (10 μM in PBS at pH 7.4) overnight at 4°C temperature. The purpose of this step was to adsorb the ss-DNA. The constructed electrode was subsequently rinsed with water and dried at room temperature. This step was denoted as ss-DNA/DA/TiO_2/FTO and the electrodes were ready to be used in the following DNA damage measurement. The electrochemical characterizations i.e. cyclic voltammetry (CV) and electrochemical impedance spectroscopy (EIS), were carried out for each modification step of the electrode in 1 mM $Fe(CN)_6^{3-/4-}$ and phosphate buffer (pH 7.4) at room temperature.

4.2.4 Electrochemical detection of DNA damage and ascorbic acid activity measurements

4.2.4.1 DNA oxidation damage measurement

For studying the photocatalytic reaction, the ss-DNA/DA/TiO_2/FTO was immersed in the deionized water. Afterward, this electrode was illuminated at 420 nm. The position of UV light was 5 cm above the electrodes. After illumination, the ss-DNA/DA/TiO_2/FTO was washed with deionized water and immersed in 10 mM $[Ru(NH_3)_6]^{3+}$ (in phosphate buffer at pH 7.4). The photocatalytic reaction was measured using square wave voltammetry (SWV) at room temperature for increments time of irradiation (i.e. 10, 20, 30, and 40 mins). The non-irradiated signal was also recorded herein as comparison.

4.2.4.2 Ascorbic acid activity measurements in protection of DNA damage

To study the ability of AA to protect the DNA damage, the ss-DNA/DA/TiO_2/FTO was immersed in 200 µM of AA. The electrode was illuminated at 420 nm to study the photocatalytic reaction. The position of UV light was 5 cm above the electrodes. After illumination, the ss-DNA/DA/TiO_2/FTO was washed with deionized water and immersed in 10 mM $[Ru(NH_3)_6]^{3+}$ (in phosphate buffer at pH 7.4). The photocatalytic reaction was measured at room temperature using SWV for different time of irradiation (i.e. 10, 20, 30, and 40 min). The electrochemical signal recorded with non-irradiated ss-DNA/DA/TiO_2/FTO was used as comparison. Instead, the optimum radiation time was determined herein in which the highest oxidation damage was measured. Then after, the abovementioned set up were also applied for other concentrations of AA (100, 300, 400, and 500 µM) using determined optimum irradiation time.

CHAPTER 5

RESULTS AND DISCUSSION

This chapter deals with the outcomes obtained from the computational and experimental methodologies, with the results discussed in subsequent sections. The computational protocols included the construction of nanostructures and Forcite-Geometry-based structural analysis, density functional theory (DFT) calculation, Metropolis Monte Carlo (MC) adsorption studies, and molecular dynamics (MD) simulations. The computational studies provided a better understanding of the interaction phenomena used to validate the experimental studies and to investigate the molecular properties of the system (structural, electronic, and vibrational) as well as the molecular behaviour under certain conditions. In the case of the experimental work, several folds of activities were completed comprising of electrode fabrication, characterization studies (i.e. X-ray diffraction (XRD), scanning electron microscope (SEM) images, and cyclic voltammetry (CV)), measurement of DNA damage, and observing the impact of antioxidant treatment on the DNA damage protection. The objective of this study was to design a new diagnostic tool for the early detection and to study the molecular properties of the DNA damage strategy in the Alzheimer's.

5.1 Computational

5.1.1 Construction of nanostructures and Forcite-Geometry-based structural analysis

5.1.1.1 Fluorine-doped tin oxide

Fluorine-doped tin oxide (FTO) corresponds to the first layer of the constructed electrode. In order to observe the feasibility of the crystal structure, prior to larger cluster's construction, the primitive (rather 'origin') cell of FTO i.e. SnO_2, was successfully generated and optimized. The results obtained from the molecular mechanics (MM)-based geometry optimization using COMPASS (Sun, 1998, Sun *et al*., 1998) commercial force field are shown in **Table 5.1** comprising of structural parameters. The overall result of lattice constants (*a*, *b*, and *c*) shows a better correlation with experimental values compared with previous theoretical values (Shi *et al*., 2013, Sun *et al*., 2016). However, the optimized lattice of SnO_2 primitive structure demonstrates no significant differences with its native form in the specific parameters including bond lengths and bridging angles.

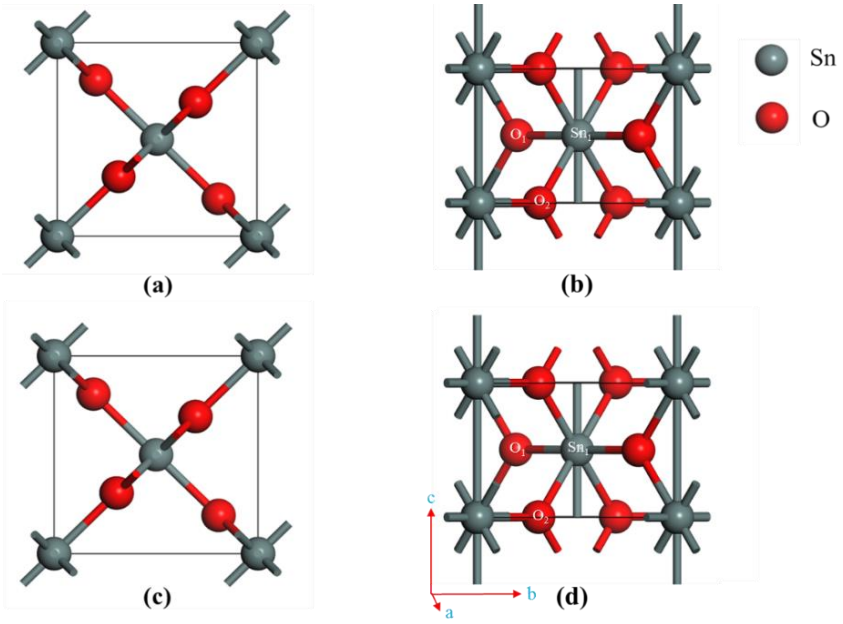

Figure 5.1 The primitive cell of un-optimized SnO_2 comprising of front (a) and top (b) view depictions and optimized SnO_2 comprising of front (c) and top (d) view depictions. The lattice constant direction is shown at the bottom of part (d).

The bond length of Sn_1-O_1 was 0.003 Å stretched upon the optimization (**Figure 5.1(d)**), while very slight shortening occurred in Sn_1-O_2 (0.001 Å). In terms of the bridging angle, Θ (°) or $\angle O_1Sn_1O_2$ was reduced to 0.050° upon geometry optimization (**Figure 5.1(d)**), indicating bond relaxation. The use of COMPASS parameterization force field provides satisfactory results on the geometry optimization, particularly for the small metal cluster or biomolecules. Overall, the results suggest that the primitive structure of SnO_2 is reliable to be used in larger cluster construction.

Table 5.1 Structural parameters of primitive SnO_2 structure optimized using Forcite with COMPASS force field and its comparison with the experiment and other works.

Lattice parameters	**This work (non-optimized structure)**	**This work (optimized structure-COMPASS)**	**Sun's work[a]**	**Shi's work[b]**	**Experiment[c]**
a (Å)	4.737	4.737	4.687	4.680	4.738
b (Å)	4.737	4.737	4.687	4.680	4.738
c (Å)	3.186	3.186	3.157	3.154	3.187
c/a	0.673	0.673	0.674	0.674	0.673
Sn_1-O_1 (Å)	2.057	2.054	*ns*	*ns*	*ns*
Sn_1-O_2 (Å)	2.052	2.053	*ns*	*ns*	*ns*
Θ (°)	129.062	129.112	*ns*	*ns*	*ns*

[a] Sun *et al*. (2016) using Cambridge Serial Total Energy Package (CASTEP) code within Local-Density Approximation (LDA) by means of Broyden-Fletcher-Goldfarb-Shanno (BFGS) minimization.
[b] Shi *et al*. (2013) using CASTEP within LDA by means of the Ceperley-Alder exchange correlation potential parameterized by Perdew and Zunger.
[c] Liu *et al*. (2010).
Abbreviations: *ns*; non-specified.

Upon the consideration of the primitive structure, the exacted nanocluster of SnO_2 was subsequently constructed. **Figures 5.2(a & b)** show a periodic cluster of SnO_2 (200) containing 96 Sn and 192 O atoms. This cluster has eight layers of atoms in which the interacting sites are predominantly accumulated on the surface (Canevali *et al*., 1997, Degler *et al*., 2016). Following the construction of SnO_2 periodic cluster, the FTO cluster was

obtained by introducing F dopants inside the SnO_2 structure. The top and side view depictions of the FTO cluster are shown in **Figures 5.2(c & d)**. The cluster contains 96 Sn, 182 O, and 10 F atoms. The 20 Å vacuum slab thickness was built along with C-plane orientation in order to facilitate the periodic boundary box of the system. This slab size was selected to constraint the adsorbate-surface interaction and to minimize the computational cost (Mdluli *et al*., 2011). The slab is an important parameter in surface chemistry, particularly on surface-interface interactions of the nanomaterials cluster and specific adsorbate. The periodic slabs are thick enough to ensure that there are no interactions between the opposite surfaces with the selected adsorbate molecules. Under proper vacuum conditions, the distance avoids more interaction within the adjacent slabs (Sun and Ceder, 2013).

Fluorine (F) is well-known as one of the favourable dopants for SnO_2, instead of popular cationic dopants such as antimony, gallium, and recently lithium (Joseph *et al*., 2009). The un-doped SnO_2 exhibits extremely high electrical resistivity due to their low intrinsic carrier mobility and density. The conductivity of this structure is relatively weak due to the doubly ionized vacancies functioning as donors (Benhaoua *et al*., 2014). The presence of F atoms in FTO enables to increase the conductivity of the un-doped SnO_2 structure and lowering the electrical resistivity. Fluorine may replace O anion atoms (O^{2-}) due to the similar electronegativity nature as well as ionic radii's (1.17 Å for F^- and 1.22 Å for O^{2-}). This atom acts as a donor in the cluster of SnO_x : F (Moholkar *et al*., 2009).

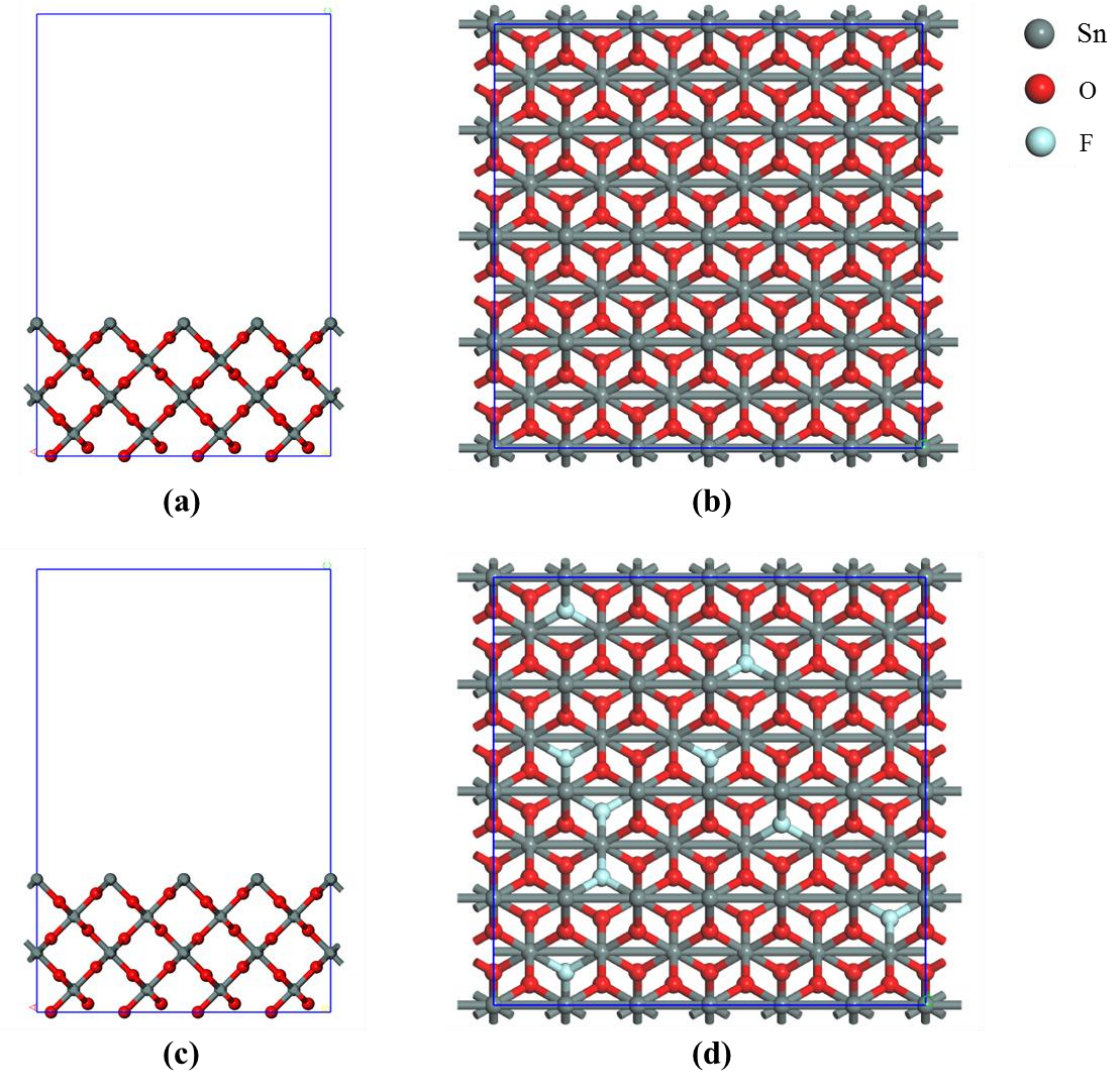

Figure 5.2 Nanocluster of SnO_2 comprising of front (a) and top (b) views and FTO comprising of front (c) and top (d) view depictions.

5.1.1.2 Titanium dioxide

Similarly, the intrinsic structure of TiO_2 crystals were initially optimized to investigate its viability to be cleaved in the subsequent cluster. The purpose of this optimization was also to observe the proper parameters of the MM-based calculations. Upon the MM-based geometry optimization, the calculated results show a good agreement with the standard experiment as well as previous theoretical considerations (**Table 5.2**). The structural

parameters i.e. bond lengths and bond angles are depicted in **Figure 5.3**. The lattice parameters of the optimized structure show slight differences with the experimental values, with deviations at 0.006 Å (*a* and *b*) and 0.016 Å (*c*) under the experimental condition (*a* = 3.782, *b* = 3.782, and *c* = 9.502). Considering other theoretical studies (Fahmi *et al*., 1993, Asahi *et al*., 2000, Lee *et al*., 2005), the calculated lattice seems to be comparable and does not show any significant differences. Instead, the bridging angle of the optimized structure was slightly overestimated upon the experimental value. The Θ of this intrinsic structure remains to be 158.208°, while for the experimental angle was observed as 156.300° (1.908° difference). It is reasonable due to bond relaxation effect within Ti and O atoms during the geometry optimization. Another consideration was given to the comparison of Θ prior to and upon the geometry optimization. The Θ was decreased upon the optimization of geometry due to the common impact of optimization itself. Interestingly, the Θ values between non-optimized and experimental structures show a better agreement than after optimization. However, these show very slight differences in lattice constants and Θ were still considered as accurate and reliable results of a TiO_2 anatase intrinsic structure. The capability of the COMPASS (Sun, 1998, Sun *et al*., 1998) force field used in the optimization may yield an accurate parameterization of the structural properties of metal oxide system.

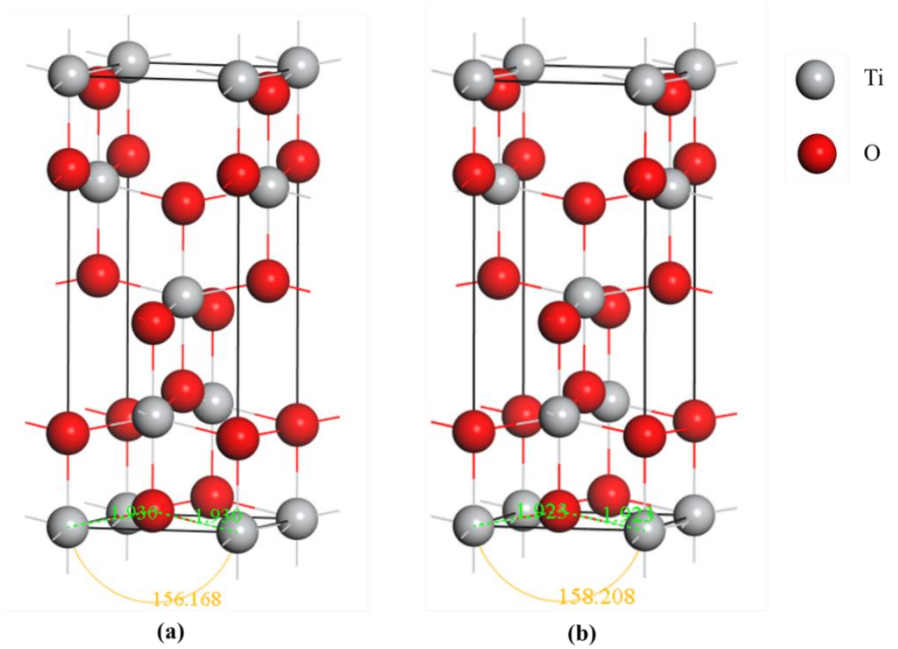

Figure 5.3 Primitive cell of TiO_2 (anatase) shown through CPK model of non-optimized (a) and optimized (b) structures by Forcite-Geometry calculations.

Table 5.2 Structural parameters of primitive TiO_2 cell optimized using Forcite with COMPASS force field and its comparison with the experiment and other previous works.

Lattice parameters	**This work (non-optimized structure)**	**This work (optimized structure)**	**Lee's work[a]**	**Fahmi's work[b]**	**Asahi's work[c]**	**Experiment[d]**
a (Å)	3.776	3.776	3.845	3.763	3.692	3.782
b (Å)	3.776	3.776	3.845	3.763	3.692	3.782
c (Å)	9.486	9.486	9.537	9.851	9.471	9.502
c/a	2.512	2.512	2.481	2.618	2.566	2.512
d_{eq} (Å); Ti-O	1.930	1.923	1.960	1.939	1.893	1.932
d_{ap} (Å); Ti-O	1.973	2.008	2.002	1.995	1.948	1.979
Θ (°)	156.168	158.208	157.600	152.100	154.400	156.300

[a] Lee *et al*. (2005) using norm-conserving pseudopotentials within LDA.
[b] Fahmi *et al*. (1993) using pseudopotential Hartree-Fock.
[c] Asahi *et al*. (2000) using full-potential linearized augmented plane-wave (FLAPW) method.
[d] Burdett *et al*. (1987).

After the construction of TiO_2 primitive cells, the larger cluster of TiO_2 was constructed (**Figure 5.4**). The periodic box of TiO_2 anatase cluster consists of 36 Ti and 72 O atoms comprising of eight perpendicular layers. Similar to FTO, the active sites were accumulated on the surface following the nature of surface chemistry (Canevali *et al*., 1997, Degler *et al*., 2016). The 20 Å vacuum slab was built along with C-plane vacuum orientation, while the crystal thickness was set at 30.378 Å. This slab size was constructed to constrain the interactions within adsorbate and substrate surface as well as to minimize the computational cost (Mdluli *et al*., 2011). The crystal type of TiO_2 anatase was obtained as tetragonal. Indeed, the anatase phase of TiO_2 was selected in the simulation based on the materials used in experimental electrode modification. In addition, anatase structure is generally favorable from the solution-phase methods (Zhang *et al*., 1998, Zaban *et al*., 2000, Oskam *et al*., 2003) as compared to other phases (i.e. brookite and rutile). The results indicated that the calculation methods and the simulated TiO_2 cell are reasonable and reliable for further studies.

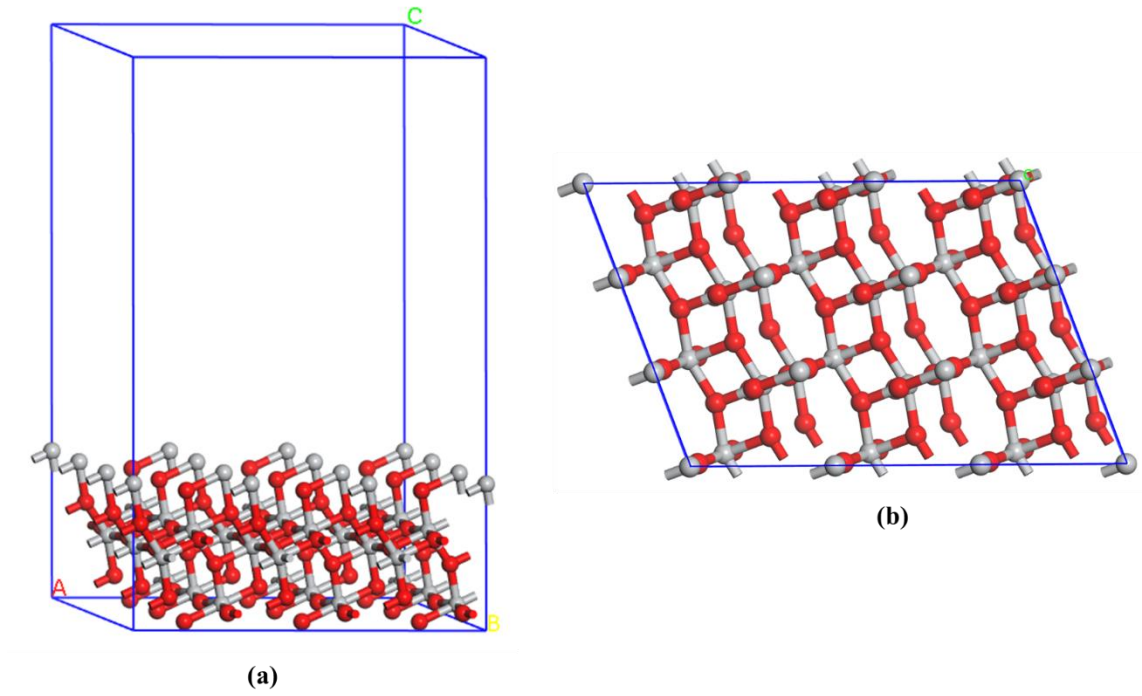

Figure 5.4 Nanocluster of TiO_2 anatase (101) comprising of front (a) and top (b) view depictions.

5.1.1.3 Dopamine

Dopamine (DA) is a unique small biomolecule owing to its two hydroxyl groups (-OH) on one side and an amine group in another side of the molecular structure which are connected with a benzenoid ring and C-H skeleton. This property has been widely used as an anchor molecule (or linker) between TiO_2 nanoparticles attached to -OH side and macromolecule of DNA attached to amine side, for the purpose of DNA recognition and detection (Vega-Arroyo *et al*., 2007, Liu *et al*., 2007), and also DNA sensor fabrication (Imani *et al*., 2014). The basic structure of dopamine (non-optimized) and the optimized geometry through Forcite codes are depicted in **Figures 5.5** and **5.6(a & b)**, respectively. In addition, the atomistic structure derived from PubChem library (as reference) is given as a comparison (**Figure 5.6(c & d)** and **Table 5.3**).

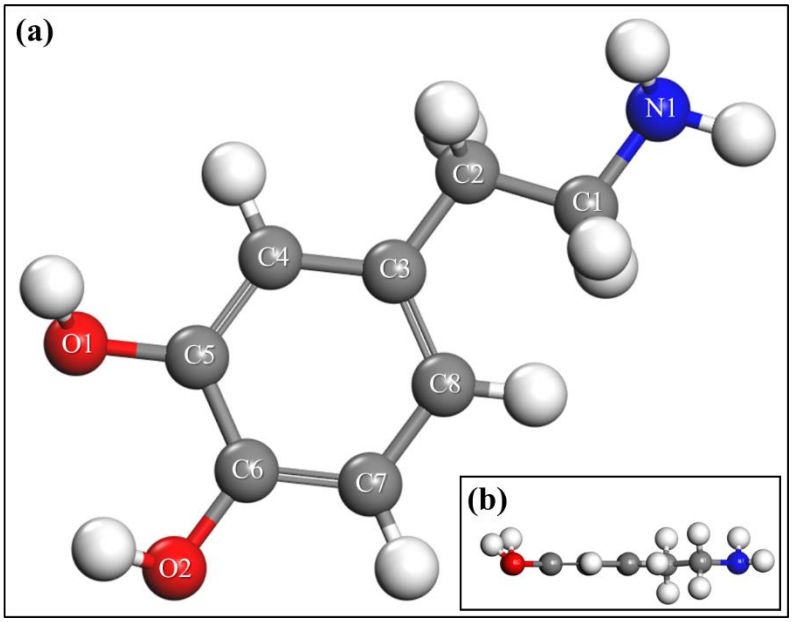

Figure 5.5 Ball and stick model of native dopamine molecule comprising of front (a) and top (b) view depictions.

Forcite code has been preferable to observe the low energy configuration (or most stable conformation) of dopamine molecule, along with 'ultrafine' quality of COMPASS (Sun, 1998, Sun *et al*., 1998) force field. Herein, the structural parameter was considered upon the geometry optimization. The calculated result, as can be seen in **Table 5.3**, shows significant differences of the structural parameters within the native (non-optimized), optimized and reference (National Center for Biotechnology Information, 2004) dopamine structures.

Dopamine structural analysis was carried out through the determination of important inter- and intramolecular geometric parameters such as bond length (d_x), bridging angles, and dihedral/torsional angles. An assessment of the optimization method with respect to reproducing the accurate result compared to the reference dopamine molecule was firstly discussed. In this study, upon the MM-based geometry optimization, the calculated result

suggests that there is no significant difference with the reference parameters. The calculated bond lengths of dC_1-N_1, dC_2-C_3, dC_5-O_1, and dC_6-O_2 which were found to be 0.001 Å, 0.020 Å, 0.008 Å and 0.006Å, were slightly greater than that of corresponding bond lengths in reference. Meanwhile, the bond lengths of dC_1-C_2 were (0.010 Å) smaller than the reference dopamine molecule. These minor differences were reasonable and corresponds to common over/underestimation of COMPASS force field (Sun, 1998, Sun *et al*., 1998, Kunzel *et al*., 2009) employed in the optimization.

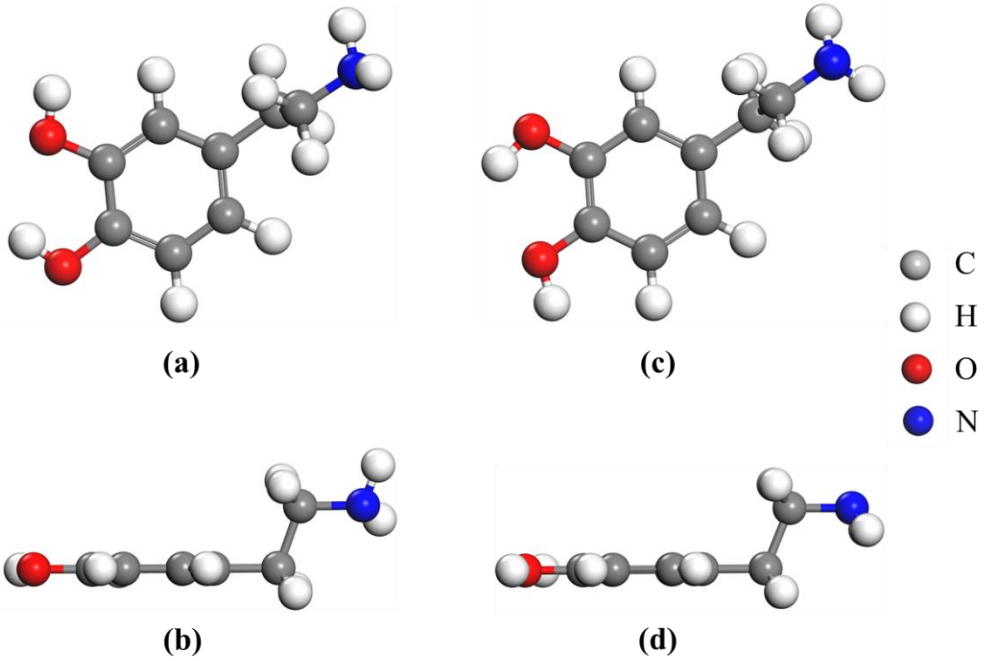

Figure 5.6 Ball and stick model of optimized dopamine molecule comprising of front (a) and top (b) view depictions, and the referential dopamine derived from PubChem library (National Center for Biotechnology Information, 2004) comprising of front (c) and top (d) view depictions.

Slight differences in values of the bridging angles of optimized dopamine ($\angle N_1$-C_1-C_2 and $\angle C_1$-C_2-C_3) with the reference were observed. Interestingly, the obvious difference was observed with the dihedral angles ($\angle C_1$-C_2-C_3-C_4, $\angle C_1$-C_2-C_3-C_8, and $\angle N_1$-C_1-C_2-C_3) prior to and upon the optimization. The geometry optimization seems to relax the bond-bond

interaction in order to search the most stable conformation of dopamine. As compared to the reference molecule, the optimized structure showed no significant differences, instead of ∠N_1-C_1-C_2-C_3 (optimized = 177.998°, reference = -178.888°) in which the positive and negative values are due to different orientation of the torsional angles. In addition, the total energy of optimized structure significantly reduces suggesting the most stable configuration of dopamine molecule. Generally, these results are in good agreement with reference molecule, indicating the usability of optimized dopamine molecule for further interaction studies.

Table 5.3 Selected bond lengths (Å), bond angles (°), and dihedral angles (°) of the dopamine (**Figure 5.5**) calculated by Forcite-COMPASS level of theory.

Parameters	**Geometry structure**	**Un-optimized structure**	**Optimized structure (COMPASS)**	**Reference[a]**
Bond lengths (Å)	C_1-N_1	1.51	1.460	1.459
	C_1-C_2	1.539	1.525	1.535
	C_2-C_3	1.539	1.511	1.491
	C_5-O_1	1.51	1.370	1.362
	C_6-O_2	1.51	1.368	1.362
Bridging angles (°)	N_1-C_1-C_2	109.251	110.343	111.57
	C_1-C_2-C_3	109.38	109.899	112.106
Dihedral angles (°)	N_1-C_1-C_2-C_3	179.29	177.998	-178.888
	C_1-C_2-C_3-C_4	176.247	93.379	90.002
	C_1-C_2-C_3-C_8	-3.2	-86.43	-89.953
Total energy (kcal/mol)	*ns*	109.05	-26.286	*ns*

[a] National Center for Biotechnology Information (2004).
Abbreviations: *ns*; non-specified.

5.1.1.4 ss-DNA of Alzheimer's

Upon the construction of s-DNA using Discovery Studio (DS) software, the initial structure was successfully obtained as depicted in **Figure 5.7(a)**. This structure remains linear since there is no folding mechanism on the structure. This unfolded structure corresponds to the

un-natural phenomenon as the ss-DNA is a part of human macromolecule. Therefore, the observation on the secondary structure of ss-DNA is important in simulation. The prediction of folding structure was carried out by minimization of energy using nearest neighbor energy parameters (Zuker, 2003). In general, there are several ways to predict the secondary structure. The first technique is in the examination of overall possibilities of the secondary structure, typically with the assistance of graphical procedure. The second corresponds to invoking the thermodynamics laws and trying to calculate minimum free-energy conformations. The third technique employs phylogeny to determine the secondary structure (Zuker and Sankoff, 1984). Herein, the folding mechanism was carried out using the Mfold web server in which the core algorithm calculates minimum free energies for the folding's including any essential base pairs (Zuker, 2003). Folding of ss-DNA was undertaken through the conversion (by algorithm) of ss-DNA sequence into RNA and then reconvert it in final. This secondary structure is important due to its minimum energy (rather 'stable') conformation dealing with the natural circumstance (in physiological pH condition) of the biomolecules. This folded structure is depicted in **Figure 5.7(b)**.

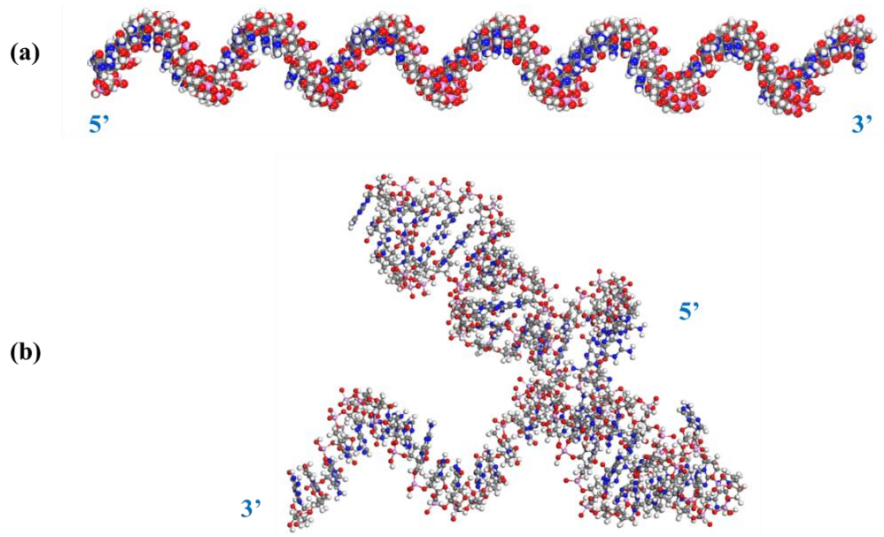

Figure 5.7 Non-optimized structures of unfolded (a) and folded (b) ss-DNA with 5'end carboxyl.

The calculated results show a stable structure as depicted in **Figure 5.8**, while the distribution of the energy within native and optimized structures are shown in **Table 5.4**. According to the total energy and its energy contributors, the stability of ss-DNA upon geometry optimization significantly increases (lowering the energy values) as compared to the native structure. This suggests that the structure was successfully optimized due to the exhibited lowest energy configuration and thereby, confirming the most stable conformation of the studied oligonucleotides. In addition, the functionalization of -COOH group at the 5'end-phosphate of oligonucleotide terminus which corresponds as the preferable position from the synthetic point of view, is highlighted by yellow atoms at **Figure 5.8**. This functionalization type was chosen in order to mimic the experimental study (Imani *et al*., 2014). The -COOH group could interact with the amine group of dopamine *via* covalent bonding (Rajh *et al*., 2004).

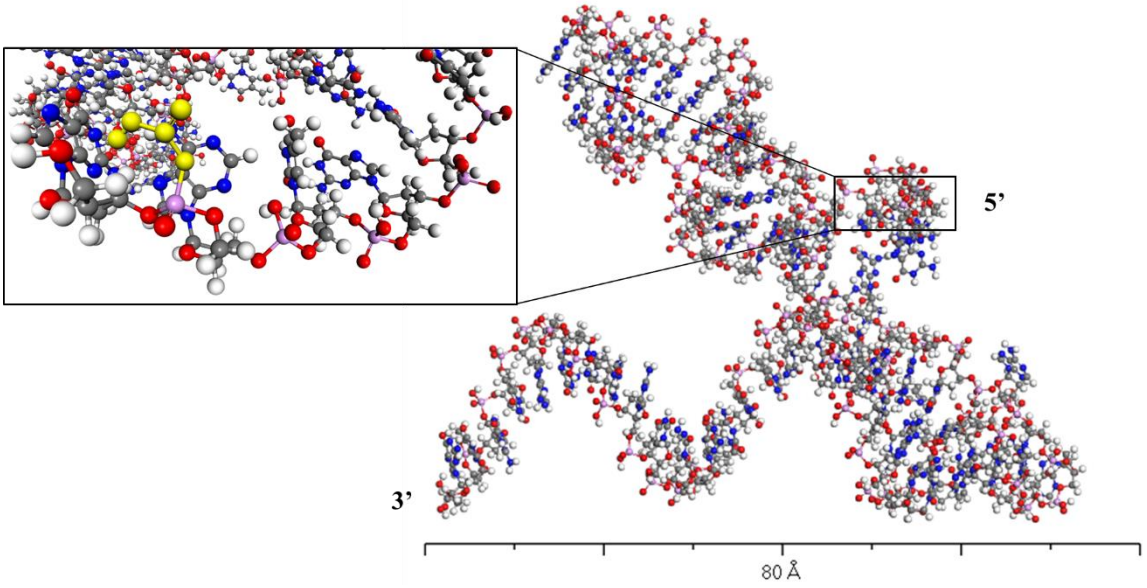

Figure 5.8 The lowest energy configuration of ss-DNA encoding amyloid peptide in Alzheimer's. The yellow atoms correspond to -COOH group attached to 5'end phosphate terminus.

Table 5.4 Contributions to total energy of native ss-DNA (non-optimized) and its optimized geometry.

Energy (kcal/mol)	Native	Optimized using COMPASS
Valence energy		
Bond	24990.789	264.246
Angle	3727.913	3198.593
Torsion	1051.593	638.074
Inversion	145.028	5.989
Non-bond energy		
Hydrogen bond	-31.350	-69.130
van der Waals	15101.515	915.377
Electrostatic	0.000	0.000
Total energy	44985.488	4953.149

5.1.2 DFT calculations

5.1.2.1 Fluorine-doped tin oxide

(i) Structure and energetics

The internal coordinates and lattice parameters were fully relaxed during the DFT calculations. The structural parameters of the optimized primitive/intrinsic SnO_2 structure are listed in **Table 5.5**. This calculation was carried out to assess the reliability of the employed DFT method using numerical parameters and standard Generalized Gradient Approximations - Perdew-Burke-Ernzerhof (GGA-PBE) functionals. Upon geometry optimization, the calculated lattice constants were in excellent agreement with the experimental values and remains better than previous calculations (Shi *et al*., 2013, Sun *et al*., 2016). In terms of the structural parameters, the bond lengths and dihedral angles (Θ) were slightly altered after optimization, due to the impact of relaxation during optimization. The electronic band gap of intrinsic SnO_2 of 5.340 eV, is 1.780 eV above the experimental band gap (3.560 eV) (Svane and Antoncik, 1987). It is not surprising due to the common under/overestimation of standard

local or semi-local exchange-correlation functionals, also consistent with the previous first principle studies (Onida *et al*., 2002, Miglio *et al*., 2014, Cheng *et al*., 2014a). However, the calculated band gap is equivalent with the high optical transparency properties of SnO_2-based transparent conducting electrodes (TCOs) having band gaps larger than 3.100 eV (Cheng *et al*., 2014a).

In terms of total energy, upon the geometry optimization, the minimum energy was achieved indicating the accomplishment of the most stable configuration of intrinsic SnO_2 structure. The results within prior to and upon the optimization show minor differences (**Table 5.5**) suggesting that the stability of the optimized structure is almost similar to the native comprising of the GGA-PBE level of theory. Herein, the total energy of native structure was determined using single point energy calculations. Overall, these results indicate the ability of the system and methods to be applied for the investigation with more complex structures.

Table 5.5 Structural parameters of intrinsic SnO_2 structure optimized using DMol3 with GGA-PBE functionals and its comparison with the experiment and other works.

Lattice parameters	**This work (un-optimized structure)**	**This work (optimized structure-GGA-PBE)**	**Sun's work[a]**	**Shi's work[b]**	**Experiment[c]**
a (Å)	4.737	4.737	4.687	4.680	4.738
b (Å)	4.737	4.737	4.687	4.680	4.738
c (Å)	3.186	3.186	3.157	3.154	3.187
c/a	0.673	0.673	0.674	0.674	0.673
Sn_1-O_1 (Å)	2.057	2.008	*ns*	*ns*	*ns*
Sn_1-O_2 (Å)	2.052	2.083	*ns*	*ns*	*ns*
Θ (°)	129.062	130.111	*ns*	*ns*	*ns*
Total energy (Ha)	-546.050	-546.055	*ns*	*ns*	*ns*
HOMO-LUMO energy gap (eV)	*ns*	5.340	*ns*	*ns*	3.560

[a] Sun *et al*. (2016) using CASTEP code within LDA by means of BFGS minimization.
[b] Shi *et al*. (2013) using CASTEP within LDA by means of the Ceperley-Alder exchange correlation potential parameterized by Perdew and Zunger.
[c] Liu *et al*. (2010) and Fröhlich *et al*. (1978).
Abbreviations: *ns*; non-specified.

For the calculation with larger clusters, the native SnO_2 (200) structure was considered in comparison with FTO (**Figure 5.2**). The purpose of this calculation was to establish the impact of F-dopant to the properties of SnO_2 (200). After the geometry optimization, the depiction of the relaxed structure for both clusters are shown in **Figure 5.9**. As can be seen, there is an obvious difference within the native SnO_2 and FTO, particularly in their structural properties. The bond lengths of the optimized FTO seems to be more relaxed (**Figures 5.9(c & d)**) as compared to the native form (**Figures 5.9(a & b)**). The atom positions (rather 'lattice') are regularly relaxed for the native structure, while the unregularly distorted lattices are observed for the corresponding FTO cluster. Herewith, F atoms significantly influences the final geometry of FTO. The bond distortion predominantly occurs in the atoms surrounding F-dopant (**Figure 5.9(d)**) i.e. Sn-F. It may be due to the defect-produced during

perturbations, therefore the neighbouring F-atoms have a tendency to displace themselves in order to discover new positions of equilibrium (Marcillo and Stashans, 2014). Furthermore, the impact of the F-dopant to the conductivity and electronic nature of SnO_2 cluster is discussed in subsequent section.

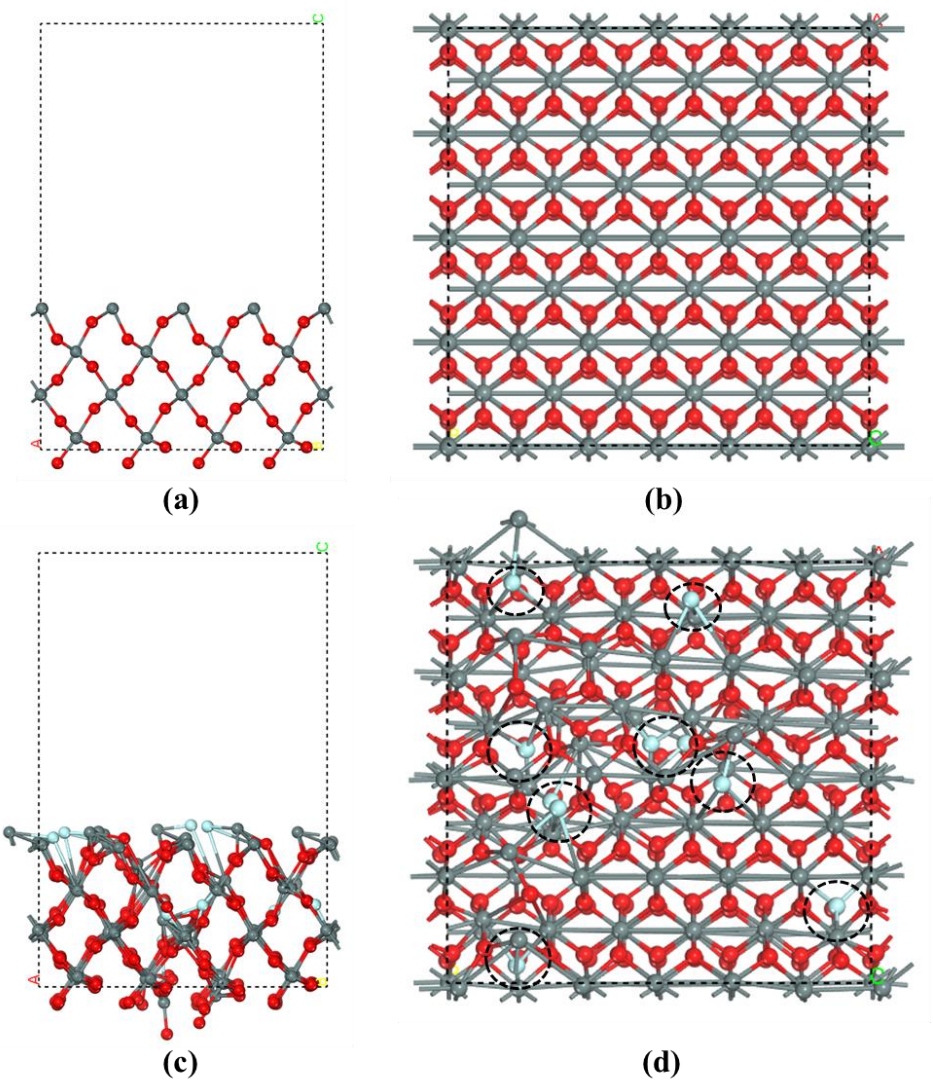

Figure 5.9 Optimized geometry structure at GGA-PBE level of theory of SnO_2 (200) comprising of front (a) and top (b) view depictions, and FTO comprising of front (c) and top (d) view depictions. The F-dopant shown by black-dashed circle line in the part (d).

(ii) Electronic properties

It is widely-known that the reliable calculation of electronic band gaps requires density functionals beyond standard GGA. Hybrid density functional (Heyd-Scuseria-Ernzerhof; HSE06) has been used to accurately predict the effective band gaps of metallic systems (i.e. semiconductors) compared to standard GGA functionals (Burbano *et al*., 2011, Ramzan *et al*., 2013). However, the computational cost of HSE06 hybrid functional is extensively higher than the standard GGA functionals. The use of the standard GGA functionals is reliable since it has been used to accurately and efficiently (rather 'less computational cost') calculate the electronic and structural parameters of the monodoping and codoping of SnO_2 (Cheng *et al*., 2014a). In this study, the GGA-PBE functionals was used to observe the structural and electronic properties of SnO_2 and F-doped SnO_2 (FTO) clusters.

Figure 5.10 shows the band gap of SnO_2 and FTO clusters calculated using the GGA-PBE functionals, while the high symmetry directions of the Brillouin zone used in calculations are shown in **Figure 5.12(a)**. It is found that the HOMO-LUMO energy gaps of the native SnO_2 is 0.501 eV, while upon the doping of F atoms with the replacement of O anions, the energy gap significantly decreases to 0.172 eV. This result indicates that the increment of electrical conductivity nature of SnO_2 while it is doped with anion dopants (i.e. F). The energy difference within valence band maximum (VBM) or HOMO and conduction band minimum (CBM) or LUMO narrows in FTO cluster suggesting the increment of electron possibility to excite from the ground state valence bands into the vacant conduction energy bands (Smith and Nie, 2010). However, the obtained band gap of SnO_2 cluster from GGA-PBE functionals is strongly underestimated, compared with the experimental value (3.560 eV) (Fröhlich *et*

al., 1978). It is due to the common underestimation of the standard GGA functionals. The obtained value is consistent with the previous calculation using similar functionals (in a smaller size of SnO_2) in which very small band gaps were observed (i.e. 0.680 eV). The band gap of FTO cluster previously predicted (i.e. 3.500 eV) and remained a significantly different in the present calculation. The difference in size and concentration of dopant may contribute to this variation (Xu *et al*., 2009). Moreover, the much larger size (288 total atoms of present calculations) of the cluster and relatively high dopant concentration (5.3%) were intended to mimic the optimal experimental conditions for FTO (Banyamin *et al*., 2014).

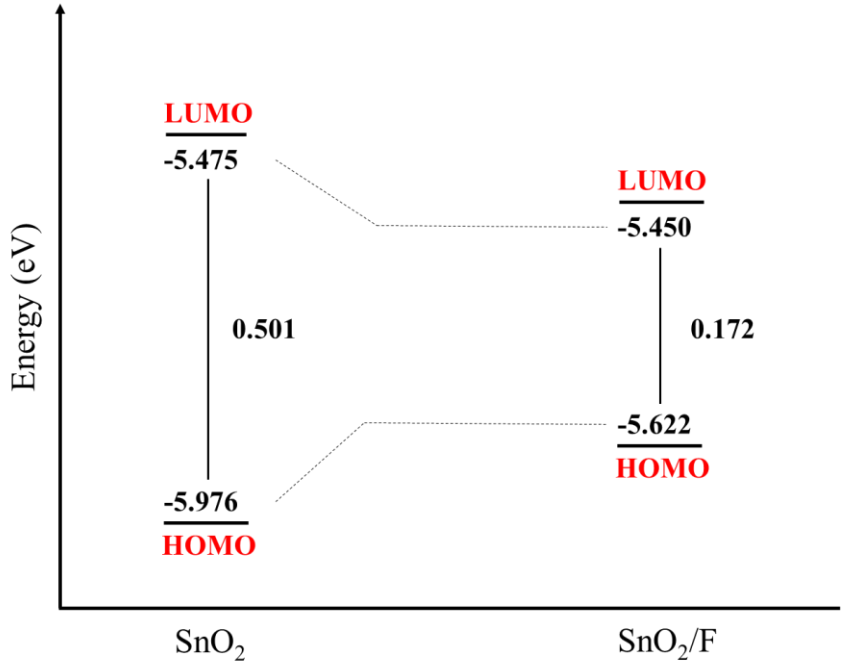

Figure 5.10 HOMO-LUMO energy band gaps of SnO_2 and SnO_2/F (or FTO).

Instead of HOMO-LUMO energy gaps, the conductivity of FTO can be further explained by Fermi energy (E_f) value. Fermi energy corresponds to a limiting value of a particular energy (Hugenholtz and van Hove, 1958). Together with density of state (DOS), E_f has been widely used to determine the conductivity (Campos and Braz, 1997, Chen *et al*., 2015a) as well as

reactivity (Wang *et al*., 2012) of the nanomaterials. Herein, the E_f of native SnO_2 cluster is found to be -5.486 eV, while upon the doping process, the E_f is lowered to -5.502 eV. It suggests the change in conductivity nature in which the FTO remains to be more conductive than SnO_2 due to the smaller E_f. This trend is in consistent with the obtained HOMO-LUMO energy gap explaining the well-observed calculation of electrical conductivity properties.

In terms of the frontier orbital analysis, the depiction of the HOMO-LUMO plots derived with 0.03 au isosurface are depicted in **Figure 5.11**. Interestingly, HOMO contours are localized in the similar position with LUMO. This is due to the relatively small differences between HOMO and LUMO energies and thus, exhibits a narrow energy gap (0.172 eV). **Figure 5.11(b)** illustrates the HOMO-LUMO isosurfaces, mostly localized in the Sn and O atoms around the F-dopants, with no contribution from the bare area without F-dopant. This figure suggests that the reactivity site of FTO is addressed into the specific area where the dopants are allocated. Fluorine may extend its electrostatic states to the neighbouring atoms. These finding is in good agreement with the energy band gap and E_f which F atoms increase the electrical conductivity of the native SnO_2 cluster. Nevertheless, the usability of F-dopant in synthesizing new SnO_2-based TCO materials have been described through theoretical (Cheng *et al*., 2014a) and experimental (Kim *et al*., 2008, Banyamin *et al*., 2014, Afzaal *et al*., 2016) works and is also currently available in the market (Ginley and Bright, 2011, Das and Jayaraman, 2014).

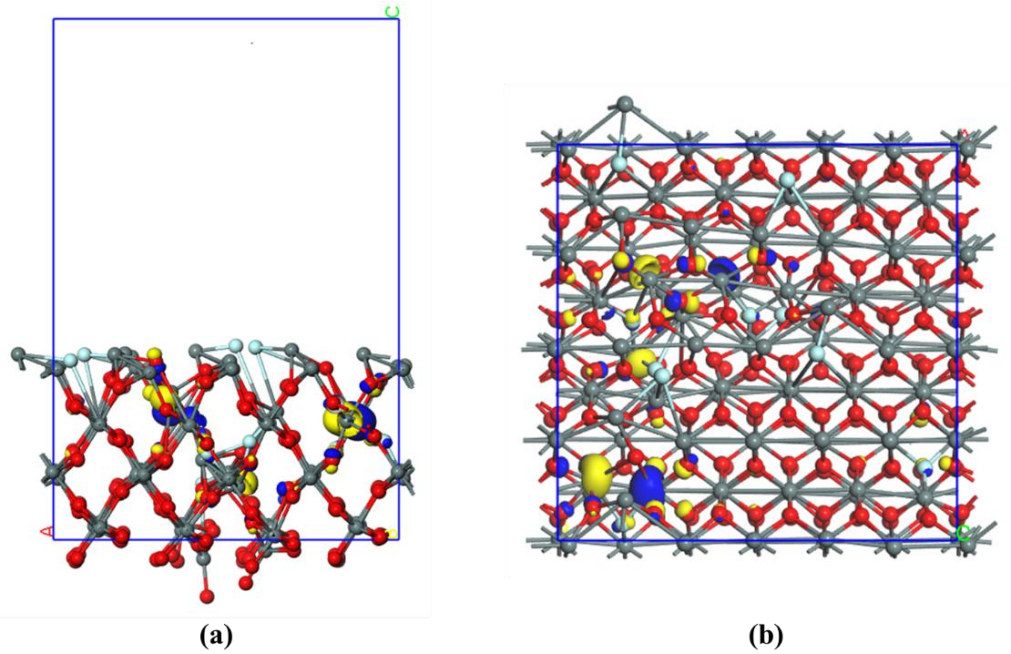

Figure 5.11 HOMO and LUMO isosurfaces of SnO_2/F (or FTO) cluster comprising of front (a) and top (b) view depictions.

In order to further study the effects of substituting the F atoms of the FTO cluster, the partial density of state (p-DOS), total density of state (t-DOS), and band structures have been calculated and compared to the results obtained for the native SnO_2 crystals. The p-DOS and t-DOS profiles may provide an in-depth understanding of the increment of electrical conductivities. The t-DOS is determined by summation over all bands obtained in the state density calculations. Whilst, the p-DOS represents the useful semi-qualitative analysis of electronic structure, p-DOS further qualifies the t-DOS by resolving the contributions of the orbitals in compliance with the angular momentum of the states. The main peaks generated by t-DOS mainly comprising of *s*, *p*, or *d* characters are the valuable parameters to observe. In the DMol3 system, p-DOS calculation is based on Mulliken population analysis, that allows the contribution from each energy band to a specified atomic orbital to be computed (BIOVIA, 2016b). Prior to DOS analysis, due to the underestimated energy gap of SnO_2 and

FTO clusters, the scissor operator (Segall *et al*., 2002) was applied herein. Scissor operator has been widely used in DFT calculation to evaluate the common errors in standard GGA functional (Tian and Liu, 2006, Hossain *et al*., 2008, Cheng *et al*., 2014a). The modification factors for both SnO_2 and FTO clusters were set as 3.050 eV and 3.328 eV, respectively, reflecting the actual difference between calculated and experimental band gaps. Upon the application of scissor operator, there is no difference in the SnO_2 band gap (i.e. orbital pattern) since the state density is only located at the Fermi level. The FTO band gap obtained at 3.335 eV is in accordance to the experimental value (3.500 eV).

Indeed, the scissor operator also helps to generate the clear separation within the valence and conduction bands as seen in **Figures 5.12(b – d)** (p-DOS and t-DOS) and **5.13** (band structure). **Figure 5.12(b)** shows the native SnO_2 and FTO, while their t-DOS patterns are depicted in **Figures 5.12(c & d)**. For the t-DOS, the spectrum of native SnO_2 shifted closer to E_f when the F-dopant were introduced. Moreover, the upper valence bands were observed across the Fermi level due to F-doping. This suggests the existence of free electrons participating in the *n*-type electrical conductivity, in accordance with several experimental reports (Elangovan and Ramamurthi, 2005, Subba Ramaiah and Sundara Raja, 2006, Yadav *et al*., 2009, Chinnappa *et al*., 2011). The defect produces several local-character perturbations upon the valence bands of the cluster (Marcillo and Stashans, 2014). It also indicates the lowering of energy differences between VBM and CBM. For the lower conduction bands, the state densities are contributed from the *d*-orbitals. The obvious gap between the upper valence and lower conduction bands suggests the semiconducting nature of FTO cluster. Most importantly, this evidence describes the fundamental change of valence band energies of FTO after the introduction of F-dopant into the internal structure.

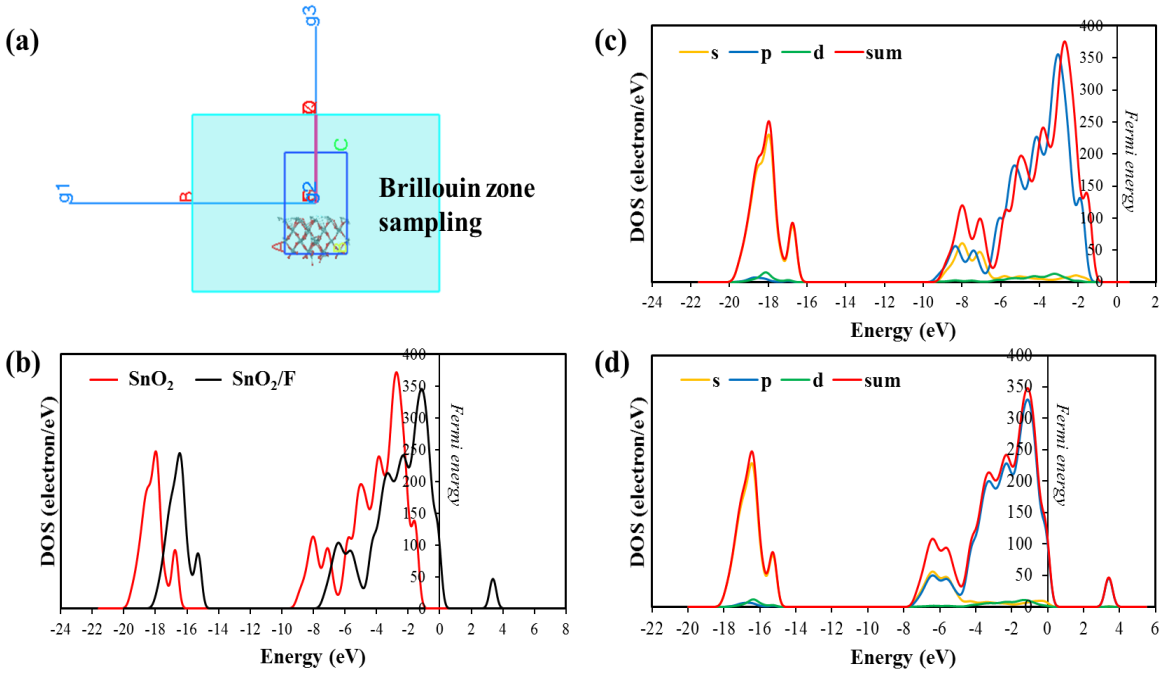

Figure 5.12 Brillouin zone sampling of SnO_2/F (a), t-DOS of SnO_2 and SnO_2/F (b), and p-DOS of SnO_2 (c) and SnO_2/F (d) comprising of *s*, *p*, and *d* orbitals.

In addition, the p-DOS is also considered in parallel with t-DOS. **Figures 5.12(c & d)** illustrates the orbital contributions of SnO_2 and SnO_2/F (or FTO) towards Fermi level which are predominantly due to the *p* orbitals from the upper valence bands. It can be seen from the *p* orbitals (shown by the blue line of **Figures 5.12(c & d)**) across the Fermi level. As compared to the native structure, the overall FTO orbitals seems to move closer to the Fermi level, with the major contributions from the *p* orbitals (O 2*p*, F 2*p*, and Sn 5*p*) and slight influences of *s* (Sn 5*s*, O 2*s*, F 2*s*) and *d* orbitals (Sn 4*d*). This implies that the main doping effects the shifting of orbitals position (*p* as the major) closer and even across the Fermi level, indicating the reduction of the valence and conduction energy differences. The occurrence of *d*-orbitals in the conduction band are also observed herein. It re-confirms the existence of free electrons donating to the *n*-type electrical conductivity of the FTO cluster.

Evidence of narrow band gap upon the F-doping into SnO_2 can be further explained by band structures. From the **Figure 5.13(a)**, the band structures correlate with the obvious differences of valence and conduction bands in accordance with the Fermi energy level of t-DOS profiles (**Figure 5.13(b)**). The high-density band thickness in the valence band area (VBM) suggests the highly electrical conductivity of FTO structure upon 5.3% F-doping concentration.

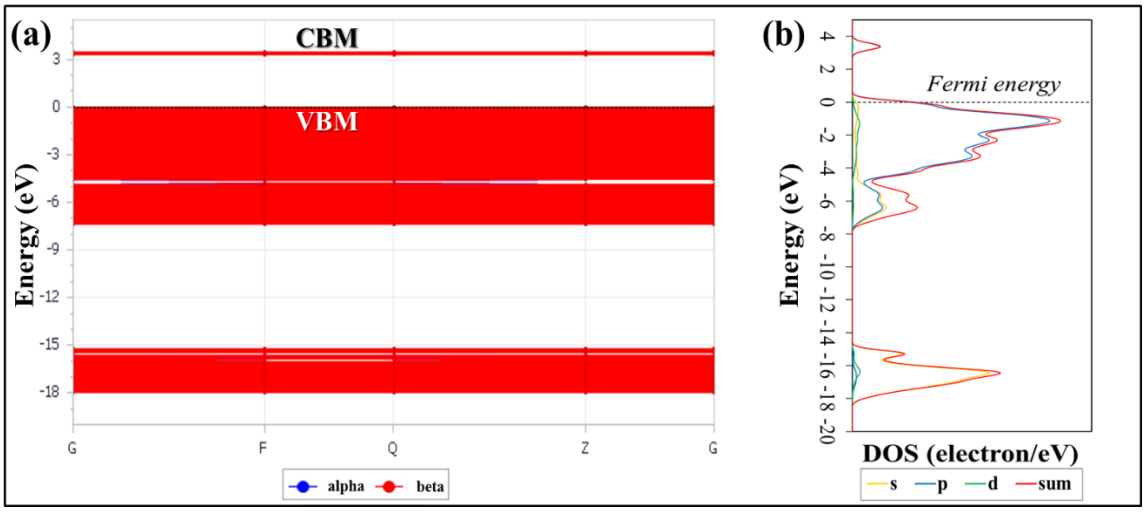

Figure 5.13 Comparison of band structure (a) and p-DOS (b) of SnO_2/F (or FTO) upon the geometry optimization.

The vibrational properties (i.e. infra-red (IR) and Raman spectra) of SnO_2 and FTO clusters are not able to be calculated due to the highly computational cost of large-scale atoms and limitation of the computational system.

5.1.2.2 Titanium dioxide

(i) Structure and energetics

Table 5.6 shows the structural parameters of the TiO_2 anatase primitive structure upon the geometry optimization using GGA-PBE functionals. It was carried out prior to the calculation of the larger clusters in order to validate the standard GGA-PBE functionals employed in DFT calculations. Similar to FTO, the calculated results are compared with the experimental values and other theoretical results. After the geometry optimization, the calculated lattice constants (*a*, *b*, and *c*) are in agreement with the experimental values (Burdett *et al*., 1987, Tang *et al*., 1993) and remains better than previous theoretical calculations (Fahmi *et al*., 1993, Asahi *et al*., 2000, Lee *et al*., 2005). Interestingly, the *c/a* value is similar to the experimental values, while other parameters (*a*, *b*, and *c*) demonstrate a closer theoretical value. In terms of bond lengths, the Ti-O distance in equatorial (d_{eq}) and apixal (d_{ap}) positions are comparable with the experimental values. Remarkably, the d_{eq} and d_{ap} values prior to geometry optimization shows a better comparison with the experimental values than upon the optimization. Likewise, similar trends are also observed in the case of torsional angles (Θ). These evidences may be due to the tight convergence criteria employed in DFT, and therefore produces more relaxed Ti-O bonds. Further consideration was given to HOMO-LUMO band gap as an effective way to describe the electronic nature. The observed result shows an excellent comparison due to the very slight difference within calculated (3.102 eV) and experimental (3.200 eV) electronic band gaps. Moreover, this energy gap value confirms the semiconducting nature of TiO_2 as observed in **Figure 4.1** (see **Chapter 4; Materials and Methods**). For the total energy calculation, the minimum energy conformation was achieved upon the optimization. The single point energy calculations were used to calculate the total

energy of the native TiO_2 crystals. The result shows almost similar total energy values in which the optimized structure exhibits slightly lower energy than the native TiO_2. It anticipates that the stability of optimized structure is almost similar to the native intrinsic TiO_2, according to standard GGA functionals. These results suggest the reliability of the crystal structures and methods to be employed in larger structure (cluster) calculations.

Table 5.6 Structural parameters of intrinsic TiO_2 structure optimized using Forcite with GGA-PBE functionals and its comparison with the experiment and other previous works.

Lattice parameters	**This work (un-optimized structure)**	**This work (optimized structure)**	**Lee's work[a]**	**Fahmi's work[b]**	**Asahi's work[c]**	**Experiment[d]**
a (Å)	3.776	3.776	3.845	3.763	3.692	3.782
b (Å)	3.776	3.776	3.845	3.763	3.692	3.782
c (Å)	9.486	9.486	9.537	9.851	9.471	9.502
c/a	2.512	2.512	2.481	2.618	2.566	2.512
d_{eq} (Å); Ti-O	1.930	1.959	1.960	1.939	1.893	1.932
d_{ap} (Å); Ti-O	1.973	1.850	2.002	1.995	1.948	1.979
Θ (°)	156.168	149.107	157.600	152.100	154.400	156.300
Total energy (Ha)	-887.211	-887.297	*ns*	*ns*	*ns*	*ns*
HOMO-LUMO energy gaps (eV)	*ns*	3.102	*ns*	*ns*	*ns*	3.200

[a] Lee *et al*. (2005) using norm-conserving pseudopotentials within LDA.
[b] Fahmi *et al*. (1993) using pseudopotential Hartree-Fock.
[c] Asahi *et al*. (2000) using FLAPW method.
[d] Burdett *et al*. (1987) and Tang *et al*. (1993).
Abbreviations: *ns*; non-specified.

Upon the validation of intrinsic crystal structure, the larger cluster of TiO_2 was elucidated by DFT calculation. **Figures 5.14(a & b)** display the non-optimized structures of anatase TiO_2 (101), while the optimized structures are depicted in **Figures 5.14(c & d)**. From the top view perspective (**Figure 5.14(b)**), it can be observed that the outer layer of the cluster's surface

are comprised of Ti atoms, while the second layer consist of O atoms. This is in line with previous reports from Thomas and Syres (Thomas and Syres, 2012) and Johansson and co-workers (Johansson *et al.*, 2010). The constructed cluster contains eight layers along the 20 Å vacuum thickness to eliminate possible interactions of the upper and lower surfaces. Comparing the native (non-optimized) and optimized clusters, the optimization using GGA-PBE functionals seems to slightly contribute to the chemical bond relaxation, resulting in both structures being similar. The obvious differences are obtained at the lowest layer of the periodic system in which the bond distortion mainly occurs in O atoms. It may be due to the common impact of geometry optimization procedures in searching the minimum energy configurations (Canfield *et al.*, 2006, Scaranto and Giorgianni, 2009).

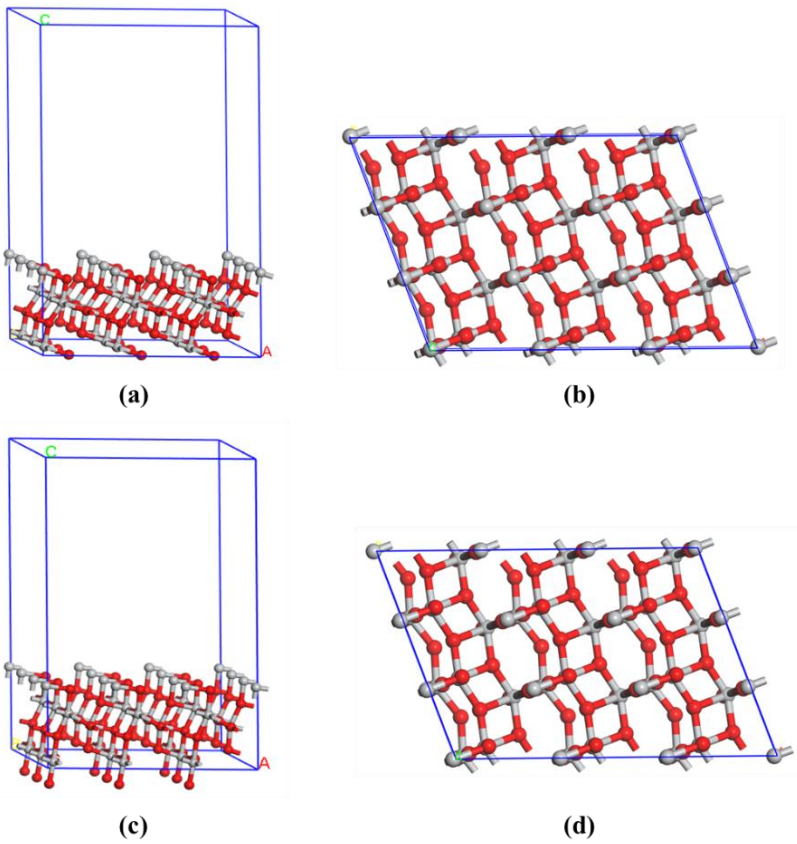

Figure 5.14 Native structure of anatase TiO_2 (101) comprising of front (a) and top (b) view depictions and its optimized geometry structure at GGA-PBE level of theory comprising of front (c) and top (d) view depictions.

(ii) Electronic properties

The energy gap of anatase TiO_2 (101) cluster was observed using GGA-PBE exchange correlation functionals. Upon the energy minimization, the HOMO band energy located at -5.725 eV, while the LUMO found at -4.582 eV and thus, the energy band gap obtained at 1.143 eV. This band gap corresponds to semiconductor materials (**Figure 4.1**, see **Chapter 4; Materials and Methods**). This result is in good accordance with the general nature of TiO_2 materials which enables the electron excitations from the valence bands towards conduction bands. However, the calculated band gaps for larger clusters of TiO_2 is underestimated since the experimental band gaps were observed at 3.200 eV (Tang *et al*., 1993). The underestimation of band gaps observed in previous theoretical calculations (Mo and Ching, 1995, Masayoshi Mikami *et al*., 2000). This evidence might be due to the smearing influence, the difference in cluster's size (i.e. number of atoms) employed in the calculation, discontinuity of exchange-correlation energy, or a part of typical error in GGA approximations (Kinga Bruska *et al*., 2009).

Further, the depiction of HOMO-LUMO isosurfaces are presented in **Figure 5.15**. Herein, the orbitals are generated by 0.03 au in order to obtain the maximum quality of the isosurfaces. The orbital contours are consistent with FTO (with the use of similar level of theory) in which the HOMO and LUMO energy levels generate no differences in the isosurfaces, due to the relatively narrow energy gaps within valence and conduction bands (**Figure 5.17**). Indeed, the orbital isosurfaces are mainly delocalized at the surface of the cluster, specifically at Ti atoms. It follows the general rule of surface chemistry, in which the reactive sites are accumulated on the surface (or outer layer) of metal oxides (Canevali *et al*., 1997, Degler *et al*., 2016). These finding suggests that the distribution probability of the

electrons (leads to reactive site accumulation) are predominantly found in the cluster's surface, i.e. the electron is limited nearby the surface (Yang *et al*., 2013).

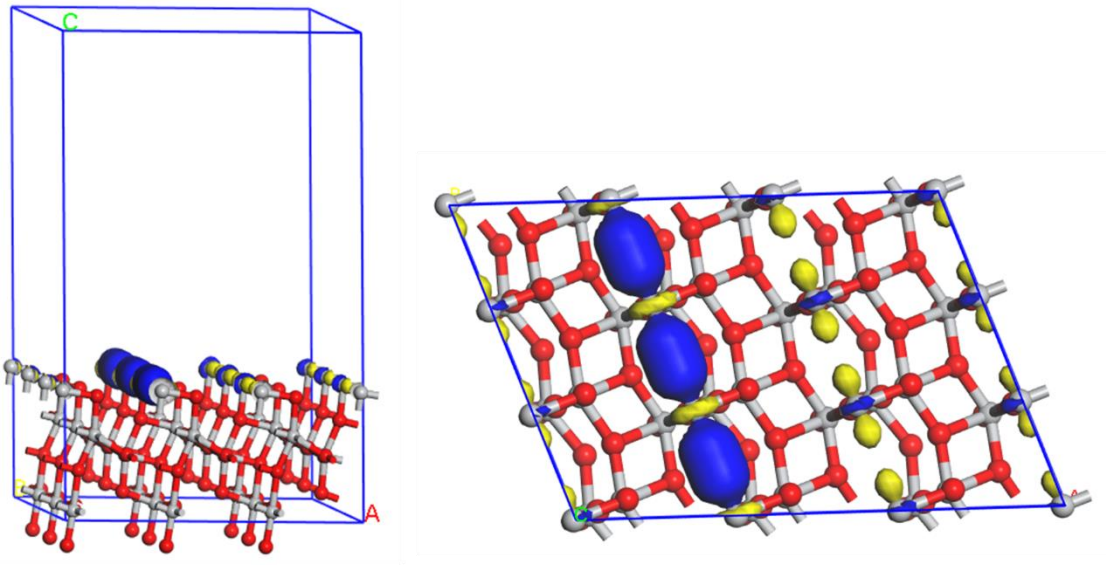

Figure 5.15 HOMO and LUMO isosurfaces of anatase TiO_2 (101) cluster comprising of front (a) and top (b) view depictions.

In order to further observe the electronic properties, the p-DOS (**Figures 5.16(b)** and **5.17(b)**) and band structures (**Figure 5.17(a)**) are considered to perceive each orbitals contribution upon the cluster construction and its correlation with the energy gap. Since the band gap is underestimated, the scissor operator (Segall *et al*., 2002) was accordingly used to evaluate the discrepancy. The scissor operator attempts to correct the TiO_2 band gap *via* conducting the clear separation between valence and conduction bands (for DOS and band structures). For this calculation, the scissor operator was set at 2.057 eV accounting for the difference between experimental (3.200 eV) and the calculated band gaps (1.143 eV). Upon the application of scissor operator, the band gap of TiO_2 cluster was 3.136 eV which is highly comparable with the experimental value (3.200 eV). From the t-DOS pattern, the clear

separation between valence and conduction bands are clearly observed. It shows the energy differences within the valence and conduction bands. The calculated band gaps also validate the semiconducting nature of the TiO_2 due to electron ability to produce relatively wide band gaps.

The p-DOS is considered to demonstrate the orbitals contribution towards the t-DOS. **Figure 5.16(a)** depicts the Brillouin sampling in the state density and band structures of TiO_2 (101) cluster. From the p-DOS profiles (**Figure 5.16(b)**), the *p* orbitals (O 2*p* and Ti 2*p*) seems to dominate the corresponding valence peaks across the Fermi energy. Meanwhile, the *s* orbital (Ti 2*s*) dominates the lower valence bands. The conduction bands show the existence of *d* orbitals with the small contributions of *s* and *p* tracks. This peak behavior is consistent with the previous theoretical investigation on anatase TiO_2 cluster (Yang *et al*., 2013), and an experimental report using X-ray photoemission in conjunction with simulation studies (Scanlon *et al*., 2013). The electronic structure of TiO_2 was further explored using band structures (**Figure 5.17**). The comparison of the band structure and p-DOS shows that the band gap location within the valence and conduction bands are responsible for the band structures. As can be seen, the thick bands at the VBM area confirms the relatively narrow band gaps of the TiO_2 cluster (i.e. 1.143 eV) prior to the scissor operator applications. TiO_2 was used in this study to harvest the photocatalytic reaction upon ultraviolet (UV) light penetration. Therefore, the optical (rather 'vibrational') nature of TiO_2 was also observed to discover the opto-chemistry behind the use of TiO_2 anatase in the electrode construction.

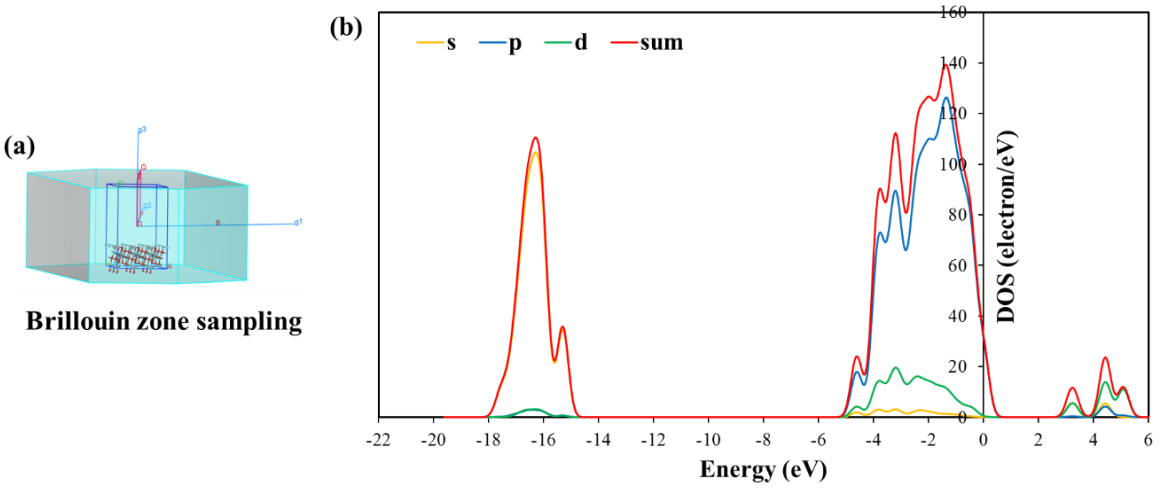

Figure 5.16 Brillouin zone sampling of anatase TiO_2 (101) (a) and p-DOS of TiO_2 (101) comprising of *s*, *p*, and *d* orbitals (b).

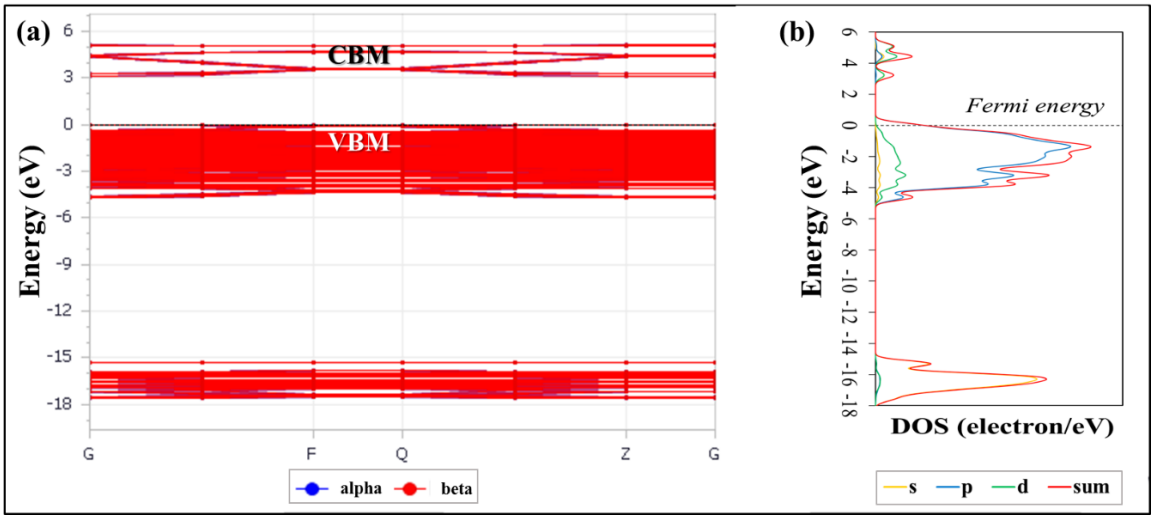

Figure 5.17 Comparison of band structure (a) and p-DOS (b) of TiO_2 (101) cluster upon the geometry optimization.

(iii) Vibrational properties

For the vibrational properties observation, the IR and Raman spectra are considered. Prior to vibrational analysis, the parameters were defined as follows: 220 cm^{-1} full width at half maximum (FWHM), 'ultrafine' graph quality, 1.0 max. amplitude, and 20 number of steps

in file in order to generate the maximum quality of IR spectrum. **Figure 5.18(a)** represents the comparison within the reference (NIST, 2005) and the calculated IR of TiO_2 cluster. From this depiction, the experimental spectrum shows an identical result with the two major peaks projected at 800-450 cm^{-1} and a small band at 3600-3400 cm^{-1}. This particular behaviour is in accordance with calculated IR spectrum with insignificant discrepancy. The two major peaks are exhibited at 1200-900 cm^{-1}, and the smaller bands found at 3600-3300 cm^{-1}. The first peak of calculated IR is overestimated approximately at 450 cm^{-1} from the peak observed experimentally. This discrepancy is known as a common limitation of standard GGA-PBE functionals in calculating the frequencies of metal oxides (Calzolari and Nardelli, 2013). However, the excellent agreement obtained in the smaller bands were revealed in the equivalent wavelengths (3600-3400 cm^{-1}). GGA, however, is able to calculate the vibrational spectra accurately (He *et al*., 2014). The choice of functionals affords a direct impact to the electrostatics energy and thus, affecting the characteristics of the vibrational response (Calzolari and Nardelli, 2013). Experimentally, the intense bands below 1000 cm^{-1} are due to O-Ti-O vibrations, while the peak at 3600-3100 cm^{-1} corresponds to -OH (Chellappa *et al*., 2015) produced from solvent.

Further observations of the vibrational properties were carried out by displaying the Raman spectra (**Figure 5.18(b)**). The Raman behaviour of the calculated systems seems to be identical with experimental spectra (Ohsaka *et al*., 1978, Hanaor and Sorrell, 2011). The calculated Raman spectrum was generated at room temperature (298 K), incident light of 514.5 nm, and Lorentzian smearing of 20 cm^{-1}. **Figure 5.18(b)** demonstrates the comparison between the calculated and the experimental Raman derived from Ohsaka and co-workers (Ohsaka *et al*., 1978). According to the experiment, the three Raman bands at 639, 197, and

144 cm^{-1} were observed as major bands of TiO_2 anatase. From the DFT calculations, the maximum Raman spectra are assigned at 684, 212, and 37 cm^{-1}. The sharp and intense peak of experiment was shown at 144 cm^{-1}, while for the calculated Raman, this peak is found at different wavelength (37 cm^{-1}). Similarly, the minor peak of 639 cm^{-1} in experiment is also shifted in calculation (684 cm^{-1}). The better agreement is made by another minor peak observed at relatively near wavelength (197 cm^{-1} for experiment and 212 cm^{-1} for calculation). The discrepancy of the Raman spectra may be due to the difference in incident light and environmental condition used in experiment. It also may be caused by the use of standard GGA-PBE functionals in DFT calculations. However, the peak of calculated Raman is comparable with experiment and therefore, confirm the vibrational active behaviour of the TiO_2 cluster used in this present simulation (in accordance with vibrational behaviour of the experiment).

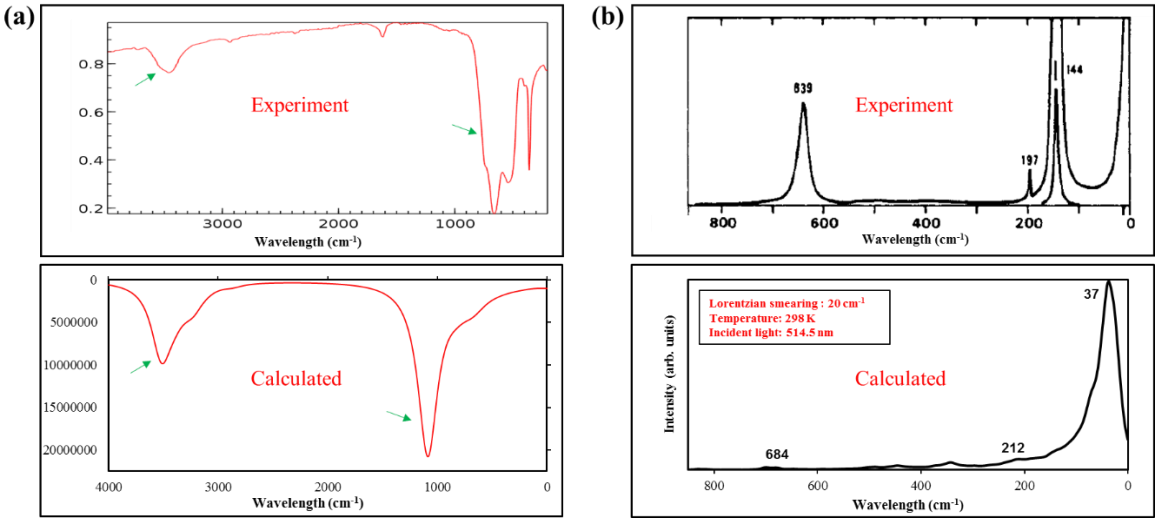

Figure 5.18 Comparison of experimental and calculated IR (a) and Raman (b) spectra of TiO_2 (101) cluster. The experimental IR and Raman data were adapted from NIST (2005) and Ohsaka *et al.* (1978), respectively.

5.1.2.3 Dopamine

(i) Structure and energetics - electronic properties

Dopamine is a small biomolecule which has been used as an anchor between TiO_2 cluster and the macromolecule of ss-DNA. Herein, the DFT calculations of dopamine were carried out with the use of different level of theories with the standard GGA-PBE functionals applied for previous calculations (i.e. FTO and TiO_2 anatase). Density functional dispersion correction (DFT-D) method along with B3LYP hybrid functionals were employed to produce a more accurate prediction of structural, electronic, and vibrational properties of a dopamine molecule. Relatively small size and bioorganic structure of dopamine exhibits the possibility of this molecule to be elucidated using a hybrid density functional (Kamachi *et al*., 2005, Pande *et al*., 2009, Karaman, 2011).

The optimized geometry of dopamine is shown in **Figures 5.19(a & b)**. Upon geometry optimization, the total energy of the system was found to be -547.276 Ha, while the native dopamine exhibited -547.273 Ha, calculated using single point energy. There is no significant difference between both values. It is due to the stable conformations of dopamine which has been reached in earlier geometry optimization. The initial structure of dopamine was derived from the stable structure of COMPASS-based MM geometry optimization applied in the previous subsection.

For observing the electronic properties, the HOMO and LUMO isosurfaces were generated with respect to discovering of electron localization towards the entire structure. The HOMO isosurfaces (**Figures 5.19(c & e)**) are mostly localized at the benzenoid ring with the small

contribution from -OH groups, and ethyl chain. For the LUMO (**Figures 5.19(d & f)**), the majority of electron density is delocalized at the benzenoid ring, in consistent with HOMO, along with minor contributions from -OH groups, ethyl chain, and the amine group. It is likely to understand that the lowest energy configuration tends to place the benzene ring of the dopamine molecule, allowing equivalent interactions with any of its atoms as the function of electron affinity and structure. The HOMO isosurface localization, in particular, modifies the dopamine application, because the associated chemical potential is entirely different (Aliste, 2000). It is also well-known that HOMO-LUMO plots depict the electronic density and therefore, corresponds to the accumulation of reactive sites of molecule or cluster. Overall, the reactive site of dopamine is mostly accumulated at benzenoid ring due to the exhibition of special stability attributable to the resonance delocalization of π-electrons. It is in line with general nature of dopamine as well as previous theoretical investigations (Lopez *et al*., 2010).

Instead, the electron localizations are also attributed from two -OH groups (shown at the HOMO and LUMO plots) and amine group (attributed from the LUMO plot only). It represents the ability of these functional groups to excite the electrons from the valence bands and thus, incorporate with another molecule or cluster surface. Nevertheless, this functionality has been widely observed previously (Lopez *et al*., 2010). Through this present theoretical investigation, it has been successfully confirmed that dopamine exhibits the active sites *via* aromatic ring, -OH groups, and the amine group. The -OH and amine groups are preferable in functionalization due to the possibility to generate the hydrogen (H)-bonding and the highly stable nature of aromatic ring.

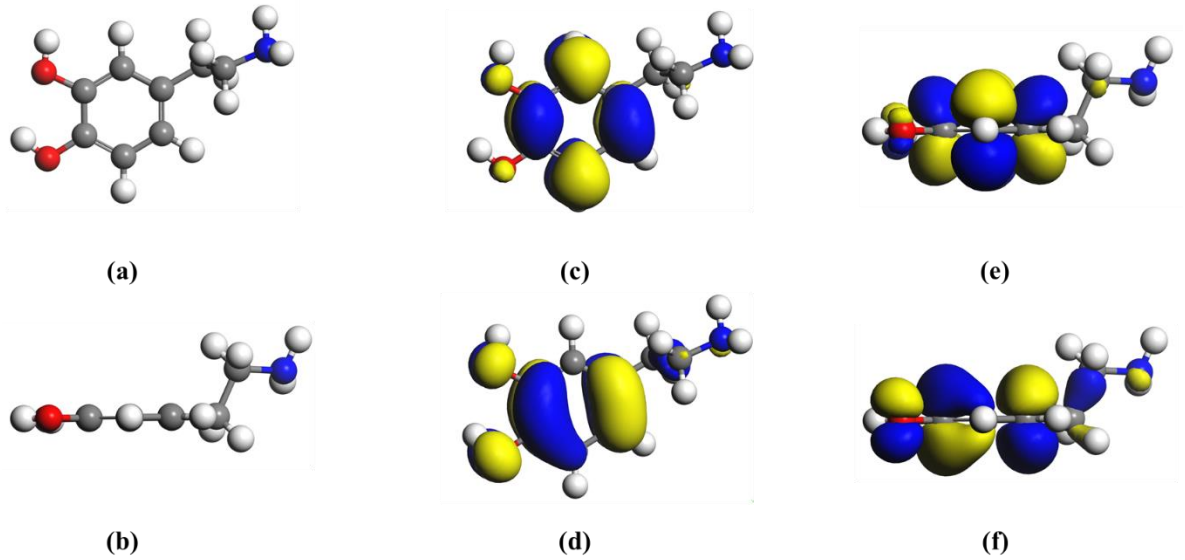

Figure 5.19 Optimized geometry of dopamine structure using B3LYP level of theory comprising of top (a) and front (b) view depictions, its HOMO (c) and LUMO (d) isosurfaces represented from front view depictions, and HOMO (e) and LUMO (f) plots depicted from top view perspectives.

(ii) Vibrational properties

In terms of vibrational properties, the IR and Raman spectra of dopamine were determined in comparison with the experimental spectra. **Figure 5.20(a)** depicts the IR spectra of dopamine comprising of the present computational and existing experimental investigations (Lopez *et al*., 2010). In order to generate the maximum quality of IR spectrum, the vibrational analysis parameters were set at 20 cm^{-1} FWHM, ultrafine graph quality, 1.0 max. amplitude, and 20 number of steps file. In general, the band behaviours of the calculated and experimental IR spectra are fairly comparable. It can be seen through the conformity of their peaks. Indeed, for the experimental spectrum, a wide band was observed for dopamine at low energy including three significant peaks. These peaks were located at 3350 cm^{-1}, 3205 cm^{-1}, and 3034 cm^{-1} which were assigned to stretching vibrations of the -OH, -CN, and =NH groups of dopamine, respectively. Other minor peaks were detected in the range of 2778-2170 cm^{-1},

confirming the different CH vibrations of either aryl or aliphatic CH bonds. At higher energy levels, several important bands were monitored at 1494 cm^{-1} and at 1252 cm^{-1}, encompassing to the bending vibration of CH and the stretching vibration of aryl oxygen, respectively. The peak at 1342 cm^{-1} was attributed to the -OH groups of the dopamine molecule (Lopez *et al*., 2010). For the calculated IR, the major and minor bands are assigned at the similar wavelength to experiment along with the appearance of several additional bands (i.e. 3900-3600 cm^{-1}). The good agreement between the calculated and the experimental IR spectra may be due to the use of hybrid functionals (i.e. B3LYP) enabling accurate vibrational spectra prediction of a single and small molecule of dopamine.

In order to obtain more information on the vibrational properties, the Raman spectra calculation was employed. The calculated Raman was compared to experimental bands (Pande *et al*., 2009) as depicted in part (b) of **Figure 5.20**. A direct comparison between both spectra exhibits a general concordance in the position of peaks as well as the intensities. As can be seen that three major peaks of experimental spectra were obtained at 750, 791, and 1288 cm^{-1}, while for the calculated Raman, the major peaks are particularly observed at different wavelengths i.e. 0-300 cm^{-1}. Whilst, the other bands show similarity with the experimental result. The disagreement of the major band positions was also observed in the previous study by Pande and co-workers who discovered the direct comparison within experimental and theoretical calculation using a similar method (i.e. B3LYP/6-31++G (d, p)) (Pande *et al*., 2009). This discrepancy corresponds to the consequence of the anharmonicity and may also due to the general tendency of the quantum mechanics (QM) methods to overestimate the force constants at the exact equilibrium geometry (Sarkar *et al*., 2005a, Sarkar *et al*., 2005b). However, the vibrational frequency calculation using DFT was carried

out in a gas phase condition which remains different with the experiment generated in the solid state and under solvent influence. Hence, the experimentally observed Raman spectra may differ from the present calculated spectrum. Other previous studies also showed discrepancies, while the QM-based Raman spectra compared to the experiments (Aroca *et al*., 2000, Bolboaca *et al*., 2003, Peica *et al*., 2007, Pande *et al*., 2009).

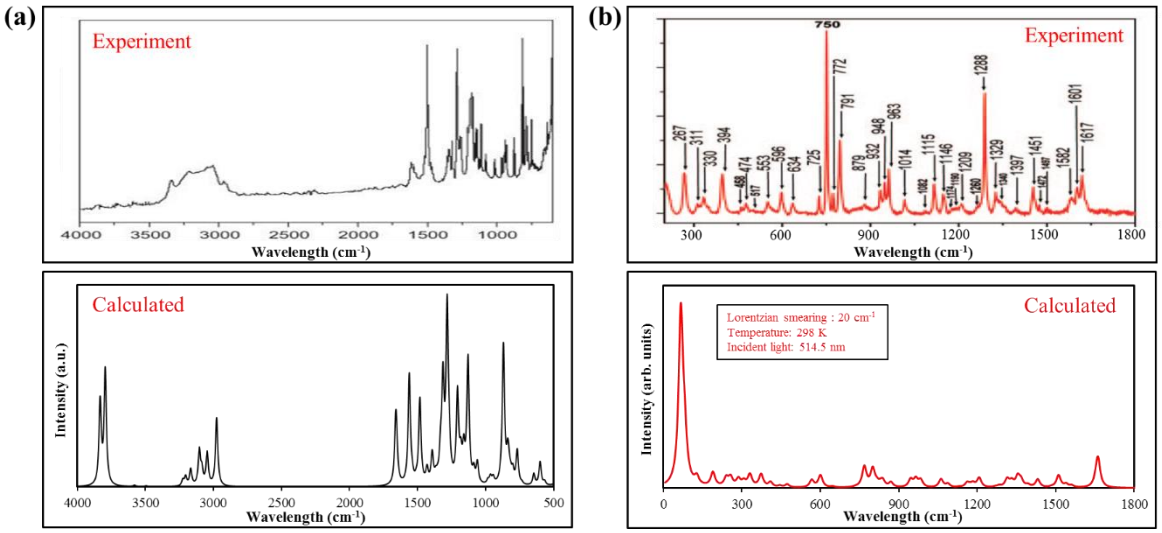

Figure 5.20 Experimental and calculated IR (a) and Raman (b) spectra of dopamine. The experimental IR and Raman data were adapted from Lopez *et al*. (2010) and Pande *et al*. (2009), respectively.

5.1.2.4 ss-DNA of Alzheimer's

(i) Structure and energetics

DFTB+ has been used to compute the energy parameters and electronic properties of ss-DNA since the common DFT is not capable in covering the large-scale atomic calculations. DFTB+ remains to be fruitful method for describing structural, electronic, and dynamics properties of large and complex molecules or materials with technologically relevant size, simulation time, and statistics demand approximate solutions (BIOVIA, 2016b). **Figure 5.21(a)**

demonstrates the native structure of ss-DNA Alzheimer's, while the optimized geometry using non-SCC DFTB+ is depicted in **Figure 5.21(b)**. Prior to optimization, the initial energy of the ss-DNA was calculated to be -236.871 x 10^4 kcal/mol, while upon the optimization, the energy lowered to -238.621 x 10^4 kcal/mol. The lowest energy function represents most stable conformation of ss-DNA. There is no significant difference within both structures instead of several relaxations of atoms and bonds function. Due to the limited literature on this particular nucleotide, the structure is not able to be compared with any references.

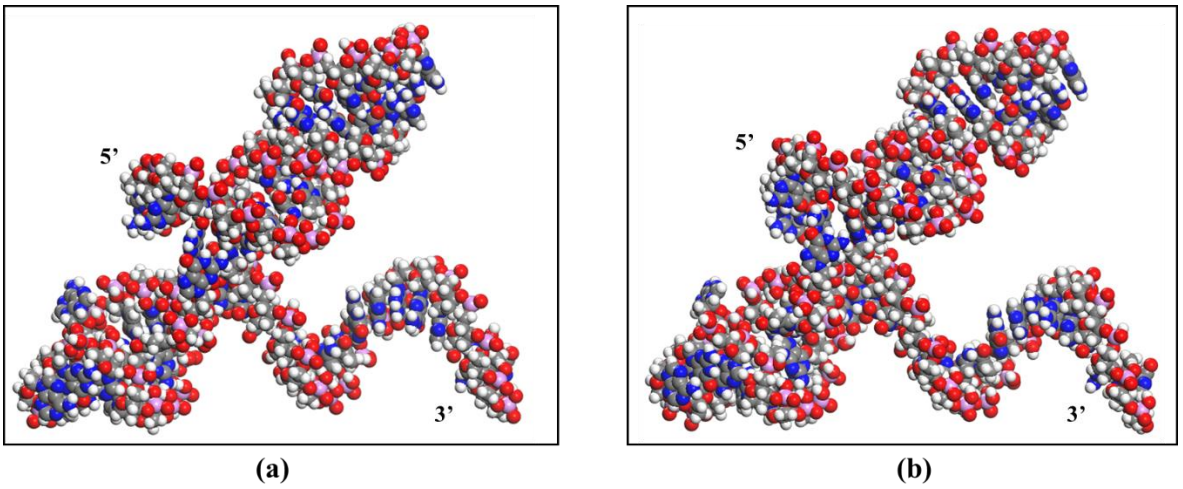

Figure 5.21 Depictions of native (a) and optimized geometry (b) of ss-DNA molecule using non-SCC DFTB+.

(ii) Electronic properties

To observe the electronic properties of ss-DNA, the HOMO and LUMO plots (**Figure 5.22**) were generated along with energy levels. The HOMO isosurface is delocalized at guanine-guanine residues (deoxyribose guanine at 51st sequence number; DG51 and DG52), while the LUMO is predominantly localized at similar nucleobases (guanine-guanine; DG66 and DG67) with the minor electron density localizations at adenine base (DA65). Interestingly, both HOMO and LUMO plots show the similar electron localizations of nucleobase i.e.

guanine bases. These plots, in general, demonstrate the reactive sites of the studied nucleotide structure which may be associated with its interaction studies with the presence of substrate layers. These orbitals density plots, however, are very well in line with (rather 'emphasize') the general understanding of guanine role in experimental DNA damage detection. Guanine is well-known as the main target for a wide spectrum of genotoxic agents (e.g. resulting from UV irradiation) as well as the most easily oxidized base among other nucleobases (Paleček and Bartošík, 2012). Therefore, guanine remains to be the reactive base for the ss-DNA configuration. For the orbitals energies, the HOMO and LUMO bands are located at -5.820 eV and -2.205 eV, respectively. Therefore, the energy gap is calculated to be 3.615 eV. This wide band gap corresponds to insulator type which does not readily conduct electrical energy. The nucleotide and protein are widely known as insulator (King *et al*., 2014) and thus, the present calculation is in accordance with the general nature of ss-DNA biomolecule.

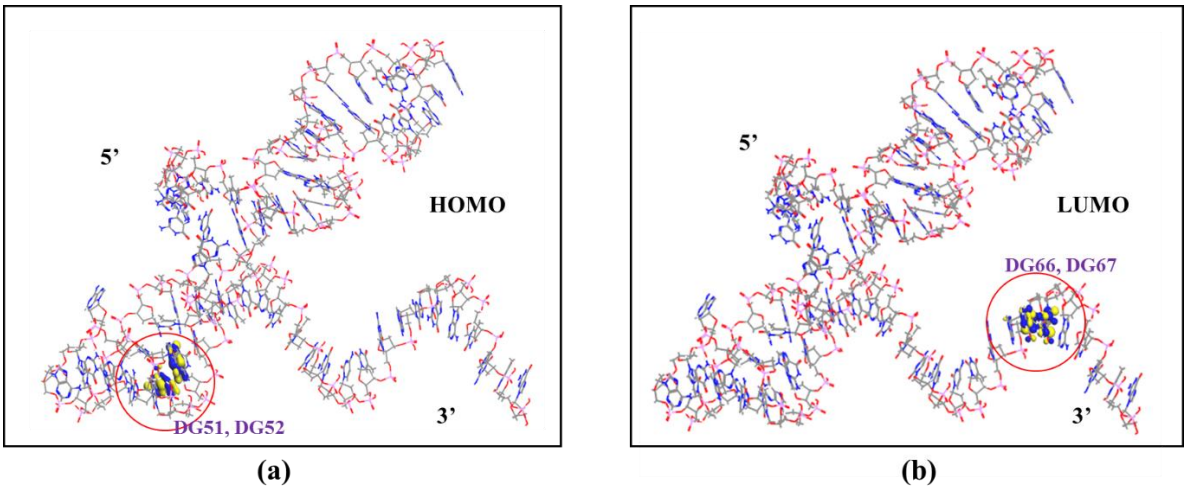

Figure 5.22 Depictions of HOMO (a) and LUMO (b) isosurfaces of optimized ss-DNA Alzheimer's.

5.1.3 Monte Carlo adsorption studies

5.1.3.1 Adsorption studies of TiO_2 onto FTO layer

In this study, the adsorption locator was employed to generate the most stable configuration of the target molecules onto the selected electrode surface. The MC-based function searches the favorable configurational space of the adsorbate molecule (i.e. TiO_2 molecule) towards the layer I containing FTO along a slowly decreasing temperature. Prior to MC simulation, the TiO_2 adsorbate is constructed and optimized using Forcite-Geometry. The geometry optimization process was performed through an iterative procedure, in which the atomic coordinates are modified until the total energy is suitably minimized. This process represents a local minimum of the potential energy surface. The basis of the geometry optimization of the adsorbate molecule was based on decreasing the calculated forces magnitude until the selected values of convergence tolerances were revealed. The forces on the adsorbates atoms were computed from the expression of potential energy and thus, depend on the used force field type (Khaled and Abdel-Shafi, 2011). Herein, the adsorption behavior of four different concentrations of TiO_2 molecule were investigated. The stable trajectories within various TiO_2 concentration comprising of 1, 5, 10, and 50 molecules along with the distribution fields are depicted in **Figure 5.23**. From this figure, the configuration of single TiO_2 molecule tends to be in a planar position right above the Sn atom. This position exhibits the strong interaction within two O atoms in TiO_2 and Sn metal atoms at the uppermost of SnO_2/F (200) (or FTO) surface. The contribution of Ti atoms may also be attributable herein to interact with O atoms of the FTO surface. This may correspond to ionic bondings which are formed by Coulombic interaction between two oppositely charged species (i.e. between metallic and O atoms of the substrate-adsorbate system or *vice versa*). Upon the increments of adsorbate concentration,

the distribution of TiO_2 adsorbate is consistently adsorbed at the surface of FTO. Interestingly, from the 10 (**Figure 5.23(e)**) to 50 adsorbate molecules (**Figure 5.23(g)**), the TiO_2 is likely adsorbed at the top of the vacuum region, instead of at the surface region, which corresponds to opposite surfaces of FTO substrate. These evidences have been confirmed by the favourability isosurfaces depicted at **Figures 5.23(b, d, f, & h)**. Basically, the observed "clouds zone" (rather 'isosurfaces') indicates the level of distribution field of the adsorbed molecule location corresponding to the bare FTO surface. It is ranging from red to blue region which comprises of lowest to highest locations of TiO_2 molecule to be distributed on the surface of FTO. More in thickness of this distribution field, the possibility of adsorbate accumulation remains higher at that corresponding location. From this depiction, it is clearly indicated that the adsorbate molecules are predominantly accumulated at the region closer to the substrate surface and the opposite surface, remaining the vacant region in between. This vacant region remains as an implausible area for the TiO_2 adsorption. For the highest studied concentration (**Figure 5.23(g)**), the adsorbate molecules were mixed up due to intermolecular forces that exist amongst the TiO_2 molecules. The difference of adsorbate concentrations plays an essential role in directing the molecular adsorption of TiO_2 and this is related to the variation of adsorption energies which explained in **Table 5.7**.

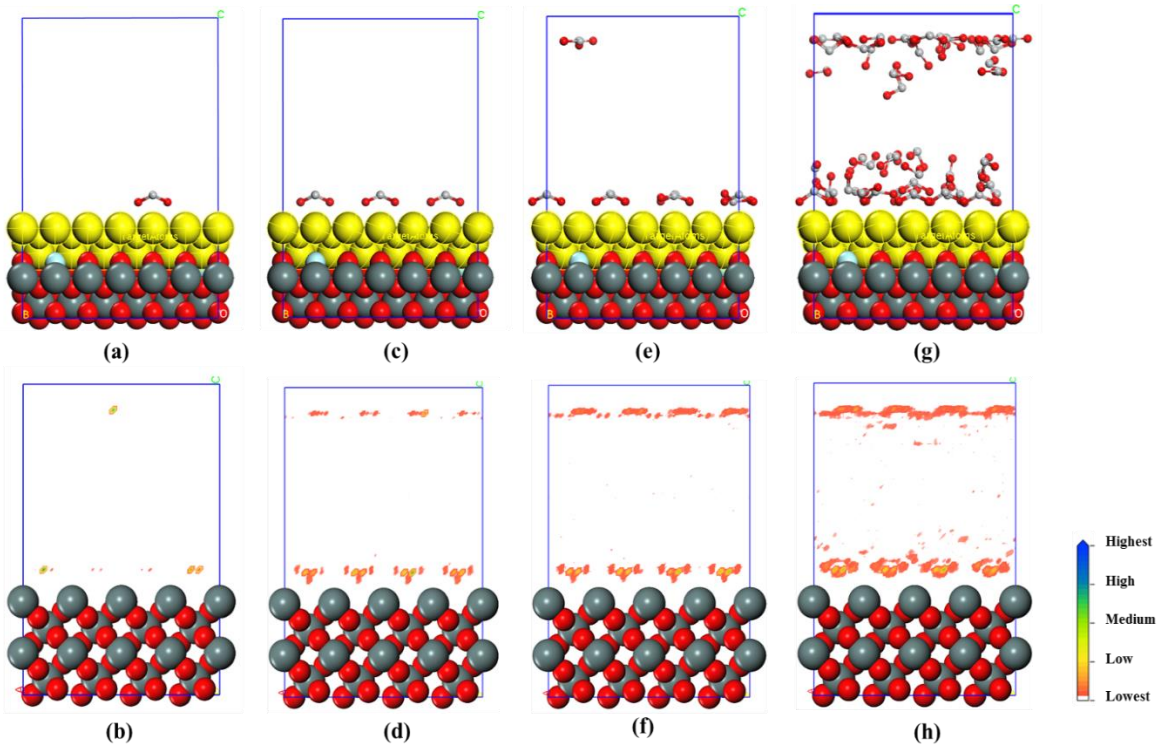

Figure 5.23 The lowest configurations of TiO_2 adsorption onto FTO surfaces comprising of 1 (a), 5 (c), 10 (e), and 50 (g) adsorbate molecule/s and their favourability isosurfaces comprising of 1 (b), 5 (d), 10 (f), and 50 (h) adsorbate molecule/s. The yellow atoms show the target regions during simulated annealing process.

Using adsorption locator simulation module, the TiO_2 - FTO surface configurations are sampled from a canonical ensemble. In this ensemble, the loading (or number) of all adsorbate molecules as well as the temperature, are kept fixed. The configuration probability, *m*, in the ensemble is provided by **Equation 5.1** (Shi and Atrens, 2011):

$$P_m = Ce^{-\beta E_m} \tag{5.1}$$

Where C corresponds to a constant of arbitrary normalization, β is the reciprocal temperature, and E_m is the total energy of configuration (m). Further, the reciprocal temperature is specified as **Equation 5.2** (BIOVIA, 2016b) below.

$$\beta = \frac{1}{k_B T} \tag{5.2}$$

Where K_b is the Boltzman constant and T corresponds to the absolute temperature. The total energy of configuration, *m*, is determined as the following sum:

$$E_m = E_m^{AA} + E_m^{AS} + U_m^A \tag{5.3}$$

Where E_m^{AA}, E_m^{AS}, and U_m^A are the intermolecular energy between adsorbate (i.e. TiO_2) molecules, interaction energy between adsorbate and the substrate (i.e. FTO), and the total intramolecular energy of all sorbate molecules, respectively. The intramolecular energy within substrate is not considered since its structure is kept fixed during simulations and therefore, the distribution of intramolecular energy is constant (**Figure 5.24**).

The first step of simulation involves the adsorption the specified loading of TiO_2 molecule. This step was carried out by a random series of insertion step and equilibration phase till the selected loading is accomplished. For this step, only insertion steps which do not produce structures with intermolecular close contacts and enable to pass all adsorbates location constraints are allowed. The initial configuration takes numerous steps for adjusting to the current temperature. An adsorption location is thus, divided into equilibrium and production stages. The last trajectories comprising of lowest energy configuration are based on production stage, particularly (Khaled and El-Sherik, 2013, BIOVIA, 2016b).

At the stages of equilibration and production, each step was started by choosing a step type by means of the selected parameters prior to simulation run. This step type corresponds to either rotation or translation procedure. Upon the selection of the step type, a random component is selected and the step type is implemented to random adsorbate of the corresponding component. Metropolis Monte Carlo algorithm is subsequently used to

determine the acceptability of the change to be accepted or rejected (Khaled and El-Sherik, 2013, BIOVIA, 2016b).

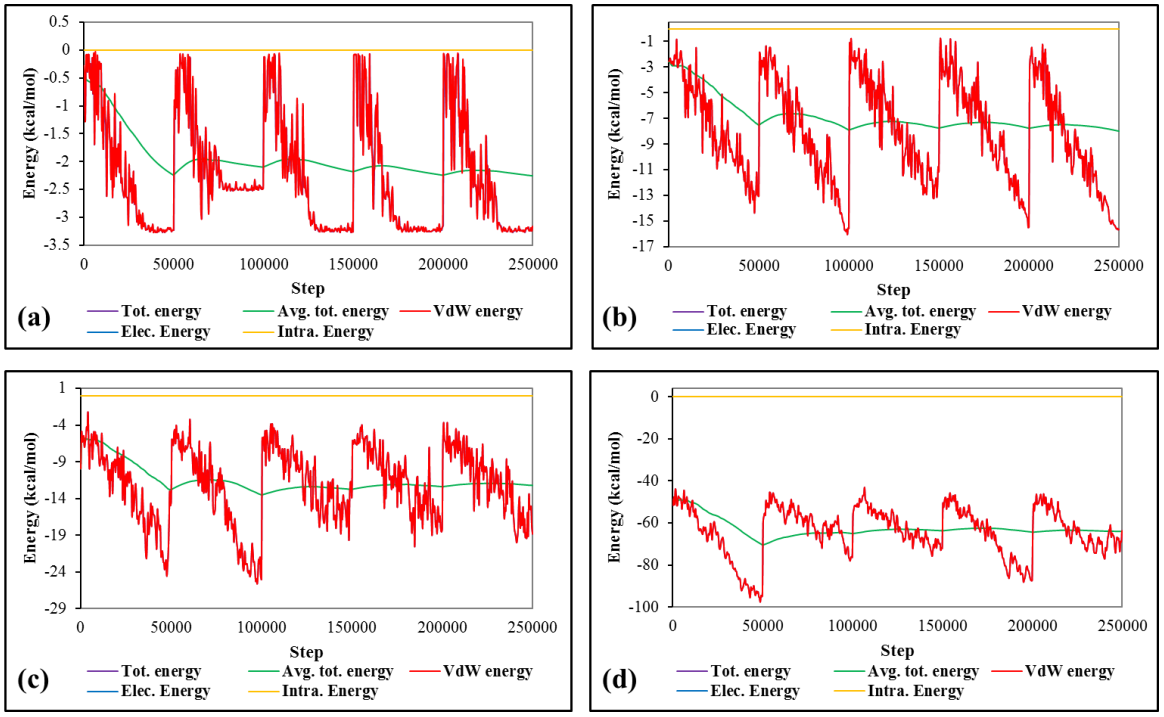

Figure 5.24 Total energy of adsorbed TiO_2 depending on the substrate concentrations. The substrate numbers comprise of 1 (a), 5 (b), 10 (c), and 50 (d) molecules.

The MC adsorption method applies four main steps for a canonical ensemble which are conformer, rotation, translation, and regrowth (BIOVIA, 2016b). This step is employed to a random adsorbate. **Figure 5.24** shows the total energy contribution of all model trajectories comprising of total and average energies, *van der Waals*, electrostatic, and intramolecular energies. As can be seen, five cycles of iteration were recorded throughout the simulations. As the most important energy parameter, the average total energy (green mark of each sub-figures) was initially decreased to reach the equilibration phase (first cycle) then continued with the production step till the end of simulation, which is depicted as constant curves. Moreover, the average energy constantly decreases by means of increasing concentrations.

More in adsorbate concentrations, less in average total energies (**Figures 5.24(a – d)** and **Table 5.7**). It indicates that the increment of adsorbate (TiO_2) molecules directly affects the total energy and therefore, elevate the stability of energetically optimized systems. This trend is in line with a recent study (Mlambo *et al*., 2017) in which the increasing number of adsorbate molecules leads to the decrease of total binding energy of the ligand. Thus, a weaker interaction energy resulting in a charge transfer between TiO_2 molecules and FTO surface. The weaker bond leads to a lower sharing of the bonding-orbital electrons in the TiO_2 and FTO surface (the electronic orbitals tend to be shifted slightly towards the TiO_2 than the FTO atoms itself) and consequently weakens the localized polarizability.

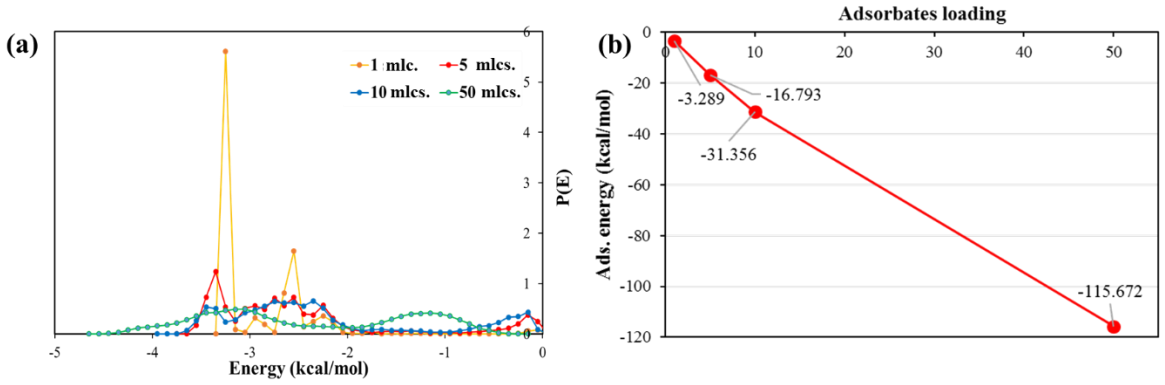

Figure 5.25 Adsorption energy distributions of TiO_2 onto FTO surfaces depending on the adsorbate concentrations (a) and its diagram function (b).

The adsorption energy distributions of all loading molecules are depicted in **Figure 5.25(a)**, while the outputs and descriptor are shown in **Table 5.7**. The adsorption energy (E_{ads}) is the energy that released (or necessitated) when the optimized adsorbate molecules are adsorbed onto the selected substrate. This is also expressed as the sum of the rigid adsorption energy (E_{rig}) and the deformation energy (E_{def}) for the components of adsorbate (**Equation 5.4**).

$$E_{ads} = E_{rig} + E_{def} \tag{5.4}$$

Whilst, the total energy (E_{tot}) corresponds to the sum of E_{ads}, E_{rig}, and E_{def} (**Equation 5.5**).

$$E_{tot} = E_{ads} + E_{rig} + E_{def} \quad (5.5)$$

Here, the energy of the substrate is occupied as zero since the substrate is constrained during simulation. The E_{rig} shows the energy, in kcal/mol, released (or required) when the unrelaxed adsorbate molecules (i.e. prior to the geometry optimization step) are adsorbed on the substrate. The E_{def} reports the energy, in kcal/mol, released when the adsorbed adsorbate molecules are relaxed on the substrate surface. **Table 5.7** also demonstrates the dE_{ads}/dN_i, which explains the energy in kcal/mol, of substrate-adsorbate configurations where one of the adsorbate molecules has been eliminated (BIOVIA, 2016b).

Figure 5.25(b) confirms the trends of adsorption energy distribution (**Figure 5.25(a)**), consistent with the average total energy (**Figure 5.24**). For the overall adsorbate concentrations, the highest adsorption energy is generated by the lowest number of adsorbate loading i.e. 1 molecule (-3.289 kcal/mol), and constantly followed by 5, 10, and 50 molecules (**Table 5.7**). This trend emphasizes that the number of TiO_2 molecules (or concentrations) provide a direct influence upon its adsorption capability onto the FTO surface. The increment of adsorbate concentrations decreases the adsorption energy (**Figure 5.25(b)**) and thus, exhibit more ability to be adsorbed onto FTO substrate surface. This evidence is further elucidated by **Table 5.7** which contains the several energy contributions instead of adsorption energy of each loading molecules.

Table 5.7 Energy distribution (kcal/mol) of TiO_2 adsorptions onto FTO surface.

Loading (adsorbate molecule/s)	E_{tot}	E_{ads}	E_{rig}	E_{def}	TiO_2: dE_{ad}/dN_i
1	-3.289	-3.289	-3.289	0.000189	-3.289
5	-16.793	-16.793	-16.794	0.000881	-3.301
10	-31.356	-31.356	-31.378	0.0213	-2.327
50	-115.672	-115.672	-115.685	0.0136	-1.0545

5.1.3.2 Adsorption of dopamine onto FTO and TiO_2/FTO layer

Upon the MC simulation using selected parameters, the trajectories containing the lowest energy configuration of dopamine (as adsorbate) onto layer I of FTO and layer II of TiO_2/FTO (as substrates) are generated along with the field of distribution for the corresponding substrate (**Figure 5.26**). The layer I (**Figures 5.26(a & e)**) and II (**Figures 5.26(c & g)**) were used to study the adsorption behaviour and energy differences towards electrode modification step. These two layers would be evaluated for the comparison studies in terms of adsorption and binding energies. On the other hands, the two types of concentrations (i.e. 1 and 5 adsorbate molecules) were particularly simulated to investigate the impact of intra/intermolecular energies on the adsorption behaviour as well as assessing the impact of adsorbate concentrations. For the single molecule adsorbate, the dopamine likely adsorbs right above the layer I surface in a planar orientation (**Figure 5.26(a)**), while the different adsorption location is observed for the layer II which dopamine adsorption tends to accumulated at the opposite surface of FTO in a similar planar tendency (**Figure 5.26(c)**). The planar positions of the dopamine at the two studied surfaces may be attributed due to the strong interactions between its benzene ring and the Sn^{2+} of FTO surface *via* ionic bonding i.e. Coulombic force (for layer I) and O^{2-} of TiO_2 opposite surface *via* non-ionic contact i.e.

covalent and H-bondings (for the layer II). Further, upon the increment of adsorbate concentration (i.e. 5 molecules), an obvious difference is shown by layer II which the molecular orientation of dopamine tends to move closer to the surface of TiO_2 (**Figure 5.26(g)**). The adsorption of layer I shows a consistent adsorption region with the lower adsorbate molecule. Herein, the intramolecular energy of dopamine molecules is taken into account and seems to force the dopamine to be adsorbed closer to the TiO_2 surfaces. Indeed, the -OH groups of dopamine may contribute to the intermolecular interactions due to the relatively close distance with the surface of layer I and II (**Figure 5.26(e & g)**).

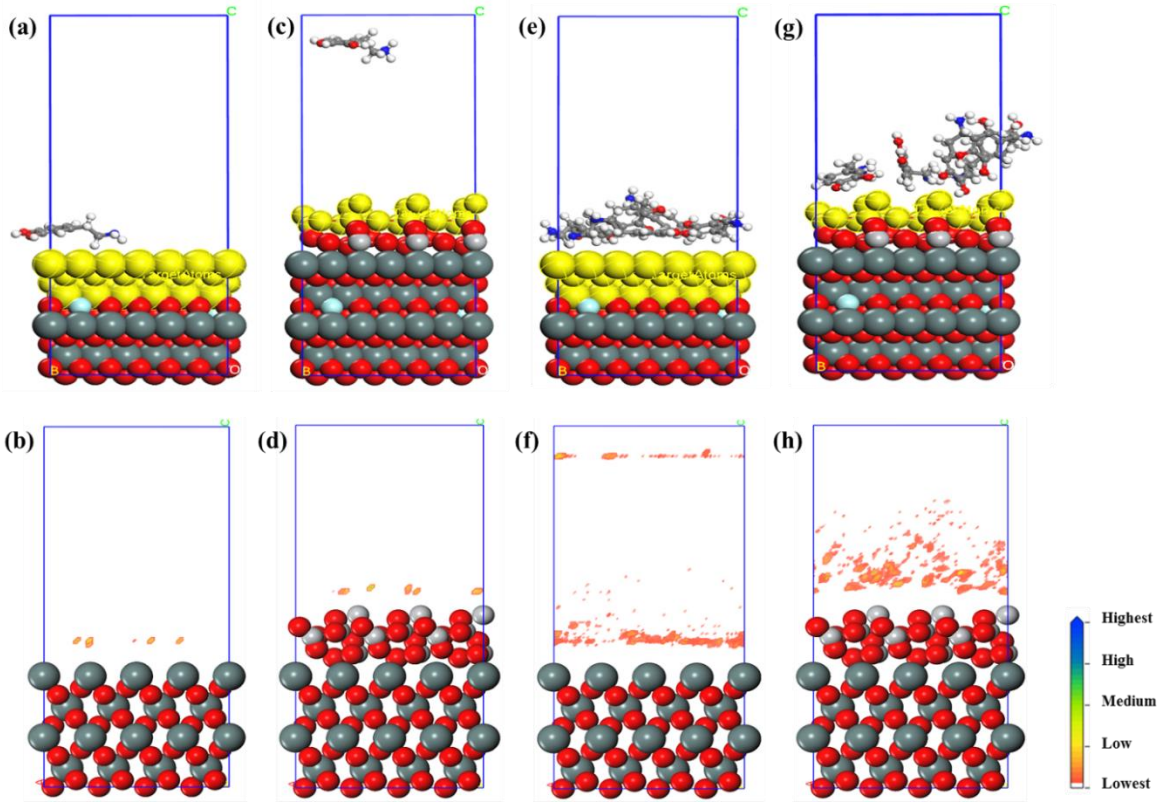

Figure 5.26 The lowest configurations of dopamine onto layer I (FTO) surface comprising of 1 (a) and 5 (e) adsorbate molecule/s, dopamine onto layer II (TiO_2/FTO) surface comprising of 1 (c) and 5 (g) adsorbate molecule/s followed by their favourability comprising of 1 (b) and 5 (f) adsorbate molecule/s for layer I, and 1 (d) and 5 (h) adsorbate molecule/s for layer II.

In terms of interaction characteristic, the ionic bonding within Sn (substrate) and amine group and benzenoid ring of dopamine (adsorbate) may predominantly role in layer I adsorption, while non-ionic bonding is involved in layer II interaction along with the possible contribution of ionic bonding within dopamine -OH groups and Ti atoms. This evidence is supported by the distribution field depicted in **Figures 5.26(b, d, f, and h)**. These figures clearly indicate the preference of dopamine to be adsorbed onto the surface of each substrate comprising of layer I and II. For the adsorption of 5 dopamine molecules (**Figures 5.26(e & g)**), the adsorbate molecules were mixed up onto substrate surface due to intermolecular forces amongst the dopamine molecules. The different of adsorbate concentrations also plays a pivotal role in directing the molecular location of dopamine on the substrate surfaces and this is considerably related to the variation of adsorption energies (**Table 5.8**).

The energy contribution of the adsorption processes comprising of 1 and 5 adsorbate molecule/s are shown in **Figures 5.27** and **5.28**, respectively. These energy parameters consist of total and average energies, *van der Waals*, electrostatic, and intramolecular energies. The five number of cycles are clearly carried out during MC simulations. Consistently, the equilibration phase of both concentrations has been reached upon the first cycle which subsequently continued with a steady total energy of production steps (shown by nearly linear total energy). There is no significant fluctuation observed, suggesting the stability of the system during simulated annealing procedure. Interestingly, the average of total energy varies depending on the substrate system (layer I; FTO and layer II; TiO_2/FTO). For the single dopamine adsorbate, the average total energy of layer I remains lower than layer II. Similar trend is also shown at higher concentration (5 molecules). It may be due to the energy contribution from TiO_2 layer to increase the total energy of the layer II system. It

is further noted that the electrostatic energies are emerged for these particular simulations as the dopamine acts as bioorganic adsorbate (**Figures 5.27 & 5.28**), in contrast with previous simulation employing metal oxide adsorbate i.e., TiO_2 (**Figure 5.24**). This evidence is influenced by the nature of adsorbate molecules which particularly, dopamine remains a tiny biomolecule containing catechol (benzene ring with a couple OH side groups at C_1 and C_2) with a hydrocarbon tail ending in an amine group. This structure can exhibit electrostatic interaction with O atoms of the substrate surface (the electrostatic energies fluctuate in the **Figures 5.27 & 5.28**), while for TiO_2 adsorbate is likely unable to produce electrostatic interaction since its structure as metal oxide molecule (the electrostatic energy remains linear in zero value; **Figure 5.24**). However, more in adsorbate concentrations decreases the average total energy of the systems (**Table 5.8**) indicating that the increment of adsorbate (dopamine) molecules directly affects the total energy of the complex and thus, promote the stability of the optimized systems.

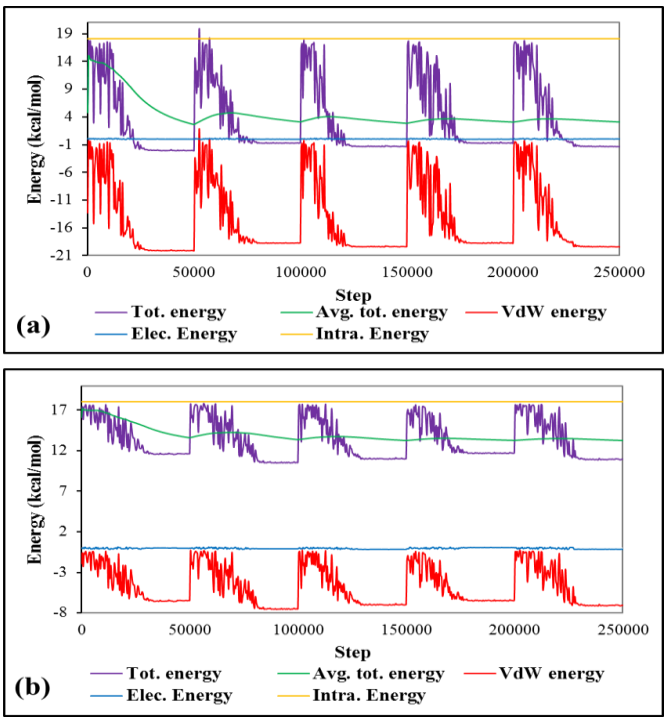

Figure 5.27 Total energy of adsorbed dopamine onto layer I (FTO) (a) and layer II (TiO_2/FTO) (b) comprising of 1 adsorbate molecule.

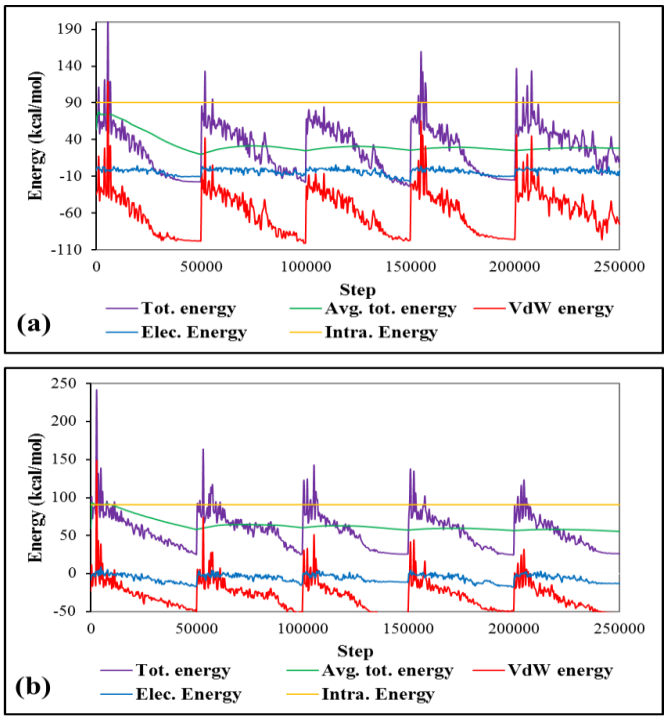

Figure 5.28 Total energy of adsorbed dopamine onto layer I (FTO) (a) and layer II (TiO_2/ FTO) (b) comprising of 5 adsorbate molecules.

The distribution of adsorption energy of layer I and II are given in **Figures 5.29(a & b)**, while the values are shown in **Table 5.8**. These two figures are in accordance with previous trends of average total energies (**Figures 5.27 & 5.28**). For the single dopamine molecule (**Figure 5.29(a)** and **Table 5.8**), the adsorption energy of layer I (-34.010 kcal/mol) is less than layer II (-27.056 kcal/mol). Likewise, the layer I (-189.536 kcal/mol) of higher dopamine concentration remains lower in adsorption energy compared to layer II (-138.783 kcal/mol). These represent the layer I exhibits more efficient energy to attain stable adsorption sites with the adsorbate molecule/s. Further, the increment of dopamine adsorbate seems to elevate the stability of substrate-adsorbate systems. This highlights the importance of concentration to determine the likelihood of dopamine adsorption as well as the stability of the complex systems (low-lying of adsorption energy).

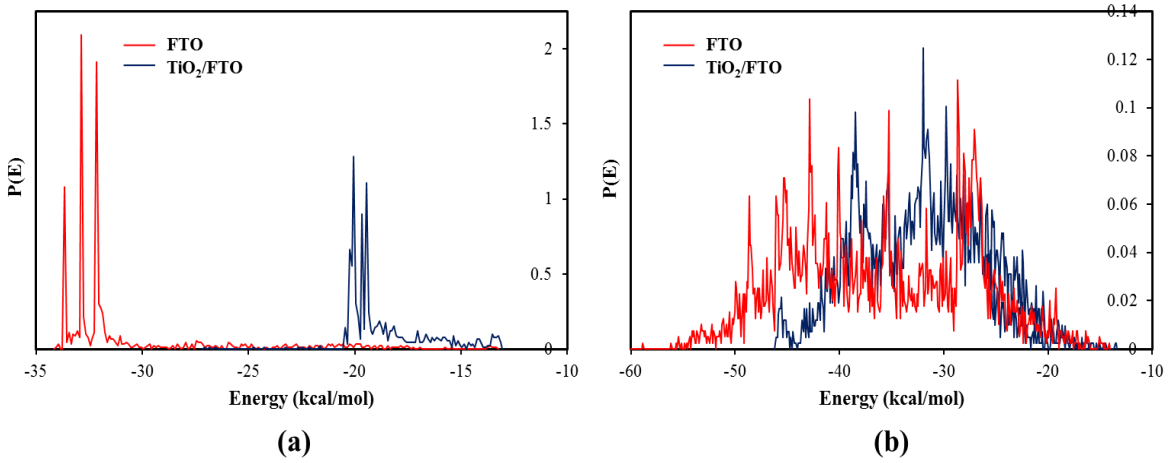

Figure 5.29 Adsorption energy distributions of dopamine onto TiO_2/FTO layer comprising of 1 (a) and 5 (b) adsorbate molecule/s.

Table 5.8 Energy distribution (kcal/mol) of dopamine adsorptions onto layer I and II surfaces.

Structures	E_{tot}	E_{ads}	E_{rig}	E_{def}	DA: dEad/dNi
1 adsorbate molecule					
FTO	-15.939	-34.010	-21.384	-12.626	-34.010
TiO_2/FTO	-8.9854	-27.056	-14.627	-12.429	-27.056
5 adsorbate molecules					
FTO	-99.181	-189.536	-128.695	-60.842	-41.043
TiO_2/FTO	-48.428	-138.783	-76.464	-62.319	-32.699

5.1.3.3 Adsorption of ss-DNA onto FTO, TiO_2/FTO, and DA/TiO_2/FTO layers

In this study, the complete scheme of the electrode was employed in the MC simulations with the ss-DNA as adsorbate. The most stable adsorption sites of the adsorbate and substrate were successfully elucidated and presented in **Figure 5.30**. The single molecule of adsorbate i.e. ss-DNA was particularly used herein due to the limitation on the vacuum slab region which is not able to simulate several large biomolecules. Upon the simulation with overall layers, the ss-DNA is adequately adsorbed onto the surfaces. The simulation on layer I and II demonstrate the planar like adsorption of ss-DNA towards each surface of the substrates. Meanwhile, the ss-DNA in layer III tend to be adsorbed in a slightly perpendicular position. The typical assembly of the surface may influence the adsorbate position upon the MC simulation since the upper side of layer III consist of dopamine molecules which can produce strong H-bond with ss-DNA biomolecules (**Figure 5.30(c & f)**). The ionic interactions may predominantly occur in the formation of stable complex of layer I and II (**Figures 5.30(a & b)**). Moreover, ss-DNA is naturally a highly negatively charged polyelectrolyte contributed from phosphate groups along the chain (Zhang *et al*., 2001). It may also contribute to the molecular position of ss-DNA adsorption. Since there is no intramolecular energy contribution within ss-DNA biomolecules, only intermolecular energy is taken into account

in determining the total energy contributions (**Figure 5.31**). The average total energy remains stable throughout the simulations indicating the stability and reliability of the systems. There are no obvious fluctuations with respect to average total energies. In general, the adsorbate molecule is able to well-adsorbed onto the surface of each substrates (layer I, II, and III).

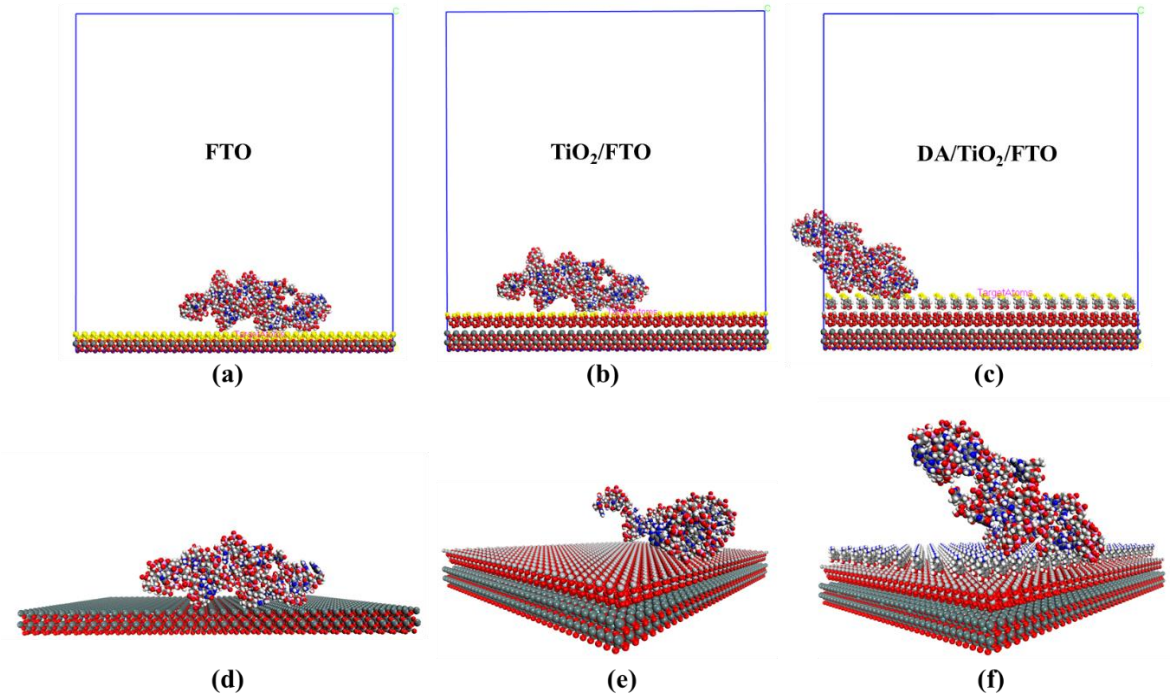

Figure 5.30 The lowest configurations of ss-DNA adsorption onto layer I (FTO), layer II (TiO_2/FTO), and layer III (DA/TiO_2/FTO) comprising of front views (a, b, c) and their orthographic depictions (d, e, f).

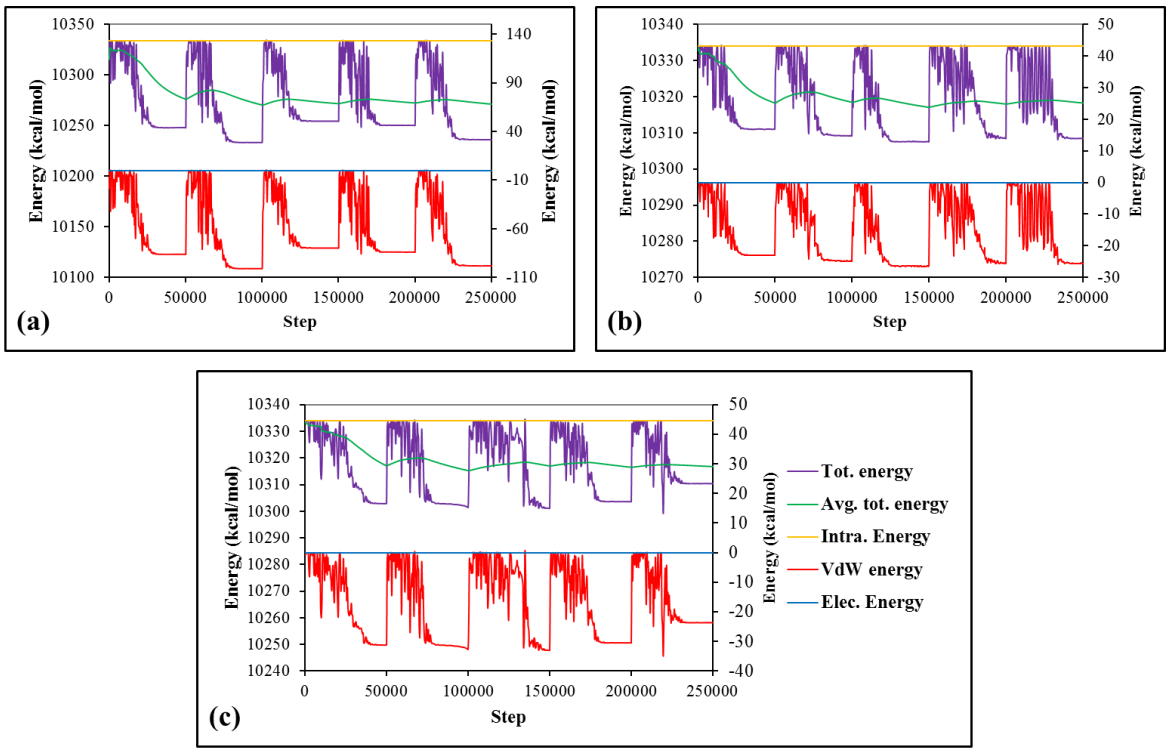

Figure 5.31 Total energy of adsorbed ss-DNA onto layer I (FTO) (a), layer II (TiO_2/FTO) (b), and layer III (DA/TiO_2/FTO) (c). The figure legend of part (c) is also used to other figures.

Further, distributions of adsorption energy comprising of layer I, II, and III are shown in **Figure 5.32**. Single molecule of ss-DNA onto layer I shows the lowest adsorption energy among others. This is merely in consistent with the previous trends of average total energy. Indeed, the trend of adsorption energies is demonstrated as follows: layer I (-2.24 x 10^3 kcal/mol) < layer III (-2.17 x 10^3 kcal/mol) < layer II (-2.16 x 10^3 kcal/mol). This tendency may be due to the energy contribution from adjoined layers i.e. TiO_2 for layer II and TiO_2 and DA for layer III which decrease the E_{ads} and E_{def} of the system (**Table 5.9**). Since the adsorption energy is the sum of E_{rig} and E_{def} energies (see **Equation 5.4**), the trend of both directly determines the adsorption energy values.

Moreover, this result suggests that the layer I exhibits more efficient energy to attain stable adsorption sites with the substrate surface than layer III and II. Likewise, layer III requires less adsorption energy compared to layer II. This emphasizes the direct influence of the appended layer to determine the ability of ss-DNA adsorption onto the electrode surface as well as the stability upon the complex formation (low-lying of adsorption energy). However, these low energy trajectories of MC simulations (i.e. overall studies) were further used as input structures of subsequent MD simulations.

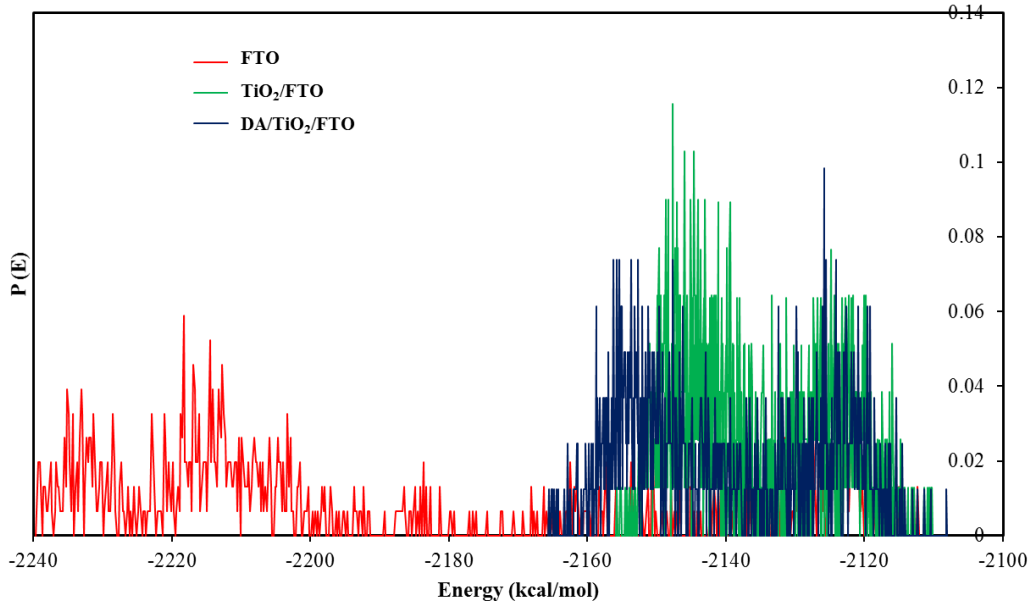

Figure 5.32 Adsorption energy distributions of ss-DNA onto simulated electrode layers.

Table 5.9 Energy distribution (kcal/mol) of ss-DNA adsorptions onto simulated electrode layers.

Substrates	E_{tot}	E_{ads}	E_{rig}	E_{def}	**ss-DNA: dEad/dNi**
FTO	8.09 x 10^3	-2.24 x 10^3	-120.967	-2.12 x 10^3	-2.24 x 10^3
TiO_2/FTO	8.18 x 10^3	-2.16 x 10^3	-25.273	-2.13 x 10^3	-2.16 x 10^3
DA/TiO_2/FTO	8.17 x 10^3	-2.17 x 10^3	-39.920	-2.13 x 10^3	-2.17 x 10^3

5.1.4 Molecular dynamics simulations

5.1.4.1 MD simulations of TiO_2 onto FTO layer

To minimize the computational cost, three types of TiO_2 concentrations were investigated for the formation of TiO_2-FTO electrode complex through MD simulations. **Figure 5.32** shows the MD trajectories upon production steps of TiO_2 molecules on the top of FTO surfaces. The number of atoms on FTO are kept constant through rigid-body constraint for good comparison by not allowing the FTO atoms to inconsiderably interact with TiO_2. This treatment also permits TiO_2 molecules to move along the surface under selected MD parameters (i.e. temperature). In this study, the temperature was set as 298 K in order to get an exact mimic with experiment. Since the FTO bonds were removed for eradicating the unphysical interaction within molecular system, the "ghost" atoms were automatically appeared at the top of periodic cells upon the Forcite (MM)-based geometry optimization. These atoms have no influence on the simulations owing to their zero-nuclear charges as well as zero electrons. They act as probes of the local effective magnetic field at their positions (Wang *et al*., 2013). In terms of simulation environment, the vacuum-based MD's was chosen in consistent with previous studies (Mdluli *et al*., 2011, Sosibo *et al*., 2011, Chen *et al*., 2012, Chen *et al*., 2015a, Bahramian, 2015, Fereidoon *et al*., 2015). The use of gas phase MD's was considerable due to several motives as follows: to minimize the computational cost due to employment of large number of atoms in simulations, relatively low capability of the software to simulate MD with solvated systems, and the ability of gas-phase simulations to provide accurate prediction to the molecular behaviour of the complex systems containing inorganic materials.

The MD simulations were carried out using the last (rather 'stable') trajectories of MC simulations. Interestingly, it can be assumed that equilibration stage has been reached prior to MD runs (Chen and Roux, 2015). However, the geometry optimization was still required as *a priori* treatment to ensure the convergence of the system during MD simulations. After the MD simulations were performed for all models, it was observed that TiO_2 molecules were expanded evenly on the surface of FTO cluster. The single molecule of TiO_2 likely move away from the surface (**Figure 5.33(a)**), while the evenly distributed molecules were captured at higher concentrations (i.e. 5 and 10 molecules of TiO_2; **Figures 5.33(b & c)**). The presence of intramolecular forces which exist amongst the TiO_2 molecules and intermolecular energy within TiO_2 and FTO cluster play substantial roles in distributing the molecular interaction of TiO_2, and this is considered as the potential factor (Mdluli *et al*., 2011) that influences the growth of FTO nanocluster.

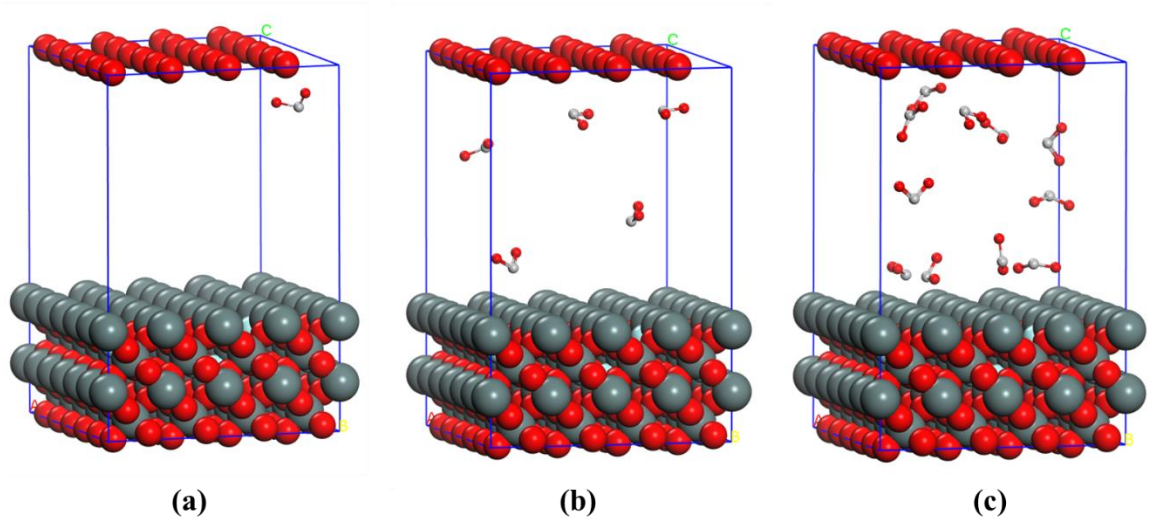

Figure 5.33 MD snapshots of TiO_2 interaction with FTO layer comprising of 1 (a), 5 (b), and 10 (c) adsorbate molecules.

For the total energy during 100 ns simulation time, the trend remains steady and no significant energy fluctuations are observed with respect to the three concentration models

(**Figure 5.34(a)**). In general, this also can be adjudicated that the systems (comprising of each adsorbate molecules) are energetically stable during MD simulations. Similarly, the temperature profiles also behave steadily throughout the simulations (**Figure 5.34(b)**). Since the canonical ensemble (NVT) was used in equilibration and production steps, the temperature of the system is undergoing to fluctuate around a stable average and shows no obvious fluctuations lead to system's error. Overall, these couple parameters corroborate the reliability of the simulated systems. The use of Andersen thermostat plays an important role herein. Further, the thermostat has been able to control the stability of the temperature specifically for nanomaterials-based simulations (Kornherr *et al*., 2004, Christianson and Schmidt, 2015, Agusta *et al*., 2016).

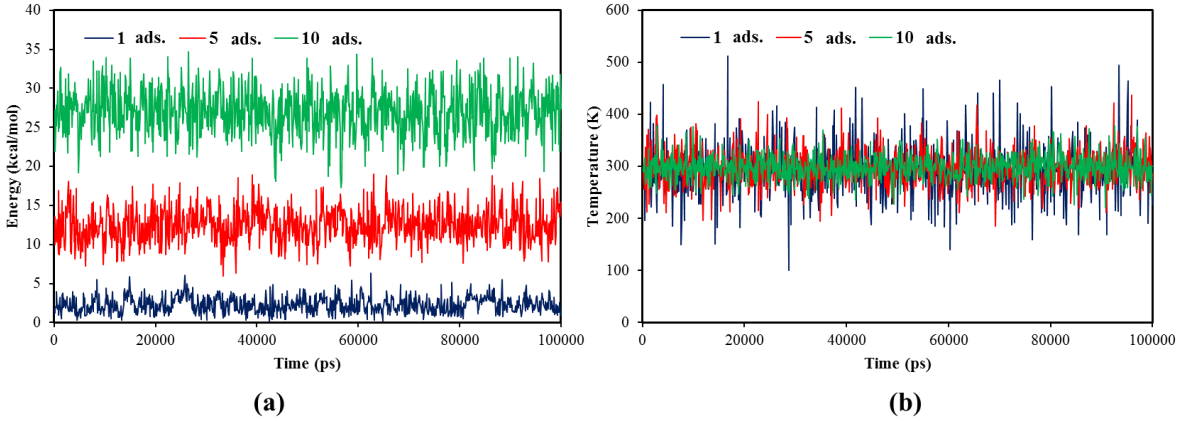

Figure 5.34 Total energies (a) and temperature profiles (b) of TiO_2 interactions with FTO layers.

It is further important of the relative molecule-to-surface orientation for the TiO_2-FTO complexes (at selected molecular ratio/concentrations). From **Figure 5.33**, the orientation of TiO_2 is relatively perpendicular to FTO surface except for the single TiO_2 molecule where the molecule moves away from the surface. However, this anomaly was subjected from the initial position prior to starting the MD simulation (i.e. preceding MC trajectory). To the best

of our knowledge, no computational investigation on the TiO_2 molecule interaction towards FTO surface has been performed. A recent experimental study (Li *et al*., 2015) showed the orientation of the TiO_2 nanosheets which stand perpendicularly to the surface of the FTO substrate, in line with the present computational MD simulations. Another study has shown similar results with the TiO_2 nanorods grown perpendicular to the FTO substrates (Liu *et al*., 2015a). The molecule-to-surface relative orientation can be tailored as a potential parameter of the nanomaterials growth and allows the emergence of the electrochemical performance (Li *et al*., 2015).

The interaction of TiO_2 molecule and the substrate surface are attributed to strong interactions between resembled atoms (Ti and O) in adsorbate and the substrate surface. Therefore, the length density profile (so-called relative concentration or concentration profile) is appropriate parameters to be examined. **Figure 5.35** shows the relative distance of the Ti and O atoms towards the substrate surface. For the single TiO_2 molecule, it was observed that 8.120% Ti atom is 0.63 Å closer on the surface of FTO cluster, whereas 6.502% O atoms (**Figure 5.35(a)**). Whilst, the maximum relative concentration of O atoms (2.274%) was observed at 9.475 Å closer than Ti atoms (for the corresponding 5 adsorbate molecules) (**Figures 5.35(b)**). However, the analogous Ti peak is also observed at the exactly similar distance with O which showing the 2.925% concentration at the recorded distance i.e. 5.369 Å (0.650 Å closer to the surface than O) (**Figure 5.35(b)**). A similar trend is also obtained when the TiO_2 concentration was increased to 10 molecules (Ti concentration is 0.869% higher than O in the exactly similar distance to the surface i.e. 11.685 Å) (**Figure 5.35(c)**). This observation suggests the important role of Ti atoms in the intermolecular interaction between

TiO_2 and FTO surface which may be triggered by strong ionic force between both substrate (O or F atoms) and adsorbate (Ti atoms) systems.

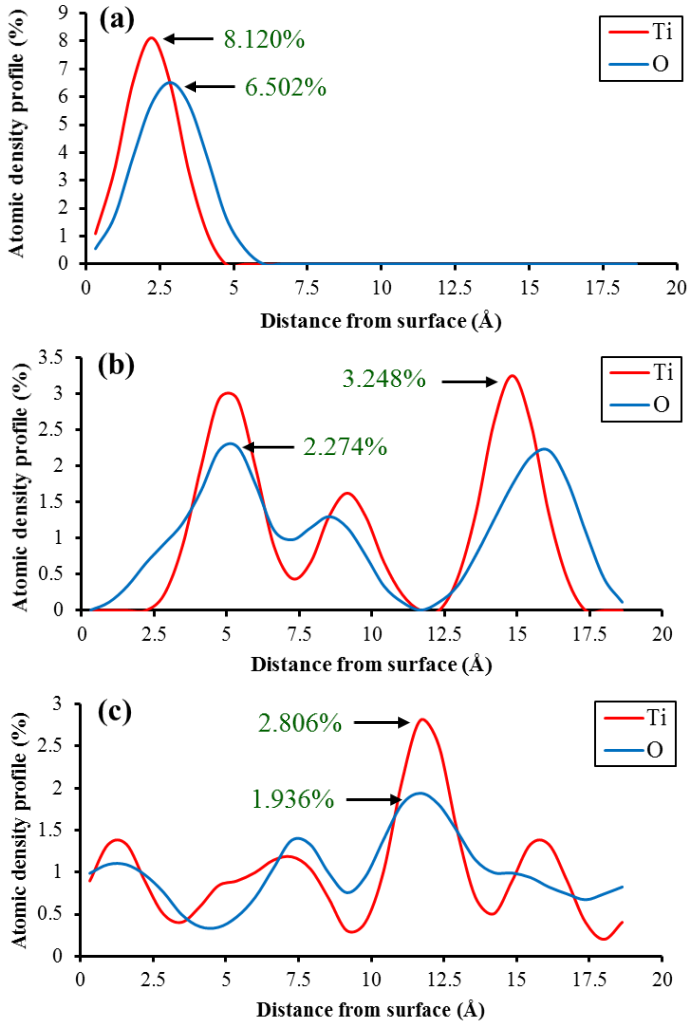

Figure 5.35 Concentration profiles of TiO_2 interactions with FTO surfaces comprising of 1 (a), 5 (b), and 10 (c) adsorbate molecules.

The further analysis involved the total potential energy components derived from the trajectories of MM-Forcite calculation which responsible for the deeper insight into the interaction mechanism of TiO_2 (as adsorbate or ligand) and FTO (as substrate or "receptor"). The potential energies were defined for the all three adsorbate molecules. The structure

coordinates combined with a UFF force field generate an *energy expression* describing the potential energy surface of a particular structure as a function of its atomic coordinates (**Equation 5.6**).

$$E_{\text{total pot.}} = E_{\text{val.}} + E_{\text{cross-term}} + E_{\text{nb}} \quad (5.6)$$

Whereas, $E_{\text{total pot.}}$ is the total potential energy, while $E_{\text{val.}}$ is the valence energy which is generally accounted from the *diagonal* terms of bond, angle, torsion, inversion, and Urey-Bradley. $E_{\text{cross-term}}$ corresponds to the cross-term energy for such a correction factor as bond or angle distortions produced by nearby atoms. E_{nb} is the non-bond energy including *van der Waals*, electrostatic, and H-bond (BIOVIA, 2016b). The energies associated with the formation of FTO – TiO_2 complexes were derived as shown in **Figure 5.36** comprising of 1 (part *a*), 5 (part *b*), and 10 (part *c*) adsorbate molecules. For the overall depictions, the energy profiles show that the total potential energies were fluctuating around the stable average suggesting the satisfied stability of the system throughout simulations. The valence and *van der Waals* energies were contributing towards the total potential energies in equivalent quantities, therefore, the both energies were observed in the equal position or contribution towards FTO-TiO_2 complexes (throughout overall concentrations).

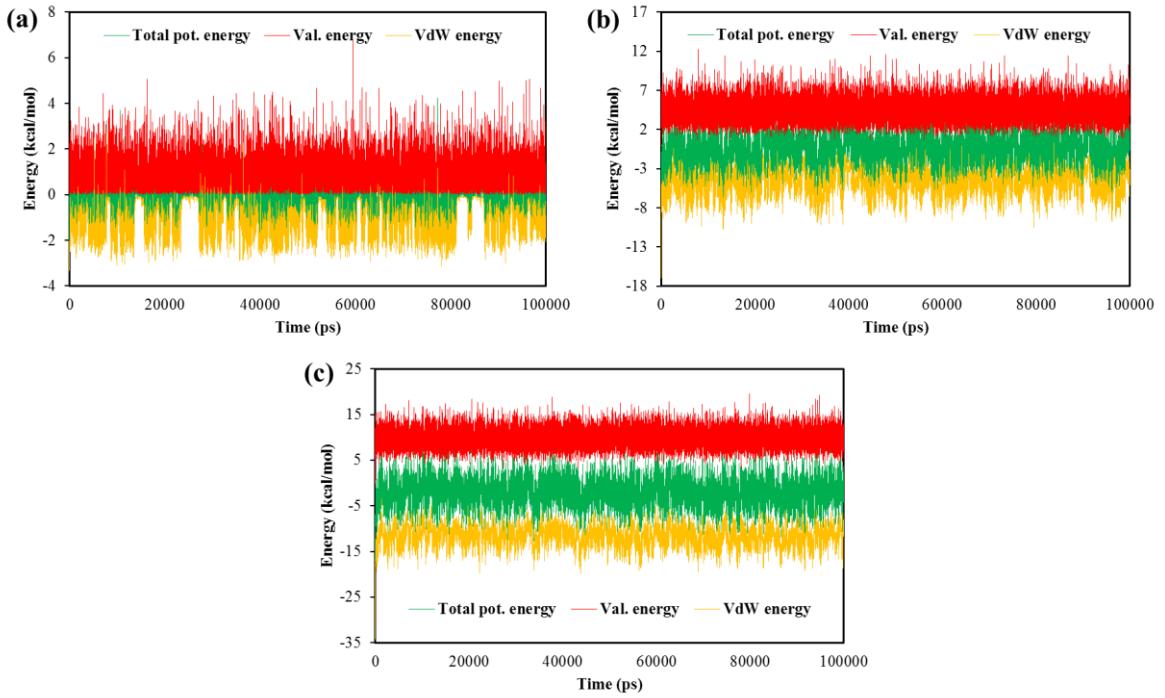

Figure 5.36 Potential energy profiles towards 1 (a), 5 (b), and 10 (c) TiO_2 adsorbate molecules onto FTO substrate.

5.1.4.2 MD simulations of dopamine onto FTO and TiO_2/FTO layers

Figure 5.37 shows the MD trajectories (after 100 ns simulation time) of dopamine molecules onto the surface of FTO (layer I; **Figures 5.37(a & c)**) and TiO_2/FTO (layer II; **Figures 5.37(b & d)**). The use of TiO_2/FTO cluster (at the substrate position) was intended to mimic the experimental electrode at the second step of modification, while FTO cluster was considered as a comparison. Herein, the two types of concentrations were employed to explore the role of intramolecular energy between dopamine in interfering their interaction sites and behaviour. For the overall models, the dopamine molecule/s likely interact with the surface except for the single dopamine molecule onto TiO_2/FTO surface which preferably interacts with 'ghost' atoms of O. Since the zero-nuclear charge and -electrons of "ghost" atoms have, this interaction can be neglected (i.e. there will be no typical interaction within

these sites) or may correspond to the interaction with opposite of TiO_2/FTO layer in periodic boundary cells. It can be assumed that single dopamine moves away from the surface due to the intermolecular steric hindrance occurrence. However, other models demonstrate that the dopamine molecule/s interacts well with the nanoparticle surface, predominantly through planar orientations. Interestingly, the molecular distributions of higher dopamine concentration (**Figures 5.37(c & d)**) end to move closer to each other (instead of moving closer to the surface). It indicates the potential role of intramolecular energy within dopamine molecules to their interaction with nanomaterial surfaces. This energy is considerable factor that influences the growth of TiO_2/FTO nanocluster.

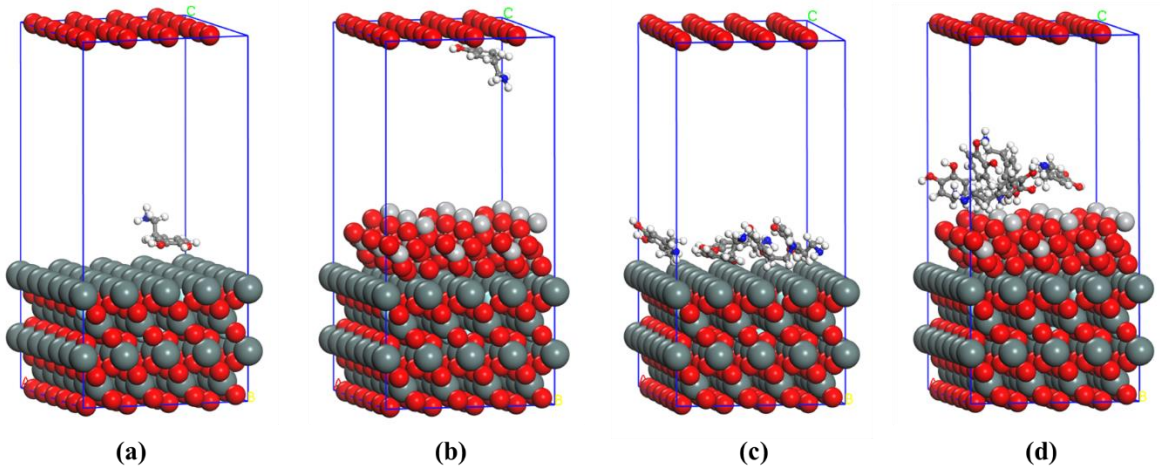

Figure 5.37 MD snapshots of dopamine interactions with FTO layers comprising of 1 (a) and 5 (c) adsorbate molecule/s and with TiO_2/FTO layers comprising of 1 (b) and 5 (d) adsorbate molecule/s.

For the total energy during simulations (**Figures 5.38(a & c)**), the peaks show a stable fluctuation in average areas. There is no significant error observed in the simulations. This indicates that the system remains physically stable during simulations and thus, the trajectories are reliable for the further analysis. Interestingly, the difference between average total energies of single dopamine interaction comprising of both studied layers (**Figure**

5.38(a)), remains to be lesser (or narrower) than five molecules of dopamine (**Figure 5.38(c)**). The role of intramolecular energy within dopamine molecules may contribute to total energy of the system. On the other hand, the profiles of temperature (**Figures 5.38(b & d)**) show steady fluctuation indicating the stability of the temperature during canonical ensemble (NVT) simulations. Since the temperature was set at 298 K to better mimic the experimental conditions, the Andersen thermostat seems to successfully maintain the temperature profile of the systems.

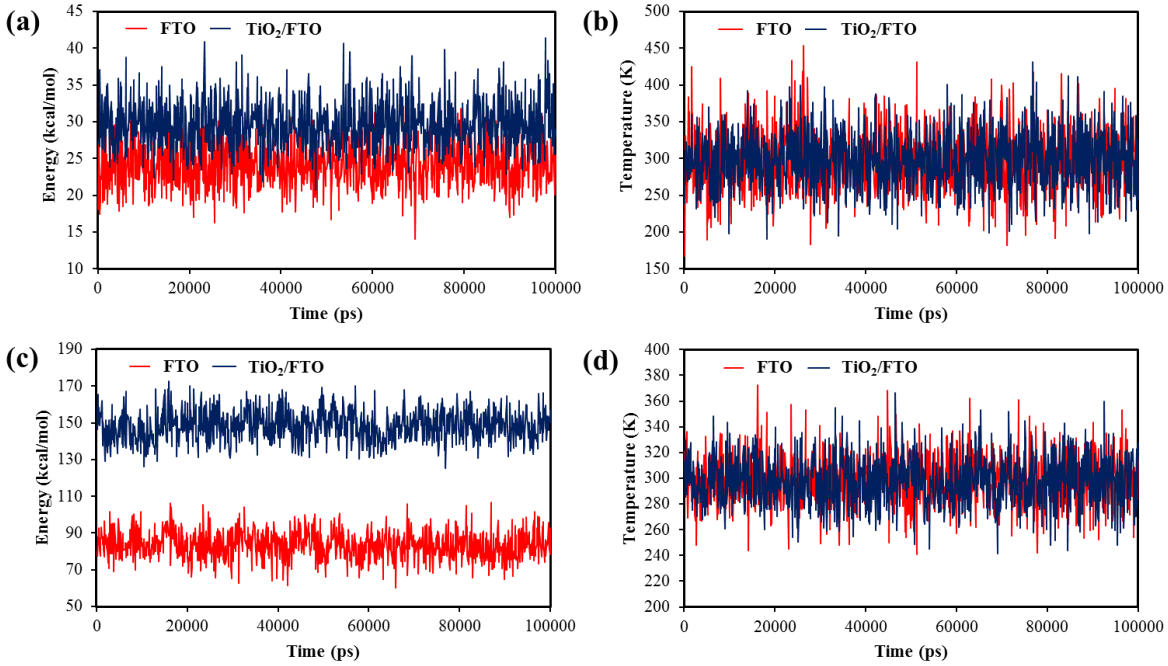

Figure 5.38 Total energies and temperature profiles of dopamine interactions with FTO and TiO_2/FTO layers comprising of 1 (a, b) and 5 (c, d) adsorbate molecule/s, respectively.

Further analysis was carried out using relative concentration showing the abundant of responsible atoms or functional groups towards the surface. Dopamine has been chosen as a chemical linker because of several considerations as stated in the previous section (see **Chapter 2; Literature Review**). Briefly, dopamine is capable to strongly bind with metal

oxide surface through the two -OH groups and is easy to interact with other biomolecules, and forming organic-inorganic hybrid materials. Several studies have established that the reduced metal coordination of metal oxide surface leads to easy metal-ligand linkage (Chen *et al*., 1997, Farges *et al*., 1997). Due to this fact, the two -OH groups of dopamine were selected as the "probe" of the analysis. The concentration profile of these functional groups towards the FTO and TiO_2/FTO surfaces are shown in **Figure 5.39**. For the single dopamine interaction, the unique "twin" peaks are observed in the FTO and TiO_2/FTO surfaces in which both have comparable relative concentrations. Similar concentration is observed (i.e. 4.060%) on the surface's models in which the -OH groups of dopamine shows 0.345 Å closer towards FTO compared to TiO_2/FTO surface (**Figure 5.39(a)**). In contrast, when the higher concentration was employed, the different trend is observed. The relative concentration of dopamine's -OH groups towards TiO_2/FTO surface is obtained to be 2.770% and remains 8.388 Å closer to the surface than 2.222% of FTO (**Figure 5.39(b)**). This study emphasizes the importance of -OH groups of dopamine to interact with surface atoms mainly to metal site *via* metal coordination bonding type. Moreover, the favourability of TiO_2/FTO (rather than FTO layer) to interact with dopamine (in higher concentration) may be attributed from the intramolecular energy between dopamine molecules. Whilst, the pushing away of dopamine molecule towards TiO_2/FTO (**Figure 5.37(b)**) may contribute to the trend of "anomaly" obtained at single molecule observation of concentration profile. The presence of steric hindrance may cause this phenomenon.

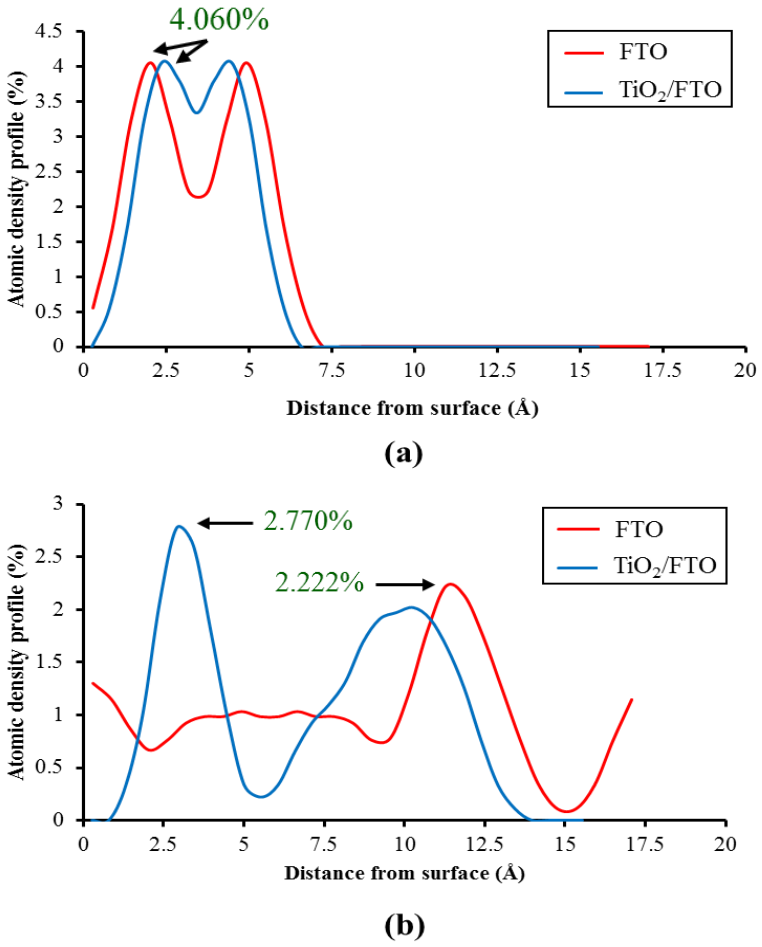

Figure 5.39 Concentration profiles of dopamine interactions with FTO and TiO_2/FTO layers comprising of 1 (a) and 5 (b) adsorbate molecule/s.

The potential energy analysis showed that the total potential energies across all models remain steady in fluctuation during dynamics simulations. Three potential energy contributors were elucidated herein, i.e. electrostatic, valence, and *van der Waals* energies. The electrostatic energy was occurred, due to the organic nature (CH skeleton) of the adsorbate (i.e. dopamine). This is in contrast with the first layer simulations (FTO-TiO_2 complex) due to the metallic nature of the adsorbate i.e. TiO_2, and thus unable to generate electrostatic energy. For the layer I interaction with single dopamine molecule (**Figure 5.40(a)**), the dynamics of FTO - DA complex shows the stable simulations in which the *van*

der Waals energy was contributing towards the total potential energies to a greater extent, as compared to valence and electrostatic energies. The more visible difference is shown with the greater concentration of dopamine (**Figure 5.40(b)**). Likewise, a similar trend of potential energy profiles was elucidated for the layer II simulations (**Figures 5.40(c & d)**). This indicates that *van der Waals* energy may dominantly role in dopamine and electrode surface interactions suggesting the physisorption evidence. The presence of electrostatic energy (i.e. H-bond) may also attributed since the energy profiles were shown in negative areas suggesting energetically favourable interactions towards the complex systems. In addition, the valence energy may confirm the possible interaction within -OH functional groups of the dopamine and Ti atoms of the TiO_2 surfaces (Syres *et al.*, 2010).

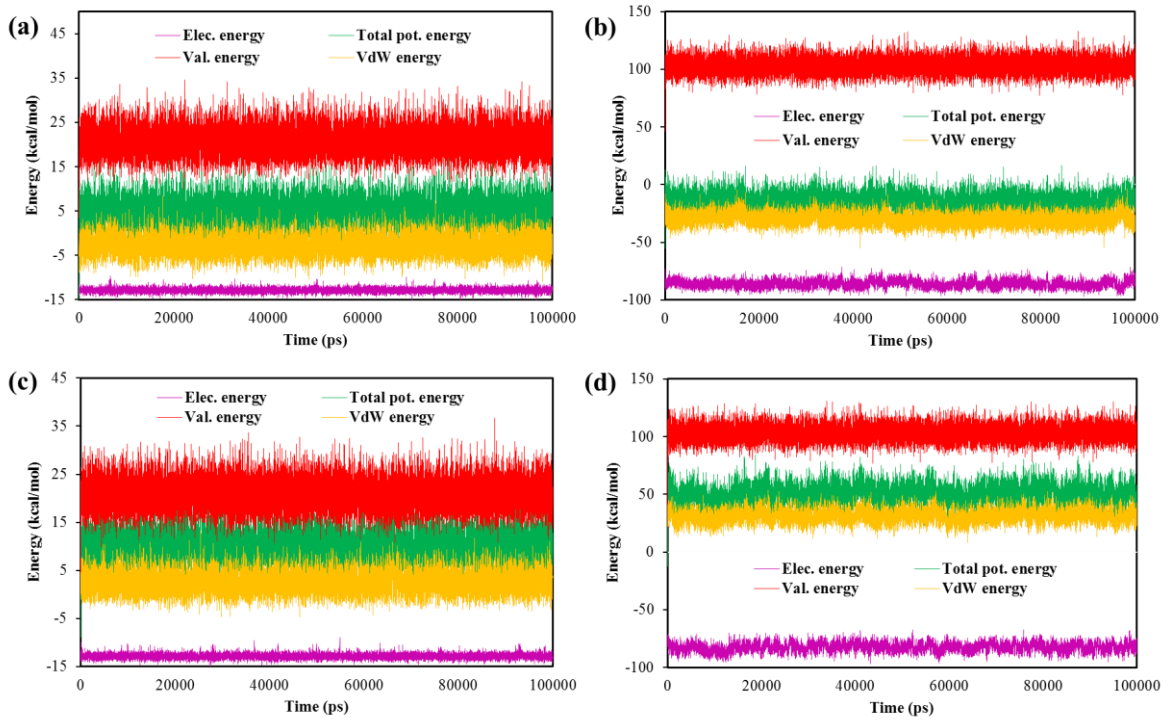

Figure 5.40 Potential energy profiles of FTO - DA complexes composing of 1 (a) and 5 (b) adsorbate molecule/s, and TiO_2/FTO - DA complexes composing of 1 (c) and 5 (d) adsorbate molecule/s.

5.1.4.3 MD simulations of ss-DNA onto FTO, TiO_2/FTO, and DA/TiO_2/FTO layers

At this stage, the MD simulations were required to reproduce the full scheme of layer-by-layer electrode assembly. The shorter simulation time was particularly used in this study. Since the employment of large-size cluster of the substrate-adsorbate complex (up to 33120 atoms in total of ss-DNA and DA/TiO_2/FTO layer), the total simulations time were reduced to 10 ns in order to diminish the cost of computational simulations (i.e. time and system capability). **Figure 5.41** depicts the stable trajectories of ss-DNA interactions with layer I, II, and III, respectively. Three different models were employed to observe the different binding energies and therefore, attributed to the favourability towards electrode constructions. From these depictions, the obvious alterations are occurred at the three employed models, subjected from their initial bodies and last MD trajectories. For the layer I (**Figure 5.41(a)**), the conformation of ss-DNA seems to be converged and planarly interacts with the surface of FTO. It suggests the escalating event of intermolecular interactions within ss-DNA and FTO surface. Unlikely, the ss-DNA conformation is changed towards more compact in the case of TiO_2/FTO surface (**Figure 5.41(b)**) indicating the reducing of intermolecular interactions. An interesting phenomenon is obtained from the full scheme of the electrode (DA/TiO_2/FTO) layers in which the biomolecule conformation tends to adsorb onto the third electrode layer containing dopamine arrays (**Figure 5.41(c)**). The non-bonding interactions seem to predominantly role herein (since the both interfaces are organic materials; DA and ss-DNA). In addition, the whole snapshots of the time-based trajectories of each layer are shown in **Appendix I**.

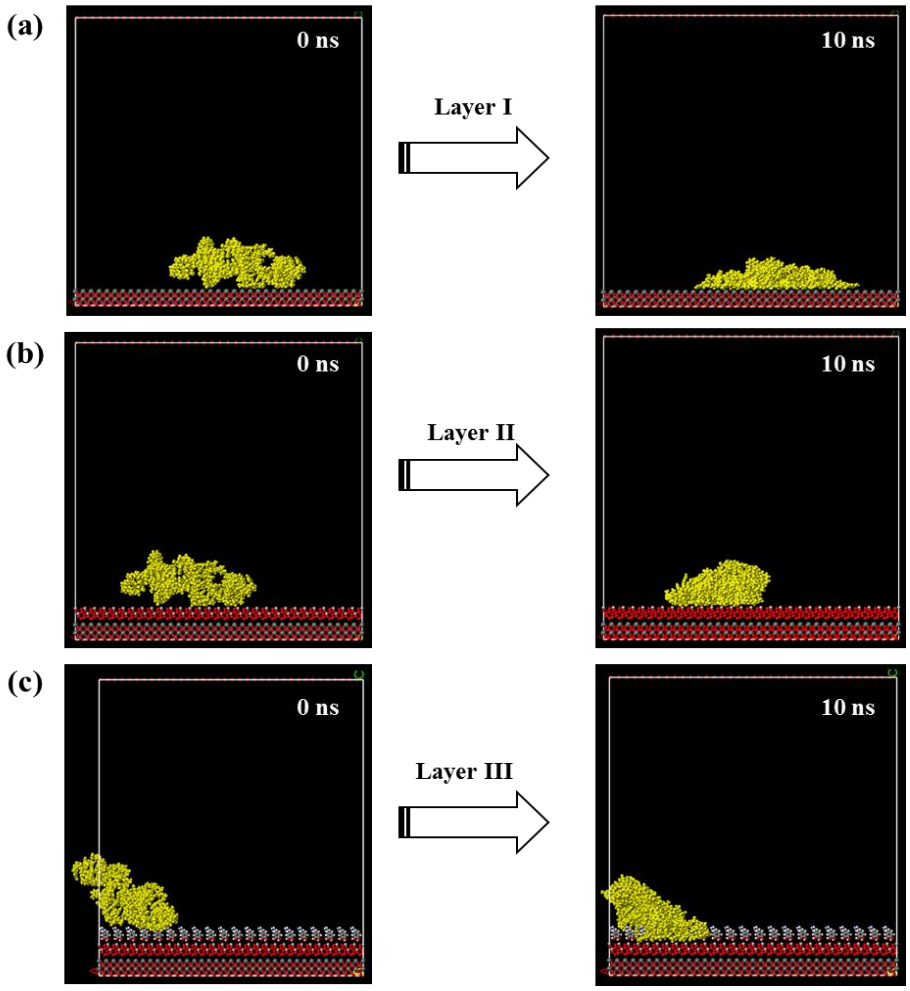

Figure 5.41 Comparison of MD trajectories for FTO (a), TiO_2/FTO (b), and DA/TiO_2/FTO (c) layers upon ss-DNA interactions.

The stability and change in overall molecular conformation of the oligonucleotide during the simulations can be monitored by radius of gyration (Rg) (Junjun *et al.*, 2009). The Rg diagram (**Figure 5.42**) suggests that ss-DNA remains in its compact form over the course of simulations. The overall Rg values (Å) of layer II (TiO_2/FTO) remains to be the lowest followed by layer III (DA/TiO_2/FTO), and layer I (FTO) except for the initial fluctuations i.e. equilibration step. The presence of dopamine molecule induces the system to be energetically active, as revealed at higher gyration of layer III upon layer II. However, the

Rg trend shown in layer II is relatively not stable enough suggesting the obvious change in ss-DNA conformation upon the initial fluctuations. The better (in stability) conformations are addressed to the layer III and I which shows more stable fluctuations during production step. This, in general, displays an acceptable stability and compactness profile of ss-DNA towards electrode layers and emphasizing the obvious change in ss-DNA conformity throughout simulations time.

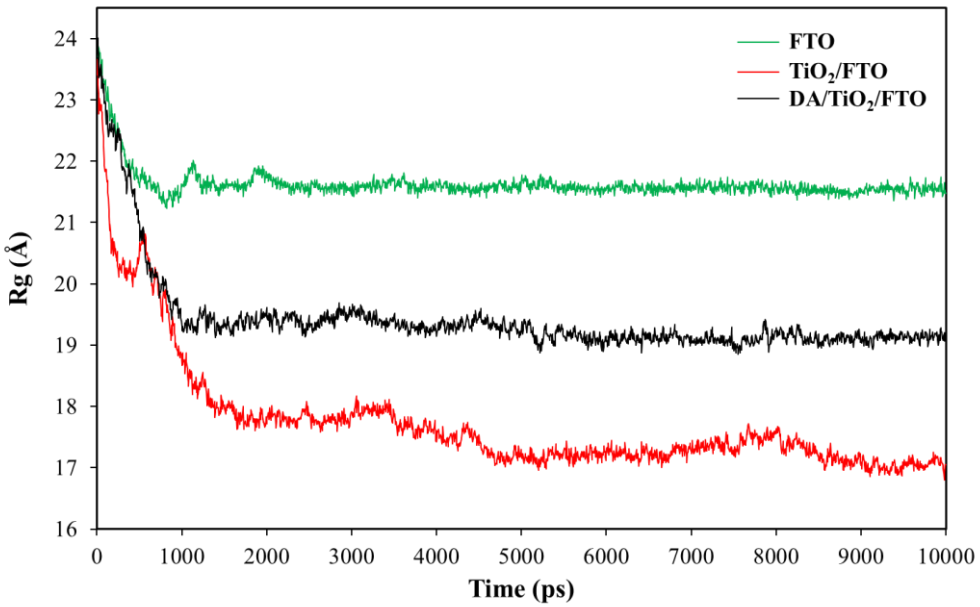

Figure 5.42 Rg of ss-DNA interactions with FTO, TiO_2/FTO, and DA/TiO_2/FTO layers.

Considering the in-depth stability of the system, the total energy and temperature profile are two reliable parameters to be examined. The total energy of the model's system is shown in **Figure 5.43(a)**, while temperature profiles have been elucidated comprising of layer I (**Figure 5.43(b)**), layer II (**Figure 5.43(c)**), and layer III (**Figure 5.43(d)**). The total energy of overall layers remains to be physically valid i.e. there is no systematic drift in the value. The temperature profiles also emphasize the reliability of the system since the overall layers

provide relatively stable temperature in 277 K. The use of 277 K is due to the use of similar parameter while the ss-DNA solution were dipped overnight at 4°C temperature experimentally. In consistent with the previous MD's, the profiles show fluctuations in average values and no significant error was recorded. The Andersen thermostat seems to appropriately maintain the temperature of the systems.

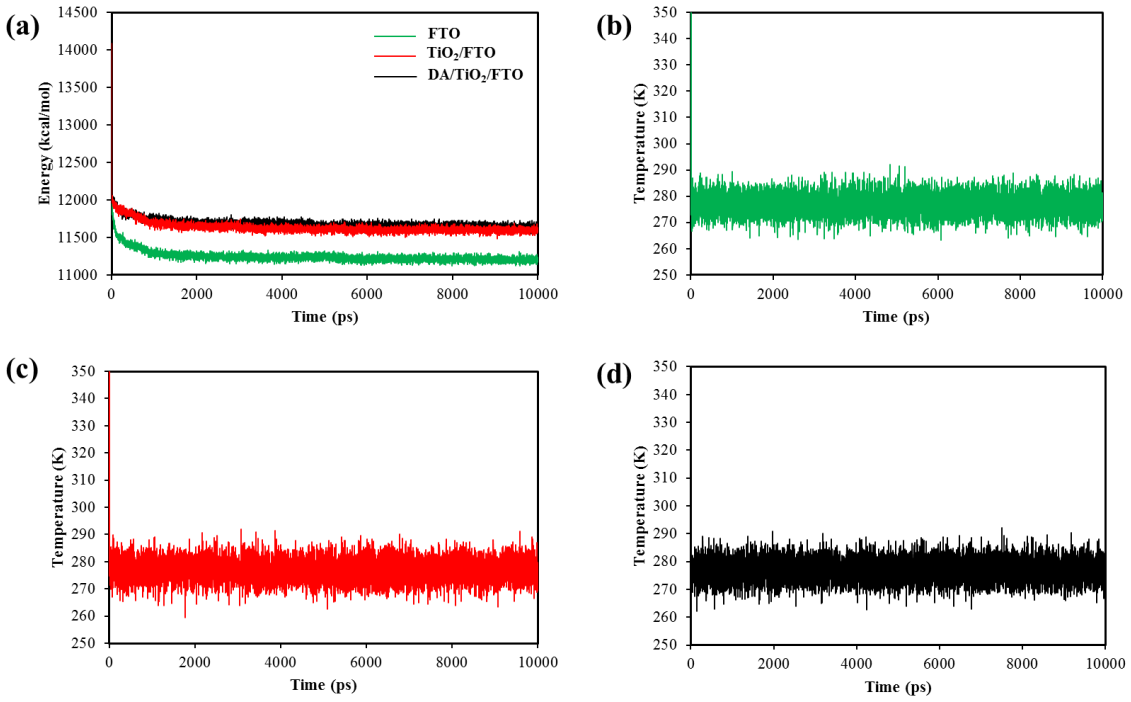

Figure 5.43 Total energies of overall layer systems (a) and temperature profiles of ss-DNA interactions with FTO (b), TiO_2/FTO (c), and DA/TiO_2/FTO (d) layer surfaces.

Since the concentration profile is one of the pivotal post-analysis upon the MD simulation of nanomaterials, **Figure 5.44** depicts the relative concentration of -COOH functional group towards three different substrate models (FTO, TiO_2/FTO, and DA/TiO_2/FTO). According to the experimental methodology, the ss-DNA has been modified at 5' end region and was intended to attach dopamine specifically at amine group. Therefore, this phenomenon was validated computationally *via* concentration profile analysis, capable of showing the relative

concentrations and distances of 5'end -COOH towards the layer surfaces including perpendicular dopamine as the outermost interface for layer III. The maximum relative concentrations of -COOH are observed as follows: DA/TiO_2/FTO (80.426%, 147.807 Å) > TiO_2/FTO (66.633%, 24.790 Å) > FTO (71.526%, 72.711 Å). While considering the distance towards the surface, the TiO_2/FTO remains to be the lowest among others, followed by FTO and subsequently DA/TiO_2/FTO. This trend may be due to the strength of intermolecular interactions in which for the FTO and TiO_2/FTO, the interactions are dominated by ionic bonding. Whilst, the interactions towards DA/TiO_2/FTO are governed by non-ionic bonding i.e. strong H-bond, covalent, weakly *van der Waals* etc. The large surface area may also be considered i.e. FTO and TiO_2 have entirely large surface areas compared to dopamine arrays (at DA/TiO_2/FTO). However, the highest concentration observed in DA/TiO_2/FTO highlights the functionality of the -COOH functional group to interact with the layer III surface, although the distance remains to be overlooked. It is further noted that the contributions of other residues may also contribute to the intermolecular interactions within ss-DNA and corresponding substrate layer/s i.e. guanine bases as reactive sites of the ss-DNA.

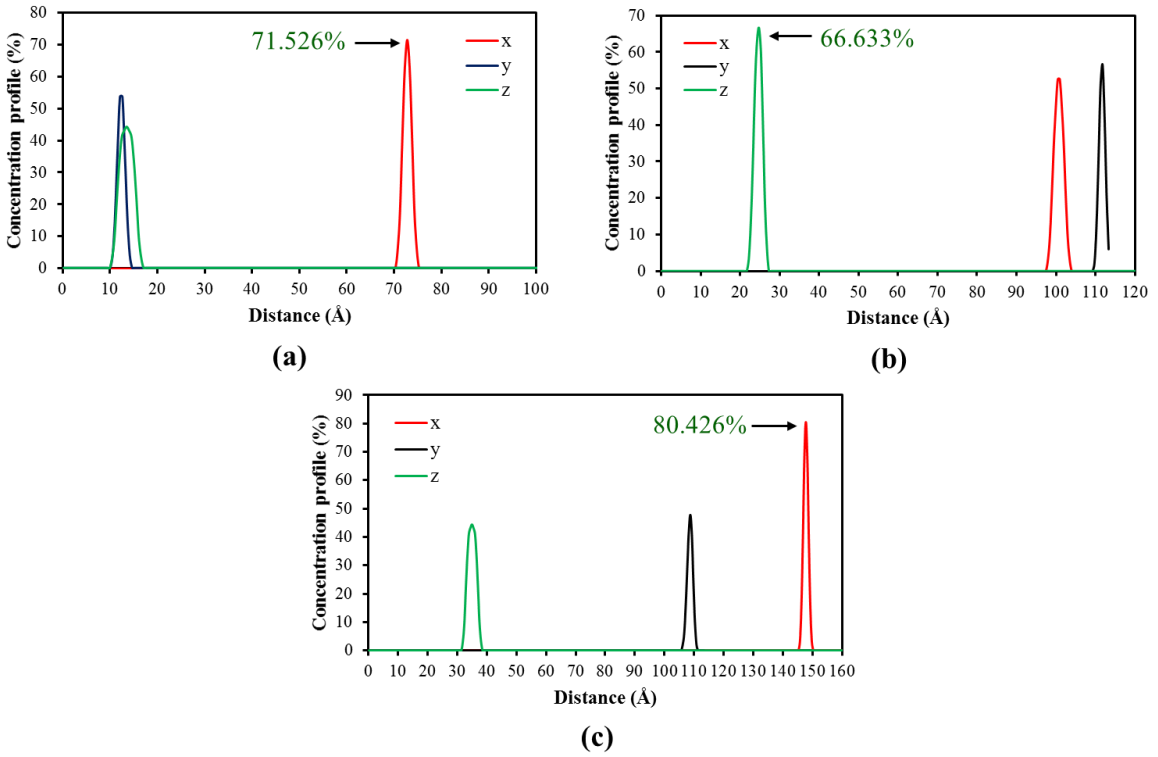

Figure 5.44 Concentration profiles of single ss-DNA molecule interactions with FTO (a), TiO_2/FTO (b), and DA/TiO_2/FTO (c) layers (**x**: (100), **y**: (010), **z**: (001) typical surfaces).

The potential energy parameters of ss-DNA interactions have been elucidated to observe the responsible energies for the ss-DNA and substrate complex surfaces. Three energies were generated from the post-dynamics analysis of MD simulations i.e. total potential energies, valence, and *van der Waals* energies. **Figure 5.45** shows stable fluctuations of the energy functions without any obvious error. The valence energy seems to contribute towards total potential energy to a greater extent as compared to *van der Waals* energy. This evidence suggests the chemisorption of 5'end carboxyl ss-DNA towards electrode surface. It may be associated with the negatively charged ss-DNA structure attributed from its sugar phosphate backbone. The energy contributions of layer I, II, and III remain similar, therefore difference in surface layers does not interfere to the potential energy profiles. The negative values

obtained at *van der Waals* energies may also contribute towards the energetically favourable complex interactions.

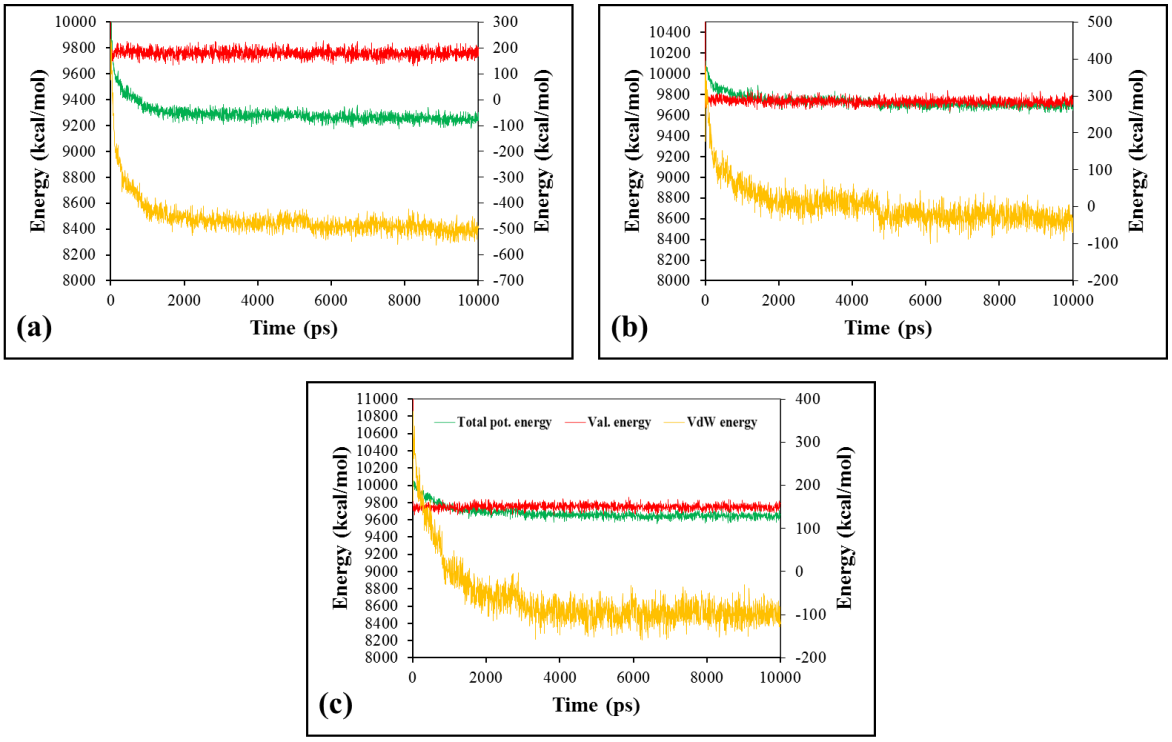

Figure 5.45 Potential energy profiles of FTO - ss-DNA (a), TiO_2/FTO - ss-DNA (b), and DA/TiO_2/FTO – ss-DNA (c) complexes. The figure legend of part (c) is also used to other figures.

5.1.4.4 Binding energy

The layer-by-layer electrode assemblies have been successfully elucidated through computational modeling (i.e. MDs), thus the binding energies were carefully determined towards all models. Due to the use of large-scale substrate-adsorbate systems, i.e. the electrode layers along with molecule or biomolecule adsorbates comprising of organic and inorganic structures, it has been considerably opted to discover the total energy of each trajectories upon the MD simulations. The binding energies were calculated according to the **Equation 4.1** (see **Chapter 4; Materials and Methods**) embracing of the current

tremendous computational demand. The total energies of each reactants (i.e. substrate structures and adsorbate molecules) and the end products (i.e. substrate-adsorbate complexes) were contributed towards binding energy values using classic and pragmatic approaches (Ashaduzzaman *et al*., 2017). Indeed, the total energy for each layer system is defined in the **Equation 5.6**. **Table 5.10** shows the calculated binding energies for overall substrate-adsorbate systems. The negative eigenvalue binding scores have been computed throughout all models showing stable complex formations. These negative values also indicate the attractive or strong adsorbate and substrate interactions. For the investigation with FTO layer and TiO_2 molecule/s as adsorbate (first step of electrode modification), it is clearly shown that the more of adsorbate loadings (rather concentrations), the lower binding energies are obtained. Thus, the binding energy values follow this trend: 1 ads. > 5 ads. > 10 ads. It suggests the concentration plays an important role in determining the binding energies. The higher concentration could exhibit less binding energy values leading to higher in interaction strength within the complex components. This trend is, however, in line with the trend of adsorption energies which previously observed. Likewise, the similar trend was also revealed with the dopamine as adsorbate molecule/s (second step of electrode modification). The binding energy trend remains as follows: 1 ads. > 5 ads. for both of FTO – DA and TiO_2/FTO – DA complexes, respectively.

Another consideration is given by deliberating layer to layer electrode's binding energies to investigate the interactions favourability towards electrode surfaces. This is only applicable to the second and the third steps of electrode modifications since only single type of electrode layer (i.e. FTO) was used in the first electrode modification steps. For the calculation of the second modification steps, two types of layer were used i.e. FTO and TiO_2/FTO, while for

the third steps, the FTO, TiO_2/FTO, and DA/TiO_2/FTO layers were employed against single adsorbate molecule. From **Table 5.10**, the TiO_2/FTO exhibits less binding energy (i.e. -406.638 x 10^3 kcal/mol) towards dopamine than FTO (-313.147 x 10^3 kcal/mol). Calculation of higher dopamine loads (i.e. 5 ads.) also shows the similar trend. This suggests that TiO_2/FTO layer provides stronger interaction with dopamine than FTO layer (in second modification step) and thus, is more favourable from the binding energies point of view. Likewise, the full scheme of electrode modification (i.e. mimicking the third modification step) shows analogous trend which DA/TiO_2/FTO produces lowest binding energy amongst FTO and TiO_2/FTO layers towards ss-DNA. The entire binding energy trend is given as follows: DA/TiO_2/FTO (-23516.955 x 10^3 kcal/mol) < TiO_2/FTO (-23508.874 x 10^3 kcal/mol) < FTO (-15539.966 x 10^3 kcal/mol). This trend suggests a very strong interaction of DA/TiO_2/FTO towards ss-DNA and gradually diminished by means of removing the last (rather 'the outer') component of the electrode (i.e. DA was removed for TiO_2/FTO layer, while DA and TiO_2 were removed for the FTO layer). Taken together, these findings have made an excellent agreement with the present experimentation, particularly for the modified electrode construction. Indeed, the computational studies have successfully validated the use (or rather 'tendency') of novel layer-by-layer strategy comprising of the full scheme ss-DNA/DA/TiO_2/FTO electrodes, for the purpose of DNA damage detection (observed in subsequent discussion on experimental works).

Table 5.10 Binding energies of overall MD trajectories.

Substrate - adsorbate systems	Binding energy (x10^3; kcal/mol)		
	1 ads. molecule	5 ads. molecules	10 ads. molecules
FTO - TiO_2	-207.308	-207.310	-207.318
FTO - DA	-313.147	-313.211	
TiO_2/FTO - DA	-406.638	-406.643	
FTO - ss-DNA	-15539.966		
TiO_2/FTO - ss-DNA	-23508.874		
DA/TiO_2/FTO - ss-DNA	-23516.955		

5.2 Experimental

5.2.2 Characterization of the mesoporous TiO_2 microbeads

5.2.2.1 X-Ray Diffraction

The mesoporous TiO_2 microbeads was successfully prepared and examined using XRD and SEM images. The XRD is an appropriate method to determine the mean size of crystallites (Holzwarth and Gibson, 2011) of mesoporous TiO_2 microbeads in nanocrystalline bulk materials. The XRD pattern of mesoporous TiO_2 microbeads is shown in **Figure 5.46**. The five strong diffraction peaks were observed which are (101), (004), (200), (105), and (211) positioned at 2θ = 25.3, 37.9, 48.1, 54 and 55.2, respectively in the XRD pattern. This observation confirms the presence of anatase phase of mesoporous TiO_2 microbeads due to its fitted with JCPDS card number 01-073-1764. The crystallite size was calculated using Debye-Scherrer formula (Debye and Scherrer, 1916) as shown in **Equation 5.7** below.

$$D = \frac{K\lambda}{\beta \cos\theta} \tag{5.7}$$

Where *D* is the crystal size (nm), K is so-called shape factor (0.94), λ is the wavelength of X-ray source (nm), β is line broadening at half the maximum intensity or FWHM (radians), and θ is Bragg diffraction angle ($^{2\theta}/_{2}$; degree). The crystallite size was found at 14 nm and was further confirmed by SEM analysis. From the XRD peaks, the highest peak was found at the (101) facet and therefore, this was chosen as the basis of the TiO_2 cluster modeling (see **Figure 5.4**). Moreover, this facet is also addressed as a merit of anatase TiO_2 cluster which has been preferably used in theoretical studies (as thoroughly discussed in **Chapter 4; Materials and Methods**). In addition, computational studies on nanoparticle surfaces of anatase TiO_2 generally adopt (101) facet-based structure due to its lowest-energy surface (Gong *et al*., 2006).

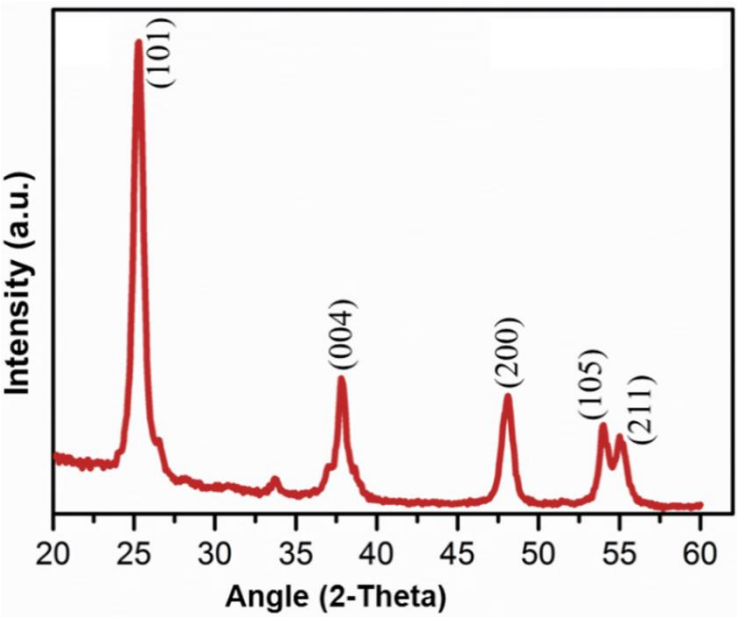

Figure 5.46 XRD pattern of mesoporous TiO_2 upon solvothermal treatment (Imani *et al*., 2014).

5.2.2.2 SEM images

Figure 5.47(a) shows the SEM images of mesoporous TiO_2 microbeads comprising of different scaling size prepared by solvothermal method. SEM enable to analyze the morphology and structural size of the mesoporous TiO_2 crystalline at the selected size range. As can be seen, the monodisperse TiO_2 microbeads with diameter 600 ± 50 nm was examined having rough surfaces. Upon the magnification of the SEM image, pores could be discovered over the surface of the TiO_2 beads containing approximately 14 nm nanocrystal size. This size is in consistent with the size obtained from XRD measurement (*via* Debye-Scherrer formula). In addition, a direct assessment of magnified mesoporous TiO_2 beads along with the simulated cluster of anatase TiO_2 (101) facet (i.e. inset figure) is illustrated in **Figure 5.47(b)**. The SEM image confirms the various shape and sizes of TiO_2 beads and is judiciously well in line with previous studies (Pazoki *et al*., 2014a, Pazoki *et al*., 2014b). However, the pores size obtained from this observation agrees with a recent study by Chen and co-workers who also discovered 14 nm pore size of TiO_2 microbeads (Chen *et al*., 2014).

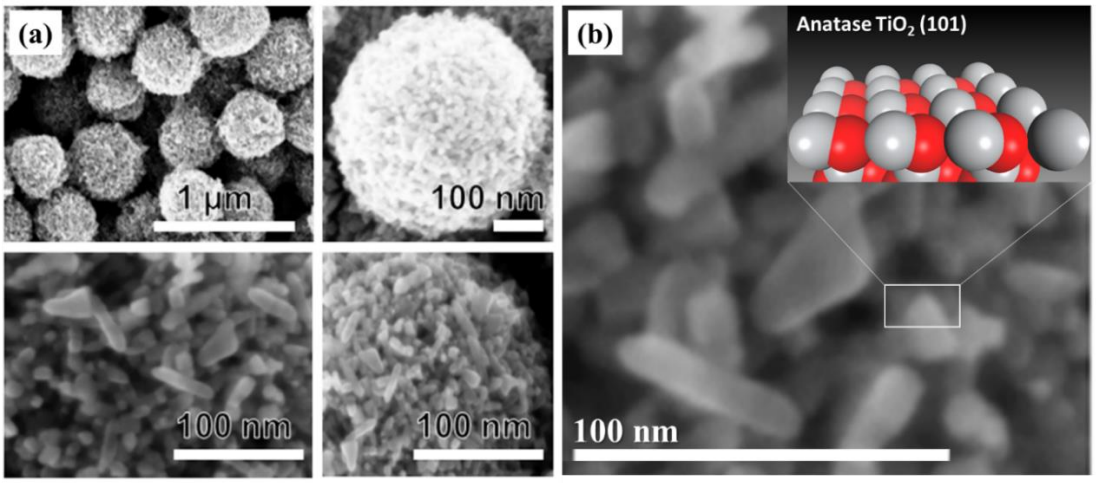

Figure 5.47 SEM images of mesoporous TiO_2 upon the solvothermal treatment (a) and its magnified image (Imani *et al*., 2014) along the TiO_2 (101) facet cluster (at inset-cross section) (b).

5.2.3 Electrochemical characterization of the modified electrode

The electrochemical characterization was performed using CV towards each modification stage. **Figure 5.48(a)** demonstrates the cyclic voltammogram accomplished layer-by-layer construction of the electrode i.e. FTO, TiO_2/FTO, DA/TiO_2/FTO, and ss-DNA/DA/TiO_2/FTO. The CV analysis was scanned in the phosphate buffer at pH 7.4 containing 1 mM $Fe(CN)_6^{3-/4-}$ as redox probe. Due to the use of redox probe, the bare FTO exhibits a pair of well-defined observed peaks and the difference between oxidation (anodic) and reduction (cathodic) peak potential (ΔE_p) was ~ 0.32 V with the scan rate of 50 mV/s. After immobilization of mesoporous TiO_2 microbeads (*via* doctor blade method) onto FTO electrode, the peak current clearly decreases and the larger peak-to-peak separation (i.e. ΔE_p) is observed as compared to bare FTO. It might be due to the electrostatic repulsion between the redox probe and mesoporous TiO_2 microbeads having highly negative charge. This observation is in accordance with the electrochemical response of the redox probe to mesoporous TiO_2 microbeads film and the bare FTO electrode. The higher in electronics band gap (i.e. 1.143 eV) or lower conductivity of TiO_2 compared to the bare FTO (i.e. 0.172 eV; **Figure 5.10**) observed in the computational study, may contribute to the decreasing event of redox current. Since the energy gap of FTO remains relatively smaller, the possibility of electron excitation from valence to conduction band is energetically more than TiO_2 and therefore, undergo the enhancement of electron transfer. It is well-understood that the electron flows from valence band (i.e. HOMO) to the conduction band (i.e. LUMO) during reduction process (Sabela *et al*., 2016). This finding is, however, in line with a very recent study reported by Lin and co-workers with the equivalent layer-by-layer strategy (Lin *et al*., 2017). When the DA/TiO_2/FTO was tested, the redox peak current decreases due to the presence of dopamine layer on the surface of TiO_2/FTO, while the ΔE_p also decreases (i.e.

become narrower) due to the electrostatic attraction between $Fe(CN)_6^{3-/4-}$ and highly positive charge of dopamine molecule. Afterwards, when the ss-DNA was immobilized onto $DA/TiO_2/FTO$ electrode, the redox current substantially decreases and the ΔE_p is observed to increase. This obvious peak decreasing confirms that the ss-DNA were successfully bound to the surface of modified electrode *via* covalent bonding between the amine group of dopamine and 5'end COOH of ss-DNA. A strong electrostatic repulsion between $Fe(CN)_6^{3-/4-}$ and negatively charged sugar-phosphate backbone of ss-DNA (Fritz *et al*., 2002) plays an important role herein. The presence of ss-DNA also could disturb the electron transfer (Lin *et al*., 2017). In general, the CV's result correlates well with each modification step of the electrode.

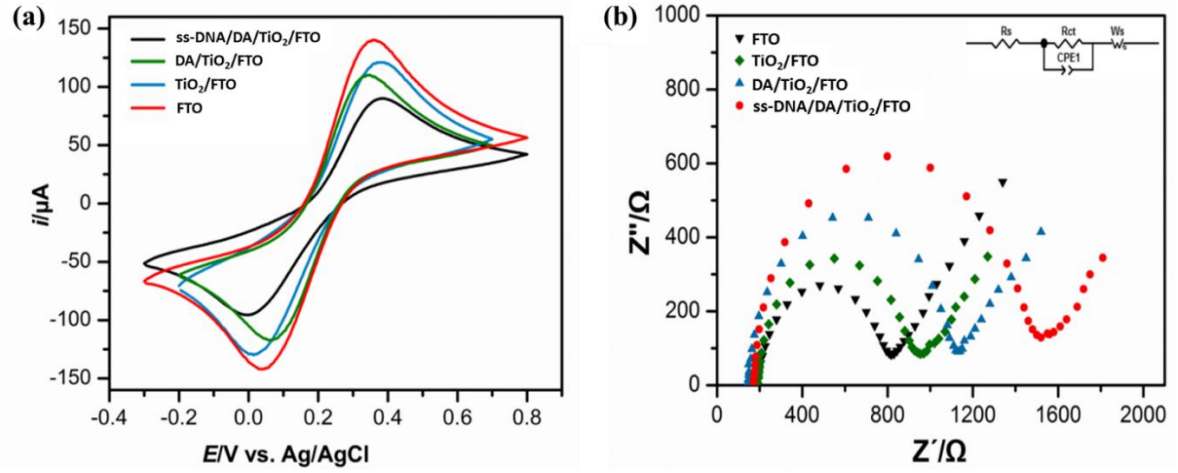

Figure 5.48 Cyclic voltammograms (a) (Imani *et al*., 2014) and Nyquist plots (inset: equivalent circuit used to fit the EIS data) (b) of modified electrode recorded upon each modification steps in the phosphate buffer at pH 7.4 containing 1 mM $Fe(CN)_6^{3-/4-}$.

Furthermore, EIS was used to evaluate the interfacial changes of the electrode during the fabrication process. The EIS is a well-known technique for the detection of DNA damage (Liao *et al*., 2010). **Figure 5.48(b)** shows the Nyquist plots of each electrode modification step recorded in the phosphate buffer (pH 7.4) containing 1 mM $Fe(CN)_6^{3-/4-}$. The

semicircles diameters of the Nyquist plots resemble the charge-transfer resistance at the electrode interface, while the straight sloping line is associated with the diffusion process of the reactive species (Wang *et al*., 2011). The inset in **Figure 5.48(b)** is the projected equivalent circuit and the fitting results for each electrode modification. *Rs* corresponds to the electrolyte resistance including the contact and charge transfer resistances at the counter electrode (or electrolyte) (Bessekhouad *et al*., 2012). *Rct* is the electron-transfer resistance. *CPE* is the constant phase element, which also characterizes the layer capacitance. *Ws* is the Warburg impedance, which is associated with the diffusion of the reactive species at the electrodes surface and is demonstrated by the straight line in the Nyquist plots (Zhao *et al*., 2014a). The bare FTO shows a small semicircle indicating a relatively low resistance to the redox probe (i.e. $Fe(CN)_6^{3-/4-}$) at the interface. After the mesoporous TiO_2 microbeads was appended to the surface of FTO (so called TiO_2/FTO layer), a larger semicircle can be observed because TiO_2 is able to disturb the transference of electrons. Upon the immersion of dopamine i.e. DA/TiO_2/FTO layer formation, the impedance value increases due to the capability of dopamine to interrupt the electron transfer within TiO_2/FTO surface. Indeed, dopamine has been computationally observed as a non-conductive molecule and is, thereby, unfavourable for the transmission of electrons. Lastly, the impedance value is also observed to increase while the ss-DNA was immobilized onto DA/TiO_2/FTO electrode. The ss-DNA may hinder the electron transfer.

5.2.4 Electrochemical detection of DNA oxidation damage

DNA damage has been a major problem in the early stage of Alzheimer's. Recently, electrochemical methods hold an important position as a reliable technique to evaluate the damage on the DNA upon a given specific pre-treatment (Fojta *et al*., 2016). It is due to

satisfactory parameters of the electroanalytical techniques such as sensitivity, selectivity, low-cost analysis etc., and remarkably their convenience in nucleic acid research (Paleček and Bartošík, 2012). Among other electrochemical techniques, SWV analysis was particularly used to measure the DNA damage evidence because of its inherent sensitivity, selectivity, and resolution. The use of SWV method has been a staple in the fabrication of sensitive electrochemical sensors and biosensors, mainly for targeting the disease-related biomarkers (Chen and Shah, 2013).

TiO_2 and dopamine are two unique part of the constructed electrode. TiO_2 could absorb light in the UV region and it is usually shielded with an organic molecule (i.e. dopamine) which capable to absorbs light in the visible region of the spectrum (O'Regan and Gratzel, 1991). TiO_2 is, however, highly biocompatible material which therefore, ideal to be used in medical applications (Tengvall and Lundström, 1992). Dopamine acts as an anchor molecule within TiO_2 to which other biomolecules i.e. 5'end carboxyl of ss-DNA. Instead, it also can facilitate the molecule-to-surface charge transfer between TiO_2 nanoparticles and the biomolecular system (Rajh *et al*., 2004). The dopamine absorbs the incident photon producing in electron-hole separation lead to rapid electron transfer to the TiO_2 conduction band (i.e. LUMO part of the frontier orbitals) (Syres *et al*., 2010).

Catechol adsorption onto TiO_2 is of interest as a light harvesting molecule. Catechol is not able to absorb light below than 4.200 eV (300 nm). The complex of DA/TiO_2 has an absorption with a shoulder of around 3.000 eV (420 nm). Entirely, the electron is immediately photoinjected from catechol into TiO_2 conduction band without any contributions from excited states of dopamine. Dopamine introduces an occupied π-level at the lower end of the

TiO_2 band gap giving intensification to the excitation of direct charge transfer from the highest occupied π-orbital (i.e. HOMO level in catechol) to the bottom of the conduction band (i.e. LUMO levels at Ti^{4+} (3d) orbital). This evidence is dominated by the significant contribution from Ti (3d) orbitals at the surface of the TiO_2 cluster (i.e. region which close to the dopamine adsorption) (Persson *et al*., 2000). The whole localization is further defined as $TiO_2/DA + h\nu \rightarrow e^- [(Ti^{3+})]/DA^+$.

In the photocatalytic study under visible light (420 nm), the similar radicals were also observed from the UV light. Moreover, the amount of generated reactive oxygen species (ROS) radicals during the photocatalytic experiment of TiO_2 was found to be lower compared to DA/TiO_2. DA/TiO_2 induces the spatial separation of photo-generated charges in which the electron holes are positioned on dopamine and electrons are injected to TiO_2 region followed by the occurrence of suppressing of charge recombination (Rajh *et al*., 2004). Instead, the mesoporous TiO_2 microbeads appended onto FTO glass electrode was also able to generate ROS *via* the photocatalytic oxidations with water (**scheme 5.1**).

Scheme 5.1: The photocatalytic oxidation of TiO_2 of water (Nagaveni *et al*., 2004).

$$TiO_2 + h\nu \longrightarrow h^+_{VB} + e^-_{CB}$$

$$h^+_{VB} + H_2O_{(ads)} \longrightarrow OH^* + H^+$$

$$h^+_{VB} + 2OH^-_{(ads)} \longrightarrow OH^- + OH^*$$

$$e^-_{CB} + O_2 \longrightarrow O_2^{*-}$$

$$2O_2^{*-} + 2H_2O \longrightarrow 2OH^* + 2OH^- + O_2$$

Whereas, h^{+}_{VB} is holes produced in the valence band of TiO_2 and e^{-}_{CB} is electrons transferred in the conducting band when TiO_2 is irradiated at the 420 nm wavelength. The resulting hydroxyl radical (OH^{*}) could oxidatively damage the DNA and cleave it into the pieces. This phenomenon could be monitored by an electrochemical probe (i.e. hexaammineruthenium; $[Ru(NH_3)_6]^{3+}$). The negatively charged oligonucleotide would adsorb the positively charged $[Ru(NH_3)_6]^{3+}$ through electrostatic interaction. Therefore, the more ss-DNA (rather 'its concentration') were attached to the DA/TiO_2/FTO *via* non-bond interactions with amine group at dopamine surface, the more $[Ru(NH_3)_6]^{3+}$ would interact with ss-DNA at the electrode surface *via* phosphoric skeleton of ss-DNA (Si *et al*., 2014). Other study assumed that probably Na^{+} at the anionic DNA backbone is also responsible herein (Yu *et al*., 2003). However, the ss-DNA was restricted into the pieces and not fixed on the surface of electrode (upon photocatalytic reaction) and therefore, unable to fixed on the electrode surface (due to the presence of OH^{*}) (Si *et al*., 2014). Consequently, a substantial decrease of $[Ru(NH_3)_6]^{3+}$ was recorded by SWV (**Figure 5.49(a)**). The surface densities of ss-DNA can be evaluated by the integration of the current for the reduction of $[Ru(NH_3)_6]^{3+}$ towards $[Ru(NH_3)_6]^{2+}$ (Yu *et al*., 2003).

Figure 5.49(a) shows the intercorrelation between oxidation peak (generated from SWV) and irradiation time. The oxidation peak dramatically decreases with the increasing time of irradiation. This is consistent with the previous study that DNA can be fatally damaged by ROS produced in photocatalytic reaction (Guo *et al*., 2011). The oxidation current of $[Ru(NH_3)_6]^{2+}$ for the various illumination times is observed at -0.21 V. The peak is directly proportional to the residual ss-DNA present on the electrode and is considered as direct

measurement of DNA damage. The stronger of the damage upon the ss-DNA, the smaller peak current is observed.

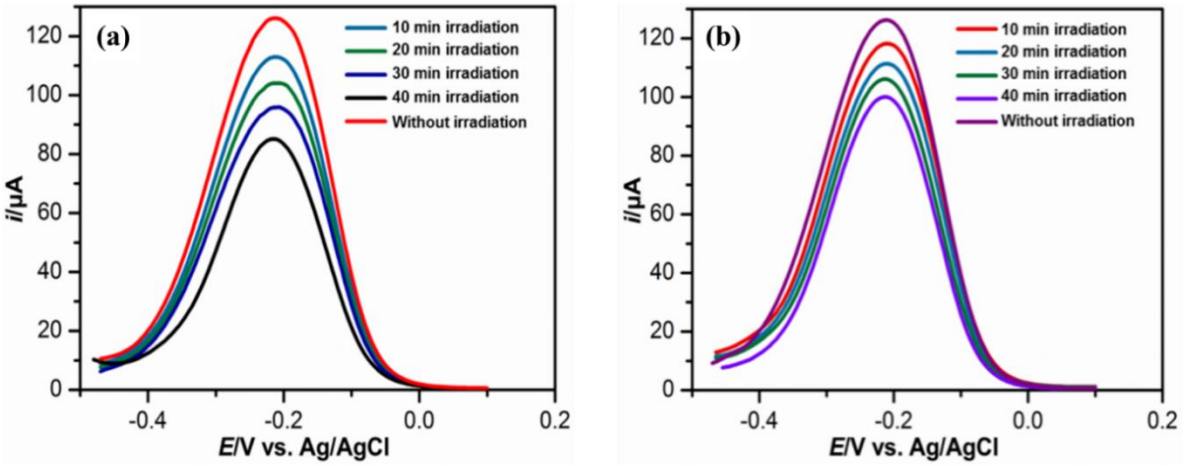

Figure 5.49 SWV curves of DNA/DA/TiO_2/FTO electrode in the absence (a) and presence of 200 μM AA (b) after the photocatalytic reactions with various irradiation times. The curves were recorded in phosphate buffer at pH 7.4 containing 1 mM $[Ru(NH_3)_6]^{3+}$ (Imani *et al*., 2014).

The ability of ascorbic acid (AA) as antioxidant treatment in Alzheimer's was observed herein to protect the damage of ss-DNA during photocatalytic reaction. **Figure 5.49(b)** shows the peak current *vs* irradiation time upon a given of 200 μM AA onto the electrode containing ss-DNA. Whilst, the peak oxidation trend *vs* the irradiation time with respect to the two different photocatalytic reactions, with and without AA treatment, is depicted at **Figure 5.50**. These results clearly show that the oxidation current in the presence of AA decreases more slowly than that of without (rather 'absence') AA treatment. DA/TiO_2 is photoactive nanostructures and thereby, capable to produce ROS under visible light exposure and damage the ss-DNA. This basically represents a well-defined strategy of the DNA damage measurement in the extremely early stage of Alzheimer's. In the absence of AA, the lowest and highest oxidation damage are measured to be 11% for 10 min and 33% for 40 min, respectively. However, the lower DNA oxidation damage was measured at 200 μM AA i.e.

merely 7% for 10 min and the highest damage was determined at approximately 22% for 40 min (**Table 5.11**). In the presence of AA (as an antioxidant), the ROS were quenched by antioxidant prior to reaching the backbone of ss-DNA and thus, the higher oxidation current was monitored.

Table 5.11 DNA damage level in the function of irradiation time.

Irradiation time (min)	**Damage without AA (%)**	**Damage with 200 µM AA (%)**
10 (lowest)	11	7
40 (highest)	33	22

Molecularly, ROS can react directly with plasmid DNA macromolecules *in vivo* to cleave one DNA strand and cause oxidative DNA damage in Alzheimer's (Lü *et al*., 2010). Herein, the ROS generated from photocatalytic reactions are enable to quench with AA exhibiting the decrease in the DNA damage. It indicates the ability of AA to protect the DNA damage, regardless of the lack of its exact role in several disease preventions such as Alzheimer's. Due to the highest oxidation damage, the 40 min's irradiation time was selected as an optimum parameter of damage for further measurement.

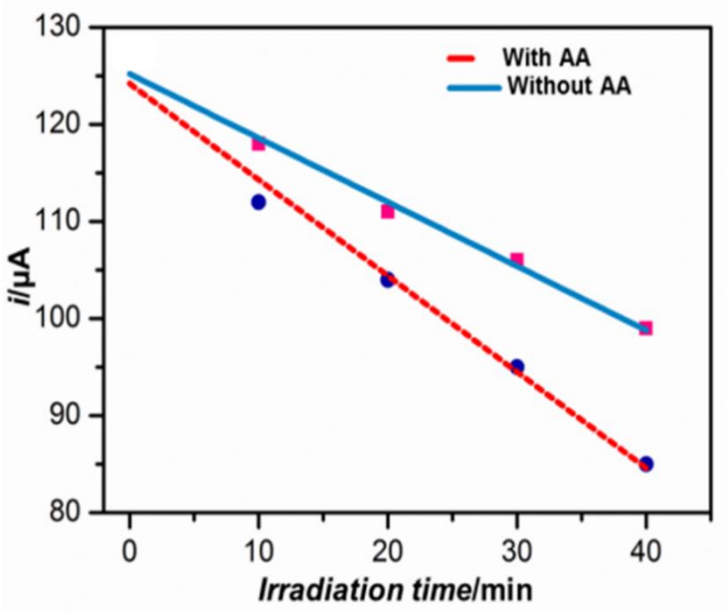

Figure 5.50 Oxidation current *vs* irradiation time of the photocatalytic reaction in the absence and presence of 200 μM AA. The data were recorded in phosphate buffer at pH 7.4 containing 1 mM $[Ru(NH_3)_6]^{3+}$ (Imani *et al*., 2014).

5.2.5 Determination of ascorbic acid activity to protect the DNA damage in the function of antioxidant concentrations

Further observation was carried out towards the DNA damage measurement upon the treatment of different concentrations of AA using optimum irradiation time (i.e. 40 min). **Figure 5.51(a)** shows the recorded oxidation peak of DNA damage with the different AA concentration (i.e. 200 – 500 μM), while the trend of AA concentrations against the current value is demonstrated in **Figure 5.51(b)**. The results show that the AA exhibits the significant impact to reduce the DNA damage levels. The more in concentration, the lesser DNA oxidation damage and a greater oxidation current are observed. In the absence of AA, the DNA oxidation damage is found at 33% and it decreases down to 17% while the 500 μM of AA was added. This suggests the key role of the antioxidant treatment towards protecting the DNA from the photocatalytic damages.

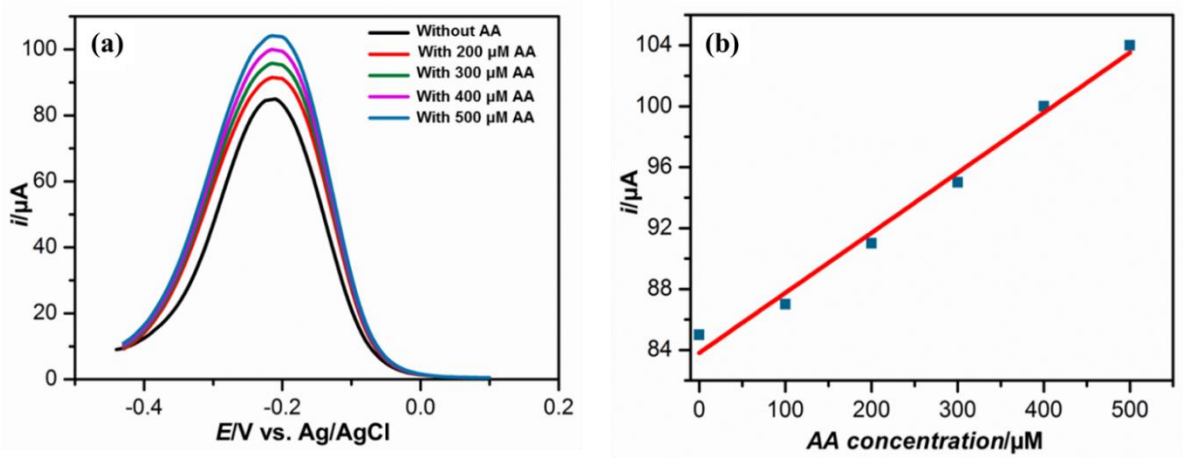

Figure 5.51 SWV curves of ss-DNA/DA/TiO_2/FTO electrode comprising of different AA concentrations at the optimum irradiation time (40 min) (a) and the relationship between oxidation current vs AA concentration (b). The curves were recorded in phosphate buffer at pH 7.4 containing 1 mM $[Ru(NH_3)_6]^{3+}$ (Imani *et al*., 2014).

5.3 Synergies between Computational and Experimental Studies

The experimental layer-by-layer electrode for the use of DNA damage detection was successfully mimicked through computational modeling studies (**Figure 5.52**). The electrode denotations were given as follows: layer I (FTO), layer II (TiO_2/FTO), layer III (DA/TiO_2/FTO), and layer IV (ss-DNA/DA/TiO_2/FTO). The reasonable model was attributed from each step of modified electrode construction. The use of specific facet for cluster's modeling (i.e. (101) facet for TiO_2) was highly considered from the dominant peak observed in XRD analysis (**Figure 5.46**). **Figure 5.52(c)** represents the SEM image of mesoporous TiO_2 microbeads containing anatase (101) as dominant crystal facet.

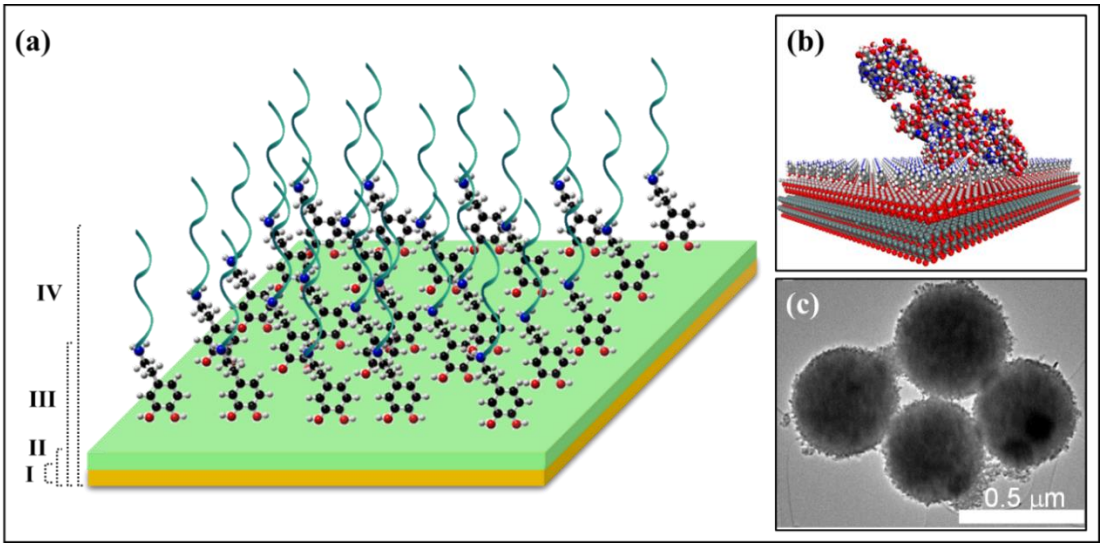

Figure 5.52 Schematic representation (a) and computational model (b) of the constructed electrode along with the SEM image of the mesoporous TiO_2 microbeads (c). The layer's type was indicated in part (a).

Further theoretical consideration was given to the correlation between peak current behaviour towards layer-by-layer assembly and binding energy profiles. Instead of tailoring HOMO-LUMO energy gaps towards CV behaviours (see **subsection of 5.2.2**), the binding energy per-electrode layer could explain the bond strength between the adsorbate and electrode surface (rather 'substrate'). The bond strength indicates to what degree of specific atom's bonding-orbital electrons of adsorbate are free to participate in the collective metallic (i.e. layer I and II), and organic electrode surfaces (layer III) with the presence of electrochemical redox probe (i.e. $Fe(CN)_6^{3-/4-}$). The higher binding energies (indicating strong adsorbate-substrate interactions) may lead to smaller changes in its electrochemical polarizability which directly affect to the decreasing of redox peak current (i.e. attraction/repulsion phenomenon with the probe) and charge transfer resistance enhancement. Charge transfer resistance is well-known as a direct quantitative measure of the electrochemical polarizability (Kakiuchi and Tsujioka, 2007). From **Table 5.10**, the binding energy of single molecule adsorbate

interaction decreases gradually (or higher in interaction) comprising of each modification step, which correlates well with the consistent decreasing of the peak current of CV (**Figure 5.48(a)**). This evidence is further confirmed by the Nyquist plots behaviour of EIS (**Figure 5.48(b)**) with the larger semicircle upon layer-by-layer modification steps. The stronger interaction (lower in binding energy) after the new component introduced to each electrode surfaces, may lead to higher in electron transfer disturbance (i.e. increasing the semicircle diameter of Nyquist plots). These findings represent the important role of binding energy towards the electrochemical behaviour (i.e. cyclic voltammogram and EIS plots) during electrode modification steps. Instead, guanine residues were predicted using DFT as the main target of DNA damage upon the SWV analysis of the photocatalytic reaction. It is, however, in line with the general understanding provided by literature (Paleček and Bartošík, 2012). The presence of AA may interfere the guanine sites upon the antioxidant treatment.

5.4 Conclusions

In this work, the electrochemical DNA sensor ss-DNA/DA/TiO_2/FTO was developed (Imani *et al*., 2014) which furnished an effective strategy for detecting ss-DNA damage induced by photocatalytic reactions. This strategy has been successfully elucidated through the supports of theoretical considerations. For the computational observations, the exact component of the modified electrode was modeled and minimized. The preliminary studies were carried out through re-examining the origin cell or molecule of the components. DFT calculation based on numerical basis set was used to characterize the structural, electronics, as well as considerably the vibrational properties of each of those components. The structural properties of FTO, TiO_2, DA, and ss-DNA were justified to meet a good agreement with the previous studies as well as literature references and therefore, was reliable to be employed for

theoretical observations. Frontier orbital analysis obtained at DFT level, were helpful in the prediction of HOMO (i.e. valence bands) and LUMO (i.e. conduction bands) energies associated with the redox process in electrochemical measurement since the electrons are well-understood to flow from valence bands to the conduction bands. Moreover, this parameter accurately predicts the reactive sites of the bulks leading to possible interaction sites with the appended layer. The t-DOS and p-DOS were also considered, herein particularly for the semiconductor elements i.e. FTO and TiO_2 clusters, to observe the semiconducting nature of these clusters as well as the change of energy gap prior to and upon the F-doping procedure towards FTO. The energy gaps of FTO and TiO_2 were under/ overestimately observed from the experimental values due to the common limitation of standard GGA/PBE functionals employed in DFT calculations. However, the DFT calculations successfully established the increment of the structure's reactivity upon the introducing of anionic dopant (F^{2-}) into the entire structure of SnO_2 (the native form of FTO). This, basically, constructs the comprehensive logics (rather 'chemistry') behind the selection of FTO electrode and mesoporous TiO_2 microbeads in the fabrication of modified electrode for DNA damage detection. In order to investigate the adsorption process of layer-by-layer electrode assembly, the interaction within substrate and adsorbates (**Table 4.1**) was elucidated using MC simulations. In general, the selected adsorbate showed stronger tendency to the substrate surface, confirming the ability of each electrode component in construction of the DNA sensor architecture. Herein, the UFF force field has been used throughout the simulations and was well-considered as appropriate function to calculate the potential energy parameters. The energy difference upon the implementation of gradual increasing the adsorbate loadings (i.e. TiO_2 and dopamine molecules) explain the important role of concentration towards electrode modifications. Interestingly, the output trajectories

of MC simulations have been employed as initial position (rather 'input structures') of MD studies due to their lowest energy configurations.

MD simulations provide valuable insight towards 3D structures and stability of layer-by-layer electrode under experimentally-used temperature. The MD was carried out during proper simulation time suggesting that the stable system has been reached towards each layer according to the justification of total energies, temperature, and potential energy profiles. As one of the atomistic parameters of nanomaterials dynamics, the concentration profiles have been generated comprising of each responsible atoms or functional groups roles in intermolecular interactions. For the TiO_2 molecule/s interactions against FTO surface, Ti atoms seem to responsible for the interactions which may be triggered by ionic force between Ti (adsorbate) and O or F (substrate) atoms. Mimicking the DA/TiO_2/FTO electrode fabrication, the dynamics simulations of dopamine onto the TiO_2/FTO surface were carried out resulting the importance of OH groups of dopamine towards the metals site of the surface *via* metal coordination bonding type. The *van der Waals* energy was elucidated as the most contributed energy towards complex formation suggesting the physisorption evidence of the dopamine onto the electrode surface. The electrostatic (i.e. H-bond) and valence energies were also taken into account due to the obtained negative energy values and possible interactions of -OH groups at the dopamine with Ti atoms of the TiO_2 surfaces (Syres *et al.*, 2010), respectively. Moreover, the study has emphasized the preferability of TiO_2/FTO (layer II) compared to FTO (layer I) layer towards dopamine interactions due to the role of intramolecular energy between dopamine molecules. For the interaction of ss-DNA towards electrode surfaces, the molecular distances of -COOH group of ss-DNA towards the surface were observed as follows: TiO_2/FTO < FTO < DA/TiO_2/FTO. Considering the relative

concentrations, the ss-DNA interaction towards DA/TiO_2/FTO layer exhibits the highest value among others indicating its high functionality and may lead to the most preferable layer compared to FTO and TiO_2/FTO layers. Due to the dominant role of valence energy, the chemisorption of 5'end carboxyl ss-DNA towards electrode surface was emerged herein. The electrostatic energy was also observed to contribute towards the complex formations of overall models. The further pivotal analysis deals with binding energy observations towards the MD trajectories of each electrode fabrication steps. The negative eigenvalues of binding scores show the stable complex formation of each simulations. Overall, the results demonstrate a well in line with the expectation and justifiably well-tailored with electrochemical behavior in experimentation.

In the experimental studies, the electrochemical DNA detection strategy using an innovative electrode composing ss-DNA/DA/TiO_2/FTO was successfully fabricated through a stepwise procedure. This electrode was illuminated under visible light exposure resulting photocatalytic reactions lead to DNA disruption. The procedure of electrode modification has been magnificently validated through the computational simulations. This experimental strategy remains as a relatively simple, easily adaptable for miniaturization, and less expensive method for the detection of DNA damage since there is no need of external ROS species. Moreover, the possibility of *in situ* analysis of generated ROS was also highlighted for the genotoxicity assessment. The XRD and SEM images were used to characterize the prepared mesoporous TiO_2 microbeads. Instead, the cyclic voltammogram and EIS plots (i.e. Nyquist plots) were applied to evaluate the electrochemical signal upon layer-by-layer construction. For the CV, the peak current was observed to gradually decrease when the subsequent layer was introduced to the assembled electrode. These results were influenced

by electrostatic attraction/repulsion between the introduced molecules and redox probe ($Fe(CN)_6^{3-/4-}$).

Another related parameter was also considered i.e. peak-to-peak separation (ΔE_p) showing a good relationship with the peak currents. Likewise, the Nyquist plots (EIS) of bare FTO showed a small semicircle indicating a relatively low resistance to the redox probe. The semicircle diameters increase along the adjoining components towards electrode layer's fabrication. This trend is strongly associated with the transference of electrons. Several theoretical considerations have successfully validated these phenomena i.e. HOMO-LUMO energy levels and binding energies resulting in a good agreement with the trend of electrochemical signals. Indeed, dopamine had dual functions herein; it acts as molecular anchor within TiO_2 and 5'end carboxyl of ss-DNA and helps in harvesting visible light during photocatalytic reaction. Further, the detection of DNA damage was investigated using SWV in which the oxidation peak dramatically decreases along the increment of illumination time. This evidence is directly proportional to the residual ss-DNA present on the electrode subjected to the "direct measurement" capability of DNA damage. The ability of the antioxidant as a "shield" from DNA damage "attack" was observed by applying AA during the photocatalytic reaction. Through the electrochemical observations on the presence of AA shows its ability to protect the DNA from the damage *via* the quenching of ROS species prior to reaching the ss-DNA backbone and inducing the damage. The application of various AA concentration provides less damage in the increasing concentrations of antioxidant. Overall, this innovative strategy of DNA damage detection was well-developed and the ability of AA to protect the damage was also established. The computational studies herein have successfully afforded the fundamental principles behind electrode modification and its

electrochemical behavior during characterization studies. This promising strategy can be applied to screen genotoxicity in Alzheimer's disease as well as provides an appropriate understanding of the antioxidant role in Alzheimer's treatment. Moreover, the theoretical studies, in general, can be used as a reliable method to predict molecular characterization and validation of the DNA-based biosensors and bioelectronics.

CHAPTER 6

CONCLUDING REMARKS AND FUTURE PERSPECTIVES

6.1 Concluding Remarks

An innovative strategy for the detection of DNA damage upon a photocatalytic reaction under visible light was introduced (Imani *et al*., 2014). This strategy was evaluated *via* emerging computational techniques. The computational protocols deal with Forcite-Geometry-based structural analysis, density functional theory (DFT) calculations, Metropolis Monte Carlo (MC) adsorption studies, and molecular dynamics (MD) simulations. The modified electrode comprising of ss-DNA/DA/TiO_2/FTO were computationally mimicked according to the exact component in the experiment followed by energy minimization. The structural-based prediction on primitive structures provides a reliable way to construct larger nanoclusters. DFT calculations carried out using the numerical basis set i.e. DMol3 and DFTB+ has been used to characterize the structural, electronics, and vibrational properties of each electrode components. The results show a good agreement of the calculated and experimental parameters. This essentially, assembles the comprehensive logics (rather 'chemistry') behind selection of the component in the electrode fabrication for the purpose of DNA damage detection. In order to predict the adsorption process within a layer-by-layer electrode assembly, the MC simulation was carried out within substrate and adsorbates (**Table 4.1**), which was further validated using MD simulations. The strong tendency of each adsorbate towards substrate system emphasize the ability of the adsorbate molecules to absorb onto the substrate surfaces. MC simulations could observe the lowest energy configuration of the substrate-adsorbate complexes which were beneficial for the initiating the MD simulations. MD simulations provide valuable insights towards 3D structures and stability of layer-by-

layer electrode under experimentally-used temperatures. The MD simulations were carried out with a canonical ensemble and proper simulation time suggesting that the stable system have been reached towards each component. This was in accordance with the justification of total energies, temperature, and potential energy profiles. Particularly, potential energy profiles observed the responsible energy parameters involved in the complex formations. Further analysis has been carried out i.e. concentration profiles applied to all trajectories and radius of gyration, particularly for abundant ss-DNA molecule interaction showing the atomic density profiles as well as stability and compactness towards complex systems. Atomic density analysis has characterized the responsible atom or functional group dominating in the adsorbate-substrate interaction. Binding energy calculation were judiciously decided as post-important analysis of MD showing the decline of binding energy upon each step of electrode modification. This suggests the increment in their interaction strength and was very well correlated with electrochemical signals in the experimental characterization studies.

The experimental studies were carried out using several protocols for the DNA damage detection as the ultimate goals. A simple, low-cost and *in situ* electrochemical DNA damage detection strategy using an innovative electrode composing of ss-DNA/DA/TiO_2/FTO was successfully fabricated through a stepwise procedure. The computational modeling has validated this step-by-step procedure. The XRD and SEM images were used to characterize the prepared mesoporous TiO_2 microbeads showing good accordance with the anatase reference data (i.e. JCPDS card number 01-073-1764) and the useful examining of TiO_2 microbead fine structure, respectively. Both have shown a very well in line of the crystallite size in which the Debye-Scherrer calculation and SEM analysis revealed similar diameter

size i.e. 14 nm. Instead, the cyclic voltammogram (CV) and Nyquist plots were applied to evaluate the electrochemical signal upon layer-by-layer construction. The CV analysis shows the decline of peak current along the step-by-step electrode modification. Likewise, the semicircle diameter increases along electrode fabrication step. These phenomena have been explicated using computational studies including HOMO-LUMO energy levels and binding energy profiles resulting in a well synergy within both. The peak-to-peak separation (ΔE_p) was also considered, showing a good relationship with the CV peak currents. Further, the detection of DNA damage was investigated using square wave voltammetry in which the oxidation peak dramatically decreases along the increment of illumination time. The ability of antioxidant as a "shield" from DNA damage "attack" was observed by applying ascorbic acid during photocatalytic reaction attributed to the quenching of reactive oxygen species (ROS) before reaching the ss-DNA backbone and inducing the damage. Guanine residues were predicted using DFT as the reactive sites (rather 'target') of the ss-DNA for the genotoxic agents leading to the DNA strand-breaks. Taken together, this promising strategy can be applied to screen the genotoxicity in Alzheimer's disease as well as providing an appropriate grasp of the antioxidant-based treatment. The *in silico* studies have successfully provided the fundamental principles of electrode modification as well as elucidating the adsorption processes.

6.2 Future Perspectives

The future works can be directed to the stability study and analysis of real biological sample i.e. blood plasma or cerebrospinal fluid containing matrix, therefore the sensor's durability and interference study could be conducted. Instead, the biocompatible nanopolymer i.e.

chitosan (Putri *et al*., 2017) may be beneficial in order to increase the electrochemical performance and stability of the device towards point-of-care diagnostics for Alzheimer's. Since the proper use of such device either to predict or diagnose/therapy is far from reality till now, the device miniaturization may be insightful towards the *ready-to-use* of the DNA-based sensor. From the *in silico* views, the MD simulations using explicit solvent may provide a better insight of the interaction studies with the use of large-atomic nanomaterials simulations i.e. Amber or LAMMPS codes.

REFERENCES

ADCOCK, S. A. & MCCAMMON, J. A. 2006. Molecular dynamics: Survey of methods for simulating the activity of proteins. *Chemical Reviews,* 106**,** 1589-615.

AFZAAL, M., YATES, H. & HODGKINSON, J. 2016. Translation effects in fluorine doped tin oxide thin film properties by atmospheric pressure chemical vapour deposition. *Coatings,* 6**,** 43(1-10).

AGASHE, C. & MAHAMUNI, S. 2010. Competitive effects of film thickness and growth rate in spray pyrolytically deposited fluorine-doped tin dioxide films. *Thin Solid Films,* 518**,** 4868-73.

AGASHE, C., TAKWALE, M. G., MARATHE, B. R. & BHIDE, V. G. 1988. Structural properties of SnO_2: F films deposited by spray pyrolysis. *Solar Energy Materials,* 17**,** 99-117.

AGUSTA, M. K., PRASETIYO, I., SAPUTRO, A. G., MAEZONO, R. & DIPOJONO, H. K. 2016. First-principles molecular dynamics study on Helium-filled carbon nanotube. *Journal of Physics: Conference Series,* 739**,** 012081.

AHIRWAR, R., NAHAR, S., AGGARWAL, S., RAMACHANDRAN, S., MAITI, S. & NAHAR, P. 2016. In silico selection of an aptamer to estrogen receptor alpha using computational docking employing estrogen response elements as aptamer-alike molecules. *Scientific Reports,* 6**,** 21285(1-11).

AKKERMANS, R. L. C., SPENLEY, N. A. & ROBERTSON, S. H. 2013. Monte Carlo methods in Materials Studio. *Molecular Simulation,* 39**,** 1153-64.

ALBERT, M. S., DEKOSKY, S. T., DICKSON, D., DUBOIS, B., FELDMAN, H. H., FOX, N. C., GAMST, A., HOLTZMAN, D. M., JAGUST, W. J., PETERSEN, R. C., SNYDER, P. J., CARRILLO, M. C., THIES, B. & PHELPS, C. H. 2011. The diagnosis of mild cognitive impairment due to Alzheimer's disease: Recommendations from the National Institute on Aging-Alzheimer's Association workgroups on diagnostic guidelines for Alzheimer's disease. *Alzheimers & Dementia,* 7**,** 270-9.

ALISTE, M. P. 2000. Theoretical study of dopamine. Application of the HSAB principle to the study of drug–receptor interactions. *Journal of Molecular Structure: THEOCHEM,* 507**,** 1-10.

ALLEN, M. P. 2004. Introduction to molecular dynamics simulation. *Computational Soft Matter: From Synthetic Polymers to Proteins,* 23**,** 1-28.

ALLEN, M. P. & TILDESLEY, D. J. 1987. *Computer simulation of liquids,* Oxford England, New York, Clarendon Press, Oxford University Press.

ALLEN, M. P. & TILDESLEY, D. J. 1989. *Computer simulation of liquids*, Oxford university press.

ALVAREZ-RAMIREZ, F. & RUIZ-MORALES, Y. 2007. *Ab initio* molecular dynamics calculations of the phase transformation mechanism for the formation of TiO_2 titanate-type nanosheets from anatase. *Chemistry of Materials,* 19**,** 2947-59.

ALZHEIMER'S ASSOCIATION 2015. Basics of Alzheimer's disease: What it is and what you can do. USA: Alzheimer's Association.

ALZHEIMER'S AUSTRALIA 2003. The dementia epidemic: Economic impact and positive solutions for Australia. Australia: Alzheimer's Australia.

ALZHEIMER'S DISEASE INTERNATIONAL 2015. World Alzheimer Report 2015; The global impact of dementia; Analysis of prevalence, incidence, cost and trends. London: Azheimer's Disease International.

ALZHEIMER, A., STELZMANN, R. A., SCHNITZLEIN, H. N. & MURTAGH, F. R. 1995. An english translation of Alzheimer's 1907 paper, "Uber eine eigenartige erkankung der hirnrinde". *Clinical Anatomy,* 8**,** 429-31.

ALZHEIMER'S ASSOCIATION. 2016. 2016 Alzheimer's disease facts and figures. *Alzheimer's & Dementia: The Journal of the Alzheimer's Association,* 12**,** 459-509.

ALZHEIMER'S DISEASE EDUCATION AND REFERRAL CENTER. 2015. Alzheimer's disease genetics fact sheet. USA: National Institue of Aging.

AMOLI, V., FAROOQUI, S., RAI, A., SANTRA, C., RAHMAN, S., SINHA, A. K. & CHOWDHURY, B. 2015. Indium oxide nanocluster doped TiO_2 catalyst for activation of molecular O_2. *RSC Advances,* 5**,** 67089-92.

ANAND, P. & SINGH, B. 2013. A review on cholinesterase inhibitors for Alzheimer's disease. *Archives of Pharmacal Research,* 36**,** 375-99.

ANDERSEN, H. C. 1980. Molecular dynamics simulations at constant pressure and/or temperature. *The Journal of Chemical Physics,* 72**,** 2384-93.

ANOOP, A., SINGH, P. K., JACOB, R. S. & MAJI, S. K. 2010. CSF biomarkers for Alzheimer's disease diagnosis. *International Journal of Alzheimer's Disease,* 2010**,** 1-12.

AROCA, R. F., CLAVIJO, R. E., HALLS, M. D. & SCHLEGEL, H. B. 2000. Surface-enhanced raman spectra of Phthalimide. Interpretation of the SERS spectra of the surface complex formed on silver islands and colloids. *The Journal of Physical Chemistry A,* 104**,** 9500-5.

ASAHI, R., TAGA, Y., MANNSTADT, W. & FREEMAN, A. J. 2000. Electronic and optical properties of anatase. *Physical Review B,* 61**,** 7459-65.

ASHADUZZAMAN, M., DESHPANDE, S. R., MURUGAN, N. A., MISHRA, Y. K., TURNER, A. P. F. & TIWARI, A. 2017. On/off-switchable LSPR nano-immunoassay for troponin-T. *Scientific Reports,* 7**,** 44027(1-10).

ATTIG, N., BINDER, K., GRUBMULLER, H. & KREMER, K. 2004. *Computational soft matter: from synthetic polymers to proteins,* Germany, John von Neumann Institute for Computing (NIC).

AZHEIMER'S DISEASE INTERNATIONAL 2016. World Alzheimer Report 2016; Improving healthcare for people living with dementia; coverage, quality and costs now and in the future. London: Azheimer's Disease International.

BAHRAMIAN, A. 2015. Molecular dynamics simulation of surface morphology and thermodynamic properties of polyaniline nanostructured film. *Surface and Interface Analysis,* 47**,** 1-14.

BANYAMIN, Z., KELLY, P., WEST, G. & BOARDMAN, J. 2014. Electrical and optical properties of fluorine doped tin oxide thin films prepared by magnetron sputtering. *Coatings,* 4**,** 732-46.

BARNARD, A. S. & CURTISS, L. A. 2005. Prediction of TiO_2 nanoparticle phase and shape transitions controlled by surface chemistry. *Nano Letters,* 5**,** 1261-6.

BARNHAM, K. J., MASTERS, C. L. & BUSH, A. I. 2004. Neurodegenerative diseases and oxidative stress. *Nature Reviews Drug Discovery,* 3**,** 205-14.

BASIUK, V. A. & BASSIOUK, M. 2008. Interaction of amino acids with single-walled carbon nanotubes: Insights from density functional theory calculations. *Journal of Computational and Theoretical Nanoscience,* 5**,** 1205-9.

BATEMAN, R. J., XIONG, C., BENZINGER, T. L., FAGAN, A. M., GOATE, A., FOX, N. C., MARCUS, D. S., CAIRNS, N. J., XIE, X., BLAZEY, T. M., HOLTZMAN, D. M., SANTACRUZ, A., BUCKLES, V., OLIVER, A., MOULDER, K., AISEN, P. S., GHETTI, B., KLUNK, W. E., MCDADE, E., MARTINS, R. N., MASTERS, C. L., MAYEUX, R., RINGMAN, J. M., ROSSOR, M. N., SCHOFIELD, P. R., SPERLING, R. A., SALLOWAY, S., & MORRIS, J. C. 2012. Clinical and biomarker changes in dominantly inherited Alzheimer's disease. *The New England Journal of Medicine,* 367**,** 795-804.

BECKE, A. D. 1988. A multicenter numerical integration scheme for polyatomic molecules. *The Journal of Chemical Physics,* 88**,** 2547-53.

BECKE, A. D. 1993. A new mixing of Hartree–Fock and local density-functional theories. *The Journal of Chemical Physics,* 98**,** 1372-7.

BENEDEK, N. A., SNOOK, I. K., LATHAM, K. & YAROVSKY, I. 2005. Application of numerical basis sets to hydrogen bonded systems: A density functional theory study. *The Journal of Chemical Physics,* 122**,** 144102(1-8).

BENHAOUA, A., RAHAL, A., BENHAOUA, B. & JLASSI, M. 2014. Effect of fluorine doping on the structural, optical and electrical properties of SnO_2 thin films prepared by spray ultrasonic. *Superlattices and Microstructures,* 70**,** 61-9.

BENILOVA, I. V., ARKHYPOVA, V. N., DZYADEVYCH, S. V., JAFFREZIC-RENAULT, N., MARTELET, C. & SOLDATKIN, A. P. 2006. Kinetics of human and horse sera cholinesterases inhibition with solanaceous glycoalkaloids: Study by potentiometric biosensor. *Pesticide Biochemistry and Physiology,* 86**,** 203-10.

BERENDSEN, H. J. C., POSTMA, J. P. M., GUNSTEREN, W. F. V., DINOLA, A. & HAAK, J. R. 1984. Molecular dynamics with coupling to an external bath. *The Journal of Chemical Physics,* 81**,** 3684-90.

BERR, C. 2000. Cognitive impairment and oxidative stress in the elderly: Results of epidemiological studies. *Biofactors,* 13**,** 205-9.

BESSEKHOUAD, Y., BRAHIMI, R., HAMDINI, F. & TRARI, M. 2012. Cu_2S/TiO_2 heterojunction applied to visible light Orange II degradation. *Journal of Photochemistry and Photobiology A: Chemistry,* 248**,** 15-23.

BHATTACHARJEE, A., AHMARUZZAMAN, M. & SINHA, T. 2015. A novel approach for the synthesis of SnO_2 nanoparticles and its application as a catalyst in the reduction and photodegradation of organic compounds. *Spectrochimica Acta Part A: Molecular and Biomolecular Spectroscopy,* 136, Part B**,** 751-60.

BIANCHI, R., KASTRISIANAKI, E., GIAMBANCO, I. & DONATO, R. 2011. S100B protein stimulates microglia migration *via* RAGE-dependent up-regulation of chemokine expression and release. *The Journal of Biological Chemistry,* 286**,** 7214-26.

BIOVIA, D. S. 2016a. Discovery Studio modelling. v.16.10.15350 ed. San Diego: Dassault Systemes.

BIOVIA, D. S. 2016b. Material Studio modelling. v.16.1.0.21 ed. San Diego: Dassault Systemes.

BLENNOW, K. & HAMPEL, H. 2003. CSF markers for incipient Alzheimer's disease. *Lancet Neurology,* 2**,** 605-13.

BLENNOW, K., HAMPEL, H., WEINER, M. & ZETTERBERG, H. 2010. Cerebrospinal fluid and plasma biomarkers in Alzheimer disease. *Nature Reviews Neurology,* 6**,** 131-44.

BLENNOW, K., HAMPEL, H. & ZETTERBERG, H. 2014. Biomarkers in Amyloid-[beta] Immunotherapy Trials in Alzheimer's Disease. *Neuropsychopharmacology,* 39**,** 189-201.

BOESE, A. D., MARTIN, J. M. L. & HANDY, N. C. 2003. The role of the basis set: Assessing density functional theory. *The Journal of Chemical Physics,* 119**,** 3005-14.

BOLBOACA, M., ILIESCU, T., PAIZS, C., IRIMIE, F. D. & KIEFER, W. 2003. Raman, infrared, and surface-enhanced raman spectroscopy in combination with *Ab initio* and density functional theory calculations on 10-Isopropyl-10H-phenothiazine-5-oxide. *The Journal of Physical Chemistry A,* 107**,** 1811-18.

BRAMBILLA, D., LE DROUMAGUET, B., NICOLAS, J., HASHEMI, S. H., WU, L.-P., MOGHIMI, S. M., COUVREUR, P. & ANDRIEUX, K. 2011. Nanotechnologies for Alzheimer's disease: Diagnosis, therapy, and safety issues. *Nanomedicine: Nanotechnology, Biology and Medicine,* 7**,** 521-40.

BRULS, D. M., EVERS, T. H., KAHLMAN, J. A., VAN LANKVELT, P. J., OVSYANKO, M., PELSSERS, E. G., SCHLEIPEN, J. J., DE THEIJE, F. K., VERSCHUREN, C. A., VAN DER WIJK, T., VAN ZON, J. B., DITTMER, W. U., IMMINK, A. H., NIEUWENHUIS, J. H. & PRINS, M. W. 2009. Rapid integrated biosensor for multiplexed immunoassays based on actuated magnetic nanoparticles. *Lab on a Chip,* 9**,** 3504-10.

BUCHHAVE, P., MINTHON, L., ZETTERBERG, H., WALLIN, A. K., BLENNOW, K. & HANSSON, O. 2012. Cerebrospinal fluid levels of beta-amyloid 1-42, but not of tau, are fully changed already 5 to 10 years before the onset of Alzheimer dementia. *Archives of General Psychiatry,* 69**,** 98-106.

BURBANO, M., SCANLON, D. O. & WATSON, G. W. 2011. Sources of conductivity and doping limits in CdO from hybrid density functional theory. *Journal of the American Chemical Society,* 133**,** 15065-72.

BURDETT, J. K., HUGHBANKS, T., MILLER, G. J., RICHARDSON, J. W. & SMITH, J. V. 1987. Structural-electronic relationships in inorganic solids: Powder neutron diffraction studies of the rutile and anatase polymorphs of titanium dioxide at 15 and 295 K. *Journal of the American Chemical Society,* 109**,** 3639-46.

BURKE, K. & WAGNER, L. O. 2013. DFT in a nutshell. *International Journal of Quantum Chemistry,* 113**,** 96-101.

CAI, H., WANG, Y., MCCARTHY, D., WEN, H., BORCHELT, D. R., PRICE, D. L. & WONG, P. C. 2001. BACE1 is the major [beta]-secretase for generation of A[beta] peptides by neurons. *Nature Neuroscience,* 4**,** 233-4.

CALZOLARI, A. & NARDELLI, M. B. 2013. Dielectric properties and Raman spectra of ZnO from a first principles finite-differences/finite-fields approach. *Scientific Reports,* 3**,** 2999(1-6).

CAMPOS, M. & BRAZ, B., JR. 1997. Mechanism of conduction in doped polyaniline. *Journal of Physics D: Applied Physics,* 30**,** 1531.

CANEVALI, C., CHIODINI, N., NOLA, P. D., MORAZZONI, F., SCOTTI, R. & BIANCHI, C. L. 1997. Surface reactivity of SnO_2 obtained by sol-gel type condensation: Interaction with inert, combustible gases, vapour-phase H_2O and air, as revealed by electron paramagnetic resonance spectroscopy. *Journal of Materials Chemistry,* 7**,** 997-1002.

CANFIELD, P., DAHLBOM, M. G., HUSH, N. S. & REIMERS, J. R. 2006. Density-functional geometry optimization of the 150000-atom photosystem-I trimer. *The Journal of Chemical Physics,* 124**,** 024301.

CAO, E., ZHANG, Y., HAO, W., PENG, H., SUN, L. & HU, J. 2013. Room temperature ferromagnetism in Sm-doped SnO_2 PLD film. *Applied Surface Science,* 282**,** 376-83.

CASEWIT, C. J., COLWELL, K. S. & RAPPE, A. K. 1992. Application of a universal force field to organic molecules. *Journal of the American Chemical Society,* 114**,** 10035-46.

CAVALCANTI, A., SHIRINZADEH, B., ZHANG, M. & KRETLY, L. 2008. Nanorobot hardware architecture for medical defense. *Sensors,* 8**,** 2932-58.

CHAI, D., XIE, Z., WANG, Y., LIU, L. & YUM, Y.-J. 2014. Molecular dynamics investigation of the adhesion mechanism acting between dopamine and the surface of dopamine-processed aramid fibers. *ACS Applied Materials & Interfaces,* 6**,** 17974-84.

CHAUHAN, N. & PUNDIR, C. S. 2014. Amperometric determination of acetylcholine-a neurotransmitter, by chitosan/gold-coated ferric oxide nanoparticles modified gold electrode. *Biosensors and Bioelectronics,* 61**,** 1-8.

CHEATHAM, T. E., 3RD & KOLLMAN, P. A. 2000. Molecular dynamics simulation of nucleic acids. *Annual Review of Physical Chemistry,* 51**,** 435-71.

CHELLAPPA, M., ANJANEYULU, U., MANIVASAGAM, G. & VIJAYALAKSHMI, U. 2015. Preparation and evaluation of the cytotoxic nature of TiO_2 nanoparticles by direct contact method. *International Journal of Nanomedicine,* 10 Suppl 1**,** 31-41.

CHEN, A. & SHAH, B. 2013. Electrochemical sensing and biosensing based on square wave voltammetry. *Analytical Methods,* 5**,** 2158-73.

CHEN, L. X., RAJH, T., WANG, Z. & THURNAUER, M. C. 1997. XAFS studies of surface structures of TiO_2 nanoparticles and photocatalytic reduction of metal ions. *The Journal of Physical Chemistry B,* 101**,** 10688-97.

CHEN, X., YUAN, C., WONG, C. K. & ZHANG, G. 2012. Molecular modeling of temperature dependence of solubility parameters for amorphous polymers. *Journal of Molecular Modeling,* 18**,** 2333-41.

CHEN, X. P., JIANG, J. K., LIANG, Q. H., YANG, N., YE, H. Y., CAI, M., SHEN, L., YANG, D. G. & REN, T. L. 2015a. First-principles study of the effect of functional groups on polyaniline backbone. *Scientific Reports,* 5**,** 16907(1-7).

CHEN, Y., HUANG, F., XIANG, W., CHEN, D., CAO, L., SPICCIA, L., CARUSO, R. A. & CHENG, Y. B. 2014. Effect of TiO_2 microbead pore size on the performance of DSSCs with a cobalt based electrolyte. *Nanoscale,* 6**,** 13787-94.

CHEN, Y. & ROUX, B. 2015. Generalized Metropolis acceptance criterion for hybrid non-equilibrium molecular dynamics-Monte Carlo simulations. *The Journal of Chemical Physics,* 142**,** 024101.

CHEN, Y., TAN, C., ZHANG, H. & WANG, L. 2015b. Two-dimensional graphene analogues for biomedical applications. *Chemical Society Reviews,* 44**,** 2681-701.

CHENG, D., ZHANG, M., CHEN, J., YANG, C., ZENG, X. & CAO, D. 2014a. Computer screening of dopants for the development of new SnO_2-based transparent conducting oxides. *The Journal of Physical Chemistry C,* 118**,** 2037-43.

CHENG, H., MA, J., ZHAO, Z. & QI, L. 1995. Hydrothermal preparation of uniform nanosize rutile and anatase particles. *Chemistry of Materials,* 7**,** 663-71.

CHENG, H. & SELLONI, A. 2010. Hydroxide ions at the water/anatase TiO_2(101) interface: Structure and electronic states from first principles molecular dynamics. *Langmuir,* 26**,** 11518-25.

CHENG, X. R., HAU, B. Y., ENDO, T. & KERMAN, K. 2014b. Au nanoparticle-modified DNA sensor based on simultaneous electrochemical impedance spectroscopy and localized surface plasmon resonance. *Biosensors and Bioelectronics,* 53**,** 513-8.

CHENG, Y., ZHAO, L., LI, Y. & XU, T. 2011. Design of biocompatible dendrimers for cancer diagnosis and therapy: Current status and future perspectives. *Chemical Society Review,* 40**,** 2673-703.

CHIKAE, M., FUKUDA, T., KERMAN, K., IDEGAMI, K., MIURA, Y. & TAMIYA, E. 2008. Amyloid-beta detection with saccharide immobilized gold nanoparticle on carbon electrode. *Bioelectrochemistry,* 74**,** 118-23.

CHINNAPPA, L., RAVICHANDRAN, K., SARAVANAKUMAR, K., MURUGANANTHAM, G. & SAKTHIVEL, B. 2011. The combined effects of molar concentration of the precursor solution and fluorine doping on the structural and electrical properties of tin oxide films. *Journal of Materials Science: Materials in Electronics,* 22**,** 1827-34.

CHRISTEN, Y. 2000. Oxidative stress and Alzheimer disease. *The American Journal of Clinical Nutrition,* 71**,** 621s-9s.

CHRISTIANSON, J. R. & SCHMIDT, J. R. 2015. Structural heterogeneity and dynamics of dyes on TiO_2: Implications for charge transfer across organic-inorganic interfaces. *Physical Chemistry Chemical Physics,* 17**,** 3731-40.

COLLINS, A. R., DUSINSKA, M., GEDIK, C. M. & STETINA, R. 1996. Oxidative damage to DNA: Do we have a reliable biomarker? *Environmental Health Perspectives,* 104 Suppl 3**,** 465-9.

COYLE, J. & PUTTFARCKEN, P. 1993. Oxidative stress, glutamate, and neurodegenerative disorders. *Science,* 262**,** 689-95.

CRAMER, C. J. 2004. *Essentials of computational chemistry: Theories and models,* Chichester, West Sussex, England ; Hoboken, NJ, Wiley.

DARVESH, S., HOPKINS, D. A. & GEULA, C. 2003. Neurobiology of butyrylcholinesterase. *Nature Reviews Neuroscience,* 4**,** 131-8.

DAS, S. & JAYARAMAN, V. 2014. SnO_2: A comprehensive review on structures and gas sensors. *Progress in Materials Science,* 66**,** 112-55.

DAVE, B. C., DUNN, B., VALENTINE, J. S. & ZINK, J. I. 1994. Sol-gel encapsulation methods for biosensors. *Analytical Chemistry,* 66**,** 1120A-7A.

DE FERRARI, G. V., CANALES, M. A., SHIN, I., WEINER, L. M., SILMAN, I. & INESTROSA, N. C. 2001. A structural motif of acetylcholinesterase that promotes amyloid beta-peptide fibril formation. *Biochemistry,* 40**,** 10447-57.

DE LA ESCOSURA-MUÑIZ, A., PLICHTA, Z., HORÁK, D. & MERKOÇI, A. 2015. Alzheimer′s disease biomarkers detection in human samples by efficient capturing through porous

magnetic microspheres and labelling with electrocatalytic gold nanoparticles. *Biosensors and Bioelectronics,* 67**,** 162-9.

DE LA TORRE, J. C. 2010. Alzheimer's disease is incurable but preventable. *Journal of Alzheimer's Disease,* 20**,** 861-70.

DEBYE, P. & SCHERRER, P. 1916. Interference in irregularly oriented particles in Röntgen light. *Zeitschrift für Physik,* 17**,** 277-83.

DEGLER, D., PEREIRA DE CARVALHO, H. W., KVASHNINA, K., GRUNWALDT, J. D., WEIMAR, U. & BARSAN, N. 2016. Structure and chemistry of surface-doped Pt: SnO_2 gas sensing materials. *RSC Advances,* 6**,** 28149-55.

DELLEY, B. 1990. An all-electron numerical method for solving the local density functional for polyatomic molecules. *The Journal of Chemical Physics,* 92**,** 508-17.

DELLEY, B. 2000. From molecules to solids with the DMol3 approach. *The Journal of Chemical Physics,* 113**,** 7756-64.

DELLEY, B. 2002. Hardness conserving semilocal pseudopotentials. *Physical Review B,* 66**,** 155125.

DELLEY, B. 2006. The conductor-like screening model for polymers and surfaces. *Molecular Simulation,* 32**,** 117-23.

DIBA, F. S., KIM, S. & LEE, H. J. 2017. Electrochemical immunoassay for amyloid-beta 1–42 peptide in biological fluids interfacing with a gold nanoparticle modified carbon surface. *Catalysis Today,* 295**,** 41-7.

DI VALENTIN, C. & COSTA, D. 2012. Anatase TiO_2 surface functionalization by alkylphosphonic acid: A DFT+D study. *The Journal of Physical Chemistry C,* 116**,** 2819-28.

DONAHUE, A. N., ASCHNER, M., LASH, L. H., SYVERSEN, T. & SONNTAG, W. E. 2006. Growth hormone administration to aged animals reduces disulfide glutathione levels in hippocampus. *Mechanisms of Ageing and Development,* 127**,** 57-63.

DREIZLER, R. M. & DA PROVIDENCIA, J. 2013. *Density functional methods in physics*, Springer Science & Business Media.

DUBOIS, B., FELDMAN, H. H., JACOVA, C., DEKOSKY, S. T., BARBERGER-GATEAU, P., CUMMINGS, J., DELACOURTE, A., GALASKO, D., GAUTHIER, S., JICHA, G., MEGURO, K., O'BRIEN, J., PASQUIER, F., ROBERT, P., ROSSOR, M., SALLOWAY, S., STERN, Y., VISSER, P. J. & SCHELTENS, P. 2007. Research criteria for the diagnosis of Alzheimer's disease: Revising the NINCDS–ADRDA criteria. *The Lancet Neurology,* 6**,** 734-46.

DUTHEY, B. 2013. *Background paper 6.11 Alzheimer's disease and other dementias,* Switzerland, World Health Organization.

DZYADEVYCH, S. V., ARKHYPOVA, V. N., SOLDATKIN, A. P., EL'SKAYA, A. V., MARTELET, C. & JAFFREZIC-RENAULT, N. 2004. Enzyme biosensor for Tomatine detection in tomatoes. *Analytical Letters,* 37**,** 1611-24.

EDWARDS, P. P., PORCH, A., JONES, M. O., MORGAN, D. V. & PERKS, R. M. 2004. Basic materials physics of transparent conducting oxides. *Dalton Transactions***,** 2995-3002.

ELANGOVAN, E. & RAMAMURTHI, K. 2005. Studies on micro-structural and electrical properties of spray-deposited fluorine-doped tin oxide thin films from low-cost precursor. *Thin Solid Films,* 476**,** 231-6.

ELSTNER, M. 2006. The SCC-DFTB method and its application to biological systems. *Theoretical Chemistry Accounts,* 116**,** 316-25.

ELSTNER, M., FRAUENHEIM, T. & SUHAI, S. 2003. An approximate DFT method for QM/MM simulations of biological structures and processes. *Journal of Molecular Structure: THEOCHEM,* 632**,** 29-41.

ELSTNER, M., POREZAG, D., JUNGNICKEL, G., ELSNER, J., HAUGK, M., FRAUENHEIM, T., SUHAI, S. & SEIFERT, G. 1998. Self-consistent-charge density-functional tight-binding method for simulations of complex materials properties. *Physical Review B,* 58**,** 7260-8.

ESTEVES-VILLANUEVA, J. O. & MARTIC-MILNE, S. 2016. Electrochemical detection of anti-tau antibodies binding to tau protein and inhibition of GSK-3β-catalyzed phosphorylation. *Analytical Biochemistry,* 496**,** 55-62.

ESTEVES-VILLANUEVA, J. O., TRZECIAKIEWICZ, H. & MARTIC, S. 2014. A protein-based electrochemical biosensor for detection of tau protein, a neurodegenerative disease biomarker. *Analyst,* 139**,** 2823-31.

EVANS, D. A. 1990. Estimated prevalence of Alzheimer's disease in the United States. *The Milbank Quarterly,* 68**,** 267-89.

EWALD, P. P. 1921. Die Berechnung optischer und elektrostatischer Gitterpotentiale. *Annalen der Physik,* 369**,** 253-287.

FADEEL, B. 2014. *Handbook of safety assessment of nanomaterials: From toxicological testing to personalized medicine,* USA, SRC Press.

FAHMI, A., MINOT, C., SILVI, B. & CAUSÁ, M. 1993. Theoretical analysis of the structures of titanium dioxide crystals. *Physical Review B,* 47**,** 11717-24.

FARGES, F., BROWN, G. E. & REHR, J. J. 1997. Ti K-edge XANES studies of Ti coordination and disorder in oxide compounds: Comparison between theory and experiment. *Physical Review B,* 56**,** 1809-19.

FENG, J., CHEN, J., XIAO, B. & YU, J. 2009. Interface structure of Ag (111)/SnO_2 (200) composite material studied by density functional theory. *Science in China Series E: Technological Sciences,* 52**,** 1258-63.

FEREIDOON, A., ALEAGHAEE, S. & TARAGHI, I. 2015. Mechanical properties of hybrid graphene/TiO_2 (rutile) nanocomposite: A molecular dynamics simulation. *Computational Materials Science,* 102**,** 220-7.

FIOLHAIS, C., NOGUEIRA, F. & MARQUES, M. A. 2003. *A primer in density functional theory*, Springer Science & Business Media.

FOJTA, M., DAŇHEL, A., HAVRAN, L. & VYSKOČIL, V. 2016. Recent progress in electrochemical sensors and assays for DNA damage and repair. *Trends in Analytical Chemistry,* 79**,** 160-7.

FRASCO, M. F. & CHANIOTAKIS, N. 2010. Bioconjugated quantum dots as fluorescent probes for bioanalytical applications. *Analytical and Bioanalytical Chemistry,* 396**,** 229-40.

FRITZ, J., COOPER, E. B., GAUDET, S., SORGER, P. K. & MANALIS, S. R. 2002. Electronic detection of DNA by its intrinsic molecular charge. *Proceedings of the National Academy of Sciences,* 99**,** 14142-6.

FRÖHLICH, D., KENKLIES, R. & HELBIG, R. 1978. Band-gap assignment in SnO_2 by two-photon spectroscopy. *Physical Review Letters,* 41**,** 1750-1.

FUJISHIMA, A., RAO, T. N. & TRYK, D. A. 2000. Titanium dioxide photocatalysis. *Journal of Photochemistry and Photobiology C: Photochemistry Reviews,* 1**,** 1-21.

FUKUI, K. 1982a. Role of frontier orbitals in chemical reactions. *Science,* 218**,** 747-54.

FUKUI, K. 1982b. The role of frontier orbitals in chemical reactions (Nobel lecture). *Angewandte Chemie International Edition in English,* 21**,** 801-9.

FUKUMOTO, H., TENNIS, M., LOCASCIO, J. J., HYMAN, B. T., GROWDON, J. H. & IRIZARRY, M. C. 2003. Age but not diagnosis is the main predictor of plasma amyloid beta-protein levels. *Archives of Neurology,* 60**,** 958-64.

GABA, R., BHANDARI, M. & KAKKAR, R. 2013. Adsorption studies of acetaldehyde on TiO_2 nanosurface. *Advanced Materials Letters,* 4**,** 769-78.

GABBITA, S. P., LOVELL, M. A. & MARKESBERY, W. R. 1998. Increased nuclear DNA oxidation in the brain in Alzheimer's disease. *Journal of Neurochemistry,* 71**,** 2034-40.

GALASKO, D. R., PESKIND, E., CLARK, C. M. & *et al*. 2012. Antioxidants for Alzheimer disease: A randomized clinical trial with cerebrospinal fluid biomarker measures. *Archives of Neurology,* 69**,** 836-41.

GELLA, A. & DURANY, N. 2009. Oxidative stress in Alzheimer disease. *Cell Adhesion & Migration,* 3**,** 88-93.

GERHARDINGER, P. F. & MCCURDY, R. J. 1996. Float line deposited transparent conductors-implications for the Pv Industry. *MRS Proceedings,* 426.

GERSTEN, J. I. & SMITH, F. W. 2001. *The physics and chemistry of materials,* Wiley New York.

GIACOVAZZI, R., CIOFINI, I., RAO, L., AMATORE, C. & ADAMO, C. 2014. Copper-amyloid-β complex may catalyze peroxynitrite production in brain: Evidence from molecular modeling. *Physical Chemistry Chemical Physics,* 16**,** 10169-74.

GILMAN, S. & MANJI, H. 2010. *Oxford American handbook of neurology,* New York, Oxford University Press.

GINLEY, D. S. & BRIGHT, C. 2011. Transparent conducting oxides. *MRS Bulletin,* 25**,** 15-8.

GLENNER, G. G. & WONG, C. W. 1984. Alzheimer's disease: Initial report of the purification and characterization of a novel cerebrovascular amyloid protein. *Biochemical and Biophysical Research Communications,* 120**,** 885-90.

GONG, X. Q., SELLONI, A., BATZILL, M. & DIEBOLD, U. 2006. Steps on anatase TiO_2(101). *Nature Materials,* 5**,** 665-70.

GRIMME, S. 2004. Accurate description of *van der Waals* complexes by density functional theory including empirical corrections. *Journal of Computational Chemistry,* 25**,** 1463-73.

GRIMME, S. 2006. Semiempirical GGA-type density functional constructed with a long-range dispersion correction. *Journal of Computational Chemistry,* 27**,** 1787-99.

GROTENDORST, J., MARX, D. & MURAMATSU, A. 2002. *Quantum simulations of complex many-body systems: From theory to algorithms,* Netherland, John von Neumann Institute for Computing (NIC).

GSELL, W., CONRAD, R., HICKETHIER, M., SOFIC, E., FROLICH, L., WICHART, I., JELLINGER, K., MOLL, G., RANSMAYR, G., BECKMANN, H. & *et al*. 1995. Decreased catalase activity but unchanged superoxide dismutase activity in brains of patients with dementia of Alzheimer type. *Journal of Neurochemistry,* 64**,** 1216-23.

GUO, Q., YUE, Q., ZHAO, J., WANG, L., WANG, H., WEI, X., LIU, J. & JIA, J. 2011. How far can hydroxyl radicals travel? An electrochemical study based on a DNA mediated electron transfer process. *Chemical Communications,* 47**,** 11906-8.

HAGFELDT, A. & GRÄTZEL, M. 2000. Molecular photovoltaics. *Accounts of Chemical Research,* 33**,** 269-77.

HAMDAN, S. K. & MOHD ZAIN, A. 2014. *In vivo* electrochemical biosensor for brain glutamate detection: A mini review. *Malaysian Journal of Medical Sciences,* 21**,** 12-26.

HAMMER, B., HANSEN, L. B. & NØRSKOV, J. K. 1999. Improved adsorption energetics within density-functional theory using revised Perdew-Burke-Ernzerhof functionals. *Physical Review B,* 59**,** 7413-21.

HAMPEL, H., MITCHELL, A., BLENNOW, K., FRANK, R. A., BRETTSCHNEIDER, S., WELLER, L. & MOLLER, H. J. 2004. Core biological marker candidates of Alzheimer's disease - perspectives for diagnosis, prediction of outcome and reflection of biological activity. *Journal of Neural Transmission,* 111**,** 247-72.

HANAOR, D. A. H. & SORRELL, C. C. 2011. Review of the anatase to rutile phase transformation. *Journal of Materials Science,* 46**,** 855-74.

HARDY, J. & SELKOE, D. J. 2002. The amyloid hypothesis of Alzheimer's disease: Progress and problems on the road to therapeutics. *Science,* 297**,** 353-6.

HARRISON, N. 2003. An introduction to density functional theory. *Nato Science Series Sub Series III Computer And Systems Sciences,* 187**,** 45-70.

HARTNAGEL, H., DAWAR, A., JAIN, A. & JAGADISH, C. 1995. *Semiconducting transparent thin films,* Institute of Physics Bristol.

HARVEY, J. N. 2006. On the accuracy of density functional theory in transition metal chemistry. *Annual Reports Section "C" (Physical Chemistry),* 102**,** 203-26.

HAYASHI, Y., SUGIYAMA, H., SUGANAMI, A., HIGASHI, K., KASHIWAGI, K., IGARASHI, K., KAWAUCHI, S. & TAMURA, Y. 2013. Prediction of the interaction between spermidine and the GG mismatch containing acceptor stem in tRNA Ile: Molecular modeling, density functional theory, and molecular dynamics study. *Biochemical and Biophysical Research Communications,* 441**,** 999-1004.

HE, L., LIU, F., HAUTIER, G., OLIVEIRA, M. J. T., MARQUES, M. A. L., VILA, F. D., REHR, J. J., RIGNANESE, G. M. & ZHOU, A. 2014. Accuracy of generalized gradient approximation functionals for density-functional perturbation theory calculations. *Physical Review B,* 89**,** 064305(1-16).

HE, Y., TILOCCA, A., DULUB, O., SELLONI, A. & DIEBOLD, U. 2009. Local ordering and electronic signatures of submonolayer water on anatase TiO_2(101). *Nature Materials,* 8**,** 585-9.

HEIAT, M., NAJAFI, A., RANJBAR, R., LATIFI, A. M. & RASAEE, M. J. 2016. Computational approach to analyze isolated ssDNA aptamers against angiotensin II. *Journal of Biotechnology,* 230**,** 34-9.

HESSE, C., ROSENGREN, L., VANMECHELEN, E., VANDERSTICHELE, H., JENSEN, C., DAVIDSSON, P. & BLENNOW, K. 2000. Cerebrospinal fluid markers for Alzheimer's disease evaluated after acute ischemic stroke. *Journal of Alzheimer's Disease,* 2**,** 199-206.

HOCKNEY, R. W. & EASTWOOD, J. W. 1988. *Computer simulation using particles,* United States, CRC Press.

HOHENBERG, P. & KOHN, W. 1964. Inhomogeneous electron gas. *Physical Review,* 136**,** B864.

HOLMES, B. B., FURMAN, J. L., MAHAN, T. E., YAMASAKI, T. R., MIRBAHA, H., EADES, W. C., BELAYGOROD, L., CAIRNS, N. J., HOLTZMAN, D. M. & DIAMOND, M. I. 2014. Proteopathic tau seeding predicts tauopathy in vivo. *Proceedings of the National Academy of Sciences of the United States of America,* 111**,** E4376-85.

HOLZWARTH, U. & GIBSON, N. 2011. The Scherrer equation versus the 'Debye-Scherrer equation'. *Nature Nanotechnology,* 6**,** 534.

HOOVER, W. G. 1985. Canonical dynamics: Equilibrium phase-space distributions. *Physical Review A,* 31**,** 1695-7.

HOSSAIN, F. M., SHEPPARD, L., NOWOTNY, J. & MURCH, G. E. 2008. Optical properties of anatase and rutile titanium dioxide: *Ab initio* calculations for pure and anion-doped material. *Journal of Physics and Chemistry of Solids,* 69**,** 1820-8.

HSIEH, B. C., MATSUMOTO, K., CHENG, T. J., YUU, G. & CHEN, R. L. 2007. Choline biosensor constructed with chitinous membrane from soldier crab and its application in measuring cholinesterase inhibitory activities. *Journal of Pharmaceutical and Biomedical Analysis,* 45**,** 673-8.

HU, J., RUAN, X. & CHEN, Y. P. 2009. Thermal conductivity and thermal rectification in graphene nanoribbons: A molecular dynamics study. *Nano Letters,* 9**,** 2730-5.

HU, W. P., KUMAR, J. V., HUANG, C. J. & CHEN, W. Y. 2015. Computational selection of RNA aptamer against angiopoietin-2 and experimental evaluation. *BioMed Research International,* 2015**,** 1-8.

HUGENHOLTZ, N. M. & VAN HOVE, L. 1958. A theorem on the single particle energy in a Fermi gas with interaction. *Physica,* 24**,** 363-76.

HUMPEL, C. 2011. Identifying and validating biomarkers for Alzheimer's disease. *Trends in Biotechnology* 29**,** 26-32.

HYE, A., LYNHAM, S., THAMBISETTY, M., CAUSEVIC, M., CAMPBELL, J., BYERS, H. L., HOOPER, C., RIJSDIJK, F., TABRIZI, S. J., BANNER, S., SHAW, C. E., FOY, C., POPPE, M., ARCHER, N., HAMILTON, G., POWELL, J., BROWN, R. G., SHAM, P., WARD, M. & LOVESTONE, S. 2006. Proteome-based plasma biomarkers for Alzheimer's disease. *Brain,* 129**,** 3042-50.

IMANI, R., IGLIČ, A., TURNER, A. P. F. & TIWARI, A. 2014. Electrochemical detection of DNA damage through visible-light-induced ROS using mesoporous TiO_2 microbeads. *Electrochemistry Communications,* 40**,** 84-7.

ISLAM, K., JANG, Y. C., CHAND, R., JHA, S. K., LEE, H. H. & KIM, Y. S. 2011. Microfluidic biosensor for beta-amyloid(1-42) detection using cyclic voltammetry. *Journal of Nanoscience and Nanotechnology,* 11**,** 5657-62.

ITO, S., CHEN, P., COMTE, P., NAZEERUDDIN, M. K., LISKA, P., PÉCHY, P. & GRÄTZEL, M. 2007. Fabrication of screen-printing pastes from TiO_2 powders for dye-sensitised solar cells. *Progress in Photovoltaics: Research and Applications,* 15**,** 603-12.

JACK, C. R., JR., ALBERT, M. S., KNOPMAN, D. S., MCKHANN, G. M., SPERLING, R. A., CARRILLO, M. C., THIES, B. & PHELPS, C. H. 2011. Introduction to the recommendations from the National Institute on Aging-Alzheimer's Association workgroups on diagnostic guidelines for Alzheimer's disease. *Alzheimers & Dementia,* 7**,** 257-62.

JANOUSCH, M., MEIJER, G. I., STAUB, U., DELLEY, B., KARG, S. F. & ANDREASSON, B. P. 2007. Role of oxygen vacancies in Cr-doped $SrTiO_3$ for resistance-change memory. *Advanced Materials,* 19**,** 2232-5.

JOHANSSON, E. M. J., PLOGMAKER, S., WALLE, L. E., SCHÖLIN, R., BORG, A., SANDELL, A. & RENSMO, H. 2010. Comparing surface binding of the maleic anhydride anchor group on single crystalline anatase TiO_2 (101), (100), and (001) surfaces. *The Journal of Physical Chemistry C,* 114**,** 15015-20.

JORGENSEN, W. L. & TIRADO-RIVES, J. 1996. Monte Carlo *vs* molecular dynamics for conformational sampling. *The Journal of Physical Chemistry,* 100**,** 14508-13.

JOSEPH, D. P., RENUGAMBAL, P., SARAVANAN, M., RAJA, S. P. & VENKATESWARAN, C. 2009. Effect of Li doping on the structural, optical and electrical properties of spray deposited SnO_2 thin films. *Thin Solid Films,* 517**,** 6129-36.

JUNJUN, S., TATSIANA, A. R., SINI, A., EMPPU, S., PU CHUN, K. & HALINA, T. K. 2009. Experimental and simulation studies of a real-time polymerase chain reaction in the presence of a fullerene derivative. *Nanotechnology,* 20**,** 415101.

KAKIUCHI, T. & TSUJIOKA, N. 2007. Electrochemical polarizability of the interface between an aqueous electrolyte solution and a room-temperature molten salt. *Journal of Electroanalytical Chemistry,* 599**,** 209-12.

KAKKAR, R., GROVER, R. & GAHLOT, P. 2006. Density functional study of the properties of isomeric aminophenylhydroxamic acids and their copper (II) complexes. *Polyhedron,* 25**,** 759-66.

KAMACHI, T., KIHARA, N., SHIOTA, Y. & YOSHIZAWA, K. 2005. Computational exploration of the catalytic mechanism of dopamine β-monooxygenase: Modeling of its mononuclear copper active sites. *Inorganic Chemistry,* 44**,** 4226-36.

KANETI, Y. V., ZHANG, X., LIU, M., YU, D., YUAN, Y., ALDOUS, L. & JIANG, X. 2016. Experimental and theoretical studies of gold nanoparticle decorated zinc oxide nanoflakes with exposed {100} facets for butylamine sensing. *Sensors and Actuators B: Chemical,* 230**,** 581-91.

KARAMAN, R. 2011. Computational-aided design for dopamine prodrugs based on novel chemical approach. *Chemical Biology & Drug Design,* 78**,** 853-63.

KARPLUS, M. & MCCAMMON, J. A. 2002. Molecular dynamics simulations of biomolecules. *Nature Structural Biology,* 9**,** 646-52.

KASAI, T., TOKUDA, T., TAYLOR, M., KONDO, M., MANN, D. M. A., FOULDS, P. G., NAKAGAWA, M. & ALLSOP, D. 2013. Correlation of Aβ oligomer levels in matched cerebrospinal fluid and serum samples. *Neuroscience Letters,* 551**,** 17-22.

KHALED, K. & ABDEL-SHAFI, N. 2011. Quantitative structure and activity relationship modeling study of corrosion inhibitors: Genetic function approximation and molecular dynamics simulation methods. *International Journal of Electrochemical Science,* 6**,** 4077-94.

KHALED, K. & EL-SHERIK, A. 2013. Using molecular dynamics simulations and genetic function approximation to model corrosion inhibition of iron in chloride solutions. *International Journal of Electrochemical Science,* 8**,** 10022-43.

KHAN, A. & AB GHANI, S. 2012. Multienzyme microbiosensor based on electropolymerized o-phenylenediamine for simultaneous in vitro determination of acetylcholine and choline. *Biosensors and Bioelectronics,* 31**,** 433-8.

KIHARA, T. & SHIMOHAMA, S. 2004. Alzheimer's disease and acetylcholine receptors. *Acta Neurobiologiae Experimentalis,* 64**,** 99-105.

KILLIANY, R. J., GOMEZ-ISLA, T., MOSS, M., KIKINIS, R., SANDOR, T., JOLESZ, F., TANZI, R., JONES, K., HYMAN, B. T. & ALBERT, M. S. 2000. Use of structural magnetic resonance imaging to predict who will g*et al*zheimer's disease. *Annals of Neurology,* 47**,** 430-39.

KIM, C. Y. & RIU, D. H. 2011. Texture control of fluorine-doped tin oxide thin film. *Thin Solid Films,* 519**,** 3081-5.

KIM, H., AUYEUNG, R. C. Y. & PIQUÉ, A. 2008. Transparent conducting F-doped SnO_2 thin films grown by pulsed laser deposition. *Thin Solid Films,* 516**,** 5052-6.

KIM, P. S., DJAZAYERI, S. & ZEINELDIN, R. 2011. Novel nanotechnology approaches to diagnosis and therapy of ovarian cancer. *Gynecologic Oncology* 120**,** 393-403.

KING, M. R., MATZAT, L. H., DALE, R. K., LIM, S. J. & LEI, E. P. 2014. The RNA-binding protein Rumpelstiltskin antagonizes gypsy chromatin insulator function in a tissue-specific manner. *Journal of Cell Science,* 127**,** 2956-66.

KINGA BRUSKA, M., SZACIŁOWSKI, K. & PIECHOTA, J. 2009. Adsorption of selected ions on the anatase TiO_2 (101) surface: A density-functional study. *Molecular Simulation,* 35**,** 567-76.

KOHN, W. & SHAM, L. J. 1965. Self-consistent equations including exchange and correlation effects. *Physical Review,* 140**,** A1133-8.

KORNHERR, A., VOGTENHUBER, D., RUCKENBAUER, M., PODLOUCKY, R. & ZIFFERER, G. 2004. Multilayer adsorption of water at a rutile TiO_2(110) surface: Towards a realistic modeling by molecular dynamics. *The Journal of Chemical Physics,* 121**,** 3722-3726.

KOROLEV, I. O. 2014. Alzheimer's disease: A Clinical and basic science review. *Medical Student Research Journal,* 4**,** 24-33.

KRAEPELIN, E. 1910. *Psychiatrie: Ein lehrbuch für studierende und ärzte,* Leipzig, Barth.

KUNZEL, D., MARKERT, T., GROSS, A. & BENOIT, D. M. 2009. Bis(terpyridine)-based surface template structures on graphite: A force field and DFT study. *Physical Chemistry Chemical Physics,* 11**,** 8867-78.

KUO, Y. M., KOKJOHN, T. A., KALBACK, W., LUEHRS, D., GALASKO, D. R., CHEVALLIER, N., KOO, E. H., EMMERLING, M. R. & ROHER, A. E. 2000. Amyloid-beta peptides interact with plasma proteins and erythrocytes: Implications for their quantitation in plasma. *Biochemical and Biophysical Research Communications,* 268**,** 750-6.

KURZĄTKOWSKA, K., JANKOWSKA, A., WYSŁOUCH-CIESZYŃSKA, A., ZHUKOVA, L., PUCHALSKA, M., DEHAEN, W., RADECKA, H. & RADECKI, J. 2016. Voltammetric detection of the S100B protein using His-tagged RAGE domain immobilized onto a gold electrode modified with a dipyrromethene–Cu(II) complex and different diluents. *Journal of Electroanalytical Chemistry,* 767**,** 76-83.

KUSAMA, H., ORITA, H. & SUGIHARA, H. 2008. DFT investigation of the TiO_2 band shift by nitrogen-containing heterocycle adsorption and implications on dye-sensitized solar cell performance. *Solar Energy Materials and Solar Cells,* 92**,** 84-7.

LAFLEUR, J. P., JÖNSSON, A., SENKBEIL, S. & KUTTER, J. P. 2016. Recent advances in lab-on-a-chip for biosensing applications. *Biosensors and Bioelectronics,* 76**,** 213-3.

LARSON, E. B. 2015. *Evaluation of cognitive impairment and dementia* [Online]. UpToDate, Inc. Available: http://www.uptodate.com/contents/evaluation-of-cognitive-impairment-and-dementia [Accessed 22 September 2015].

LAZZERI, M., VITTADINI, A. & SELLONI, A. 2001. Structure and energetics of stoichiometric TiO_2 anatase surfaces. *Physical Review B,* 63**,** 155409(1-9).

LEE, C., YANG, W. & PARR, R. G. 1988. Development of the Colle-Salvetti correlation-energy formula into a functional of the electron density. *Physical Review B,* 37**,** 785-9.

LEE, J. Y., PARK, J. & CHO, J. H. 2005. Electronic properties of N- and C-doped TiO_2. *Applied Physics Letters,* 87**,** 011904.

LEE, S. H. & RASAIAH, J. C. 1996. Molecular dynamics simulation of ion mobility. 2. alkali metal and halide ions using the SPC/E model for water at 25 °C. *The Journal of Physical Chemistry,* 100**,** 1420-5.

LEVY, M. 1979. Universal variational functionals of electron densities, first-order density matrices, and natural spin-orbitals and solution of the v-representability problem. *Proceedings of the National Academy of Sciences,* 76**,** 6062-5.

LEVY, M. 1982. Electron densities in search of Hamiltonians. *Physical Review A,* 26**,** 1200-8.

LI, F., LI, X., YANG, S., FU, Z. & LU, Y. 2015. Tailoring of {116} faceted single crystalline anatase nanosheet arrays and their improved electrochemical performance. *Crystal and Engineering Communications,* 17**,** 4377-82.

LI, J. G., ISHIGAKI, T. & SUN, X. 2007. Anatase, brookite, and rutile nanocrystals via redox reactions under mild hydrothermal conditions: Phase-selective synthesis and physicochemical properties. *The Journal of Physical Chemistry C,* 111**,** 4969-76.

LI, S. C., LOSOVYJ, Y. & DIEBOLD, U. 2011. Adsorption-site-dependent electronic structure of catechol on the anatase TiO_2(101) surface. *Langmuir,* 27**,** 8600-4.

LI, S. S., LIN, C. W., WEI, K. C., HUANG, C. Y., HSU, P. H., LIU, H. L., LU, Y. J., LIN, S. C., YANG, H. W. & MA, C. C. M. 2016. Non-invasive screening for early Alzheimer's disease diagnosis by a sensitively immunomagnetic biosensor. *Scientific Reports,* 6**,** 25155(1-11).

LIAO, T., WANG, Y., ZHOU, X., ZHANG, Y., LIU, X., DU, J., LI, X. & LU, X. 2010. Detection of DNA damage induced by styrene oxide in dsDNA layer-by-layer films using adriamycin as electroactive probe. *Colloids and Surfaces B: Biointerfaces,* 76**,** 334-9.

LIEN, T. T., TAKAMURA, Y., TAMIYA, E. & VESTERGAARD, M. C. 2015. Modified screen printed electrode for development of a highly sensitive label-free impedimetric immunosensor to detect amyloid beta peptides. *Analytica Chimica Acta,* 892**,** 69-76.

LIM, S., PATERSON, B. M., FODERO-TAVOLETTI, M. T., O'KEEFE, G. J., CAPPAI, R., BARNHAM, K. J., VILLEMAGNE, V. L. & DONNELLY, P. S. 2010. A copper radiopharmaceutical for diagnostic imaging of Alzheimer's disease: A bis(thiosemicarbazonato)copper(II) complex that binds to amyloid-beta plaques. *Chemical communications,* 46**,** 5437-9.

LIN, L., LIU, Y., TANG, L. & LI, J. 2011. Electrochemical DNA sensor by the assembly of graphene and DNA-conjugated gold nanoparticles with silver enhancement strategy. *Analyst,* 136**,** 4732-7.

LIN, X., NI, Y., PEI, X. & KOKOT, S. 2017. Electrochemical detection of DNA damage induced by clenbuterol at a reduced graphene oxide-Nafion modified glassy carbon electrode. *Analytical Methods,* 9**,** 1105-11.

LIU, B., SUN, Y., WANG, X., ZHANG, L., WANG, D., FU, Z., LIN, Y. & XIE, T. 2015a. Branched hierarchical photoanode of anatase TiO_2 nanotubes on rutile TiO_2 nanorod arrays for efficient quantum dot-sensitized solar cells. *Journal of Materials Chemistry A,* 3**,** 4445-52.

LIU, J., DE LA GARZA, L., ZHANG, L., DIMITRIJEVIC, N. M., ZUO, X., TIEDE, D. M. & RAJH, T. 2007. Photocatalytic probing of DNA sequence by using TiO_2/dopamine-DNA triads. *Chemical Physics,* 339**,** 154-63.

LIU, L., HE, Q., ZHAO, F., XIA, N., LIU, H., LI, S., LIU, R. & ZHANG, H. 2014a. Competitive electrochemical immunoassay for detection of beta-amyloid (1-42) and total beta-amyloid peptides using p-aminophenol redox cycling. *Biosensors and Bioelectronics,* 51**,** 208-12.

LIU, L., XIA, N., JIANG, M., HUANG, N., GUO, S., LI, S. & ZHANG, S. 2015b. Electrochemical detection of amyloid-β oligomer with the signal amplification of alkaline phosphatase plus electrochemical–chemical–chemical redox cycling. *Journal of Electroanalytical Chemistry,* 754**,** 40-5.

LIU, X., IQBAL, J., WU, Z., HE, B. & YU, R. 2010. Structure and room-temperature ferromagnetism of Zn-doped SnO_2 nanorods prepared by solvothermal method. *The Journal of Physical Chemistry C,* 114**,** 4790-6.

LIU, Y., JIAO, Y., ZHANG, Z., QU, F., UMAR, A. & WU, X. 2014b. Hierarchical SnO_2 nanostructures made of intermingled ultrathin nanosheets for environmental remediation, smart gas sensor, and supercapacitor applications. *ACS Applied Materials & Interfaces,* 6**,** 2174-84.

LIVRAGHI, S., VOTTA, A., PAGANINI, M. C. & GIAMELLO, E. 2005. The nature of paramagnetic species in nitrogen doped TiO_2 active in visible light photocatalysis. *Chemical Communications***,** 498-500.

LOPERA, F., ARDILLA, A., MARTINEZ, A., MADRIGAL, L., ARANGO-VIANA, J. C., LEMERE, C. A., ARANGO-LASPRILLA, J. C., HINCAPIE, L., ARCOS-BURGOS, M., OSSA, J. E., BEHRENS, I. M., NORTON, J., LENDON, C., GOATE, A. M., RUIZ-LINARES, A., ROSSELLI, M. & KOSIK, K. S. 1997. Clinical features of early-ons*et al*zheimer disease in a large kindred with an E280A presenilin-1 mutation. *The Journal of the American Medical Association,* 277**,** 793-9.

LOPEZ-DE-IPINA, K., ALONSO, J. B., TRAVIESO, C. M., SOLE-CASALS, J., EGIRAUN, H., FAUNDEZ-ZANUY, M., EZEIZA, A., BARROSO, N., ECAY-TORRES, M., MARTINEZ-LAGE, P. & MARTINEZ DE LIZARDUI, U. 2013. On the selection of non-invasive methods based on speech analysis oriented to automatic Alzheimer disease diagnosis. *Sensors (Basel),* 13**,** 6730-45.

LOPEZ, T., BATA-GARCIA, J. L., ESQUIVEL, D., ORTIZ-ISLAS, E., GONZALEZ, R., ASCENCIO, J., QUINTANA, P., OSKAM, G., ALVAREZ-CERVERA, F. J., HEREDIA-LOPEZ, F. J. & GONGORA-ALFARO, J. L. 2010. Treatment of Parkinson's disease: nanostructured sol-gel silica-dopamine reservoirs for controlled drug release in the central nervous system. *International Journal of Nanomedicine,* 6**,** 19-31.

LOVELL, M. A., GABBITA, S. P. & MARKESBERY, W. R. 1999. Increased DNA oxidation and decreased levels of repair products in Alzheimer's disease ventricular CSF. *Journal of Neurochemistry,* 72**,** 771-6.

LOVELL, M. A. & MARKESBERY, W. R. 2007. Oxidative DNA damage in mild cognitive impairment and late-stage Alzheimer's disease. *Nucleic acids research,* 35**,** 7497-504.

LOW, J. J., BENIN, A. I., JAKUBCZAK, P., ABRAHAMIAN, J. F., FAHEEM, S. A. & WILLIS, R. R. 2009. Virtual high throughput screening confirmed experimentally: porous coordination polymer hydration. *Journal of the American Chemical Society,* 131**,** 15834-842.

LÜ, J.-M., LIN, P. H., YAO, Q. & CHEN, C. 2010. Chemical and molecular mechanisms of antioxidants: experimental approaches and model systems. *Journal of Cellular and Molecular Medicine,* 14**,** 840-60.

LUBIN, A. A. & PLAXCO, K. W. 2010. Folding-based electrochemical biosensors: The case for responsive nucleic acid architectures. *Accounts of Chemical Research,* 43**,** 496-505.

LUNDQVIST, S. & MARCH, N. H. 2013. *Theory of the inhomogeneous electron gas,* Germany, Springer Science & Business Media.

LUO, Y., ZHANG, L., LIU, W., YU, Y. & TIAN, Y. 2015. A single biosensor for evaluating the levels of Copper ion and L-cysteine in a live rat brain with Alzheimer's disease. *Angewandte Chemie (International ed. in English),* 54**,** 14053-6.

LY, S. Y., JANG, M.-H., CHA, J.-M., KIM, M.-Y., OH, H.-S., JO, D.-H. & CHOI, S.-S. 2012. Ex vivo assay of trace nicotine using a voltammetric modified biosensor. *Journal of the Korean Oil Chemists Society,* 29**,** 40-6.

MADABHUSHI, R., PAN, L. & TSAI, L. H. 2014. DNA damage and its links to neurodegeneration. *Neuron,* 83**,** 266-82.

MADDALENA, A., PAPASSOTIROPOULOS, A., MULLER-TILLMANNS, B., JUNG, H. H., HEGI, T., NITSCH, R. M. & HOCK, C. 2003. Biochemical diagnosis of Alzheimer disease by measuring the cerebrospinal fluid ratio of phosphorylated tau protein to beta-amyloid peptide42. *Archives of Neurology,* 60**,** 1202-6.

MAGUIRE-ZEISS, K. A., SHORT, D. W. & FEDEROFF, H. J. 2005. Synuclein, dopamine and oxidative stress: co-conspirators in Parkinson's disease? *Molecular Brain Research,* 134**,** 18-23.

MAITLAND, G. C. 1981. *Intermolecular forces: Their origin and determination,* England, Oxford University Press.

MAKARUCHA, A. J., TODOROVA, N. & YAROVSKY, I. 2011. Nanomaterials in biological environment: A review of computer modelling studies. *European Biophysics Journal,* 40**,** 103-15.

MALPASS, K. 2012. Alzheimer disease: DNA damage provides novel and powerful biomarkers of Alzheimer disease. *Nature Reviews Neurology,* 8**,** 178.

MAO, P. & REDDY, P. H. 2011. Aging and amyloid beta-induced oxidative DNA damage and mitochondrial dysfunction in Alzheimer's disease: Implications for early intervention and therapeutics. *Biochimica et Biophysica Acta (BBA) - Molecular Basis of Disease,* 1812**,** 1359-70.

MARCILLO, F. & STASHANS, A. 2014. DFT calculations of tin dioxide crystals containing heavily-doped fluorine. *Journal of Theoretical and Computational Chemistry,* 13**,** 1450069(1-15).

MARKESBERY, W. R. & LOVELL, M. A. 2006. DNA oxidation in Alzheimer's disease. *Antioxidants & Redox Signaling,* 8**,** 2039-45.

MASAYOSHI MIKAMI, SHINICHIRO NAKAMURA, OSAMU KITAO, HIRONORI ARAKAWA & XAVIER GONZE 2000. First-principles study of titanium dioxide: Rutile and anatase. *Japanese Journal of Applied Physics,* 39**,** L847-50.

MATHEW, A., GOWRAVARAM, M. R. & NOOKALA, M. 2013. Application of mesoporous anatase TiO_2 microspheres for dye sensitized solar cell on flexible titanium metal photo anode. *Advanced Materials Letters***,** 737-41.

MATHIS, C. A., WANG, Y., HOLT, D. P., HUANG, G. F., DEBNATH, M. L. & KLUNK, W. E. 2003. Synthesis and evaluation of 11C-labeled 6-substituted 2-arylbenzothiazoles as amyloid imaging agents. *Journal of Medicinal Chemistry,* 46**,** 2740-54.

MATSUZAWA, N., SETO, J. E. & DIXON, D. A. 1997. Density functional theory predictions of second-order hyperpolarizabilities of metallocenes. *The Journal of Physical Chemistry A,* 101**,** 9391-8.

MATTSON, M. P. & CHAN, S. L. 2003. Neuronal and glial calcium signaling in Alzheimer's disease. *Cell Calcium,* 34**,** 385-97.

MAURER, K., VOLK, S. & GERBALDO, H. 1997. Auguste D and Alzheimer's disease. *Lancet,* 349**,** 1546-9.

MAYO, S. L., OLAFSON, B. D. & GODDARD, W. A. 1990. DREIDING: A generic force field for molecular simulations. *The Journal of Physical Chemistry,* 94**,** 8897-909.

MCKHANN, G. M., KNOPMAN, D. S., CHERTKOW, H., HYMAN, B. T., JACK, C. R., JR., KAWAS, C. H., KLUNK, W. E., KOROSHETZ, W. J., MANLY, J. J., MAYEUX, R., MOHS, R. C., MORRIS, J. C., ROSSOR, M. N., SCHELTENS, P., CARRILLO, M. C., THIES, B., WEINTRAUB, S. & PHELPS, C. H. 2011. The diagnosis of dementia due to Alzheimer's disease: recommendations from the National Institute on Aging-Alzheimer's

Association workgroups on diagnostic guidelines for Alzheimer's disease. *Alzheimer's & Dementia: The Journal of the Alzheimer's Association,* 7**,** 263-9.

MCKINNON, P. J. 2013. Maintaining genome stability in the nervous system. *Nature Neuroscience,* 16**,** 1523-9.

MDLULI, P. S., SOSIBO, N. M., MASHAZI, P. N., NYOKONG, T., TSHIKHUDO, R. T., SKEPU, A. & VAN DER LINGEN, E. 2011. Selective adsorption of PVP on the surface of silver nanoparticles: A molecular dynamics study. *Journal of Molecular Structure,* 1004**,** 131-7.

MECOCCI, P., MACGARVEY, U. & BEAL, M. F. 1994. Oxidative damage to mitochondrial DNA is increased in Alzheimer's disease. *Annals of Neurology,* 36**,** 747-51.

MEDINA-SÁNCHEZ, M., MISERERE, S., MORALES-NARVÁEZ, E. & MERKOÇI, A. 2014. On-chip magneto-immunoassay for Alzheimer's biomarker electrochemical detection by using quantum dots as labels. *Biosensors and Bioelectronics,* 54**,** 279-84.

METROPOLIS, N., ROSENBLUTH, A. W., ROSENBLUTH, M. N., TELLER, A. H. & TELLER, E. 1953. Equation of state calculations by fast computing machines. *The Journal of Chemical Physics,* 21**,** 1087-92.

MIAO, L., BHETHANABOTLA, V. R. & JOSEPH, B. 2005. Melting of Pd clusters and nanowires: A comparison study using molecular dynamics simulation. *Physical Review B,* 72**,** 134109(1-12).

MIGLIO, A., SANIZ, R., WAROQUIERS, D., STANKOVSKI, M., GIANTOMASSI, M., HAUTIER, G., RIGNANESE, G. M. & GONZE, X. 2014. Computed electronic and optical properties of SnO_2 under compressive stress. *Optical Materials,* 38**,** 161-6.

MIKULA, E., WYSLOUCH-CIESZYNSKA, A., ZHUKOVA, L., PUCHALSKA, M., VERWILST, P., DEHAEN, W., RADECKI, J. & RADECKA, H. 2014. Voltammetric detection of S100B protein using His-tagged receptor domains for advanced glycation end products (RAGE) immobilized onto a gold electrode surface. *Sensors (Basel),* 14**,** 10650-63.

MISRA, R., ACHARYA, S. & SAHOO, S. K. 2010. Cancer nanotechnology: Application of nanotechnology in cancer therapy. *Drug Discovery Today,* 15**,** 842-50.

MIURA, Y., YASUDA, K., YAMAMOTO, K., KOIKE, M., NISHIDA, Y. & KOBAYASHI, K. 2007. Inhibition of Alzheimer amyloid aggregation with sulfated glycopolymers. *Biomacromolecules,* 8**,** 2129-34.

MLAMBO, M., HARRIS, R. A., MASHAZI, P., SABELA, M., KANCHI, S., MADIKIZELA, L. M., SHUMBULA, P. N., MOLOTO, N., HLATSHWAYO, T. T. & MDLULI, P. S. 2017. Computational and experimental evaluation of selective substitution of thiolated coumarin derivatives on gold nanoparticles: Surface enhancing Raman scattering and electrochemical studies. *Applied Surface Science,* 396**,** 695-704.

MO, S.-D. & CHING, W. Y. 1995. Electronic and optical properties of three phases of titanium dioxide: Rutile, anatase, and brookite. *Physical Review B,* 51**,** 13023-32.

MOHOLKAR, A. V., PAWAR, S. M., RAJPURE, K. Y., BHOSALE, C. H. & KIM, J. H. 2009. Effect of fluorine doping on highly transparent conductive spray deposited nanocrystalline tin oxide thin films. *Applied Surface Science,* 255**,** 9358-64.

MOULIN, C. J. A., LAINE, M., RINNE, J. O., KAASINEN, V., SIPILA, H., HILTUNEN, J. & KANGASMAKI, A. 2007. Brain function during multi-trial learning in mild cognitive impairment: A PET activation study. *Brain Research,* 1136**,** 132-41.

MURAMATSU, H., KIM, J. M. & CHANG, S. M. 2002. Quartz-crystal sensors for biosensing and chemical analysis. *Analytical and Bioanalytical Chemistry,* 372**,** 314-21.

NAGAVENI, K., HEGDE, M. S., RAVISHANKAR, N., SUBBANNA, G. N. & MADRAS, G. 2004. Synthesis and structure of nanocrystalline TiO_2 with lower band gap showing high photocatalytic activity. *Langmuir: The ACS Journal of Surfaces and Colloids* 20**,** 2900-7.

NAICKER, P. K., CUMMINGS, P. T., ZHANG, H. & BANFIELD, J. F. 2005. Characterization of titanium dioxide nanoparticles using molecular dynamics simulations. *The Journal of Physical Chemistry B,* 109**,** 15243-49.

NAKAJIMA, T. & GROULT, H. 2005. *Fluorinated materials for energy conversion*, Netherland, Elsevier.

NATIONAL CENTER FOR BIOTECHNOLOGY INFORMATION 2004. PubChem Compound Database; CID=681.

NAZEM, A. & MANSOORI, G. A. 2011. Nanotechnology for Alzheimer's disease detection and treatment. *Insciences Journal,* 1**,** 169-93.

NGAOJAMPA, C., NIMMANPIPUG, P., YU, L., ANUNTALABHOCHAI, S. & LEE, V. S. 2010. Molecular simulations of ultra-low-energy nitrogen ion bombardment of A-DNA in vacuum. *Journal of Molecular Graphics and Modelling,* 28**,** 533-9.

NISHIMOTO, Y., FEDOROV, D. G. & IRLE, S. 2014. Density-Functional Tight-Binding combined with the fragment molecular orbital method. *Journal of Chemical Theory and Computation,* 10**,** 4801-12.

NIST 2005. *NIST Chemistry WebBook, NIST Standard Reference Database Number 69,* United States, National Institute of Standards and Technology.

NORBERG, J. & NILSSON, L. 2002. Molecular dynamics applied to nucleic acids. *Accounts of Chemical Research,* 35**,** 465-72.

NORDBERG, A. 2001. Nicotinic receptor abnormalities of Alzheimer's disease: Therapeutic implications. *Biological Psychiatry,* 49**,** 200-10.

NOSÉ, S. 1984a. A molecular dynamics method for simulations in the canonical ensemble. *Molecular physics,* 52**,** 255-68.

NOSÉ, S. 1984b. A unified formulation of the constant temperature molecular dynamics methods. *The Journal of Chemical Physics,* 81**,** 511-9.

NUNOMURA, A., PERRY, G., ALIEV, G., HIRAI, K., TAKEDA, A., BALRAJ, E. K., JONES, P. K., GHANBARI, H., WATAYA, T., SHIMOHAMA, S., CHIBA, S., ATWOOD, C. S., PETERSEN, R. B. & SMITH, M. A. 2001. Oxidative damage is the earliest event in Alzheimer disease. *Journal of Neuropathology and Experimental Neurology,* 60**,** 759-67.

NUNOMURA, A., PERRY, G., PAPPOLLA, M. A., WADE, R., HIRAI, K., CHIBA, S. & SMITH, M. A. 1999. RNA oxidation is a prominent feature of vulnerable neurons in Alzheimer's disease. *The Journal of Neuroscience: The Official Journal of the Society for Neuroscience,* 19**,** 1959-64.

O'BRYANT, S. E., GUPTA, V., HENRIKSEN, K., EDWARDS, M., JEROMIN, A., LISTA, S., BAZENET, C., SOARES, H., LOVESTONE, S., HAMPEL, H., MONTINE, T., BLENNOW, K., FOROUD, T., CARRILLO, M., GRAFF-RADFORD, N., LASKE, C., BRETELER, M., SHAW, L., TROJANOWSKI, J. Q., SCHUPF, N., RISSMAN, R. A., FAGAN, A. M., OBEROI, P., UMEK, R., WEINER, M. W., GRAMMAS, P., POSNER, H. & MARTINS, R. 2015. Guidelines for the standardization of preanalytic variables for blood-based biomarker studies in Alzheimer's disease research. *Alzheimer's & Dementia: The Journal of the Alzheimer's Association,* 11**,** 549-60.

O'REGAN, B. & GRATZEL, M. 1991. A low-cost, high-efficiency solar cell based on dye-sensitized colloidal TiO_2 films. *Nature,* 353**,** 737-40.

OGAWA, T., KURITA, N., SEKINO, H., KITAO, O. & TANAKA, S. 2003. Hydrogen bonding of DNA base pairs by consistent charge equilibration method combined with universal force field. *Chemical Physics Letters,* 374**,** 271-8.

OH, J., YOO, G., CHANG, Y. W., KIM, H. J., JOSE, J., KIM, E., PYUN, J.-C. & YOO, K.-H. 2013. A carbon nanotube metal semiconductor field effect transistor-based biosensor for detection of amyloid-beta in human serum. *Biosensors and Bioelectronics,* 50**,** 345-50.

OHSAKA, T., IZUMI, F. & FUJIKI, Y. 1978. Raman spectrum of anatase, TiO_2. *Journal of Raman Spectroscopy,* 7**,** 321-4.

ONIDA, G., REINING, L. & RUBIO, A. 2002. Electronic excitations: density-functional versus many-body Green's-function approaches. *Reviews of Modern Physics,* 74**,** 601-59.

OSIKOYA, A. O. & TIWARI, A. 2016. Recent advances in 2D bioelectronics. *Biosensors and Bioelectronics,* 89**,** 1-7.

OSKAM, G., NELLORE, A., PENN, R. L. & SEARSON, P. C. 2003. The growth kinetics of TiO_2 nanoparticles from titanium(iv) alkoxide at high water/titanium ratio. *The Journal of Physical Chemistry B,* 107**,** 1734-8.

OSNIS, A., SUKENIK, C. N. & MAJOR, D. T. 2012. Structure of carboxyl-acid-terminated self-assembled monolayers from molecular dynamics simulations and hybrid quantum mechanics–molecular mechanics vibrational normal-mode analysis. *The Journal of Physical Chemistry C,* 116**,** 770-82.

OTTO, M., WILTFANG, J., TUMANI, H., ZERR, I., LANTSCH, M., KORNHUBER, J., WEBER, T., KRETZSCHMAR, H. A. & POSER, S. 1997. Elevated levels of tau-protein in cerebrospinal fluid of patients with Creutzfeldt-Jakob disease. *Neuroscience Letters,* 225**,** 210-2.

PADURARIU, M., CIOBICA, A., LEFTER, R., SERBAN, I. L., STEFANESCU, C. & CHIRITA, R. 2013. The oxidative stress hypothesis in Alzheimer's disease. *Psychiatria Danubina,* 25**,** 401-9.

PAIER, J., MARSMAN, M. & KRESSE, G. 2007. Why does the B3LYP hybrid functional fail for metals? *The Journal of Chemical Physics,* 127**,** 024103(1-10).

PALEČEK, E. & BARTOŠÍK, M. 2012. Electrochemistry of nucleic acids. *Chemical Reviews,* 112**,** 3427-81.

PANDE, S., JANA, S., SINHA, A. K., SARKAR, S., BASU, M., PRADHAN, M., PAL, A., CHOWDHURY, J. & PAL, T. 2009. Dopamine molecules on Aucore−Agshell bimetallic nanocolloids: Fourier Transform Infrared, Raman, and Surface-Enhanced Raman Spectroscopy study aided by density functional theory. *The Journal of Physical Chemistry C,* 113**,** 6989-7002.

PARLAK, O., TURNER, A. P. F. & TIWARI, A. 2014. On/Off-switchable zipper-like bioelectronics on a graphene interface. *Advanced Materials,* 26**,** 482-6.

PATRA, S., ROY, E., TIWARI, A., MADHURI, R. & SHARMA, P. K. 2016. 2-Dimensional graphene as a route for emergence of additional dimension nanomaterials. *Biosensors and Bioelectronics,* 89**,** 8-27.

PAUNESKU, T., RAJH, T., WIEDERRECHT, G., MASER, J., VOGT, S., STOJICEVIC, N., PROTIC, M., LAI, B., ORYHON, J., THURNAUER, M. & WOLOSCHAK, G. 2003. Biology of TiO_2-oligonucleotide nanocomposites. *Nature Materials,* 2**,** 343-6.

PAZOKI, M., OSCARSSON, J., YANG, L., PARK, B. W., JOHANSSON, E. M. J., RENSMO, H., HAGFELDT, A. & BOSCHLOO, G. 2014a. Mesoporous TiO_2 microbead electrodes for solid state dye-sensitized solar cells. *RSC Advances,* 4**,** 50295-300.

PAZOKI, M., TAGHAVINIA, N., HAGFELDT, A. & BOSCHLOO, G. 2014b. Mesoporous TiO_2 microbead electrodes for cobalt-mediator-based dye-sensitized solar cells. *The Journal of Physical Chemistry C,* 118**,** 16472-8.

PEICA, N., LEHENE, C., LEOPOLD, N., SCHLÜCKER, S. & KIEFER, W. 2007. Monosodium glutamate in its anhydrous and monohydrate form: Differentiation by Raman spectroscopies and density functional calculations. *Spectrochimica Acta Part A: Molecular and Biomolecular Spectroscopy,* 66**,** 604-15.

PELAEZ, M., NOLAN, N. T., PILLAI, S. C., SEERY, M. K., FALARAS, P., KONTOS, A. G., DUNLOP, P. S. M., HAMILTON, J. W. J., BYRNE, J. A., O'SHEA, K., ENTEZARI, M. H. & DIONYSIOU, D. D. 2012. A review on the visible light active titanium dioxide photocatalysts for environmental applications. *Applied Catalysis B: Environmental,* 125**,** 331-49.

PERDEW, J. P., BURKE, K. & ERNZERHOF, M. 1996. Generalized Gradient Approximation made simple. *Physical Review Letters,* 77**,** 3865-68.

PERDEW, J. P., RUZSINSZKY, A., CSONKA, G. I., VYDROV, O. A., SCUSERIA, G. E., CONSTANTIN, L. A., ZHOU, X. & BURKE, K. 2008. Restoring the density-gradient expansion for exchange in solids and surfaces. *Physical Review Letters,* 100**,** 136406(1-4).

PERDEW, J. P. & SCHMIDT, K. 2001. Jacob's ladder of density functional approximations for the exchange-correlation energy. *In:* VAN DOREN, V., VAN ALSENOY, C. & GEERLINGS, P. (eds.) *Density functional theory and its application to materials.* Belgium: AIP Conference Proceedings.

PERDEW, J. P. & WANG, Y. 1992. Accurate and simple analytic representation of the electron-gas correlation energy. *Physical Review B,* 45**,** 13244-9.

PERRIG, W. J., PERRIG, P. & STAHELIN, H. B. 1997. The relation between antioxidants and memory performance in the old and very old. *Journal of the American Geriatrics Society,* 45**,** 718-24.

PERSSON, P., BERGSTRÖM, R. & LUNELL, S. 2000. Quantum chemical study of photoinjection processes in dye-sensitized TiO_2 nanoparticles. *The Journal of Physical Chemistry B,* 104**,** 10348-51.

PERSSON, T., POPESCU, B. O. & CEDAZO-MINGUEZ, A. 2014. Oxidative stress in Alzheimer's disease: Why did antioxidant therapy fail? *Oxidative Medicine and Cellular Longevity,* 2014**,** 427318(1-11).

PLASSMAN, B. L., LANGA, K. M., FISHER, G. G., HEERINGA, S. G., WEIR, D. R., OFSTEDAL, M. B., BURKE, J. R., HURD, M. D., POTTER, G. G., RODGERS, W. L., STEFFENS, D. C., WILLIS, R. J. & WALLACE, R. B. 2007. Prevalence of dementia in the United States: The aging, demographics, and memory study. *Neuroepidemiology,* 29**,** 125-32.

POHANKA, M. 2014a. Alzheimer's disease and oxidative stress: A review. *Current Medicinal Chemistry,* 21**,** 356-64.

POHANKA, M. 2014b. Biosensors containing acetylcholinesterase and butyrylcholinesterase as recognition tools for detection of various compounds. *Chemical Papers***,** 1-13.

POHANKA, M., ADAM, V. & KIZEK, R. 2013. An acetylcholinesterase-based chronoamperometric biosensor for fast and reliable assay of nerve agents. *Sensors (Basel),* 13**,** 11498-506.

POLIDORI, M. C. & SCHULZ, R.-J. 2014. Nutritional contributions to dementia prevention: Main issues on antioxidant micronutrients. *Genes & Nutrition,* 9**,** 382(1-11).

PRATHAB, B., SUBRAMANIAN, V. & AMINABHAVI, T. M. 2007. Molecular dynamics simulations to investigate polymer–polymer and polymer–metal oxide interactions. *Polymer,* 48**,** 409-16.

PTASIŃSKA, S., LI, Z., MASON, N. J. & SANCHE, L. 2010. Damage to amino acid–nucleotide pairs induced by 1 eV electrons. *Physical Chemistry Chemical Physics,* 12**,** 1-15.

PUNDIR, S., CHAUHAN, N., NARANG, J. & PUNDIR, C. S. 2012. Amperometric choline biosensor based on multiwalled carbon nanotubes/zirconium oxide nanoparticles electrodeposited on glassy carbon electrode. *Analytical Biochemistry,* 427**,** 26-32.

PUTRI, A. D., TRI MURTI, B., SABELA, M., KANCHI, S. & BISETTY, K. 2017. Nanopolymer chitosan in cancer and Alzheimer biomedical application. *In:* AHMED, S. & IKRAM, S. (eds.) *Chitosan: Derivatives, composites and applications.* USA: Wiley-Scrivener.

RAJH, T., SAPONJIC, Z., LIU, J., DIMITRIJEVIC, N. M., SCHERER, N. F., VEGA-ARROYO, M., ZAPOL, P., CURTISS, L. A. & THURNAUER, M. C. 2004. Charge transfer across the nanocrystalline-DNA interface: Probing DNA recognition. *Nano Letters,* 4**,** 1017-23.

RAMACHANDRAN, K. I., DEEPA, G. & NAMBOORI, K. 2008. *Computational chemistry and molecular modeling: Principles and applications,* Germany, Springer.

RAMZAN, M., LI, Y., CHIMATA, R. & AHUJA, R. 2013. Electronic, mechanical and optical properties of Y2O3 with hybrid density functional (HSE06). *Computational Materials Science,* 71**,** 19-24.

RAPPE, A. K., CASEWIT, C. J., COLWELL, K. S., GODDARD, W. A. & SKIFF, W. M. 1992. UFF, a full periodic table force field for molecular mechanics and molecular dynamics simulations. *Journal of the American Chemical Society,* 114**,** 10024-35.

RAPPE, A. K., COLWELL, K. S. & CASEWIT, C. J. 1993. Application of a universal force field to metal complexes. *Inorganic Chemistry,* 32**,** 3438-50.

RAY, S., BRITSCHGI, M., HERBERT, C., TAKEDA-UCHIMURA, Y., BOXER, A., BLENNOW, K., FRIEDMAN, L. F., GALASKO, D. R., JUTEL, M., KARYDAS, A., KAYE, J. A., LESZEK, J., MILLER, B. L., MINTHON, L., QUINN, J. F., RABINOVICI, G. D., ROBINSON, W. H., SABBAGH, M. N., SO, Y. T., SPARKS, D. L., TABATON, M., TINKLENBERG, J., YESAVAGE, J. A., TIBSHIRANI, R. & WYSS-CORAY, T. 2007. Classification and prediction of clinical Alzheimer's diagnosis based on plasma signaling proteins. *Nature Medicine,* 13**,** 1359-62.

RAYCHAUDHURI, S. Introduction to monte carlo simulation. Simulation Conference, 2008. WSC 2008. Winter, 2008 United States. IEEE, 91-100.

REYES-CORONADO, D., RODRÍGUEZ-GATTORNO, G., ESPINOSA-PESQUEIRA, M. E., CAB, C., COSS, R. D. & OSKAM, G. 2008. Phase-pure TiO_2 nanoparticles: Anatase, brookite and rutile. *Nanotechnology,* 19**,** 145605(1-10).

REZAEI, B., BOROUJENI, M. K. & ENSAFI, A. A. 2015. Fabrication of DNA, o-phenylenediamine, and gold nanoparticle bioimprinted polymer electrochemical sensor for the determination of dopamine. *Biosensors and Bioelectronics,* 66**,** 490-6.

RHODES, C. L., BREWER, S. H., FOLMER, J. & FRANZEN, S. 2008a. Investigation of hexadecanethiol self-assembled monolayers on cadmium tin oxide thin films. *Thin Solid Films,* 516**,** 1838-42.

RHODES, C. L., LAPPI, S., FISCHER, D., SAMBASIVAN, S., GENZER, J. & FRANZEN, S. 2008b. Characterization of monolayer formation on aluminum-doped zinc oxide thin films. *Langmuir,* 24**,** 433-40.

ROBAKIS, N. K., RAMAKRISHNA, N., WOLFE, G. & WISNIEWSKI, H. M. 1987. Molecular cloning and characterization of a cDNA encoding the cerebrovascular and the neuritic plaque amyloid peptides. *Proceedings of the National Academy of Sciences of the United States of America,* 84**,** 4190-4.

RODRIGUEZ, J. A., HANSON, J. C., CHATURVEDI, S., MAITI, A. & BRITO, J. L. 2000. Phase transformations and electronic properties in mixed-metal oxides: Experimental and theoretical studies on the behavior of $NiMoO_4$ and $MgMoO_4$. *The Journal of Chemical Physics,* 112**,** 935-45.

RUSHWORTH, J. V., AHMED, A., GRIFFITHS, H. H., POLLOCK, N. M., HOOPER, N. M. & MILLNER, P. A. 2014. A label-free electrical impedimetric biosensor for the specific detection of Alzheimer's amyloid-beta oligomers. *Biosensors and Bioelectronics,* 56**,** 83-90.

SABELA, M. I., MPANZA, T., KANCHI, S., SHARMA, D. & BISETTY, K. 2016. Electrochemical sensing platform amplified with a nanobiocomposite of L-phenylalanine ammonia-lyase enzyme for the detection of capsaicin. *Biosensors and Bioelectronics,* 83**,** 45-53.

SAMOLETOV, A. A., DETTMANN, C. P. & CHAPLAIN, M. A. J. 2007. Thermostats for "slow" configurational modes. *Journal of Statistical Physics,* 128**,** 1321-36.

SANDHU, S. K. & KAUR, G. 2002. Alterations in oxidative stress scavenger system in aging rat brain and lymphocytes. *Biogerontology,* 3**,** 161-73.

SANG, L., ZHANG, Y., WANG, J., ZHAO, Y. & CHEN, Y.-T. 2016. Correlation of the depletion layer with the Helmholtz layer in the anatase TiO_2-H_2O interface via molecular dynamics simulations. *Physical Chemistry Chemical Physics,* 18**,** 15427-35.

SANKARA SUBRAMANIAN, N., SANTHI, B., SUNDARESWARAN, S. & VENKATAKRISHNAN, K. S. 2006. Studies on spray deposited SnO_2, Pd:SnO_2 and F:SnO_2 thin films for gas sensor applications. *Synthesis and Reactivity in Inorganic, Metal-Organic, and Nano-Metal Chemistry,* 36**,** 131-5.

SANTOS, R. X., CORREIA, S. C., ZHU, X., LEE, H. G., PETERSEN, R. B., NUNOMURA, A., SMITH, M. A., PERRY, G. & MOREIRA, P. I. 2012. Nuclear and mitochondrial DNA oxidation in Alzheimer's disease. *Free Radical Research,* 46**,** 565-76.

SARKAR, J., CHOWDHURY, J., GHOSH, M., DE, R. & TALAPATRA, G. B. 2005a. Adsorption of 2-aminobenzothiazole on colloidal silver particles: An experimental and theoretical Surface-Enhanced Raman Scattering study. *The Journal of Physical Chemistry B,* 109**,** 12861-67.

SARKAR, J., CHOWDHURY, J., GHOSH, M., DE, R. & TALAPATRA, G. B. 2005b. Experimental and theoretical Surface Enhanced Raman Scattering study of 2-amino-4-methylbenzothiazole adsorbed on colloidal silver particles. *The Journal of Physical Chemistry B,* 109**,** 22536-44.

SAYRE, L. M., PERRY, G. & SMITH, M. A. 2008. Oxidative stress and neurotoxicity. *Chemical Research in Toxicology,* 21**,** 172-88.

SCANLON, D. O., DUNNILL, C. W., BUCKERIDGE, J., SHEVLIN, S. A., LOGSDAIL, A. J., WOODLEY, S. M., CATLOW, C. R. A., POWELL, M. J., PALGRAVE, R. G., PARKIN, I. P., WATSON, G. W., KEAL, T. W., SHERWOOD, P., WALSH, A. & SOKOL, A. A. 2013. Band alignment of rutile and anatase TiO_2. *Nature Materials,* 12**,** 798-801.

SCARANTO, J. & GIORGIANNI, S. 2009. A DFT study of CO adsorbed on clean and hydroxylated anatase TiO_2 (001) surfaces. *Molecular Physics,* 107**,** 1997-2003.

SCHAEFER, C., BRÄUER, G. & SZCZYRBOWSKI, J. 1997. Low emissivity coatings on architectural glass. *Surface and Coatings Technology,* 93**,** 37-45.

SCHLICK, T. 2010. *Molecular modeling and simulation: An interdisciplinary guide,* Germany, Springer

SCHNEIDER, P., HAMPEL, H. & BUERGER, K. 2009. Biological marker candidates of Alzheimer's disease in blood, plasma, and serum. *CNS Neuroscience & Therapeutics,* 15**,** 358-74.

SCOUTEN, W. H., LUONG, J. H. T. & STEPHEN BROWN, R. 1995. Enzyme or protein immobilization techniques for applications in biosensor design. *Trends in Biotechnology,* 13**,** 178-85.

SEGALL, M. D., PHILIP, J. D. L., PROBERT, M. J., PICKARD, C. J., HASNIP, P. J., CLARK, S. J. & PAYNE, M. C. 2002. First-principles simulation: Ideas, illustrations and the CASTEP code. *Journal of Physics: Condensed Matter,* 14**,** 2717-44.

SHAO, Y., MOLNAR, L. F., JUNG, Y., KUSSMANN, J., OCHSENFELD, C., BROWN, S. T., GILBERT, A. T. B., SLIPCHENKO, L. V., LEVCHENKO, S. V., O'NEILL, D. P., DISTASIO JR, R. A., LOCHAN, R. C., WANG, T., BERAN, G. J. O., BESLEY, N. A., HERBERT, J. M., YEH LIN, C., VAN VOORHIS, T., HUNG CHIEN, S., SODT, A., STEELE, R. P., RASSOLOV, V. A., MASLEN, P. E., KORAMBATH, P. P., ADAMSON, R. D., AUSTIN, B., BAKER, J., BYRD, E. F. C., DACHSEL, H., DOERKSEN, R. J., DREUW, A., DUNIETZ, B. D., DUTOI, A. D., FURLANI, T. R., GWALTNEY, S. R., HEYDEN, A., HIRATA, S., HSU, C. P., KEDZIORA, G., KHALLIULIN, R. Z., KLUNZINGER, P., LEE, A. M., LEE, M. S., LIANG, W., LOTAN, I., NAIR, N., PETERS, B., PROYNOV, E. I., PIENIAZEK, P. A., MIN RHEE, Y., RITCHIE, J., ROSTA, E., DAVID SHERRILL, C., SIMMONETT, A. C., SUBOTNIK, J. E., LEE WOODCOCK III, H., ZHANG, W., BELL, A. T., CHAKRABORTY, A. K., CHIPMAN, D. M., KEIL, F. J., WARSHEL, A., HEHRE, W. J., SCHAEFER III, H. F., KONG, J., KRYLOV, A. I., GILL, P. M. W. & HEAD-GORDON, M. 2006. Advances in methods and algorithms in a modern quantum chemistry program package. *Physical Chemistry Chemical Physics,* 8**,** 3172-91.

SHI, L. B., QI, G. Q. & DONG, H. K. 2013. First-principles study of the magnetic properties of Zn-doped SnO_2. *Materials Science in Semiconductor Processing,* 16**,** 877-83.

SHI, Z. & ATRENS, A. 2011. An innovative specimen configuration for the study of Mg corrosion. *Corrosion Science,* 53**,** 226-46.

SHIN, K. S., JI, J. H., PARK, M. C., KIM, M. & KANG, J. Y. 2015a. Highly sensitive detection of amyloid beta for Alzheimer's disease diagnosis using bead-based impedance spectrometry. *Alzheimer's & Dementia: The Journal of the Alzheimer's Association,* 11**,** P352.

SHIN, K. S., KIM, M. J., LEE, S. H. & KANG, J. Y. Novel detection platform for Alzheimer's amyloid-beta using magnetic beads in electrochemical impedance spectroscopy. Micro Electro Mechanical Systems (MEMS), 2015 28th IEEE International Conference on, 2015b Portugal. IEEE, 604-7.

SHOGHI-JADID, K., SMALL, G. W., AGDEPPA, E. D., KEPE, V., ERCOLI, L. M., SIDDARTH, P., READ, S., SATYAMURTHY, N., PETRIC, A., HUANG, S. C. & BARRIO, J. R. 2002. Localization of neurofibrillary tangles and beta-amyloid plaques in the brains of living patients with Alzheimer disease. *The American Journal of Geriatric Psychiatry: Official Journal of The American Association for Geriatric Psychiatry,* 10**,** 24-35.

SHRUTHI, G. S., AMITHA, C. V. & MATHEW, B. B. 2014. Biosensors: A Modern Day Achievement. *Journal of Instrumentation Technology,* 2**,** 26-39.

SHUICHI, N. 1991. Constant temperature molecular dynamics methods. *Progress of Theoretical Physics Supplement,* 103**,** 1-46.

SI, J. C., LU, L., GAO, Z. F., ZHANG, Y., LUO, H. Q. & BING LI, N. 2014. A sensitive electrochemical method based on Fenton-induced DNA oxidation for detection of hydroxyl radical. *Analytical Methods,* 6**,** 6536-40.

SILVERMAN, D. H., GAMBHIR, S. S., HUANG, H. W., SCHWIMMER, J., KIM, S., SMALL, G. W., CHODOSH, J., CZERNIN, J. & PHELPS, M. E. 2002. Evaluating early dementia with and without assessment of regional cerebral metabolism by PET: A comparison of predicted costs and benefits. *Journal of Nuclear Medicine: Official Publication, Society of Nuclear Medicine,* 43**,** 253-66.

ŞIMŞEK, Ş., AYNACı, E. & ARSLAN, F. 2016. An amperometric biosensor for L-glutamate determination prepared from L-glutamate oxidase immobilized in polypyrrole-polyvinylsulphonate film. *Artificial Cells, Nanomedicine, and Biotechnology,* 44**,** 356-61.

SKRABANA, R., SKRABANOVA-KHUEBACHOVA, M., KONTSEK, P. & NOVAK, M. 2006. Alzheimer's-disease-associated conformation of intrinsically disordered tau protein studied by intrinsically disordered protein liquid-phase competitive enzyme-linked immunosorbent assay. *Analytical Biochemistry,* 359**,** 230-7.

SMALL, G. W., DONOHUE, J. A. & BROOKS, R. L. 1998. An economic evaluation of donepezil in the treatment of Alzheimer's disease. *Clinical Therapeutics,* 20**,** 838-50.

SMITH, A. M. & NIE, S. 2010. Semiconductor nanocrystals: Structure, properties, and band gap engineering. *Accounts of Chemical Research,* 43**,** 190-200.

SMITH, D. P., CICCOTOSTO, G. D., TEW, D. J., FODERO-TAVOLETTI, M. T., JOHANSSEN, T., MASTERS, C. L., BARNHAM, K. J. & CAPPAI, R. 2007. Concentration dependent Cu^{2+} induced aggregation and dityrosine formation of the Alzheimer's disease amyloid-beta peptide. *Biochemistry,* 46**,** 2881-91.

SOLDATKIN, O., NAZAROVA, A., KRISANOVA, N., BORYSOV, A., KUCHERENKO, D., KUCHERENKO, I., POZDNYAKOVA, N., SOLDATKIN, A. & BORISOVA, T. 2015. Monitoring of the velocity of high-affinity glutamate uptake by isolated brain nerve terminals using amperometric glutamate biosensor. *Talanta,* 135**,** 67-74.

SOPER, S. A., BROWN, K., ELLINGTON, A., FRAZIER, B., GARCIA-MANERO, G., GAU, V., GUTMAN, S. I., HAYES, D. F., KORTE, B., LANDERS, J. L., LARSON, D., LIGLER, F., MAJUMDAR, A., MASCINI, M., NOLTE, D., ROSENZWEIG, Z., WANG, J. & WILSON, D. 2006. Point-of-care biosensor systems for cancer diagnostics/prognostics. *Biosensors and Bioelectronics,* 21**,** 1932-42.

SORESCU, D. C., AL-SAIDI, W. A. & JORDAN, K. D. 2011. CO_2 adsorption on TiO_2 (101) anatase: A dispersion-corrected density functional theory study. *The Journal of Chemical Physics,* 135**,** 124701(1-17).

SOSIBO, N. M., MDLULI, P. S., MASHAZI, P. N., DYAN, B., REVAPRASADU, N., NYOKONG, T., TSHIKHUDO, R. T., SKEPU, A. & VAN DER LINGEN, E. 2011. Synthesis, density functional theory, molecular dynamics and electrochemical studies of 3-thiopheneacetic acid-capped gold nanoparticles. *Journal of Molecular Structure,* 1006**,** 494-501.

SOUSA, S. F., FERNANDES, P. A. & RAMOS, M. J. 2007. General performance of density functionals. *The Journal of Physical Chemistry A,* 111**,** 10439-52.

SPERLING, R. A., AISEN, P. S., BECKETT, L. A., BENNETT, D. A., CRAFT, S., FAGAN, A. M., IWATSUBO, T., JACK, C. R., JR., KAYE, J., MONTINE, T. J., PARK, D. C., REIMAN, E. M., ROWE, C. C., SIEMERS, E., STERN, Y., YAFFE, K., CARRILLO, M. C., THIES, B., MORRISON-BOGORAD, M., WAGSTER, M. V. & PHELPS, C. H. 2011. Toward defining the preclinical stages of Alzheimer's disease: recommendations from the National Institute on Aging-Alzheimer's Association workgroups on diagnostic guidelines for Alzheimer's disease. *Alzheimer's & Dementia: The Journal of the Alzheimer's Association,* 7**,** 280-92.

STASHANS, A., MARCILLO, F. & CASTILLO, D. 2015. Dopamine Adsorption Configurations On Anatase (101) Surface. *Surface Review and Letters,* 22**,** 1550052(1-6).

STEPHENS, P. J., DEVLIN, F. J., CHABALOWSKI, C. F. & FRISCH, M. J. 1994. Ab initio calculation of vibrational absorption and circular dichroism spectra using density functional force fields. *The Journal of Physical Chemistry,* 98**,** 11623-7.

SUBBA RAMAIAH, K. & SUNDARA RAJA, V. 2006. Structural and electrical properties of fluorine doped tin oxide films prepared by spray-pyrolysis technique. *Applied Surface Science,* 253**,** 1451-8.

SUN, G., YAN, J., NIU, P. & MENG, D. 2016. Electronic structure and optical property of p-type Zn-doped SnO 2 with Sn vacancy. *Journal of Semiconductors,* 37**,** 023005(1-6).

SUN, H. 1998. COMPASS: An ab initio force-field optimized for condensed-phase applicationsoverview with details on alkane and benzene compounds. *The Journal of Physical Chemistry B,* 102**,** 7338-64.

SUN, H., REN, P. & FRIED, J. R. 1998. The COMPASS force field: Parameterization and validation for phosphazenes. *Computational and Theoretical Polymer Science,* 8**,** 229-46.

SUN, W. & CEDER, G. 2013. Efficient creation and convergence of surface slabs. *Surface Science,* 617**,** 53-9.

SUPRUN, E. V., KHMELEVA, S. A., RADKO, S. P., ARCHAKOV, A. I. & SHUMYANTSEVA, V. V. 2016a. Electrochemical analysis of amyloid-β domain 1-16 isoforms and their complexes with Zn(II) ions. *Electrochimica Acta,* 187**,** 677-83.

SUPRUN, E. V., KHMELEVA, S. A., RADKO, S. P., KOZIN, S. A., ARCHAKOV, A. I. & SHUMYANTSEVA, V. V. 2016b. Direct electrochemical oxidation of amyloid-β peptides via tyrosine, histidine, and methionine residues. *Electrochemistry Communications,* 65**,** 53-6.

SUPRUN, E. V., ZARYANOV, N. V., RADKO, S. P., KULIKOVA, A. A., KOZIN, S. A., MAKAROV, A. A., ARCHAKOV, A. I. & SHUMYANTSEVA, V. V. 2015. Tyrosine based electrochemical analysis of amyloid-β fragment (1-16) binding to metal(II) ions. *Electrochimica Acta,* 179**,** 93-9.

SVANE, A. & ANTONCIK, E. 1987. Electronic structure of rutile SnO_2, GeO_2 and TeO_2. *Journal of Physics and Chemistry of Solids,* 48**,** 171-80.

SYRES, K., THOMAS, A., BONDINO, F., MALVESTUTO, M. & GRÄTZEL, M. 2010. Dopamine adsorption on anatase TiO_2(101): A photoemission and NEXAFS spectroscopy study. *Langmuir,* 26**,** 14548-55.

SYRES, K. L., THOMAS, A. G., FLAVELL, W. R., SPENCER, B. F., BONDINO, F., MALVESTUTO, M., PREOBRAJENSKI, A. & GRÄTZEL, M. 2012. Adsorbate-Induced modification of surface electronic structure: Pyrocatechol adsorption on the anatase TiO_2 (101) and rutile TiO_2 (110) surfaces. *The Journal of Physical Chemistry C,* 116**,** 23515-25.

TAHANY RAMZY, H. W., MERVAT HARVY, SAFAA MORSY, MAGDY ASHOUR, FATMA MORSY 2011. Serum levels of S100B and oxidative stress parameters in Alzheimer's disease (AD) in experimental animals. *Journal of Applied Sciences Research,* 7**,** 1411-8

TANG, H., BERGER, H., SCHMID, P. E., LÉVY, F. & BURRI, G. 1993. Photoluminescence in TiO_2 anatase single crystals. *Solid State Communications,* 87**,** 847-50.

TANG, Y., PAN, X., ZHANG, C., DAI, S., KONG, F., HU, L. & SUI, Y. 2010. Influence of different electrolytes on the reaction mechanism of a triiodide/iodide redox couple on the platinized FTO glass electrode in dye-sensitized solar cells. *The Journal of Physical Chemistry C,* 114**,** 4160-7.

TELES, F. R. R. & FONSECA, L. R. 2008. Trends in DNA biosensors. *Talanta,* 77**,** 606-23.

TENGVALL, P. & LUNDSTRÖM, I. 1992. Physico-chemical considerations of titanium as a biomaterial. *Clinical Materials,* 9**,** 115-34.

TESFAMICHAEL, T., WILL, G., COLELLA, M. & BELL, J. 2003. Optical and electrical properties of nitrogen ion implanted fluorine doped tin oxide films. *Nuclear Instruments and Methods in Physics Research Section B: Beam Interactions with Materials and Atoms,* 201**,** 581-8.

THAL, L. J., KANTARCI, K., REIMAN, E. M., KLUNK, W. E., WEINER, M. W., ZETTERBERG, H., GALASKO, D., PRATICO, D., GRIFFIN, S., SCHENK, D. & SIEMERS, E. 2006. The role of biomarkers in clinical trials for Alzheimer disease. *Alzheimer Disease & Associated Disorders,* 20**,** 6-15.

THANGARAJU, B. 2002. Structural and electrical studies on highly conducting spray deposited fluorine and antimony doped SnO_2 thin films from $SnCl_2$ precursor. *Thin Solid Films,* 402**,** 71-8.

THÉVENOT, D. R., TOTH, K., DURST, R. A. & WILSON, G. S. 2001. Electrochemical biosensors: Recommended definitions and classification1. *Biosensors and Bioelectronics,* 16**,** 121-31.

THOMAS, A. G. & SYRES, K. L. 2012. Adsorption of organic molecules on rutile TiO_2 and anatase TiO_2 single crystal surfaces. *Chemical Society Reviews,* 41**,** 4207-17.

THORNALLEY, P. J. 1998. Glutathione-dependent detoxification of alpha-oxoaldehydes by the glyoxalase system: Involvement in disease mechanisms and antiproliferative activity of glyoxalase I inhibitors. *Chemico-Biological Interactions,* 111-112**,** 137-51.

TIAN & LIU 2006. DFT description on electronic structure and optical absorption properties of anionic S-doped anatase TiO_2. *The Journal of Physical Chemistry B,* 110**,** 17866-71.

TIWARI, A. & SYVÄJÄRVI, M. 2015. *Graphene materials: Fundamentals and emerging applications,* United States, John Wiley & Sons.

TOSI, M., SEITZ, F. & TURNBULL, D. 1964. *Solid State Physics,* United States, Academic Press.

TOTHILL, I. E. 2009. Biosensors for cancer markers diagnosis. *Seminars in Cell & Developmental Biology,* 20**,** 55-62.

TOUKMAJI, A. Y. & BOARD, J. A. 1996. Ewald summation techniques in perspective: A survey. *Computer Physics Communications,* 95**,** 73-92.

TSUKAMOTO, T., ISHIKAWA, Y., SENGOKU, Y. & KURITA, N. 2009. A combined DFT/Green's function study on electrical conductivity through DNA duplex between Au electrodes. *Chemical Physics Letters,* 474**,** 362-5.

TSUNEDA, T., SUZUMURA, T. & HIRAO, K. 1999. A new one-parameter progressive Colle–Salvetti-type correlation functional. *The Journal of Chemical Physics,* 110**,** 10664-78.

VAN REENEN, A., DE JONG, A. M., DEN TOONDER, J. M. J. & PRINS, M. W. J. 2014. Integrated lab-on-chip biosensing systems based on magnetic particle actuation - a comprehensive review. *Lab on a Chip,* 14**,** 1966-86.

VANOMMESLAEGHE, K., GUVENCH, O. & MACKERELL, A. D. 2014. Molecular Mechanics. *Current Pharmaceutical Design,* 20**,** 3281-92.

VARGHESE, O. K., GONG, D., PAULOSE, M., ONG, K. G., DICKEY, E. C. & GRIMES, C. A. 2003. Extreme changes in the electrical resistance of titania nanotubes with hydrogen exposure. *Advanced Materials,* 15**,** 624-7.

VASHIST, S., VENKATESH, A. G., MITSAKAKIS, K., CZILWIK, G., ROTH, G., VON STETTEN, F. & ZENGERLE, R. 2012. Nanotechnology-Based biosensors and diagnostics: Technology push versus industrial/healthcare requirements. *BioNanoScience,* 2**,** 115-26.

VASSAR, R., KOVACS, D. M., YAN, R. & WONG, P. C. 2009. The beta-secretase enzyme BACE in health and Alzheimer's disease: regulation, cell biology, function, and therapeutic potential. *The Journal of Neuroscience: The Official Journal of The Society for Neuroscience,* 29**,** 12787-94.

VEGA-ARROYO, M., LEBRETON, P. R., ZAPOL, P., CURTISS, L. A. & RAJH, T. 2007. Quantum chemical study of TiO_2/dopamine-DNA triads. *Chemical Physics,* 339**,** 164-72.

VESTERGAARD, M. D., KERMAN, K., KIM, D.-K., HIEP, H. M. & TAMIYA, E. 2008. Detection of Alzheimer's tau protein using localised surface plasmon resonance-based immunochip. *Talanta,* 74**,** 1038-42.

VOSKO, S. H., WILK, L. & NUSAIR, M. 1980. Accurate spin-dependent electron liquid correlation energies for local spin density calculations: a critical analysis. *Canadian Journal of Physics,* 58**,** 1200-11.

WAGEMAKER, M., KEARLEY, G. J., VAN WELL, A. A., MUTKA, H. & MULDER, F. M. 2003. Multiple Li positions inside oxygen octahedra in lithiated TiO_2 Anatase. *Journal of the American Chemical Society,* 125**,** 840-8.

WALTON, H. S. & DODD, P. R. 2007. Glutamate–glutamine cycling in Alzheimer's disease. *Neurochemistry International,* 50**,** 1052-66.

WANG, H., FORSE, A. C., GRIFFIN, J. M., TREASE, N. M., TROGNKO, L., TABERNA, P.-L., SIMON, P. & GREY, C. P. 2013. In situ NMR spectroscopy of supercapacitors: Insight into the charge storage mechanism. *Journal of the American Chemical Society,* 135**,** 18968-80.

WANG, H., LIU, H. & LIU, R. M. 2003. Gender difference in glutathione metabolism during aging in mice. *Experimental Gerontology,* 38**,** 507-17.

WANG, H., ZHANG, C., LIU, Z., WANG, L., HAN, P., XU, H., ZHANG, K., DONG, S., YAO, J. & CUI, G. 2011. Nitrogen-doped graphene nanosheets with excellent lithium storage properties. *Journal of Materials Chemistry,* 21**,** 5430-4.

WANG, J., LIU, G. & LIN, Y. 2006. Amperometric choline biosensor fabricated through electrostatic assembly of bienzyme/polyelectrolyte hybrid layers on carbon nanotubes. *Analyst,* 131**,** 477-83.

WANG, J. T., SHI, X. L., LIU, W. W., ZHONG, X. H., WANG, J. N., PYRAH, L., SANDERSON, K. D., RAMSEY, P. M., HIRATA, M. & TSURI, K. 2014. Influence of preferred orientation on the electrical conductivity of fluorine-doped tin oxide films. *Scientific Reports,* 4**,** 3679(1-9).

WANG, Q. H., JIN, Z., KIM, K. K., HILMER, A. J., PAULUS, G. L. C., SHIH, C.-J., HAM, M.-H., SANCHEZ-YAMAGISHI, J. D., WATANABE, K., TANIGUCHI, T., KONG, J., JARILLO-HERRERO, P. & STRANO, M. S. 2012. Understanding and controlling the substrate effect on graphene electron-transfer chemistry via reactivity imprint lithography. *Nature Chemistry,* 4**,** 724-32.

WEINAN, E. & DONG, C. 2008. The Andersen thermostat in molecular dynamics. *Communications on Pure and Applied Mathematics,* 61**,** 96-136.

WHITE, A. R., BARNHAM, K. J. & BUSH, A. I. 2006. Metal homeostasis in Alzheimer's disease. *Expert Review of Neurotherapeutics,* 6**,** 711-22.

WILLIAMS, S. C. P. 2013. Alzheimer's disease: Mapping the brain's decline. *Nature,* 502**,** S84-5.

WOLFBEIS, O. S. 2008. Fiber-optic chemical sensors and biosensors. *Analytical Chemistry,* 80**,** 4269-83.

WORLD HEALTH ORGANIZATION 2015. The epidemiology and impact of Dementia current state and future trends. Switzerland: World Health Organization.

WU, C. C., KU, B. C., KO, C. H., CHIU, C. C., WANG, G. J., YANG, Y. H. & WU, S. J. 2014. Electrochemical impedance spectroscopy analysis of A-beta (1-42) peptide using a nanostructured biochip. *Electrochimica Acta,* 134**,** 249-57.

XIA, N., ZHANG, Y., GUAN, P., HAO, Y. & LIU, L. 2015. A simple and label-free electrochemical method for detection of beta-site amyloid precursor protein cleaving enzyme and screening of its inhibitor. *Sensors and Actuators B: Chemical,* 213**,** 111-5.

XU, J., HUANG, S. & WANG, Z. 2009. First principle study on the electronic structure of fluorine-doped SnO_2. *Solid State Communications,* 149**,** 527-31.

YADAV, A. A., MASUMDAR, E. U., MOHOLKAR, A. V., NEUMANN-SPALLART, M., RAJPURE, K. Y. & BHOSALE, C. H. 2009. Electrical, structural and optical properties of SnO_2:F thin films: Effect of the substrate temperature. *Journal of Alloys and Compounds,* 488**,** 350-5.

YAN, L., ELENEWSKI, J. E., JIANG, W. & CHEN, H. 2015. Computational modeling of self-trapped electrons in rutile TiO_2. *Physical Chemistry Chemical Physics,* 17**,** 29949-57.

YANG, H. G., SUN, C. H., QIAO, S. Z., ZOU, J., LIU, G., SMITH, S. C., CHENG, H. M. & LU, G. Q. 2008. Anatase TiO_2 single crystals with a large percentage of reactive facets. *Nature,* 453**,** 638-41.

YANG, J., REN, Y., TIAN, A. M. & SUN, H. 2000. COMPASS force field for 14 inorganic molecules, He, Ne, Ar, Kr, Xe, H_2, O_2, N_2, NO, CO, CO_2, NO_2, CS_2, and SO_2, in liquid phases. *The Journal of Physical Chemistry B,* 104**,** 4951-7.

YANG, Y., FENG, Q., WANG, W. & WANG, Y. 2013. First-principle study on the electronic and optical properties of the anatase TiO_2 (101) surface. *Journal of Semiconductors,* 34**,** 073004(1-5).

YIN, H., WADA, Y., KITAMURA, T., KAMBE, S., MURASAWA, S., MORI, H., SAKATA, T. & YANAGIDA, S. 2001. Hydrothermal synthesis of nanosized anatase and rutile TiO_2 using amorphous phase TiO_2. *Journal of Materials Chemistry,* 11**,** 1694-1703.

YOGESWARAN, U. & CHEN, S.-M. 2008. A Review on the electrochemical sensors and biosensors composed of nanowires as sensing material. *Sensors,* 8**,** 290-313.

YOUNG, D. 2001. *Computational chemistry: A practical guide for applying techniques to real world problems,* USA, John Wiley & Sons.

YU, H. Z., LUO, C. Y., SANKAR, C. G. & SEN, D. 2003. Voltammetric procedure for examining DNA-modified surfaces: Quantitation, cationic binding activity, and electron-transfer kinetics. *Analytical Chemistry,* 75**,** 3902-7.

YUE, J., JIANG, X. & YU, A. 2013. Adsorption of the OH Group on SnO_2(110) oxygen bridges: A molecular dynamics and density functional theory study. *The Journal of Physical Chemistry C,* 117**,** 9962-9.

ZABAN, A., ARUNA, S. T., TIROSH, S., GREGG, B. A. & MASTAI, Y. 2000. The effect of the preparation condition of TiO_2 colloids on their surface structures. *The Journal of Physical Chemistry B,* 104**,** 4130-3.

ZAMPA, M. F., ARAÚJO, I. M. D. S., DOS SANTOS JÚNIOR, J. R., ZUCOLOTTO, V., LEITE, J. R. D. S. A. & EIRAS, C. 2012. Development of a novel biosensor using cationic antimicrobial peptide and nickel phthalocyanine ultrathin films for electrochemical detection of dopamine. *International Journal of Analytical Chemistry,* 2012**,** 1-7.

ZHANG, H. & F. BANFIELD, J. 1998. Thermodynamic analysis of phase stability of nanocrystalline titania. *Journal of Materials Chemistry,* 8**,** 2073-6.

ZHANG, L., HAN, Y., ZHAO, F., SHI, G. & TIAN, Y. 2015. A selective and accurate ratiometric electrochemical biosensor for monitoring of Cu^{2+} ions in a rat brain. *Analytical Chemistry,* 87**,** 2931-6.

ZHANG, X., CHEN, Q., TANG, J., HU, W. & ZHANG, J. 2014. Adsorption of SF6 decomposed gas on anatase (101) and (001) surfaces with oxygen defect: A density functional theory study. *Scientific Reports,* 4**,** 4762(1-11).

ZHANG, Y., ZHOU, H. & OU-YANG, Z. C. 2001. Stretching single-stranded DNA: Interplay of electrostatic, base-pairing, and base-pair stacking interactions. *Biophysical Journal,* 81**,** 1133-43.

ZHANG, Z., WANG, C. C., ZAKARIA, R. & YING, J. Y. 1998. Role of particle size in nanocrystalline TiO_2-based photocatalysts. *The Journal of Physical Chemistry B,* 102**,** 10871-8.

ZHANG, Z. W., ZHENG, W. T. & JIANG, Q. 2011. Hydrogen adsorption on Ce/SWCNT systems: A DFT study. *Physical Chemistry Chemical Physics,* 13**,** 9483-9.

ZHAO, W., AI, Z., DAI, J. & ZHANG, M. 2014a. Enhanced photocatalytic activity for H_2 evolution under irradiation of UV–Vis light by Au-modified nitrogen-doped TiO_2. *PLoS ONE,* 9**,** e103671(1-10).

ZHAO, Y., LIU, D., TANG, H., LU, J. & CUI, F. 2014b. A MD simulation and analysis for aggregation behaviors of nanoscale zero-valent iron particles in water via MS. *The Scientific World Journal,* 2014**,** 1-13.

ZHOU, J., WANG, W., YU, P., XIONG, E., ZHANG, X. & CHEN, J. 2014. A simple label-free electrochemical aptasensor for dopamine detection. *RSC Advances,* 4**,** 52250-5.

ZHU, Y., CARVEY, P. M. & LING, Z. 2006. Age-related changes in glutathione and glutathione-related enzymes in rat brain. *Brain Research,* 1090**,** 35-44.

ZUKER, M. 2003. Mfold web server for nucleic acid folding and hybridization prediction. *Nucleic Acids Research,* 31**,** 3406-15.

ZUKER, M. & SANKOFF, D. 1984. RNA secondary structures and their prediction. *Bulletin of Mathematical Biology,* 46**,** 591-621.

APPENDICES

APPENDIX I: MD trajectories for FTO, TiO_2/FTO, and DA/TiO_2/FTO layers upon ss-DNA interactions (1-9 ns)

Layer I (FTO)

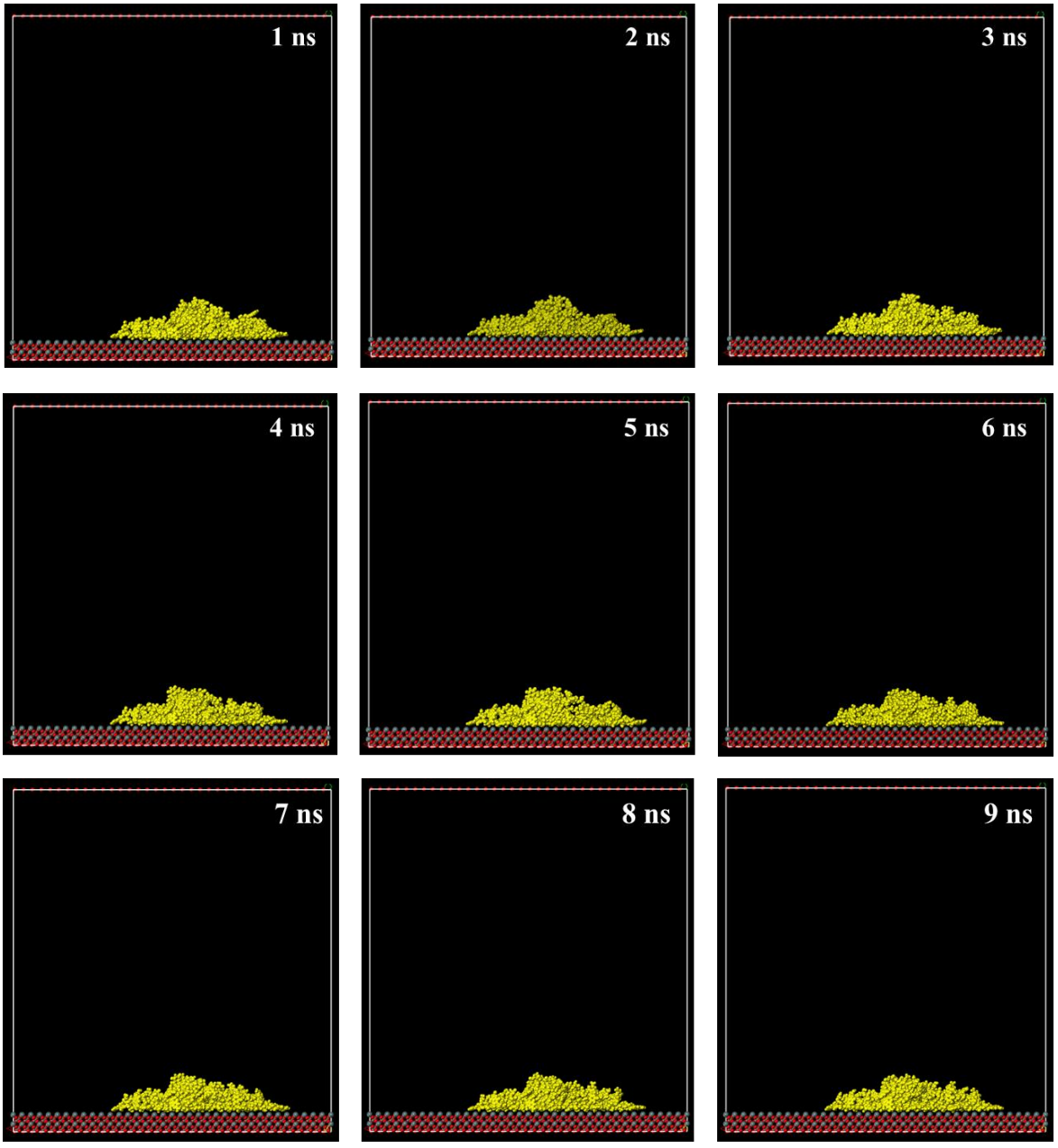

Layer II (TiO_2/FTO)

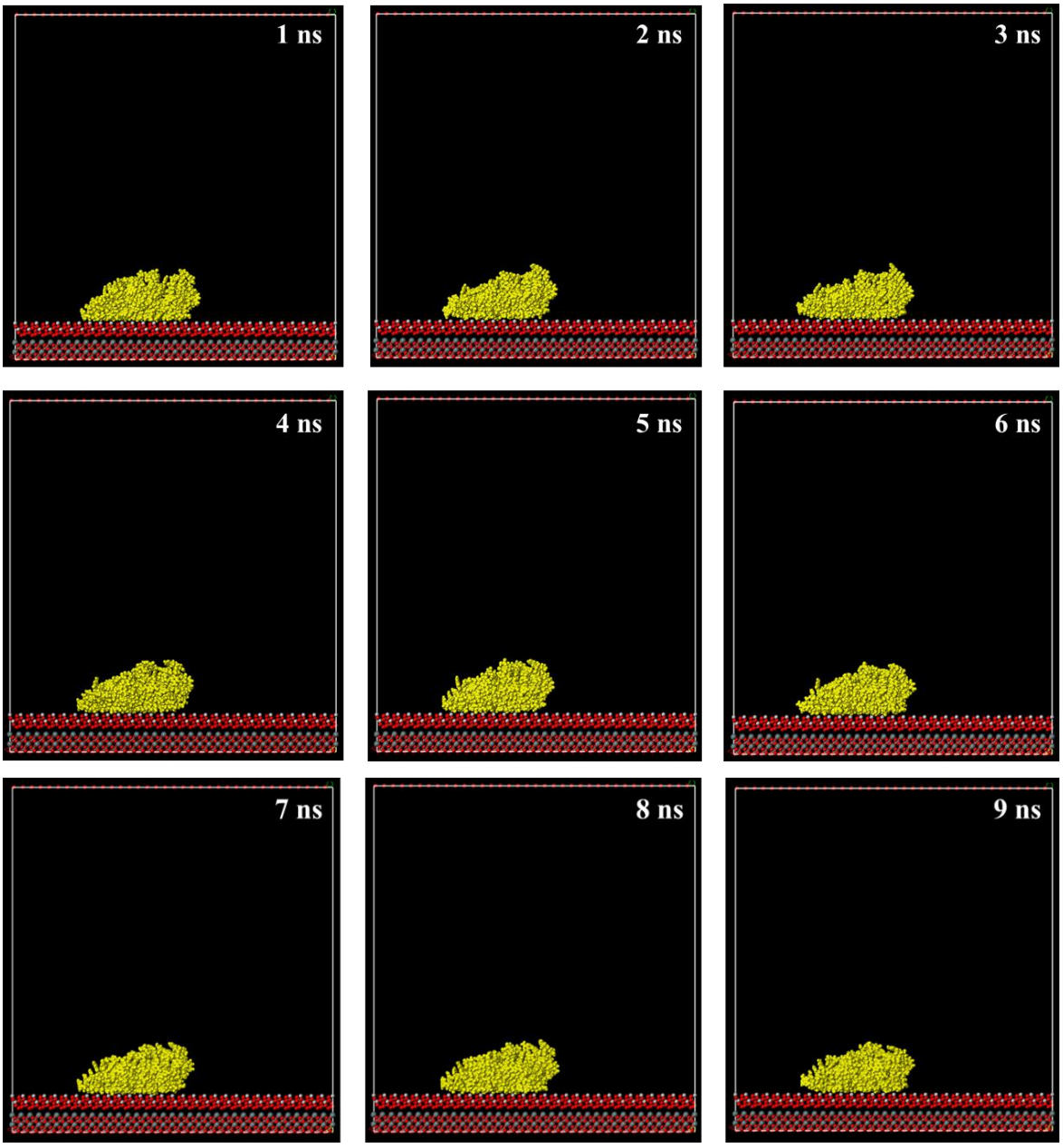

Layer III (DA/TiO_2/FTO)